Design of a Fuel Cell Hybrid Electric Vehicle Drive System

Schaltz, Erik

Publication date:
2010

Document Version
Publisher's PDF, also known as Version of record

Dissertation submitted to the Faculties of Engineering, Science and Medicine at Aalborg University in partial fulfillment of the requirements for the degree of Doctor of Philosophy in Electrical Engineering

Design of a Fuel Cell Hybrid Electric Vehicle Drive System

by

Erik Schaltz

Aalborg University
Department of Energy Technology
Aalborg, Denmark
August 2010

Design of a Fuel Cell Hybrid Electric Vehicle Drive System

Printed in Denmark by Uniprint, 2010

Second print, August 2010

ISBN 978-87-89179-81-0

Aalborg University
Department of Energy Technology
Pontoppidanstraede 101
9220 Aalborg
Denmark

Preface

In order to fulfill the requirements for obtaining the PhD degree, this thesis is submitted to the Faculties of Engineering, Science and Medicine at Aalborg University.

This PhD project was initiated by Prof. Frede Blaabjerg, who also was my supervisor the first two months of the project period. Due to outer circumstances my current supervisor Assoc. Prof. Peter Omand Rasmussen took over where Prof. Frede Blaabjerg left. I would like to thank them both for their support.

The PhD project is a part of the consortium Fuel Cell Shaft Power Pack (FCSPP), which is supported by The Danish Council for Technology and Innovation and several companies and research institutions. I would like to thank all the consortium partners for the cooperation during the project period. Especially thanks to Anders Elkjær Tønnesen, Danish Technological Institute, for providing field measurements, and to Claus Marcussen, previously Migatronic, for the construction of a fuel cell converter.

A special thanks also goes to Søren Juhl Andreassen, Torben Nørregaard Matzen, Uffe Jakobsen, Laszlo Mathe (all colleagues at Department of Energy Technology), and Jesper Lebæk (industrial PhD student at the Danish Technological Institute) for their support and interesting discussions during the PhD period.

During the project period I was visiting the Illinois Institute of Technology, Chicago, USA, for three months. I would like to thank Prof. Ali Emadi and Assis. Prof. Alireza Khaligh for their kind hospitably and cooperation.

Great thanks go also to Exide Technologies A/S for sponsoring batteries to the project.

Finally I would like to thank my family for the wonderful support I always have received.

Aalborg, Denmark, August 2010

Erik Schaltz

Abstract

Fuel cells achieve more and more attention due to their potential of replacing the traditional internal combustion engine (ICE) used in the area of transportation. In this PhD thesis a fuel cell shaft power pack (FCSPP) is designed and implemented in a small truck. The FCSPP replaces the original supply system of the truck which was powered by a lead-acid battery package. The FCSPP includes fuel storage, a fuel cell system, an energy storage device, power electronics, an electric machine, and the necessary control. The FCSPP therefore converts the energy of the fuel to a shaft torque and speed of the electric machine.

In this thesis the High Temperature Proton Exchange Membrane Fuel Cell (HT-PEMFC) is used as it has promising properties for being supplied by reformed methanol, instead of pure hydrogen, which is more practical feasible. It takes approximately 6 minutes before the fuel cell is ready to produce power. In this period an energy storage device is necessary in order to provide power for the electric machines, and to heat-up the fuel cell stack. The energy storage device also takes care of the peak loads, the high load dynamics, and it utilizes the braking energy in order to increase the efficiency. In this work a lead-acid battery, an ultracapacitor, or a combination of both are considered as energy storage devices.

A FCSPP is designed for 10 different configurations of connecting the energy storage device(s) and fuel cell to a common bus, which comply with the 42V PowerNet standard. Each of the ten configurations is designed for different fuel cell power ratings. The FCSPP is designed in an iterative process where the power flow through the system is under the influence of a certain energy management strategy and charging strategy, which sufficiently divides the power between the units.

The FCSPP is designed from a driving cycle which is constructed from field measurements of the original battery-powered truck.

Due to the long heating-time of the fuel cell, it is not appropriate to use ultracapacitors as the only energy storage device, because the system then becomes too big and heavy, even though they provides the highest system efficiency among the three options of energy storage devices. The system volume, mass, and efficiency are improved by increasing the rated fuel cell power. However, when a battery is included it has a negative effect on the battery lifetime to increase the fuel cell power rating, as the partial load cycles then becomes dominating. Simulation result indicates that the system efficiency and battery lifetime can be improved by adding ultracapacitors, because they can handle the shallow cycles, so they not are directed to the battery. However, this indication is based on insufficient data of the battery lifetime at small cycles, and a better model for the battery lifetime is therefore necessary.

The used 42V PowerNet standard is within the range of the voltage characteristic

of the used fuel cell stack. Therefore a non-inverting buck-boost converter is inserted in the between, which is able to both buck and boost the voltage depending on the actual fuel cell power level. A method where the converter is operated in a combination of buck-mode and boost-mode provides the smoothest transition between the two modes.

Dansk Resumé

Brændselsceller opnår større og større opmærksomhed, da de har et potentiale til at erstatte den traditionelle forbrændingsmotor, der bliver brugt til transportformål. I denne ph.d. afhandling designes og implementeres en Fuel Cell Shaft Power Pack (FCSPP) i et lille køretøj. FCSPPen erstatter køretøjets oprindelige drivsystem, der blev forsynet af en bly-syre batteripakke. FCSPPen indeholder et brændselslager, en brændselscelle, et energilager, effektelektronik, en elektrisk maskine, og den nødvendige kontrol. I en FCSPP er energien i brændslet derfor konverteret om til en given hastighed og moment på motorakslen.

I denne afhandling benyttes en High Temperature Proton Exchange Membran Fuel Cell (HTPEMFC) som brændselscelle, da den har lovende egenskaber til at kunne udnytte reformeret metanol, der er nemmere at håndtere end brint under tryk. Det tager ca. 6 minutter at varme brændselscellen op. I dette tidsrum kan brændselscellen ikke producere strøm, og det er derfor nødvendigt med et energilager, der kan forsyne motorerne og opvarme brændselscellen. Energilagret tager sig desuden af spidsbelastningerne, de hurtige last ændringer, og det kan også opsamle bremseenergien, hvorved virkningsgraden kan øges. I denne afhandling benyttes et bly-syre batteri, en ultrakondensator eller en kombination af begge som energilagre.

Ti forskellige konfigurationer til at forbinde energilagret og brændselscellen til en fælles bus undersøges. Den valgte bus benytter 42V PowerNet standarden. Hver af de 10 konfigurationer designes for forskellige nominelle brændselscelleeffekter. FCSPPen designes i en iterativ proces, hvor en energistyringsstrategi og opladningsstrategi fordeler effekten mellem de forskellige enheder på en hensigtsmæssig måde.

For at designe FCSPPen, benyttes en drivcyklus, der er konstrueret ud fra målinger foretaget på det oprindelige batteridrevne køretøj.

På grund af den lange opvarmningstid, er det uhensigtsmæssigt kun at benytte ultrakondensatorer som energilager, da systemet derved bliver for stort og tungt. Den største systemvirkningsgrad opnås dog på denne måde. Systemvirkningsgraden, størrelsen og massen forbedres ved at øge den nominelle brændselscelleeffekt. Når et batteri indgår mindskes batterilevetiden dog ved at øge brændselscelleeffekten, da de cykliske dellaster derved er dominerende med hensyn til levetiden. Simuleringsresultater indikerer, at system virkningsgraden og batterilevetiden kan forbedres ved at inkludere ultrakondensatorer, da ultrakondensatorerne derved kan tage sig af de cykliske dellaster i stedet for batteriet. Denne indikation er dog baseret på utilstrækkelig data angående batterilevetiden ved små cyklusser. En bedre model af batterilevetiden er derfor nødvendig.

Den benyttede 42V PowerNet standard har en spænding, der ligger mellem brændselscellens yderpunkter. En ikke-inverterende buck-boost-konverter er derfor

indsat mellem brændselscellestakken og bussen. Konverteren skal både kunne øge og sænke spændingen alt afhæng af, hvilken strøm der trækkes fra brændselscellen. En metode, hvor konverteren opererer i både buck-tilstand og boost-tilstand, resulterer i den mest glatte overgang mellem de to tilstande.

Nomenclature

AC	Alternating Current
Bat	Battery
CCM	Continuous Conduction Mode
DC	Direct Current
DSP	Digital Signal Processor
EIS	Electrochemical Impedance Spectroscopy
EM	Electric Machine
EMF	Electro Motive Force
EMI	Electro Magnetic-Interference
EMS	Energy Management Strategy
EUDC	Extra Urban Driving Cycle
FC	Fuel Cell
FCSPP	Fuel Cell Shaft Power Pack
HTPEMFC	High Temperature Proton Exchange Membrane Fuel Cell
HS	Hydrogen Storage
ICE	Internal Combustion Engine
IM	Induction Machine
LiIon	Lithium Ion
LTPEMFC	Low Temperature Proton Exchange Membrane Fuel Cell
MOSFET	Metal Oxide Semiconductor Field Effect Transistor
NiCd	Nickel Cadmium
NiMH	Nickel Metal Hydride
NYCC	New York City Cycle
PE	Power Electronics
PEM	Proton Exchange Membrane
PMSM	Permanent Magnet Synchronous Machine
PWM	Pulse Width Modulation
RMS	Root Mean Square
SRM	Switch Reluctance Machine
UC	Ultracapacitor

Contents

Preface iii

Abstract v

Dansk Resumé vii

Nomenclature ix

Contents x

I Preliminaries 1

1 Introduction 3
- 1.1 Background of the PhD Project . . . 3
- 1.2 The GMR Truck . . . 5
- 1.3 Objective and Scope of the PhD Project . . . 7
- 1.4 Outline of Thesis . . . 8

2 Load Analysis 11
- 2.1 Simulation Analysis . . . 11
- 2.2 Field Measurements . . . 16
- 2.3 Selection of Driving Cycle . . . 25
- 2.4 Conclusion . . . 25

II Modeling 27

3 Fuel Cell 29
- 3.1 Fuel Cell Types . . . 29
- 3.2 Fuel Cell Characteristics . . . 29
- 3.3 Electrochemical Impedance Spectroscopy . . . 32
- 3.4 Conclusion . . . 36

4 Battery 39
- 4.1 Battery Types . . . 39
- 4.2 Specifications . . . 40
- 4.3 Voltage Modeling . . . 40

4.4 Power Capability . . . 42
4.5 Capacity Modeling . . . 42
4.6 Modeling Lifetime . . . 46
4.7 Conclusion . . . 48

5 Ultracapacitor Modeling 49
5.1 Specifications . . . 49
5.2 Inner Resistance and Equivalent Capacitance . . . 49
5.3 Self Discharge . . . 51
5.4 Charge Recovery . . . 54
5.5 Results . . . 61
5.6 Conclusion . . . 66

6 Fuel Cell Converter 69
6.1 Topology . . . 69
6.2 Efficiency . . . 71
6.3 Conclusion . . . 76

7 Drive System 79
7.1 Electric Machine . . . 79
7.2 Inverter . . . 82
7.3 Conclusion . . . 84

III Fuel Cell Truck 85

8 Design 87
8.1 System Overview . . . 87
8.2 Bus Voltage . . . 89
8.3 Configurations . . . 89
8.4 Modeling and Parameter Calculation . . . 91
8.5 Energy Management Strategy . . . 101
8.6 Design Strategy . . . 107
8.7 Simulation Results . . . 109
8.8 System Selection . . . 119
8.9 Conclusion . . . 121
8.10 Discussion . . . 122

9 Implementation 125
9.1 Overview . . . 125
9.2 Fuel Cell Converter . . . 127
9.3 Status of Implementation . . . 141
9.4 Conclusion . . . 141

IV Conclusion, Contributions, and Future Work 143

10 Conclusion 145

10.1 Preliminaries 145
10.2 Modeling 145
10.3 Design 146
10.4 Implementation 147

11 Scientific Contributions **149**

12 Future Work **151**

Bibliography **153**

V Appendices **161**

A Publications of the Author **163**

B Drive Train Modeling of the GMR Truck **165**
B.1 Battery 165
B.2 Electric Machine 165
B.3 Gear-Boxes 172
B.4 Conclusion 177

C Fuel Cell Converter Equations **179**
C.1 Circuit Diagram 179
C.2 Modes of Operation 179
C.3 Method 179
C.4 Current Controller 188
C.5 Conclusion 190

D Equations of Bi-Directional DC/DC Converter **195**
D.1 Circuit Diagram 195
D.2 Quadrant 1 195
D.3 Quadrant 2 196
D.4 Quadrant 3 197
D.5 Quadrant 4 198
D.6 Summary 199
D.7 Conclusion 199

Part I

Preliminaries

1 Introduction

One of the main sources of energy today is due to fossil fuels, i.e. coal, natural gas and fuels obtained from crude oil. However, their resources are limited, they give rise to pollution, and they have also caused political turbulence. It is therefore important to find renewable alternatives in order to satisfy the increasing energy consumption of the world. Fuel cells are a promising technology with this focus in mind.

1.1 Background of the PhD Project

This PhD project is a part of the innovation consortium Fuel Cell Shaft Power Pack (FCSPP). The consortium was initiated by the Danish Technological Institute, and it includes several research institutions and companies. The consortium partners are listed in Table 1.1.

Companies	Research institutions
Cykellet / DSR Scandinavia	Aalborg University
Dantherm A/S	Copenhagen Business School
EGJ Udvikling A/S	Danish Technological Institute
Falsled Højtryk	Hydrogen Innovation & Research Center
GMR Maskiner A/S	
H2 Logic Aps.	
KK-Electronic A/S	
Migatronic A/S	
Parker Hannifin DK	
Serenergy A/S	
Trans-Lift	
Xperion	

Table 1.1: Companies and research institutions of the FCSPP consortium per November 2009.

The purpose of the consortium is to create an alternative to the traditional internal combustion engine (ICE) used in the transportation sector, with special attention on small mobile units, e.g. mopeds, scooters, lawnmowers, etc. Even though mopeds only contribute with $0.5\,\%$ of the total amount of driven kilometers of personal transportation in Denmark, they contribute with $7\,\%$ of the hydrocarbon emissions [25]. These small motors also pollute in terms of acoustic noise, and there is therefore a need for another solution, i.e. a FCSPP.

The FCSPP Concept

The principle of a FCSPP is sketched in Figure 1.1. The FCSPP is fueled from a filling station by pure hydrogen or a hydrogen rich fuel, e.g. methanol or natural gas. The fuel is led from storage to a fuel cell system, which converts the energy of the hydrogen into electric energy. The output of the FCSPP is the shaft power of an electric machine. In order to be able to control the torque and speed of the electric machine, it is necessary also to control the current and voltage of it. This is done by power electronics, which interface the fuel cell and the electric machine.

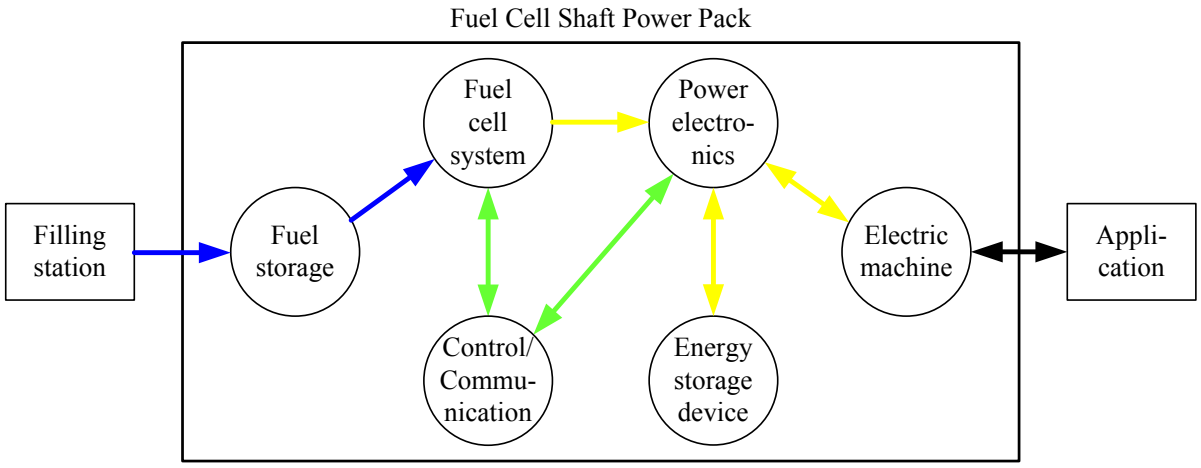

Figure 1.1: Concept of a FCSPP. Blue lines: fuel flow. Yellow lines: electric power flow. Green line: control or communication signals. Thick black line: shaft power flow.

In Figure 1.1 it is seen that an energy storage device also is a part of the FCSPP. An energy storage device offers many advantages in a fuel cell application. If the application of the FCSPP is of high dynamic, the fuel cell might not be able to regulate the power as fast as needed. The limited dynamics could either be due to the fuel cell itself, the components controlling the fuel cell, or the reforming process if the hydrogen rich fuel needs to be converted into pure, or close to pure, hydrogen before it is used by the fuel cell. An energy storage device can therefore act as a buffer, i.e. assist the fuel cell with supplying power to the load, until it can provide the power itself, or to receive power from the fuel cell due to a sudden decrease in load power. In mobile applications there is often a high short term power demand due to accelerations or up-hill driving. If the fuel cell should be able to provide this peak power the whole system might be unnecessary big, heavy, and expensive. Therefore, if the energy storage device could take care of the peak powers, the fuel cell power rating can be reduced.

Depending on the surrounding temperature, and the type of fuel cell, it might be necessary to heat-up the fuel cell to a certain temperature. While the fuel cell is being heated-up it cannot produce power, and in this period the energy storage device can supply the load with power, so the user is not delayed. The energy storage device can also provide the necessary energy to heat-up the fuel cell.

The last important feature of the energy storage device is the bi-directional power flow, i.e. it can both receive and provide power. If the application for example is a vehicle, the energy due to braking or down-hill driving can be fed to the energy storage

device instead of being wasted in the brakes of the vehicle. Thereby less fuel is being used, depending on the driving pattern of course. Many types of energy storage devices exist, but two promising technologies for vehicles are batteries and ultracapacitors. Batteries are good because of their relative high energy density, and ultracapacitors are attractive due to their high power density. Depending on the application it might also be advantageous to combine these two units.

If the voltage level of the energy storage device(s) does not suit the fuel cell or electric machine, power electronics can be inserted in between. It might also be necessary to include power electronics in order to be able to control the power flow of the energy storage device(s).

The last block of the FCSPP in Figure 1.1 is the control and communication. The control includes three aspects. The first aspect is the control of the balance-of-plant components of the fuel cell system, i.e. valves, fans, pumps, etc. They need to be controlled sufficiently to insure that the fuel cell is being operated in a proper manner. The second aspect is the control of the power electronics, e.g. if a power converter is demanded to deliver a certain amount of power, it should also deliver that amount of power, and if the user demands a specific shaft torque or speed, that power converter connected to the electric machine needs also to be controlled sufficiently so the user demanded shaft torque or speed are obtained. The third control aspect is the control of the power flow between the units, i.e. electric machine, fuel cell, and energy storage device(s). The control of the power flow is usually outside the influence of the user, and it is therefore controlled by a well defined energy management strategy (EMS). The EMS takes many issues into account when deciding the power flow, e.g. system efficiency and the health and states of the different units.

Demonstration Projects

In the consortium three demonstration projects have been carried out in order to demonstrate the FCSPP concept. The demonstration projects are in the area of small transportation vehicles and mobile units. Each vehicle or unit is already on the market, but not with a fuel cell system. The original system will therefore be replaced by a FCSPP. The three demonstration projects are

1. A truck used for parks, cemeteries, green areas, etc. The truck that is going to be converted is made by the consortium partner GMR Maskiner A/S.
2. A scooter used by the Danish postal service. The scooter used for modification is distributed by the consortium partner Cykellet.
3. A forklift truck used for ware houses. The forklift truck that will be converted is produced by the consortium partner Trans-Lift.

The research institutions and companies have therefore in cooperation built these three demonstration projects. In this PhD project the demonstration project 1, i.e. the truck from GMR Maskiner A/S, is used as application. In the following the truck will therefore be denoted the GMR Truck or simply "the truck".

1.2 THE GMR TRUCK

The GMR Truck can be seen in Figure 1.2. It has a truck bed which can turn around and tipple, and several external tools can be mounted at the back or at the front of the truck. Below the truck bed six series connected lead-acid batteries are placed. They

Mass of frame	M_{Frame}	$760\,\mathrm{kg}$
Mass of batteries	M_b	$174\,\mathrm{kg}$
Maximum load	$M_{Load,max}$	$1000\,\mathrm{kg}$
Maximum speed	$v_{Truck,max}$	$15\,\mathrm{km/h}$
Acceleration ($0\,\frac{\mathrm{km}}{\mathrm{h}}$ to $v_{Truck,max}$)	a_{Truck}	$3\,\mathrm{s}$-$5\,\mathrm{s}$
Maximum slope of road	α_{max}	$15\,\%$
Light consumption	P_{Light}	$170\,\mathrm{W}$

Table 1.2: Specifications of the GMR Truck.

provide a bus voltage of $V_b = 36\,\mathrm{V}$ and a 5 hour capacity of $Q_5 = 180\,\mathrm{Ah}$, i.e. the battery package provides a discharge current of $I_b = \frac{Q_5}{5\,\mathrm{h}} = 36\,\mathrm{A}$ for 5 hours before it is empty. The energy content is therefore $E_5 = V_b Q_5 = 6.48\,\mathrm{kWh}$. The specifications of the batteries can be seen in Table B.1 on page 165. For the propulsion two separately excited DC-motors are mounted to the rear wheels through gear-boxes. The motors each have a nominal power of $2\,\mathrm{kW}$. The specifications of the motors can be seen in Table B.2 on page 166, and the specifications of the truck itself can be seen in Table 1.2.

Figure 1.2: GMR Stama El-truck from GMR Maskiner A / S [25].

The maximum speed of the truck is $v_{Truck,max} = 15\,\mathrm{km/h}$ and it has an acceleration from 0 to full speed of $3\,\mathrm{s}$ to $5\,\mathrm{s}$. It is capable of climbing an $\alpha_{max} = 15\,\%$ slope. The maximum load that the truck can have on the truck bed is $M_{Load,max} = 1000\,\mathrm{kg}$.

Limitations of the GMR Truck

As mentioned before the truck is powered by a lead-acid battery package. This causes the following issues for the user of the truck [63]:

- Long charging time from $6\,\mathrm{h}$ to $12\,\mathrm{h}$. This means that if the battery pack is fully discharged, the user has to wait until the next day to use the truck. This is a problem if the user has forgotten to charge it the previous day or if the truck one day is used more intensive than it is designed for.
- Short hours of operation. Because of the capacity of the battery package and the long charging time the hours of operation of the truck is limited. Of course a larger battery package could be installed, but this will increase the cost.

- Short area of operation. Again because of the capacity of the battery package and long charging time, the truck is limited only to work in a short radius from its charging station as it has to be able to return to the charging spot.
- The battery package has a limited lifetime and it is therefore regularly replaced by a new one, which is quite costly and should therefore be avoided.
- Desire of an electric outlet. Sometimes the user is long away from the electric grid. It will therefore be desirable if the truck has an electric $230\,\mathrm{V}$-$50\,\mathrm{Hz}$ outlet for electric tools. However, if an outlet is mounted on the battery package it will soon be drained.

1.3 Objective and Scope of the PhD Project

All limitations of the GMR Truck mentioned above are due to the long charging time and limited capacity of the batteries. In order to overcome these limitations, the company behind the truck, GMR Maskiner A/S, prefers a solution where the truck is powered by a fuel cell, instead of only the lead-acid battery package. A fuel cell is fueled by hydrogen which can be refilled much faster than the batteries can be charged, and hydrogen storage can store more energy than a battery for the same volume or mass. The objective of this PhD project is therefore:

To design and implement a FCSPP for the GMR Truck.

Constraints

The GMR Truck that will have a FCSPP implemented will be denoted the "FC Truck", in order to differ between the original truck and the new FCSPP implementation. As mentioned in Section 1.1 the FCSPP consists of a fuel storage, fuel cell system, energy storage device, electric machine, power electronics, and the necessary control of the whole system. In the design and implementation process of the FCSPP, the project is under the following constraints:

- The FC Truck will not be designed from scratch, but it will be based on the original GMR Truck. This means that the body-frame, gear-boxes, wheels, light system, etc. will be reused. The FCSPP is therefore installed in the original chassis of the GMR Truck.
- The control and implementation of the fuel cell and the systems required to make it produce power is done in another PhD project [3] which also is a part of the FCSPP consortium.
- The fuel cell type used for implementation is of type High Temperature Proton Exchange Membrane Fuel Cell (HTPEMFC) and it will be supplied by pressurized hydrogen. See [3] for further information.
- The only external energy added to the FC Truck is the hydrogen, that the user adds to the FC Truck. Therefore, for example, an ICE cannot be added to the system, and no interaction with the electric grid is considered. Useful energy due to braking, downhill driving, or wind, are however, allowed.
- The FC Truck should at least have the same performance as the original GMR Truck with respect to driving distance, hours of operation, acceleration, speed, load capability, etc.
- As energy storage device only batteries, ultracapacitors, or a combination of these will be considered.

Methodology

In order to fulfill the objective of this PhD project the following steps will be carried out:

Load analysis In order to be able to design the FCSPP it is essential to know the load profile of the truck, as this specifies the power end energy requirements of the FCSPP. The load profile is based on simulation and field measurements.

Modeling Many units are included in the FCSPP, and it is therefore important to know how they will behave in the whole system. The modeling includes steady-state characteristics and dynamics performances. The following units will be modeled: a fuel cell, battery, ultracapacitor, electric machine, inverter, and a fuel cell DC/DC converter. The modeling is based on laboratory experiments and data sheet specifications.

Design A program that combines all the different models is created. The program investigates different configurations of FCSPPs for several fuel cell power ratings in order to be able to select the most suitable combination of the fuel cell power ratings and FCSPP configurations. The program simulates the power flow through the FCSPP, when the different constraints and characteristics of each unit are taken into account. Thereby the power and energy demands can be specified, and each unit can be sized in order to fulfill the requirements. The power flow is due to a certain energy management strategy and charging strategy of the energy storage device(s). In the design procedure it is strived to minimize the rating of the energy storage device(s) in order to reduce the system volume and mass. However, this might not have a positive effect on the system efficiency and for the configurations that include a battery, it might also be critical to the battery lifetime to try to minimize the battery. Therefore, the system volume, mass, efficiency, and battery lifetime are compared for the different configurations and fuel cell power ratings.

Implementation The different units of the FCSPP are implemented in the FC Truck. It turns out that the voltage characteristic of the used fuel cell is between the chosen bus voltage, which means that it is necessary to be able to both buck and boost the voltage. This means that it also is necessary to transit between the buck and boost modes. Different methods for transition are therefore investigated.

1.4 OUTLINE OF THESIS

The structure of the thesis is given below. The thesis consists of five parts.

Part I - Preliminaries The background of the PhD project is given and load analysis of the vehicle is performed in order to be able to design and size the FCSPP of the FC Truck later.

- **Chapter 1 - Introduction** This chapter provides the necessary background of the PhD project and the thesis. The objective, constraints and methodology of the project are presented.
- **Chapter 2 - Load Analysis** The load consumption of the GMR Truck is analyzed. The analysis is based on a simulation model of the vehicle and on field measurements.

Part II - Modeling In this part the most essential components of the FCSPP are modeled. The models are based on laboratory experiments and data sheet specifications. The models are used for the design of the FCSPP of the FC Truck.

- **Chapter 3 - Fuel Cell** In this chapter a fuel cell is modeled. Both a steady-state and dynamic model of a single cell are performed.
- **Chapter 4 - Battery** In this chapter a battery will be modeled. The model can provide the voltage, state-of-charge, and lifetime of a battery.
- **Chapter 5 - Ultracapacitor** A dynamic model of an ultracapacitor is created. It includes modeling of the capacitance, self discharge, and the slow charge recovery.
- **Chapter 6 - Fuel Cell Converter** A converter interfacing the fuel cell to the rest of the system is modeled both in steady-state and dynamic mode.
- **Chapter 7 - Drive System** The drive system consist of the electric machines and inverters. This chapter describes their models.

Part III - Fuel Cell Truck This part adds the work of the two previous parts together. The load analysis and models are used for designing and sizing the FCSPP for the FC Truck.

- **Chapter 8 - Design** In this chapter a method for designing the FCSPP of the FC Truck is presented, and a design program is created. Different configurations of a fuel cell system are investigated, and an energy management strategy and charging strategy of the energy storage device(s) are introduced. By using the design program the different combinations of the fuel cell power ratings and FCSPP configurations are sized. Afterwards the designs are compared in terms of system volume, mass, efficiency, and battery lifetime.
- **Chapter 9 - Implementation** This chapter describes the implementation of the FCSPP in the GMR truck.

Part IV - Conclusion, Contributions, and Future Work This part contains the conclusion, scientific contributions, and recommendations for future work.

- **Chapter 10 - Conclusion** This chapter contains the conclusion of the thesis.
- **Chapter 11 - Scientific Contributions** This chapter emphases the scientific contributions of the work carried out.
- **Chapter 12 - Future Work** In this chapter recommendations for future work are presented.

Part V - Appendices The appendices are supporting the main parts of the thesis.

- **Appendix A - Publications of the Author** The publications of the author during the PhD project period are here listed.
- **Appendix B - Drive Train Modeling of the GMR Truck** The drive train of the original GMR Truck is modeled in order to be able to carry out the load analysis.
- **Appendix C - Fuel Cell Converter Equations** This appendix is related to Chapter 6. Relevant transfer functions and steady-state expressions are derived, and current controllers are designed and verified.
- **Appendix D - Equations of Bi-Directional DC/DC Converter** Essential equations of a bi-directional non-inverting buck-boost converter are derived.

2 Load Analysis

The design and sizing of the FCSPP strongly depends on the load profile of the truck. In this chapter the GMR Truck load profile will therefore be analyzed. The analysis consists of two parts, i.e. a simulation analysis and an analysis based on field measurements. In the first part a simple vehicle simulation model of the truck is created so it is possible to analyze the power consumption due to the performance specifications. In the second part field measurements have been done in order to get an idea of the actual usage of the truck.

2.1 Simulation Analysis

In this section the GMR Truck will be modeled and the power consumption will be investigated for several constraints.

Vehicle Model

An often used approach is to setup a free body diagram of the vehicle. When one knows the forces affecting the vehicle, it is possible to calculate the required shaft torque and power to a specific time. In Figure 2.1, the forces acting on the truck can be seen. The forces which the motors of the truck must overcome are the forces due to gravity, wind, rolling resistance, and inertial effect. The forces of the two driving wheels on the GMR Truck are described by Equation (2.1) [21].

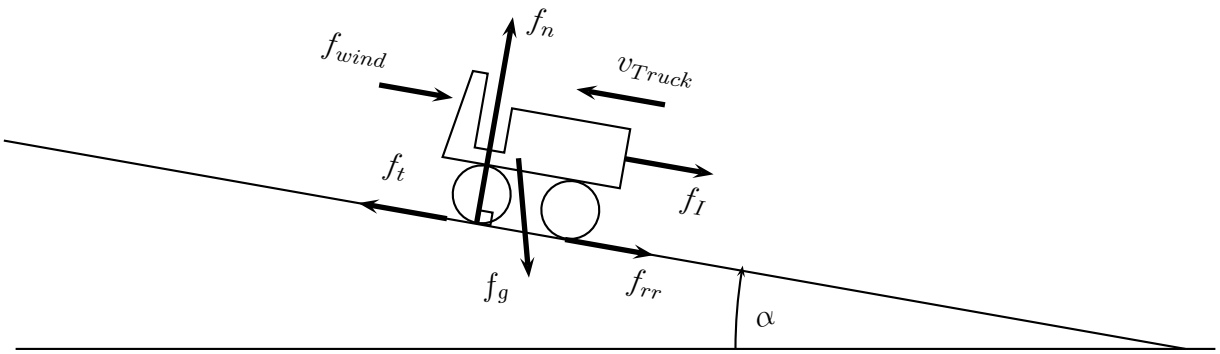

Figure 2.1: Forces acting on the truck.

$$
\begin{aligned}
2f_t = & \underbrace{\left(M_{Truck} - 2M_{gw}\right)\dot{v}_{Truck}}_{f_I} + \underbrace{M_{Truck} \cdot g}_{f_g} \cdot \sin(\alpha) \\
& + \text{sign}(v_{Truck}) \underbrace{\overbrace{M_{Truck} \cdot g \cdot \cos(\alpha)}^{f_n} \cdot C_{rr}}_{f_{rr}} \\
& + \text{sign}(v_{Truck} + v_{wind}) \underbrace{\frac{1}{2}\rho_{air} C_{drag} A_{front} \left(v_{Truck} + v_{wind}\right)^2}_{f_{wind}} \qquad [\text{N}]
\end{aligned} \tag{2.1}
$$

where	f_t	[N]	Traction force of each driving wheel
	f_I	[N]	Inertial force of the vehicle
	f_{rr}	[N]	Rolling resistance force of the wheels
	f_g	[N]	Gravitational force of the vehicle
	f_n	[N]	Normal force of the vehicle
	f_{wind}	[N]	Force due to wind resistance
	α	[rad]	Angle of the driving surface
	M_{Truck}	[kg]	Total mass of the vehicle including passengers and load
	M_{gw}	[kg]	Mass of wheel and rotating part of the gear-box
	v_{Truck}	[m/s]	Velocity of the truck
	$\dot{v}_{Truck}$	[m/s^2]	Acceleration of the truck
	$g = 9.81$	[m/s^2]	Gravity
	$\rho_{air} = 1.2041$	[kg/m^3]	Air density of dry air at 20 °C
	C_{rr}	[−]	Tire rolling resistance coefficient
	C_{drag}	[−]	Aerodynamic drag coefficient
	A_{front}	[m^2]	Front area
	v_{wind}	[m/s]	Headwind speed

Modeling of Propulsion System

The traction force f_t of the two driving wheels originates from the two electric machines of the truck. A gear-box with gear ratio G is placed between the electric machines and the wheels in order to amplify the shaft torque τ_s and to reduce the shaft angular velocity ω_s. In Appendix B on page 165 the friction torque and moment of inertia of the gear-box and wheel have been modeled as one unit. This can also be seen in Figure 2.2 where the propulsion system of the GMR Truck is shown. This unit (with moment of inertia J^s_{gw}) is placed between the electric motor and the ideal gear-box to which the wheel is attached. From Appendix B on page 165 the relationship between shaft torque τ_s and angular velocity ω_s of the electric machine, the traction force f_t and

the truck speed v_{Truck} are therefore given by the following equations:

$$\tau_s = J^s_{gw}\frac{d\omega_s}{dt} + B^s_{v,gw}\omega_s + \text{sign}(\omega_s)\tau^s_{c,gw} + \tau^s_t \quad [\text{Nm}] \quad (2.2)$$

$$\tau_t = G\tau^s_t \quad [\text{Nm}] \quad (2.3)$$

$$f_t = \frac{\tau_t}{r_w} \quad [\text{N}] \quad (2.4)$$

$$\omega_w = \frac{\omega_s}{G} \quad [\text{rad/s}] \quad (2.5)$$

$$v_{Truck} = r_w\omega_w \quad [\text{m/s}] \quad (2.6)$$

where			
	τ_s	[Nm]	Shaft torque of the electric machine
	τ_t	[Nm]	Traction torque of the wheel
	τ^s_t	[Nm]	Traction force seen from the shaft side
	ω_s	[rad/s]	Shaft angular velocity of the electric machine
	ω_w	[rad/s]	Wheel angular velocity
	v_{Truck}	[m/s]	Speed of the truck
	G	[−]	Gear ratio
	J^s_{gw}	[kgm^2]	Equivalent moment of inertia of the gear-box and wheel seen from the shaft side
	$B^s_{v,gw}$	[Nms/rad]	Equivalent viscous friction coefficient of the gear-box and wheel seen from the shaft side
	$\tau^s_{c,gw}$	[Nm]	Equivalent coulomb torque of the gear-box and wheel seen from the shaft side

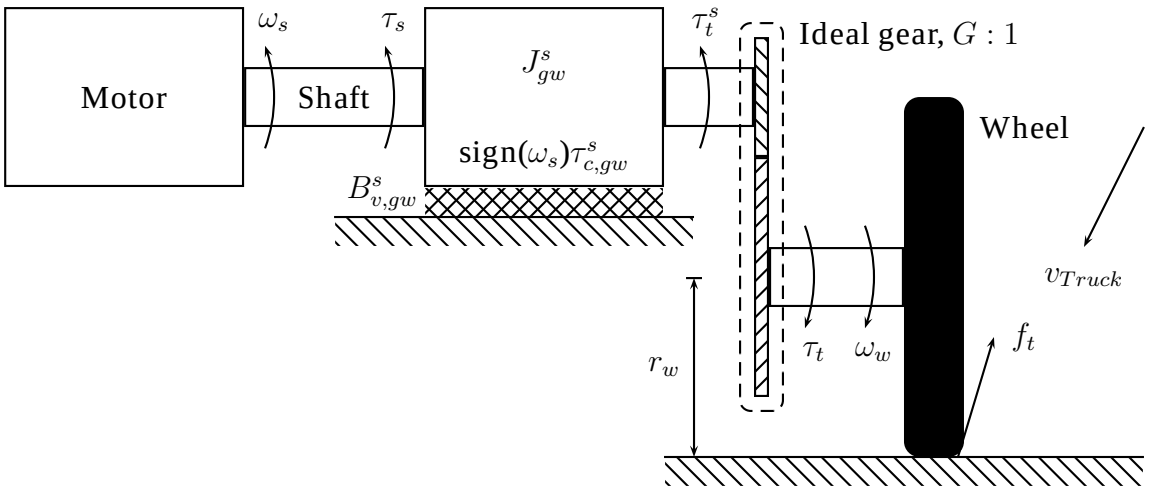

Figure 2.2: Propulsion system of the GMR Truck.

Simulation Results

A Simulink® model that is able to simulate the vehicle has been created. The input to the model is the speed and slope of a road. By using Equation (2.1) the traction force

of one wheel f_t can be calculated. Thereby the shaft torque τ_s and power p_s of one electric machine can be calculated by using Equation (2.2)- (2.6).

The truck will experience different road materials, which means that the rolling resistance coefficient can have many different values. It is chosen to use the rolling resistance coefficient of a car tire on rolled gravel, i.e. $C_{rr} = 0.02$ [21] as this is an often used underlay on cemeteries. The aerodynamic drag coefficient is chosen to be $C_{drag} = 0.6$, which is similar to a van [21]. The front area has been estimated to $A_{front} = 1.0\,\mathrm{m}^2$. The parameters of the GMR Truck can be seen in Table 2.1.

Wheel radius	r_w	$0.224\,\mathrm{m}$
Gear ratio	G	15
Rolling resistance coefficient	C_{rr}	0.02
Aerodynamic drag coefficient	C_{drag}	0.6
Front area	A_{front}	$1.0\,\mathrm{m}^2$

Table 2.1: Parameters of the GMR Truck.

A simulation is executed with a load of $0\,\mathrm{kg}$ and $1000\,\mathrm{kg}$, respectively. The results can be seen in Figure 2.3 and are due to a wind speed of $v_{wind} = 0\,\mathrm{m/s}$. The mass of the driver is assumed to be $100\,\mathrm{kg}$. The simulation is carried out in order to investigate the power consumption due to the specifications in Table 1.2 on page 6, i.e. with respect to load mass, maximum speed, maximum acceleration, and maximum gradient of the road. The slope of the road is shown in Figure 2.3(a). The slope is either zero or the maximum specified value, i.e. $\alpha = 15\,\%$. The speed of the truck can be seen in Figure 2.3(b). The truck accelerates and decellerates with the maximum value, i.e. $3\,\mathrm{s}$ from zero to the maximum speed of $v_{Truck,max} = 15\,\mathrm{km/h}$.

In Figure 2.3(c-d) it is seen that the shaft torque and power needed for accelerations and gradients is much higher than the power needed to maintain the speed at zero slope. The power consumption of the truck in Figure 2.3(d) is given in Table 2.2. From Table 2.2 it can be seen that the load mass, acceleration, and gradient have a significant influence on the power consumption. The continuous consumption at $0\,\%$ gradient is $\frac{1035-626}{626} \approx 65\,\%$ higher with full load, than with no load.

	$\alpha = 0\,\%$ $\dot{v}_{Truck} > 0$	$\alpha = 0\,\%$ $\dot{v}_{Truck} < 0$	$\alpha = 0\,\%$ $\dot{v}_{Truck} = 0$	$\alpha = 15\,\%$ $\dot{v}_{Truck} = 0$	$\alpha = -15\,\%$ $\dot{v}_{Truck} = 0$
$M_{Load} = 0\,\mathrm{kg}$	$3659\,\mathrm{W}$	$-2407\,\mathrm{W}$	$626\,\mathrm{W}$	$3774\,\mathrm{W}$	$-2532\,\mathrm{W}$
$M_{Load} = 1000\,\mathrm{kg}$	$6985\,\mathrm{W}$	$-4914\,\mathrm{W}$	$1035\,\mathrm{W}$	$7210\,\mathrm{W}$	$-5159\,\mathrm{W}$

Table 2.2: Maximum shaft power of Figure 2.3(d) under different conditions.

If the FC Truck only has one power source, i.e. the fuel cell, this power source should be able to provide the double of the maximum power of Table 2.2, i.e. at least $2 \cdot 7210\,\mathrm{W} = 14.41\,\mathrm{kW}$ for the shafts, and this is even without taking the loss from the fuel cell terminals to the shafts of the motors into consideration. However, the FCSPP for the FC Truck also has an energy storage device, which gives more degrees of freedom to rate the peak and continuous power capability of the fuel cell and energy storage device. Usually the power system of a vehicle can be designed by providing

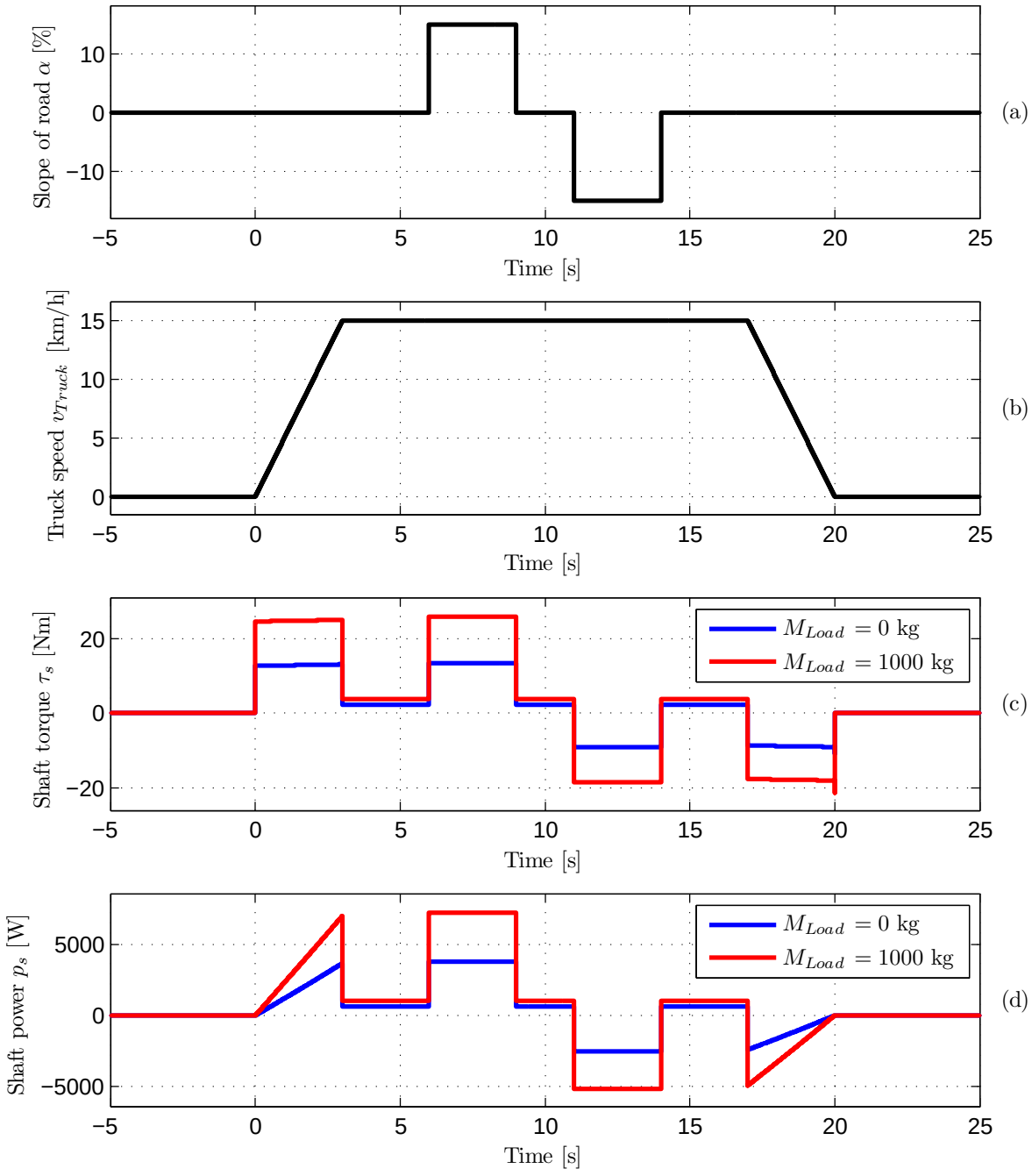

Figure 2.3: Simulation of truck for two different load masses. (a) Slope of road. (b) Truck speed. (c) Shaft torque. (d) Shaft power.

a certain driving cycle to a vehicle model, as done in this section. However, due to the big influence of the load mass and slope of the road, a time-speed profile is not enough to design the system. Therefore, in order to obtain a realistic load profile, field measurements of the vehicle have been carried out.

2.2 FIELD MEASUREMENTS

The power and energy requirements of the FC Truck strongly depend on the driving profile and the conditions the truck is exposed to. In the car industry standard driving cycles, e.g. Extra Urban Driving Cycle (EUDC), New York City Cycle (NYCC), etc, are used in order to be able to compare the fuel consumption and emissions of the cars. These standard driving cycles show a time-speed curve which then can be applied to a simulation program like the one developed in Section 2.1 or others, and thereby the power and energy requirements can be calculated. However, the vehicle in focus in this PhD project is used for special applications and no standard driving cycles therefore exist. Therefore, in order to have a realistic foundation of the power and energy requirements of the FC Truck a data logger has been mounted on one of the GMR Trucks. The truck with the data logger was used by a customer at a graveyard in Nyborg and Herning, Denmark, during the summer of 2006 and 2007, respectively.

Data Collection

The armature windings of the motors are connected in parallel, and the field windings are connected in series. Thereby only one converter is used to control the armature voltages of the motors, and also only one converter is needed in order to control the field winding currents of the motors. The overall wiring diagram of the propulsion system of the truck can be seen in Figure 2.4. The power flow is also shown. The main power flows between the right and left motors EM_r and EM_l, respectively, and the battery. However, a small portion of the battery power p_{Bat} is also used for the light p_{Light} and auxiliary devices p_{Aux}. The auxiliary devices include instrument panel, hydraulic system for the truck bed, horn, etc.

For each motor, the armature voltage and current, and the field winding current, have been measured. The battery voltage of the truck and that part of the battery current supplying the motors, have also been measured. That part of the battery current due to the two motors will in the rest of this document be denoted the "battery current", even though it is not the total battery current, but only that part which is running through the motors. In Figure 2.4 this current is denoted i_b and the corresponding power is called p_b. For the rest of this chapter this power will also be denoted the "battery power" even though it is only that part of the total battery power that is flowing to the motors. This means that the energy consumption of the light, instrument panel, etc. cannot be calculated from the data.

The time was also saved. When the absolute value of the battery current was greater than $15\,\mathrm{A}$ all the data was saved with a frequency of $100\,\mathrm{Hz}$; otherwise the frequency was $1\,\mathrm{Hz}$. All the measured signals can be seen in Table 2.3. It may be mentioned that the armature voltages are the output of a 1st order low-pass filter. Otherwise one will only see a pulsed voltage due to the DC/DC converter of the armature winding.

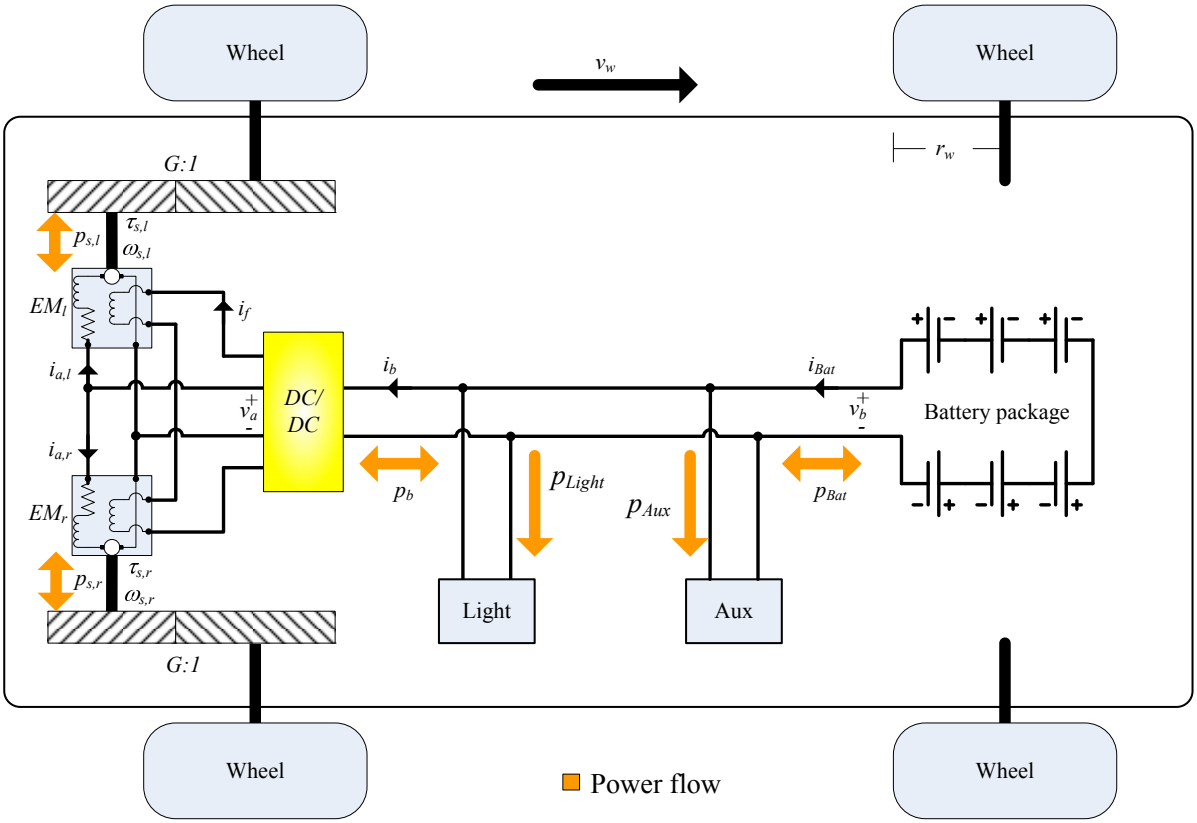

Figure 2.4: Sketch of the power and propulsion system of the GMR Truck.

Measurement	Symbol	Unit
Time	t	[s]
Battery voltage	v_b	[V]
Battery current	i_b	[A]
Armature voltage of left motor	$v_{a,l}$	[V]
Armature current of left motor	$i_{a,l}$	[A]
Field current	i_f	[A]
Armature voltage of right motor	$v_{a,r}$	[V]
Armature current of right motor	$i_{a,r}$	[A]

Table 2.3: Field measurements of the GMR Truck.

From the measurements in Table 2.3 the motor shaft torque τ_s and angular velocity ω_s can be calculated by utilizing the motor model described in Appendix B.

Presentation of Field Data

In Figure 2.5 approximately $200\,\mathrm{s}$ of the field measurements are shown. Not surprising the armature voltage (Figure 2.5(a)) follows the shaft angular velocities (Figure 2.5(d)) and the armature currents (Figure 2.5(b)) follows the shaft torques (Figure 2.5(c)) of the two machines.

The battery voltage and current are also shown in Figure 2.5(a) and Figure 2.5(b), respectively. It is noticed that during accelerations when the battery current is high the battery voltage drops due to the inner resistance of the batteries. Therefore the battery voltage increases when the braking energy is fed back to the battery, i.e. the battery current becomes negative. The field current is shown in Figure 2.5(b) also. It is seen that the field current most of the time is close to its nominal value, i.e. $I_{f,nom} = 8\,\mathrm{A}$. However, when extra torque is needed (both positive and negative) the field current is increased to values even higher than the maximum value ($I_{f,max} = 15\,\mathrm{A}$) specified on the nameplate. The maximum shaft torque of Figure 2.5(c) is $\tau_s = 23\,\mathrm{Nm}$. However, for all the data collected the highest shaft torque calculated from the measurements is $\tau_s = 41\,\mathrm{Nm}$ with an armature current of $i_a = 255\,\mathrm{A}$ which is $264\,\%$ higher than the nominal armature current $I_{a,nom} = 70\,\mathrm{A}$. The maximum shaft power of Figure 2.5(e) is $p_s = 3850\,\mathrm{W}$. The maximum battery power is $p_b = 7740\,\mathrm{W}$. Even though the battery should provide power for both machines the battery power is significant higher than the shaft power of the two machines. This is because the machines are not operated at their nominal point of operation ($\omega_{s,nom} = 279\,\mathrm{rad/s}$, $\tau_{s,nom} = 7.2\,\mathrm{Nm}$) where the efficiency is high (see Figure B.6 on page 172). The shaft angular velocities of the two machines are almost the same which indicates that the driver is driving strait ahead. However, it seems to that the left machine is more loaded than the right, as the armature current of the left machine generally is higher than the current of the right machine. From Figure 2.5(d) it can be seen that it takes approximately $1\,\mathrm{s}$ to accelerate from 0 to $\omega_s = 150\,\mathrm{rad/s}$ ($\approx 8\,\mathrm{km/h}$). This sounds reasonable as the truck according to Table 1.2 should be able to accelerate from 0 to the maximum speed $V_{Truck,max} = 15\,\mathrm{km/h}$ in $3\,\mathrm{s}$ to $5\,\mathrm{s}$.

In Figure 2.6 the speed of all the days with useful field measurements are shown. The speed of the truck is calculated as an average of the shaft angular velocities of the left and right motor, i.e.

$$v_{Truck} = \frac{r_w}{G}\frac{\omega_{s,l} + \omega_{s,r}}{2}\frac{3600\,\mathrm{s/h}}{1000\,\mathrm{m/km}} \qquad [\mathrm{km/h}] \tag{2.7}$$

Totally $N_{day} = 24\,\mathrm{days}$ of field measurement were obtained and these will be used for the further analysis. First of all it can be seen that the truck has not been operated all the days, and sometimes it is passive for several days in a row. It is also seen that the truck usually operates from 7 am to 3 pm. It should also be noticed that in this period there are many small intervals with both active and passive modes, but the distribution of these are quite different for each day. Finally it can be seen that the maximum speed of $15\,\mathrm{km/h}$ seldom is reached, and that the truck moves more in forward than in reverse direction, which is not surprising.

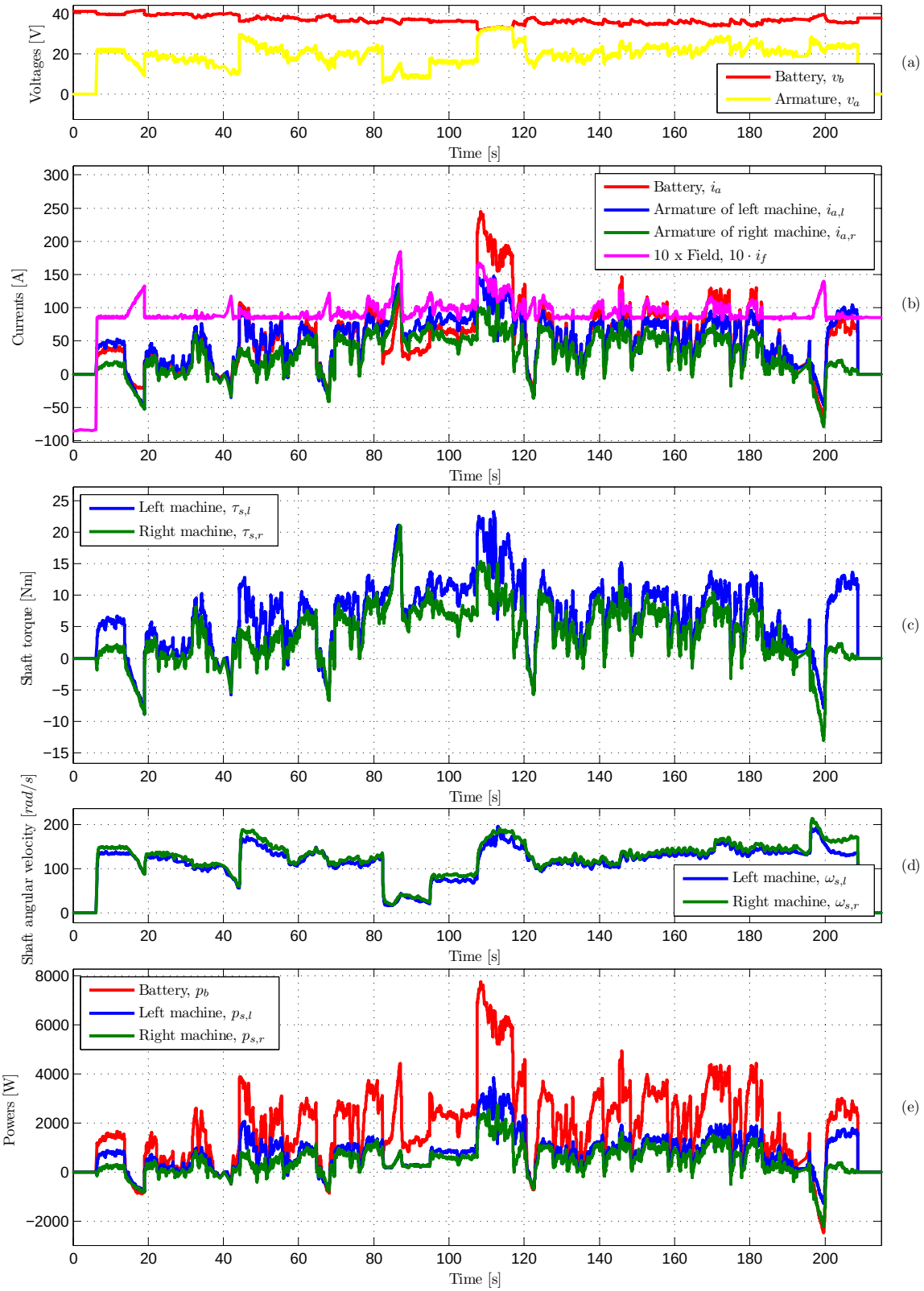

Figure 2.5: Measured field data after data treatment. (a) Battery and armature voltages. (b) Armature, battery and field currents. (c) Shaft torques. (d) Shaft angular velocities. (e) Battery and shaft powers.

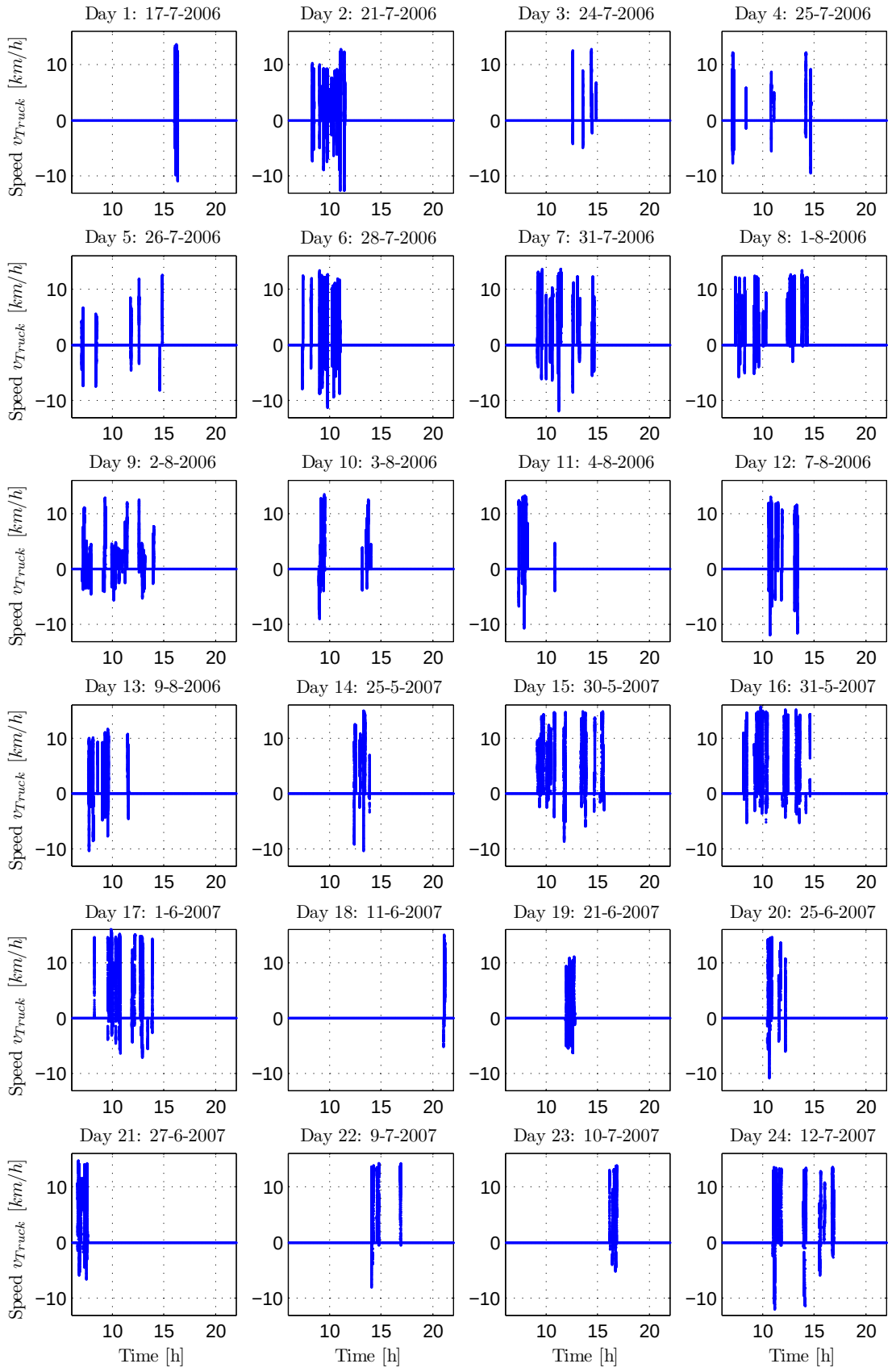

Figure 2.6: Truck speed of all the days with useful data.

Data Analysis

The time where the driver uses the truck the first time of the day is denoted T_{start} and the time where the driver stops using the truck that day is denoted T_{stop}. This means that for day 2 in Figure 2.6 the start time is $T_{start} = 8.3\,\mathrm{h}$ and the stop time is $T_{stop} = 11.5\,\mathrm{h}$. The operation interval of the truck for each day is therefore

$$T_{operation} = T_{stop} - T_{start} \qquad [\mathrm{h}] \tag{2.8}$$

The traveled distance of the truck can be calculated by integrating the speed, i.e.

$$D_{Truck} = \int_{T_{start}}^{T_{stop}} |v_{Truck}|\, dt \qquad [\mathrm{km}] \tag{2.9}$$

The absolute sign is used as the speed also can be negative when the driver is backing. As it can be seen from Figure 2.7(a) the traveled distance is different from day to day. The minimum is $D_{Truck} = 580\,\mathrm{m}$ and the maximum is $D_{Truck} = 3.9\,\mathrm{km}$.

The total shaft power is the sum of the two machines, i.e.

$$p_{s,tot} = p_{s,l} + p_{s,r} \qquad [\mathrm{W}] \tag{2.10}$$

The energy of the battery E_b and shafts $E_{s,tot}$ are given by

$$E_b = \int_{T_{start}}^{T_{stop}} p_b dt \qquad [\mathrm{Wh}] \tag{2.11}$$

$$E_{s,tot} = \int_{T_{start}}^{T_{stop}} p_{s,tot} dt \qquad [\mathrm{Wh}] \tag{2.12}$$

In Figure 2.7(b) the battery and shaft energy are shown. It can be understood that a significant amount of energy is lost between the battery terminals and shafts of the two machines. The overall efficiency from the battery to the shafts of all the days is

$$\eta_{GMR} = 100\,\% \frac{\sum_{i_{day}=1}^{i_{day}=24} E_{s,tot}(i_{day})}{\sum_{i_{day}=1}^{i_{day}=24} E_b(i_{day})} = 55\,\% \tag{2.13}$$

This efficiency is not very high and leaves room for improvement of the FC Truck.

The operation interval $T_{operation}$ can be divided into an active interval T_{Active} and passive interval $T_{Passive}$, i.e.

$$T_{operation} = T_{Active} + T_{Passive} \qquad [\mathrm{h}] \tag{2.14}$$

The active interval is when the speed or torque is different from zero, and the passive interval is when the truck is not in the active interval, i.e.

```
if (|ω_{s,l}| > 0) OR (|ω_{s,r}| > 0) OR (|τ_{s,l}| > 0) OR (|τ_{s,r}| > 0)
   Active interval
else
   Passive interval
end
```

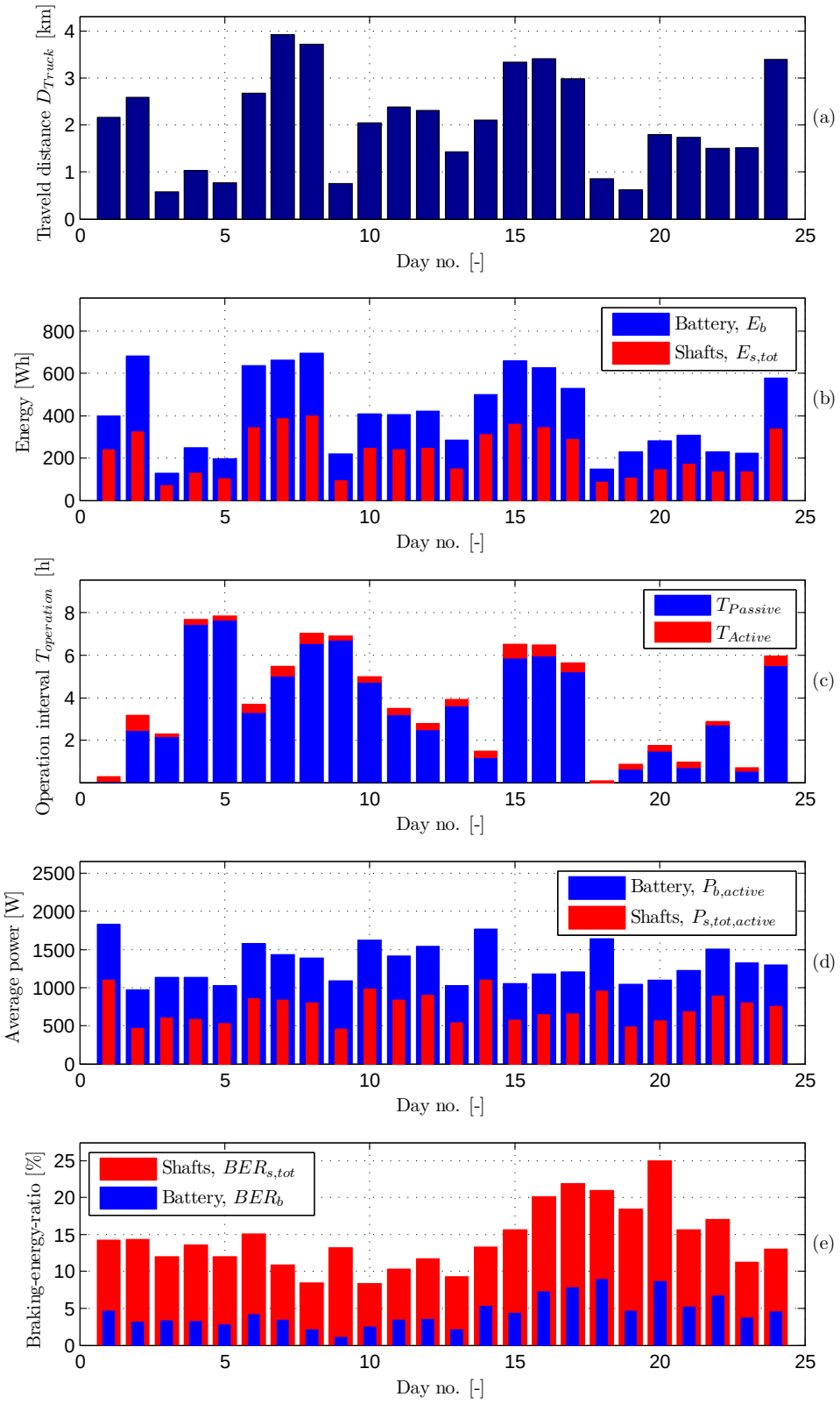

Figure 2.7: Key numbers of the field measurements.

In Figure 2.7(c) it is shown how much of the operation interval $T_{operation}$ is spent in the active interval T_{Active} and passive interval $T_{Passive}$. It can be seen that only for day 1 and 18 almost all the operation time is in active interval. For almost all the other days there is a significant fraction of passive interval. It is also noticed that for all the days the active interval is very small. The maximum active interval for all the days is $T_{Active} = 42\,\mathrm{min}$ at day 2. This might give some ideas of how the fuel cell and energy storage device should be rated. Due to the relative long passive-mode a significant amount of energy can be added to the energy storage device from a relative small fuel cell.

Because of the long passive interval the average battery and shaft power in the operation interval $T_{operation}$ will be relative small. The average power is therefore calculated in the active time interval, i.e.

$$P_{b,active} = \frac{E_b}{T_{Active}} \quad [\mathrm{W}] \tag{2.15}$$

$$P_{s,tot,active} = \frac{E_{s,tot}}{T_{Active}} \quad [\mathrm{W}] \tag{2.16}$$

The total average power in the active time interval can be seen in Figure 2.7(d). The maximum is $P_{b,active} = 1833\,\mathrm{W}$ and $P_{s,tot,active} = 1100\,\mathrm{W}$ for the battery and shaft, respectively. From Table 2.2 the continuous shaft power of one wheel (not both) is $P_s = 626\,\mathrm{W}$ and $P_s = 1035\,\mathrm{W}$ for a load of $M_{Load} = 0\,\mathrm{kg}$ and $M_{Load} = 1000\,\mathrm{kg}$, respectively, when the truck speed is $v_{Truck} = 15\,\mathrm{km/h}$ and the slope of the road is $\alpha = 0$. This indicates that the load of the truck was very low during the field test, the speed is low, or that the tire rolling resistance coefficient is better than the value used for the simulation. In the simulation the truck is operated at maximum speed $v_{Truck,max} = 15\,\mathrm{km/h}$. However, as it is seen in Figure 2.6 the truck is seldom operated at maximum speed. For all the days the average speed is

$$v_{Truck,av} = \frac{\sum_{i_{day}=1}^{i_{day}=24} D_{Truck}(i_{day})}{\sum_{i_{day}=1}^{i_{day}=24} T_{active}(i_{day})} = 6.6\,\mathrm{km/h} \tag{2.17}$$

This is less than half of the maximum speed. Another simulation has therefore been done with a reference speed of $v_{Truck} = 6.6\,\mathrm{km/h}$. The shaft power for each motor in this situation is $P_s = 242\,\mathrm{W}$ and $P_s = 412\,\mathrm{W}$ for $M_{Load} = 0\,\mathrm{kg}$ and $M_{Load} = 1000\,\mathrm{kg}$, respectively. The simulation result for $M_{Load} = 1000\,\mathrm{kg}$ at this speed provides a total shaft power of the two motors of $2 \cdot 412\,\mathrm{W} = 824\,\mathrm{W}$, which is near to the maximum "measured" average total shaft power of $P_{s,tot,active} = 1100\,\mathrm{W}$.

The maximum traveling distance is $D_{Truck} = 3.9\,\mathrm{km}$ at day 7. At this day the average battery power and energy consumption is $P_{b,active} = 1436\,\mathrm{W}$ and $E_b = 663\,\mathrm{Wh}$, respectively. From Table B.1 on page 165 the $5\,\mathrm{h}$ capacity is $Q_5 = 180\,\mathrm{Ah}$. The total battery voltage of the battery pack is $V_{b,tot} = 36\,\mathrm{V}$ which means that the $5\,\mathrm{h}$ discharge power of the battery pack is $P_{b,5} = \frac{V_{b,tot} \cdot Q_5}{5\,\mathrm{h}} = 1296\,\mathrm{W}$. This discharge power is approximately $10\,\%$ smaller than the average battery power at day 7. However, if this difference is ignored and it is assumed that the capacity still is $180\,\mathrm{Ah}$ for an average battery power $P_{b,tot} = 1436\,\mathrm{W}$ the truck can theoretically be operated for $T_{active} = \frac{V_{b,tot} Q_5}{P_{b,active}} = 4.5\,\mathrm{h}$. This means that if the battery is fully charged from the begin-

ning the truck can be used for $T_{active} = 4.5\,\mathrm{h}$ before it is drained. At day 7 the truck required $E_b = 663\,\mathrm{Wh}$ to go $D_{Truck} = 3.9\,\mathrm{km}$. This means that the truck theoretically can go $D_{Truck} = 3.9\,\mathrm{km}\frac{V_{b,tot}Q_5}{E_b} = 38\,\mathrm{km}$ before it needs to be recharged. During the 24 days of field measurements the battery package delivered $E_{b,all} = \sum_{i_{day}=1}^{i_{day}=24} = 9.71\,\mathrm{kWh}$. This means that for one fully charged battery package the truck can be operated $\frac{V_{b,tot}Q_5}{E_{b,all}}24\,\mathrm{days} \approx 16\,\mathrm{days}$ before it needs to be recharged. It can therefore be concluded that the 24 days of field measurements does not indicate that there is a problem with the time and area of operation as it was stated in [63]. The capacity of the battery package seems to be sufficient for the actual usage of the truck.

Braking Energy

The last issue to investigate is the quantity of the braking energy. The battery power can be divided into a charging power $p_{b,cha}$ and a discharging power $p_{b,dis}$ and the shaft power can be divided into a motor power $p_{s,tot,mot}$ and generator power $p_{s,tot,gen}$. Therefore

$$p_b = p_{b,cha} + p_{dis} \quad [\mathrm{W}] \tag{2.18}$$

$$p_{b,cha} = \begin{cases} p_b & , \quad p_b < 0\,\mathrm{W} \\ 0 & , \quad p_b \geq 0\,\mathrm{W} \end{cases} \quad [\mathrm{W}] \tag{2.19}$$

$$p_{b,dis} = \begin{cases} p_b & , \quad p_b > 0\,\mathrm{W} \\ 0 & , \quad p_b \leq 0\,\mathrm{W} \end{cases} \quad [\mathrm{W}] \tag{2.20}$$

$$p_{s,tot} = p_{s,tot,mot} + p_{s,tot,gen} \quad [\mathrm{W}] \tag{2.21}$$

$$p_{s,tot,mot} = \begin{cases} p_{s,tot} & , \quad p_{s,tot} > 0\,\mathrm{W} \\ 0 & , \quad p_{s,tot} \leq 0\,\mathrm{W} \end{cases} \quad [\mathrm{W}] \tag{2.22}$$

$$p_{s,tot,gen} = \begin{cases} p_{s,tot} & , \quad p_{s,tot} < 0\,\mathrm{W} \\ 0 & , \quad p_{s,tot} \geq 0\,\mathrm{W} \end{cases} \quad [\mathrm{W}] \tag{2.23}$$

In order to assess the amount of braking energy, a braking-energy-ratio is defined. The braking-energy-ratio expresses the quantity of energy entering a unit relative to the quantity leaving the unit. A braking-energy-ratio of the battery BER_b and the motor shafts $BER_{s,tot}$ can therefore from Equation (2.19)-Equation (2.23) be defined as

$$BER_b = \left| \frac{\int_{T_{start}}^{T_{stop}} p_{b,cha} dt}{\int_{T_{start}}^{T_{stop}} p_{b,dis} dt} \right| \cdot 100\,\% \quad [\%] \tag{2.24}$$

$$BER_{s,tot} = \left| \frac{\int_{T_{start}}^{T_{stop}} p_{s,tot,gen} dt}{\int_{T_{start}}^{T_{stop}} p_{s,tot,mot} dt} \right| \cdot 100\,\% \quad [\%] \tag{2.25}$$

The braking-energy-ratio of the battery and motor shafts can be seen in Figure 2.7(e). The highest relative amount of braking energy is at day 20 where $BER_{s,tot} = 25\,\%$ of the shaft powers in motor-mode $p_{s,tot,mot}$ is returned as braking energy. However, due to the low efficiency of the drive system the amount of braking energy at the battery is significant lower, i.e. $BER_b = 8\,\%$. In the FC Truck this should therefore be improved. The braking-energy-ratio depends on the driving pattern, e.g. if there are many stop-and-goes, the braking-energy-ratio will be high, but if the truck operates

with constant speed for a long period and only brake one time in order to stop the vehicle, the braking-energy-ratio will be very low.

2.3 Selection of Driving Cycle

The 24 days of field measurements do not indicate that there should be a problem with the hours of operation and area of operation as the current battery package contains sufficient energy for the actual usage of the truck. The 24 days of field measurements are therefore not considered to represent a proper load profile of the truck. In Chapter 8 it is shown that it requires $1500\,\mathrm{W}$ for 6 minutes, i.e. $150\,\mathrm{Wh}$, to heat-up a fuel cell stack with a rated power of $1\,\mathrm{kW}$, before it is ready to produce power. In Figure 2.7 it is seen that $150\,\mathrm{Wh}$ is more energy than the truck uses some of the days, and the maximum shaft energy consumption of all the days was approximately $400\,\mathrm{Wh}$. The driving cycle used for designing purpose should therefore require much more power to the driving wheels in order to suppress the energy that is needed for operating the fuel cell stack. Therefore a new driving cycle will be created. In Figure 2.7 it is seen that day number 1 has almost no passive time interval. In compare to the other days, day number 1 also has a relatively high shaft energy and average power consumption. The shaft angular velocity, torque, and power of day 1 can be seen in Figure 2.8. Day number 1 has a total duration of $16.78\,\mathrm{min}$. In Figure 2.6 it was seen that the working day usually starts at 7 am and ends at 3 pm, i.e. it has a duration of 8 hours. In order to have a driving cycle that requires a significant amount of energy, it is therefore chosen to repeat the driving cycle of day number 1: $\frac{8\,\mathrm{h}\cdot 60\,\mathrm{min/h}}{16.78\,\mathrm{min}} \approx 29$ times.

2.4 Conclusion

In this chapter the load profile of the GMR Truck is analyzed. A vehicle model based on the forces acting on the truck has been created. The model indicates that the load power strongly depends on the load mass of the truck, accelerations, and the slope of the road. To obtain a better understanding of the actual usage of the truck totally 24 days of field measurement are collected. By applying a motor model of the GMR Truck the speed and torque of the vehicle are calculated. The analysis shows that during a day the truck is seldom used but is in passive mode most of the time. The maximum usage of the truck is $T_{Active} = 42\,\mathrm{min}$ and the maximum traveling distance is $D_{Truck} \approx 4\,\mathrm{km}$. There are many stop-and-goes of the truck and the maximum speed is seldom reached. Due to the low efficiency of the drive train only a small fraction of the braking energy can be used by the battery. The maximum braking-energy-ratio of the battery is $BER_b = 8\,\%$. Due to the low usage of the truck a new driving cycle has been created by repeating the driving cycle with the highest load requirement 29 times.

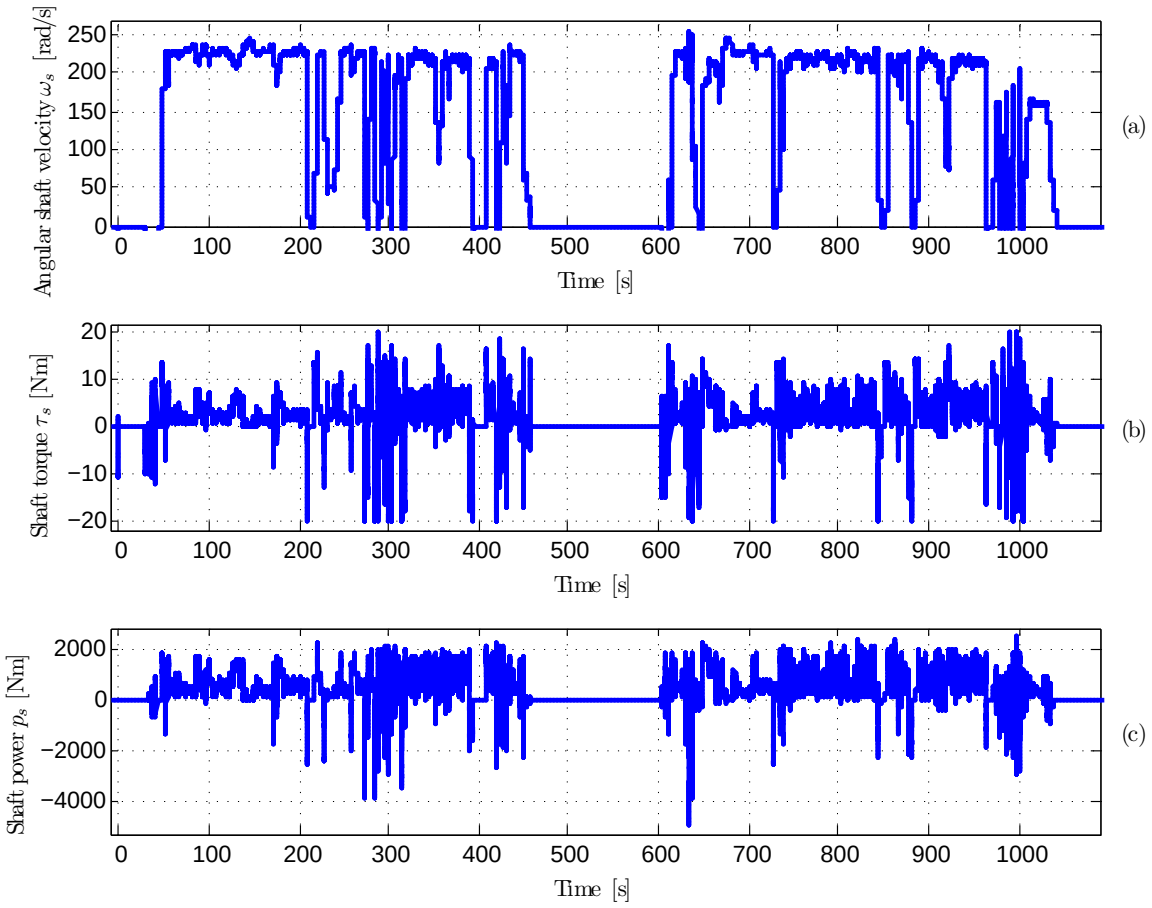

Figure 2.8: Used driving cycle which will be repeated 29 times. (a) Shaft angular velocity. (b) Shaft torque. (c) Shaft power.

Part II

Modeling

3 Fuel Cell

Fuel cells have the capability of converting chemical energy into heat and electric power. In this project the heat production is seen as waste, and it is therefore the electric power production that is interesting. That amount of energy of the hydrogen that is converted into electric power depends on the point of operating, and in this chapter a steady-state characteristic is therefore modeled. A dynamic model is also created in order to be able to model the transient behavior.

3.1 Fuel Cell Types

Several types of fuel cells exist, e.g. Alkaline Fuel Cell, Proton Exchange Membrane Fuel Cell (PEMFC), Direct methanol Fuel Cell, Phosphoric Acid Fuel Cell, Molten Carbonate Fuel Cell, and Solid Oxide Fuel Cell [18, 22, 41, 72]. Each type has advantages and disadvantages. However, the PEMFC are generally considered to be the best option for mobile applications due to its low operating temperature, high efficiency, high power density, rapid start-up, and a potential for low cost for high volume production [22, 51, 72].

The PEMFC can be divided into two categories, i.e. a Low Temperature PEMFC (LTPEMFC), and the HTPEMFC. The LTPEMFC is known as the traditional PEMFC, but the HTPEMFC is another type, which is operated above $100\,^{\circ}\mathrm{C}$. The HTPEMFC is simpler to control than the LTPEMFC, and it can tolerate a higher CO concentration [3]. The drawbacks of the HTPEMFC is a lower efficiency, and the higher temperature requires higher demands for the materials, and the start-up time becomes longer [6]. Due to the higher tolerances of CO poisoning, reformed methanol can be used as a fuel instead of compressed hydrogen, which is more practical for a mobile application. For this reason and due to the simpler system operation of the HTPEMFC, the HTPEMFC is used in this project [3].

3.2 Fuel Cell Characteristics

Even though fuel cells give a DC output voltage, this voltage is only constant if the operating conditions (load, temperature, pressure, humidity, etc.) also are constants. Therefore the fuel cell cannot be seen as a fixed DC voltage source, and the relationship between the voltage and current is therefore not linear.

Voltage Modeling

Fuel cells have a characteristic voltage curve, i.e. the polarization curve. The polarization curve is characterized by five phenomena [40], i.e.

Open circuit voltage The voltage measured when no current is drawn from the fuel cell, i.e. $i_{FC} = 0\,\mathrm{A}$. This voltage is decreased when the temperature decreases [94].

Activation losses This phenomenon causes the voltage to drop quite significant even for relatively small currents. Activation losses are due to the slowness of the reaction taking place on the surface of the electrodes. The chemical reaction that transfers the electrons to or from the electrodes causes a little voltage drop of the voltage generated [27].

Fuel crossover and internal currents The purpose of the electrolyte is to transfer ions. However, a certain amount of the fuel and electrons also passes through. If the fuel passes through, it will react with the oxygen without producing any current, and the fuel is therefore wasted. This situation is denoted fuel crossover. The internal current is due to the electrons flowing from the anode to the cathode through the electrolyte.

Ohmic losses This voltage drop is due to the resistive nature of the electrodes, interconnections and electrolyte. This voltage drop is proportional to the current and is therefore linear.

Mass transport or concentration losses As the fuel is being used, the concentration of the reactants at the surface of the electrodes is changed. Therefore the name concentration losses. However, this kind of loss is also denoted mass transportation losses due to the fact that the losses is a result of insufficient transportation of reactants to the electrode surface [27]. This phenomenon can be seen at high current levels.

In Figure 3.1 is shown an electric circuit diagram which can be used for modeling the polarization curve. It consist of a series resistor R_{FC} and a current depending internal voltage source $v_{FC,int}$. The fuel cell voltage is therefore

$$v_{FC} = v_{FC,int} - R_{FC} i_{FC} \qquad [\mathrm{V}] \tag{3.1}$$

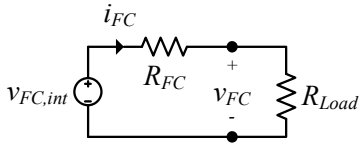

Figure 3.1: Equivalent circuit diagram of a fuel cell used for modeling of the polarization curve.

In Figure 3.2(a) is shown a polarization curve for a single HTPEMFC. It is seen that for currents higher than $i_{FC} = 5\,\mathrm{A}$ the voltage drops linearly. This indicates that the given fuel cell does not suffer from mass transport or concentration loss. Otherwise an exponential voltage drop at high current levels would have been seen [40]. For current levels higher than $i_{FC} = 5\,\mathrm{A}$ the voltage can therefore be approximated to a first order polynomial with slope $-R_{FC}$. Therefore

$$R_{FC} = -\frac{dv_{FC}}{di_{FC}} = 5.6\,\mathrm{m\Omega} \tag{3.2}$$

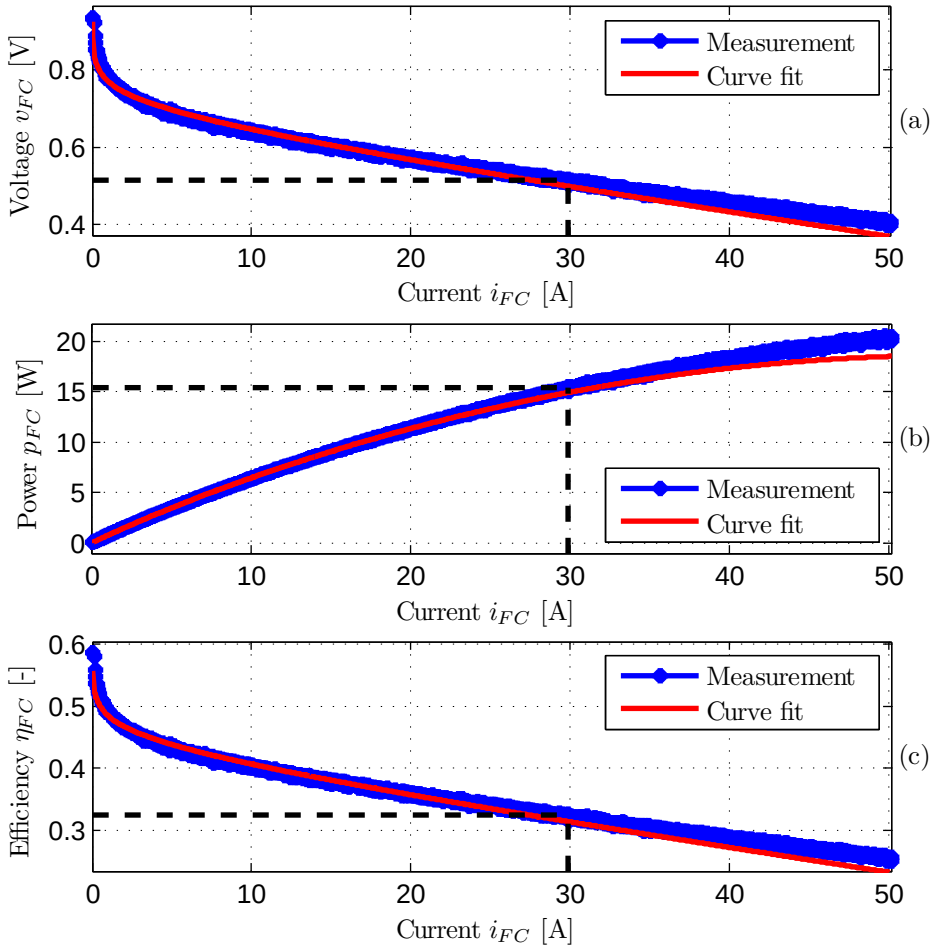

Figure 3.2: Characteristics of a single fuel cell at $T_{FC} = 160\,^{\circ}\mathrm{C}$. Dashed lines indicate the nominal point of operation. (a) Polarization curve. (b) Electric fuel cell output power. (c) Fuel cell efficiency.

As no mass transport or concentration loss is present, the internal voltage source $v_{FC,int}$ is due to an open circuit voltage, activation loss, fuel crossover, and internal currents. The activation loss, fuel crossover, and internal current can be modeled by a $\log$-function [40]. By using Matlab® curve fitting tool-box, the internal voltage source is therefore given by

$$v_{FC,int} = v_{FC} + R_{FC} i_{FC} \quad [\mathrm{V}] \tag{3.3}$$

$$= V_{FC,oc} - a_{FC}\left(\log\left(\frac{i_{FC}+I_n}{b_{FC}}\right) - \log\left(\frac{I_n}{b_{FC}}\right)\right) \quad [\mathrm{V}] \tag{3.4}$$

where	$V_{FC,oc}$	=	$0.922\,\mathrm{V}$	Open circuit voltage
	I_n	=	$0.01\,\mathrm{A}$	Fuel crossover and internal currents
	a_{FC}	=	$0.0318\,\mathrm{V}$	Constant
	b_{FC}	=	$0.72\,\mathrm{V}$	Constant

The fuel crossover and internal currents I_n is relatively small, so it actually could have been set to zero. However, it has the nice property of avoiding $\log(0)$ for $i_{FC} =$

0 A. The nominal voltage is from Figure 3.2(a) $V_{FC,nom} = 0.516\,\mathrm{V}$. In Figure 3.2(b) the electric power of the single fuel cell is shown. At the nominal current $I_{FC,nom} = 29.8\,\mathrm{A}$ the nominal power is $P_{FC,nom} = 15.4\,\mathrm{W}$.

Efficiency

The fuel cell produces heat, electricity, and water. The fuel cell electric power is given by

$$p_{FC} = v_{FC} i_{FC} \qquad [\mathrm{W}] \tag{3.5}$$

The input power of a fuel cell is the power of the hydrogen fed to the anode.

The mass flow and power of the hydrogen are therefore [59]

$$\dot{m}_{H2} = N_{FC,s} \frac{M_{H2,mol}}{2F} i_{FC} \qquad [\mathrm{kg/s}] \tag{3.6}$$

$$p_{H2} = \dot{m}_{H2} HHV_{H2} \qquad [\mathrm{W}] \tag{3.7}$$

where			
	$F = 96485$	$[\mathrm{C/mol}]$	Faraday's constant
	$\dot{m}_{H2}$	$[\mathrm{kg/s}]$	Mass flow of hydrogen
	$N_{FC,s}$	$[-]$	Number of series connected fuel cells
	$M_{H2,mol} = 0.00216$	$[\mathrm{kg/mol}]$	Hydrogen molar mass
	i_{FC}	$[\mathrm{C/s}]$	Fuel cell current
	p_{H2}	$[\mathrm{W}]$	Power of hydrogen
	HHV_{H2}	$[\mathrm{J/kg}]$	Higher heating value of hydrogen

The electric efficiency of the fuel cell can be expressed as follows:

$$\eta_{FC} = \frac{p_{FC}}{p_{H2}} \qquad [\%] \tag{3.8}$$

The fuel cell efficiency can be seen in Figure 3.2(c). It is noticed that the efficiency is highest for low power levels. At the nominal current level the efficiency is $\eta_{FC} = 33\,\%$.

The graph in Figure 3.2(a) shows the steady-state voltage of the fuel cell. However, in a fuel cell hybrid system the power flow to the energy storage device depend on the dynamic behavior of the fuel cell. Therefore, in order to investigate the dynamic performance of the fuel cell a technique called Electrochemical Impedance Spectroscopy (EIS) is utilized.

3.3 ELECTROCHEMICAL IMPEDANCE SPECTROSCOPY

When using electrochemical impedance spectroscopy one is superposing a sinusoidal current to a DC current. This is done for many different frequencies. Thereby, when measuring the corresponding voltage response the impedance can be calculated for each frequency [2, 35, 70].

Laboratory Setup

The equipment used for the experiment is shown in Figure 3.3. It can be seen that an electronic load module (TDI Dynaload RBL488 50-150-800) is connected to the fuel cell. The current drawn of the fuel cell consist of a sinusoidal part and a DC part. The

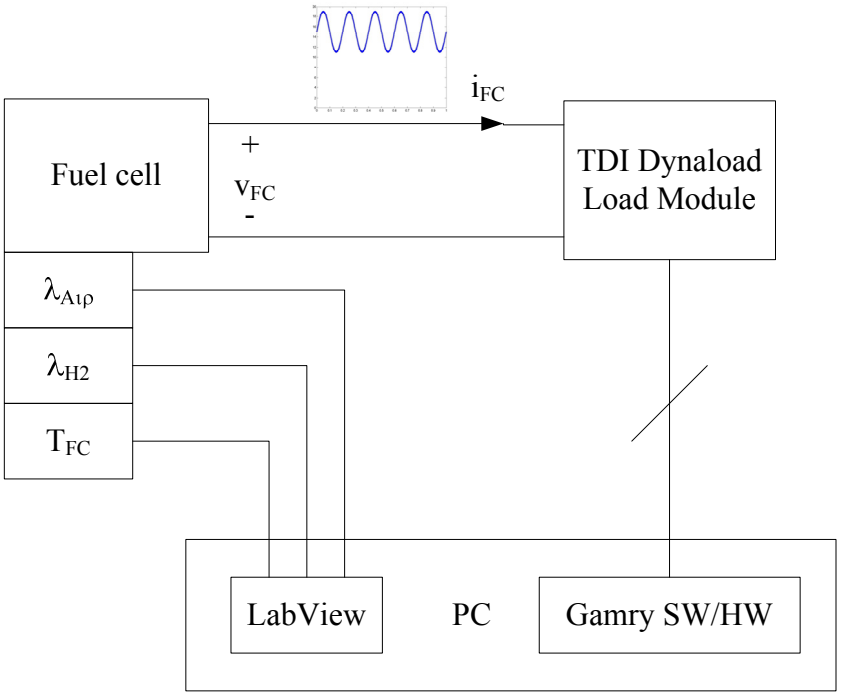

Figure 3.3: Setup of the equipment used for the electrochemical impedance spectroscopy.

current drawn by the load module is controlled by a PCI-slot module from Gamry® (FC350 Fuel Cell Monitor). The FC350 Fuel Cell Monitor was operating in hybrid mode, i.e. it controls the injected current in such a manner, that the voltage response always is at $2.5\,\mathrm{mV}$. This insures that the voltage response not exceeds the linear area when the impedance increases. The fuel cell conditions, i.e. the temperature T_{FC}, air stoichiometry λ_{Air}, and hydrogen stoichiometry λ_{H2} are all controlled from a PC trough a LabView® interface. The Gamry® software calculates the impedance for each injected frequency and saves the result in a txt-file which can be used for further data analysis.

Results

The EIS were applied for different points of operation, which can be seen in Figure 3.4 [70]. All the measurements are in the frequency range $60\,\mathrm{mHz} - 20\,\mathrm{kHz}$ which are the boundaries of the load module. From the Nyquist plots in Figure 3.4 two low and one high frequency semicircles can be identified. However, for most of the operation points in Figure 3.4 the semicircle of the lowest frequency is insignificant or not present at all. From the plots it is also seen that the impedances all becomes inductive at high frequencies. It is noticed that the cell used for the EIS experiment not is the same cell used for characterizing the polarization curve, but it is still of HTPEMFC type.

In Figure 3.4(a) the impedances are shown for different points of operation of the temperature. It is seen that the higher the temperature gets, the smaller the diameter of the semicircle becomes. This phenomenon is also seen in LTPEMFC [92] and is due to the oxygen electrode kinetics, i.e. the higher temperature the faster reactions. It is

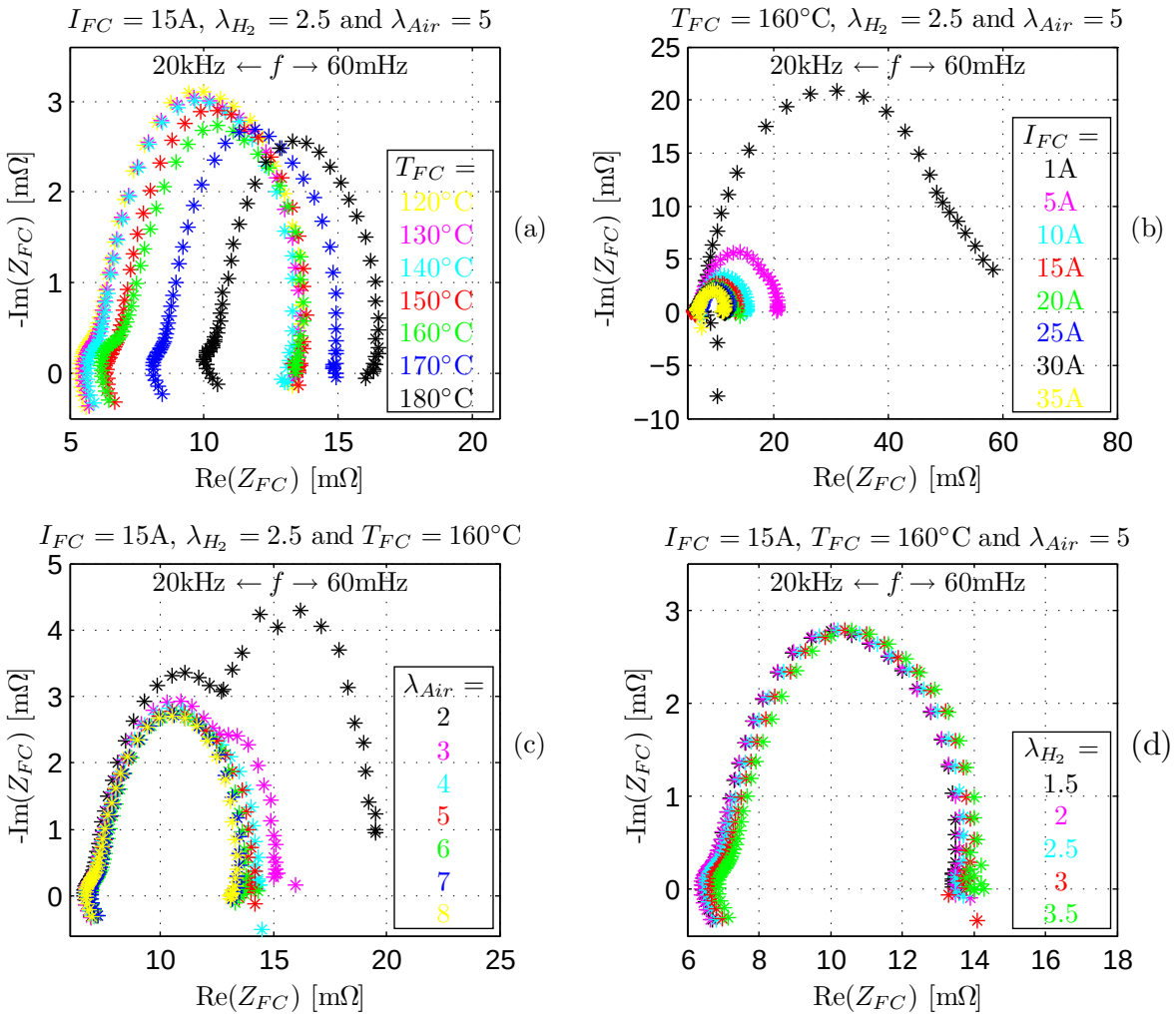

Figure 3.4: Nyquist plots of a HTPEMFC at different points of operation. (a) Variation of fuel cell temperature T_{fc}. (b) Variation of fuel cell current I_{fc}. (c) Variation of air stoichiometry λ_{Air}. (d) Variation of hydrogen stoichiometry λ_{H_2}.

seen that the semicircles are moving to the right when the temperature increases, i.e. the membrane resistance increases. This is however, not seen in other publications where EIS is applied on the LTPEMFC. In other publications the membrane resistance is almost the same independent on the temperature [35, 92]. The cell used for test was not new, but has been used many times. It is therefore evaluated that the used cell is damaged, as this phenomena not has been reported for new cells [37].

In Figure 3.4(b) the impedances are shown for different points of operation of the current. For the low currents ($I_{FC} = 1$ A and $I_{FC} = 5$ A) a third semicircle is present. This is not the case for higher values of the current. It is also noticed that at low currents the semicircle becomes relatively wide. This is because of the activation losses which cause steep slopes of the polarization curve.

In Figure 3.4(c) the impedances are shown for different points of operation of the air stoichiometry. For low values of the air stoichiometry ($\lambda_{FC} = 2$ and $\lambda_{FC} = 3$) a semicircle again is present. This is not the case for higher values of air stoichiometry.

The third semicircle is probably due to mass transport phenomena, i.e. insufficient air supply.

In Figure 3.4(d) the impedances are shown for different points of operation of the hydrogen stoichiometry. It is seen that variation of the hydrogen stoichiometry has a little influence of the impedances.

From the Nyquist plots in Figure 3.4 it is seen that the characteristics of the HT-PEMFC impedances are almost equal for all the variation of the operating points. This means that only one type of a circuit diagram is necessary when simulating the HT-PEMFC performance as it then will be valid for all the operating points.

Dynamic Electric Circuit Modeling

Usually the fuel cell can be modeled by two RC-circuits (one for the anode side and one for the cathode side) and a resistance (membrane resistance) [36]. However, from the results in Figure 3.4 three semicircles are seen, and at higher frequencies the impedance becomes inductive. Many types of electric equivalent circuits of fuel cells exist, that are capable of modeling different characteristics [66]. For the results obtained in Figure 3.4 the equivalent circuit diagram in Figure 3.5 of the HTPEMFC are therefore proposed. The three RC circuit models the three semicircles of the Nyquist plots, the two inductors L_{d_1} and L_{d_2} and the resistance R_d models the high frequency inductive behavior of the fuel cell and the resistance R_m models the resistive offset of the Nyquist plots, i.e. the membrane resistance. The voltage source V_{nl} is the no-load voltage one will obtain if the polarization curve is approximated to be a first order polynomial, i.e. $v_{FC} = V_{nl} - R_{FC} i_{FC}$.

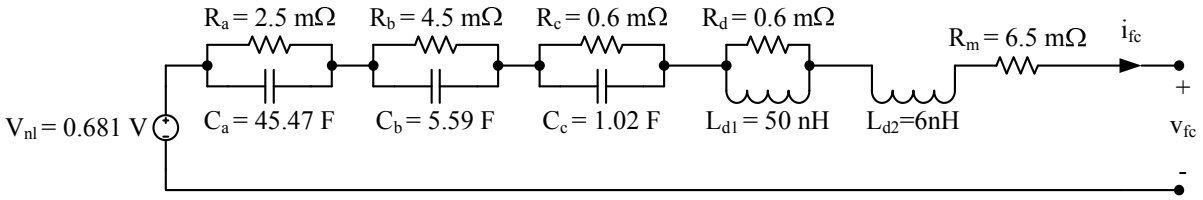

Figure 3.5: Equivalent circuit model of a HTPEMFC.

In Figure 3.6 a Nyquist plot of the HTPEMFC at an operating point at $I_{FC} = 15\,\mathrm{A}$, $\lambda_{Air} = 5$ and $\lambda_{H_2} = 2.5$ is shown. The Nyquist plot of the circuit in Figure 3.5 is also shown. It is seen that the simulated Nyquist plot fits the measured Nyquist plot well.

It may be mentioned that the model in Figure 3.5 only are capable of modeling relatively short term time constants, i.e. a long term time constant due to drift of the fuel cell cannot be simulated with the proposed model.

In order to verify the proposed model in Figure 3.5 laboratory results are compared to simulation results. In Figure 3.7(a) a measured and simulated fuel cell voltage response are shown. The voltage responses are due to the $20\,\mathrm{kHz}$ sinusoidal current excitation of Figure 3.7(c). The model in Figure 3.5 are implemented in Saber®, and the fuel cell current of Figure 3.7(c) are applied to the model. From Figure 3.7(a) it is seen that the model are capable of both simulating the phase and amplitude of the voltage response properly. However, a little offset error is noticed.

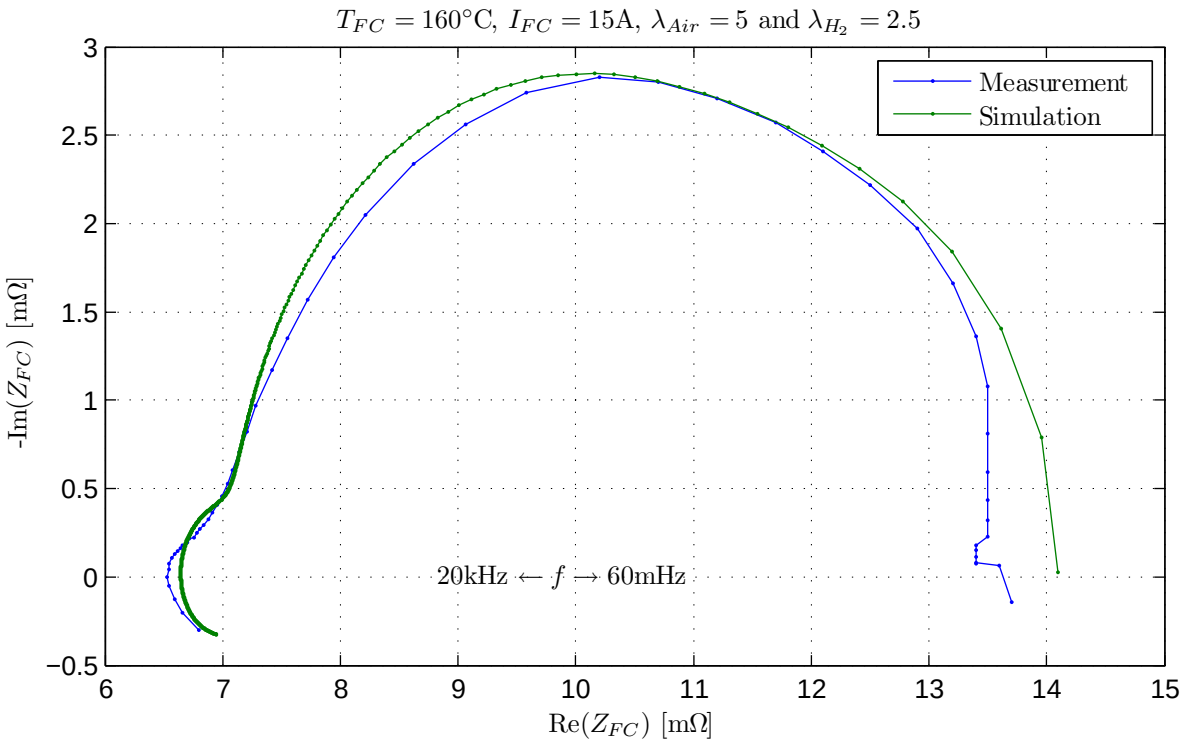

Figure 3.6: Nyquist plot

In Figure 3.7(b) again a measured and simulated voltage response are shown. The voltage responses are due to the current step excitation in Figure 3.7(d). It is seen that the simulation result fits the measured voltage response. However, offset errors are present when the operation points are different from the operation point the model was constructed from, i.e. $I_{FC} = 15\,\mathrm{A}$. In order to obtain a more precise model, the elements of the circuit model in Figure 3.5 could be implemented with a look-up table. In compare to the polarization curve in Figure 3.2(a) it is seen that there is a significant voltage difference of approximately $130\,\mathrm{mV}$ for a current of $I_{FC} = 15\,\mathrm{A}$. This indicates that it is a used cell that has been used for the dynamic modeling.

3.4 CONCLUSION

It is chosen to use a HTPEMFC due to its promising potential for mobile applications, e.g. it can handle hydrogen with a higher CO concentration, which means that it can be fueled by reformed methanol. A HTPEMFC single cell has been modeled in steady-state and dynamic situations. In steady-state the voltage drop of the fuel cell were due to activation losses and resistive losses. Losses due to internal currents, fuel cross over, mass transport limitation, or concentration losses were not present for the test cell.

For the dynamic modeling EIS were applied. The HTPEMFC has been applied to EIS for different operation conditions of the temperature, current, air stoichiometry and hydrogen stoichiometry. The temperature and current seems to be the parameters that affect the impedance of the HTPEMFC most significant. Basically the impedances

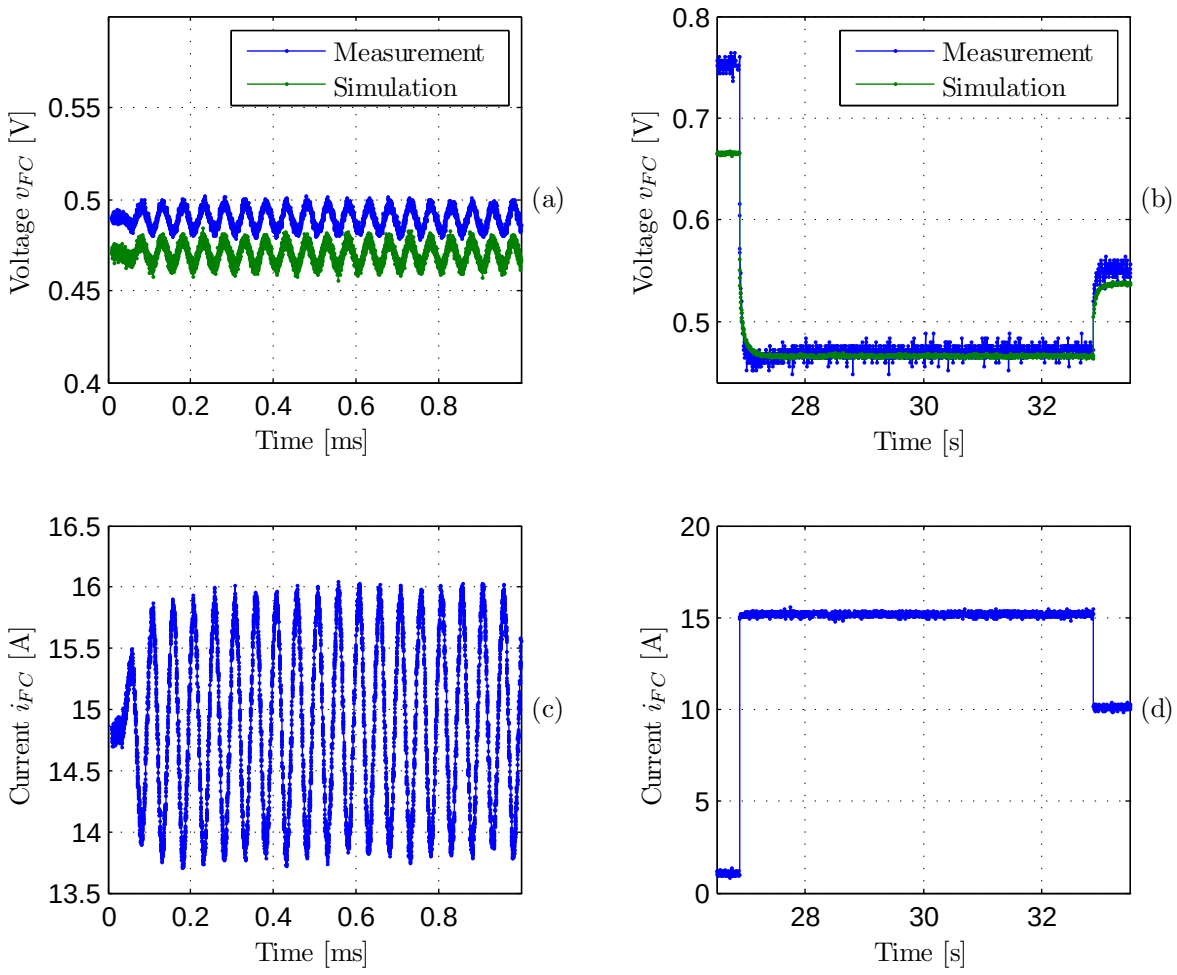

Figure 3.7: Verification of HTPEMFC model. (a) Measured and simulated voltage response due to the sinusoidal current excitation of Figure 3.7(c). (b) Measured and simulated voltage response due to the current step excitation of Figure 3.7(d).

for all the measured operating points fit into the same equivalent circuit model structure. However, for low values of the current and air stoichiometry, the impedance of the HTPEMFC includes a third time constant. An equivalent circuit diagram of the HTPEMFC has been proposed. The simulation result shows good agreement with the laboratory results. However, the model is only valid in a single point of operation, and it could be improved by using look-up tables.

4 Battery

Every car has a battery used for all the electric loads, and a battery is therefore an obvious candidate as energy storage device in hybrid vehicles. A battery is flexible, easy to replace, provide an almost constant voltage, and only need a few or none external components in order to deliver or receive energy. In this chapter a battery will be selected and modeled. The model contains several issues, i.e. voltage characteristics, charge and discharge efficiency, state-of-charge, and lifetime. The model is based on data sheet specifications, and only steady-state performances are considered.

4.1 Battery Types

As for the case of the fuel cells, many types of batteries also exist. For the purpose of energy storage device or propulsion power for mobile applications the following batteries below are usually considered. The little review is based on [17, 87].

Lead-acid This battery has been know for many years, is commercial available, widely used, highly recyclable, and relatively cheap. The drawbacks of this type of battery are the low energy density and low lifetime.

Nickel Cadmium (NiCd) The NiCd has a high cycle life and a low internal resistance which is required for high discharge rates. However, it suffers from low energy density, environmental concerns due to the cadmium, and a significant memory effect, i.e. it should be totally discharged before it is recharged; otherwise the capacity is reduced.

Nickel Metal Hydride (NiMH) This battery was created to replace the NiCd battery. The NiMH has no outstanding performances when compared to the alternatives, but it is in many cases used because it offers a good compromise among the different performance parameters, i.e. power and energy density, lifetime, cost, etc. One of the main weaknesses of the NiMH is the high self discharge rate, complicated charging management, and tricky state-of-charge estimation. The NiMH is less expensive, but not as cheap as the lead-acid battery.

Lithium The lithium batteries can be divided into four main categories, i.e. lithium metal, lithium metal polymer, lithium ion, and lithium ion polymer. The most "famous" lithium battery type is the lithium ion (LiIon). The LiIon has a high cycle life and higher power and energy density. The lithium-battery technology is not yet mature and these batteries are therefore relatively expensive when compared to the alternatives, and there are some safety concerns which need to be solved. They require also individual cell balancing.

The lithium-battery types will probably be the preferred solution in the mid-term and long-term path for energy storage devices for electric or hybrid vehicles [17]. However, a lot of research and development is still necessary. In this PhD project a battery

and ultracapacitor are considered as energy storage devices. The ultracapacitor has a higher specific power density than the batteries, even though, the LiIon are competitive. Lead-acid batteries in general have a low specific power, if they also should have certain specific energy [17]. Combining ultracapacitors with LiIon batteries might not be so advantageous as combining ultracapacitors with lead-acid batteries. Therefore, e.g. a lead-acid / ultracapacitor solution might be competitive with a pure LiIon solution in terms of cost, mass, volume, efficiency, etc. For this reason, and due to the fact that it provides a simple operation, low cost, availability, the lead-acid battery is chosen.

4.2 SPECIFICATIONS

The battery used for the modeling is from Sonnenschein®. It consist of 6 series connected cells, which are forming one block. The specifications can be seen in Table 4.1.

Manufacture	Sonnenschein®
Type	A512 / 40 A
Nominal voltage	$V_{Bat,nom} = 12\,\mathrm{V}$
Maximum open circuit voltage	$V_{Bat,max} = 13.8\,\mathrm{V}$
Minimum open circuit voltage	$V_{Bat,min} = 10.5\,\mathrm{V}$
$20\,\mathrm{h}$ capacity at $20\,^{\circ}\mathrm{C}$	$Q_{Bat,20} = 40\,\mathrm{Ah}$
$10\,\mathrm{h}$ capacity at $20\,^{\circ}\mathrm{C}$	$Q_{Bat,10} = 37\,\mathrm{Ah}$
Internal resistance, $20\,^{\circ}\mathrm{C}$	$R_{Bat,nom} = 11.6\,\mathrm{m\Omega}$
Volume	$6.4\,\mathrm{L}$
Mass	$14.5\,\mathrm{kg}$

Table 4.1: Data of the used battery [24].

4.3 VOLTAGE MODELING

As for the case of the fuel cells, many types of equivalent circuit models of batteries also exist [14]. Usually it is sufficient to model the battery voltage by an internal voltage source $v_{Bat,oc}$ and an inner series resistance R_{Bat}, as shown in Figure 4.1. The battery current i_{Bat} is treated as positive in charging mode. The voltage at the terminals of the battery is therefore

$$v_{Bat} = v_{Bat,oc} + R_{Bat} i_{Bat} \qquad [\mathrm{V}] \tag{4.1}$$

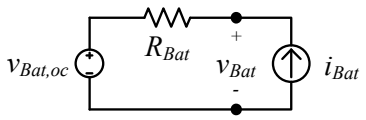

Figure 4.1: Equivalent circuit used for battery voltage modeling.

Inner Resistance Modeling

The inner resistance is specified in Table 4.1 for a certain point of operation. However, the inner resistance depend on several parameters, e.g. depth-of-discharge, current level, temperature, and the sign of the current. The per unit inner resistance as a function of the depth-of-discharge at $20\,^{\circ}\mathrm{C}$ is shown in Figure 4.2. The base value is the value in Table 4.1. It can be seen that the per unit inner resistance can be approximated by a third order polynomial, i.e.

$$r_{Bat,pu} = a_{r,Bat} DoD_{Bat}^3 + b_{r,Bat} DoD_{Bat}^2 + c_{r,Bat} DoD_{Bat} + d_{r,Bat} \qquad [-] \qquad (4.2)$$

where	DoD_{Bat}	$[-]$	Depth-of-discharge
	$a_{r_{Bat}} = 1.279$	$[-]$	Constant
	$b_{r_{Bat}} = -0.694$	$[-]$	Constant
	$c_{r_{Bat}} = 0.214$	$[-]$	Constant
	$d_{r_{Bat}} = 0.994$	$[-]$	Constant

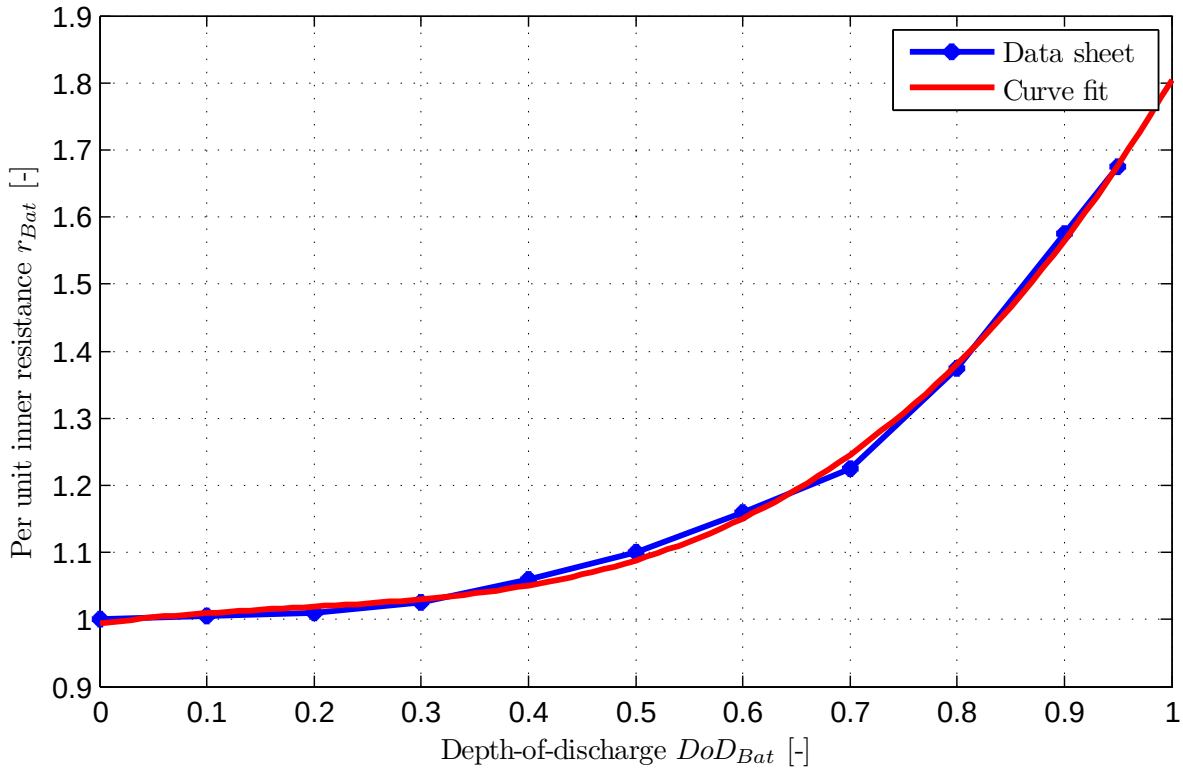

Figure 4.2: Per unit inner resistance of battery at $20\,^{\circ}\mathrm{C}$.

Even though it has been shown in [81, 91], that the inner resistance also depend on the actual current level, and the sign of the current, the expression in Equation (4.2) will be used, due to the lack of better data. Temperature dependency is also neglected. The inner resistance is therefore given by

$$R_{Bat} = R_{Bat,nom} \cdot r_{Bat,pu} \qquad [\Omega] \qquad (4.3)$$

Open Circuit Voltage Modeling

If one is showing the voltage as a function of the Ah taken out of the battery with a constant current, one will see a shape similar to the polarization curve of a fuel cell, i.e. at the beginning and end, the voltage drops quite fast, but in the between it drops with an almost constant slope. This means that the inner voltage of the battery also depend on the charge level of the battery. Due to the lack of better data, it is assumed that the open circuit voltage is linear depending of the state-of-charge SoC_{Bat} [81, 91]. Therefore

$$SoC_{Bat} = 1 - DoD_{Bat} \qquad [-] \qquad (4.4)$$

$$v_{Bat,oc} = (V_{Bat,max} - V_{Bat,min})\, SoC_{Bat} + V_{Bat,min} \qquad [\mathrm{V}] \qquad (4.5)$$

4.4 POWER CAPABILITY

An important parameter of a battery is its power capability. The power capability depends on several parameters, e.g. state-of-charge level, accepted minimum voltage, temperature, age, and the time interval of the drawn power. In the data sheet the highest constant discharge power is specified to be $P_{Bat} = 1226\,\mathrm{W}$. The maximum constant current discharge is $I_{Bat} = 1500\,\mathrm{A}$ for 5 seconds. However, even when fully discharged the battery terminal voltage will be $V_{Bat,max} - R_{Bat,nom} \cdot 1500\,\mathrm{A} = -3.6\,\mathrm{V}$. This means that for such high currents the model in Figure 4.1 cannot be used. Usually it is not recommended to discharge lead-acid batteries below $SoC_{Bat} = 0.2$ [87]. The open circuit voltage is from Equation (4.5) at this charge level $v_{Bat,oc}(SoC_{Bat} = 0.2) = 11.16\,\mathrm{V}$. The per unit battery inner resistance is from Figure 4.2 $r_{Bat,pu}(DoD_{Bat} = 0.8) = 1.35$. When manipulating Equation (4.1) the maximum continuous power at $SoC_{Bat} = 0.2$ is given by [16].

$$P_{Bat,max}(SoC_{Bat} = 0.2) = \frac{(v_{Bat,oc}(SoC_{Bat} = 0.2))^2}{4R_{Bat,nom}r_{Bat,pu}(DoD_{Bat} = 0.8)} = 1988\,\mathrm{W} \qquad (4.6)$$

The current at this power level is

$$\begin{aligned} I_{Bat}(P_{Bat,max}(SoC_{Bat} = 0.2)) &= \frac{v_{Bat,oc}(SoC_{Bat} = 0.2)}{2R_{Bat,nom}r_{Bat,pu}(DoD_{Bat} = 0.8)} \\ &= 356.3\,\mathrm{A} \end{aligned} \qquad (4.7)$$

In the data sheet the maximum continuous discharge current is specified to be $I_{Bat} = 400\,\mathrm{A}$. This is $11\,\%$ different than calculated. However, it is not specified at which voltage level this current can be drawn. It is therefore chosen to use the maximum power level calculated above even though it might be a little too conservative.

4.5 CAPACITY MODELING

The capacity modeling will be divided into a discharge and charge mode.

During Discharging

The capacities are in Table 4.1 specified to be $Q_{Bat,20} = 40\,\mathrm{Ah}$ and $Q_{Bat,10} = 37\,\mathrm{Ah}$ for a discharge time of $T_{Bat,20} = 20\,\mathrm{h}$ and $T_{Bat,10} = 10\,\mathrm{h}$, respectively. The corresponding discharge currents are therefore

$$I_{Bat,20} = \frac{Q_{Bat,20}}{T_{Bat,20}} = 2\,\mathrm{A} \tag{4.8}$$

$$I_{Bat,10} = \frac{Q_{Bat,10}}{T_{Bat,10}} = 3.7\,\mathrm{A} \tag{4.9}$$

It is well known that the amount of charge that can be taken out of a battery depend on several conditions, e.g. the temperature, age, current level, and accepted minimum voltage level. The minimum accepted voltage level is $\frac{V_{Bat,min}}{6\,\mathrm{cells}} = 1.75\,\mathrm{V/cell}$ of the battery in Table 4.1. When fully charged one can therefore draw $I_{Bat,20} = 2\,\mathrm{A}$ for $T_{Bat,20} = 20\,\mathrm{h}$ at $20\,^{\circ}\mathrm{C}$ before the limit of $1.75\,\mathrm{V/cell}$ is reached, i.e. $SoC_{Bat} = 0$. In Figure 4.3(a) the capacities at $20\,^{\circ}\mathrm{C}$ for different current levels are shown. For currents higher than the nominal current the capacity is lower than the nominal. This phenomena can also be described by the Peukert equation [20, 52, 77], i.e.

$$Q_{Bat,\,1\mathrm{A}} = I_{Bat}^{k} T_{Bat} \qquad [\mathrm{Ah}] \tag{4.10}$$

where	$Q_{Bat,\,1\mathrm{A}}$	$\left[\mathrm{A^k h}\right]$	Capacity for for a discharge current of $I_{Bat} = 1\,\mathrm{A}$
	I_{Bat}	$[\mathrm{A}]$	Constant discharge current
	T_{Bat}	$[\mathrm{h}]$	Time the current I_{Bat} can be drawn before the voltage limit $V_{Bat,min}$ is reached
	k	$[-]$	Peukert number

As Equation (4.10) has to be fulfilled for all current levels, the discharge time T_{Bat} will either be shorter or longer than the nominal discharge time. When manipulating Equation (4.10) it can be shown that the capacity Q_{Bat} for a given constant current discharge I_{Bat} can be written as [52]:

$$Q_{Bat} = Q_{Bat,20} \left(\frac{I_{Bat,20}}{I_{Bat}} \right)^{k-1} \qquad [\mathrm{Ah}] \tag{4.11}$$

However, when solving for k in Equation (4.11) the result in Figure 4.3(b) is obtained. It is seen that the number k not is constant as it was expected. This is not against the study in [20], where it was shown that the capacity of a battery not always follows the Peukert equation. In the study it was shown that if the battery apparently is total discharged, more energy can be taken out of the battery after a rest period. However, in Figure 4.3(b) it can be seen that the number k can be described by a first order polynomial, i.e.

$$k = a_k I_{Bat} + b_k \qquad [-] \tag{4.12}$$

where	a_k	=	0.0024	Constant
	b_k	=	1.1519	Constant

When applying Equation (4.12) to Equation (4.11) the result in Figure 4.3(a) is obtained. The approximation of the capacity Q_{Bat} seems to be appropriate.

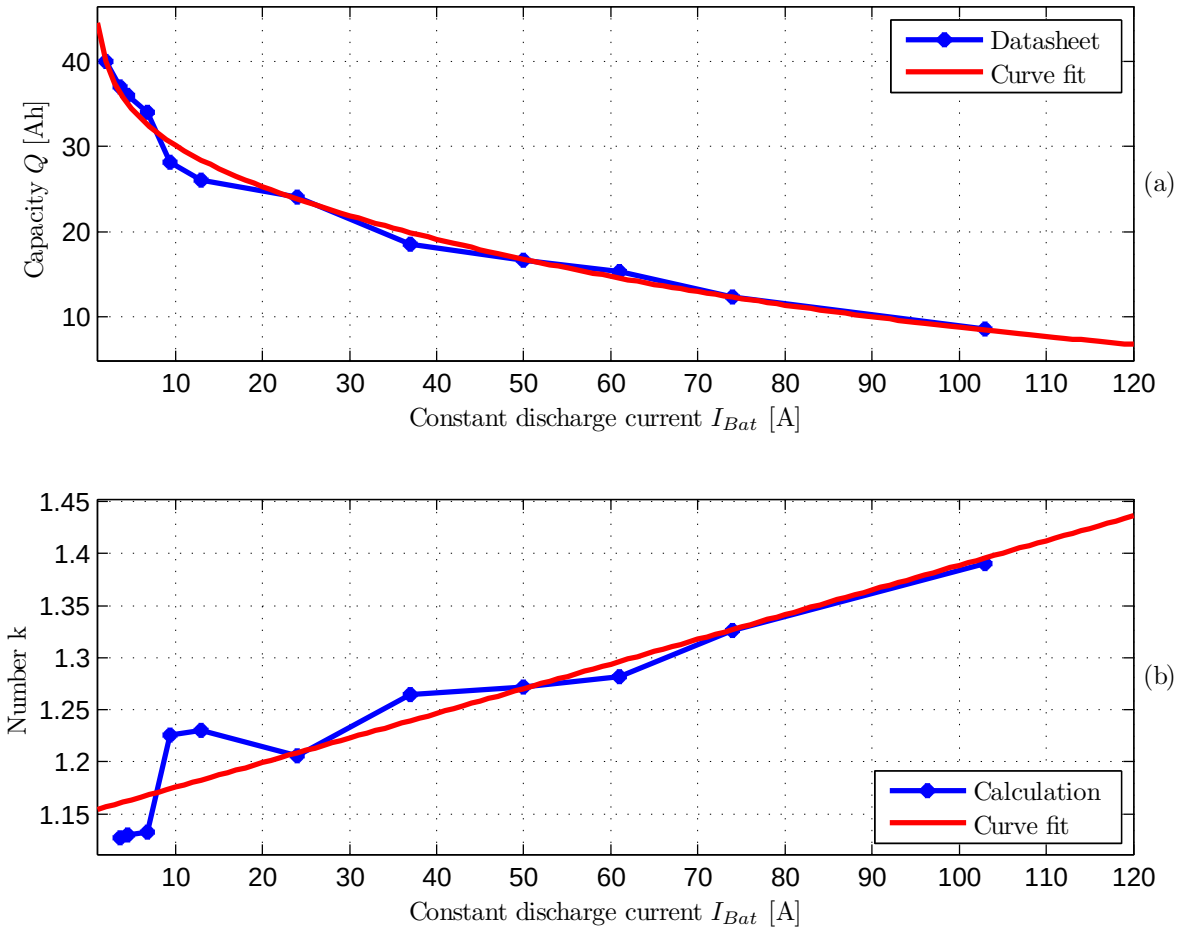

Figure 4.3: (a) Data sheet and approximated capacity of the battery for different current levels. (b) Calculated and approximated number k.

During Charging

In the previous section the Peukert equation was introduced in order to describe the available capacity as a function of the discharge current. The other way around, i.e. how much of the charging current that actually will be useful for discharging again, is however not described as much in the literature. In the data sheet of the battery, it is shown how much of the input charge which is converted into storage for different charging currents, i.e. the amount of input charge that actual is available for discharging again. In Figure 4.4 is shown the fraction of the 10 hour discharge capacity $Q_{Bat,10}$ that is stored when the battery is charged with different fractions of the 10 hour discharge current $I_{Bat,10}$ during a charge time of $T_{cha} = 3\,\mathrm{h}$. The battery is charged from total emptiness, i.e. $DoD_{Bat} = 1$. The input charge $I_{Bat}T_{cha}$ is converted into useful charge storage Q_{sto} with a charge efficiency of

$$\eta_{cha} = \frac{Q_{sto}}{I_{Bat}T_{cha}} \qquad [-] \tag{4.13}$$

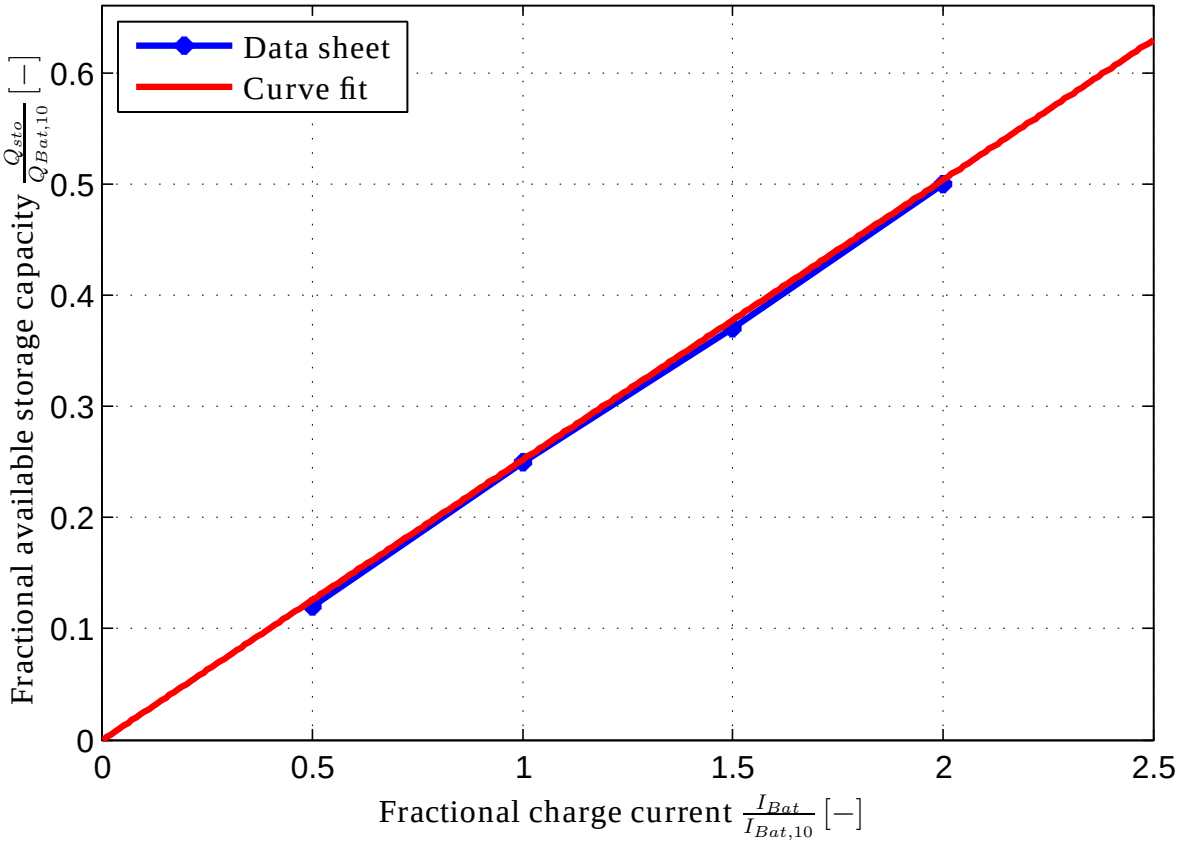

Figure 4.4: Fractional charge storage as a function of the fractional charge current.

The fractional charge storage is therefore given by

$$\frac{Q_{sto}}{Q_{Bat,10}} = \frac{\eta_{cha} I_{Bat} T_{cha}}{I_{Bat,10} T_{Bat,10}} = \frac{T_{cha}}{T_{Bat,10}} \eta_{cha} \frac{I_{Bat}}{I_{Bat,10}} \qquad [-] \tag{4.14}$$

From Equation (4.14) it is understood that the charge efficiency η_{cha} is the slope of the curve in Figure 4.4 multiplied by $\frac{T_{Bat,10}}{T_{cha}} = \frac{10}{3}$. It is seen that the slope is almost constant, which means that the charge efficiency also is constant for the provided data. The slope of the graph in Figure 4.4 is $a = 0.252$. The charge efficiency is therefore $\eta_{cha} = a\frac{10}{3} = 0.84$. In Figure 4.4 it is seen that this approximation fits the data sheet values sufficiently.

State-of-Charge Modeling

The state-of-charge SoC_{Bat} of the battery is an approximation of how much energy that can be taken out of the battery before it is "empty". In the data sheet of the battery is that part of the current that is turned into useful storage specified as a function of the 10 hour capacity $Q_{Bat,10}$.

The time that a given current can be drawn from the battery is from Equation (4.11) given by

$$T_{Bat} = \frac{Q_{Bat}}{I_{Bat}} = \left(\frac{I_{Bat,20}}{I_{Bat}}\right)^k T_{Bat,20} \qquad [\mathrm{h}] \tag{4.15}$$

This means that the equivalent discharge current $I_{Bat,eq,dis}$ that is drawn for a given discharge time period T_{Bat}, when $Q_{Bat,10}$ is the charge reference, is given by

$$I_{Bat,eq,dis} = \frac{Q_{Bat,10}}{T_{Bat}} = \frac{Q_{Bat,10}}{T_{Bat,20}} \left(\frac{I_{Bat}}{I_{Bat,20}} \right)^k \quad [\mathrm{A}] \tag{4.16}$$

In the same way the equivalent charge current is given by

$$I_{Bat,eq,cha} = \eta_{Bat,cha} I_{Bat} \quad [\mathrm{A}] \tag{4.17}$$

An equivalent discharge and charge current that are valid for a charge reference of $Q_{Bat,10}$ have now been defined. In order to summarize, the instantaneous state-of-charge for the battery current i_{Bat} can therefore be calculated as follows:

$$k = a_k |i_{Bat}| + b_k \quad [-] \tag{4.18}$$

$$i_{Bat,eq} = \begin{cases} -\frac{Q_{Bat,10}}{T_{Bat,20}} \left(\frac{|i_{Bat}|}{I_{Bat,20}} \right)^k & , i_{Bat} < 0\,\mathrm{A} \\ \eta_{Bat,cha} i_{Bat} & , i_{Bat} \geq 0\,\mathrm{A} \end{cases} \quad [\mathrm{A}] \tag{4.19}$$

$$SoC_{Bat} = 1 + \frac{1}{Q_{Bat,10} 3600\,\mathrm{s/h}} \int i_{Bat,eq} dt \quad [-] \tag{4.20}$$

In Equation (4.20) it is seen that the state-of-charge is the integral of the equivalent current relative to the nominal capacity of the battery [52, 77]. Due to the sign convention is $i_{Bat,eq}$ negative for a negative battery current i_{Bat}, i.e. during discharging.

4.6 MODELING LIFETIME

The lifetime of a battery depends on several parameters, e.g. temperature, stress, insufficient charging, age, and the depth-of-discharge [8, 68], but usually only the cycle-to-failure of a battery is specified in the data sheet.

Cycle-to-failure

In Figure 4.5 the cycles-to-failure N_{ctf} for a certain depth-of-discharge is shown. The depth-of-discharge is relative to $Q_{Bat,10}$ and is measured at $20\,^{\circ}\mathrm{C}$ with a current of $I_{Bat} = 2I_{Bat,10}$. It is seen that the deeper the battery is discharged less cycles the battery can handle. In Figure 4.5 it is also seen that the cycle-to-failure can be approximated by a fourth order polynomial, i.e.

$$N_{ctf} = a_{ctf} DoD_{Bat}^4 + b_{ctf} DoD_{Bat}^3 + c_{ctf} DoD_{Bat}^2 + d_{ctf} DoD_{Bat} + e_{ctf} \quad [-] \tag{4.21}$$

where
$a_{ctf} = 9406.6$ $[-]$ Constant
$b_{ctf} = -27512$ $[-]$ Constant
$c_{ctf} = 30527$ $[-]$ Constant
$d_{ctf} = -15984$ $[-]$ Constant
$e_{ctf} = 3932.7$ $[-]$ Constant

In its lifetime the battery is not discharged to the same specific level all the time. Sometimes it is deeply discharged and sometimes it is only slightly discharged before it is recharged. Therefore, in order to be able to calculate how the number of cycles with different discharge levels affects the lifetime the rain-flow-counting method is introduced [8].

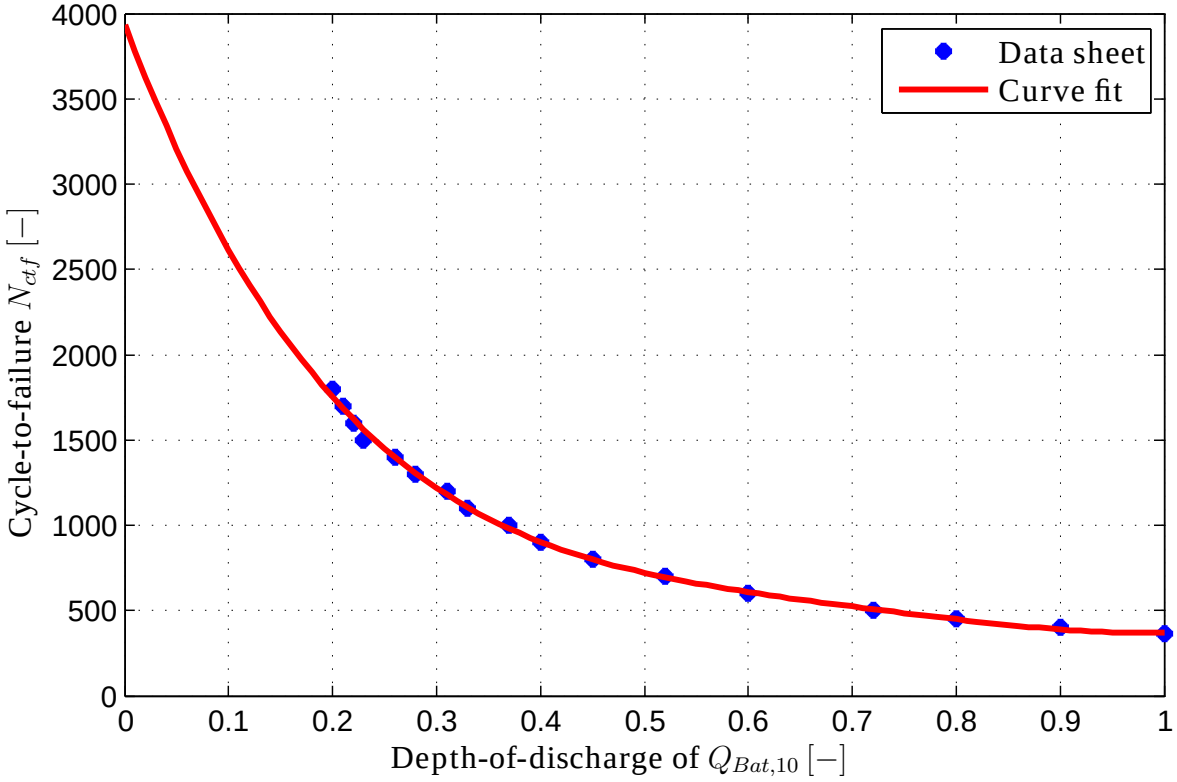

Figure 4.5: Cycles-to-failure for different depth-of-discharges relative to $Q_{Bat,10}$.

Rain-Flow-Counting

The rain flow counting method is often used in mechanical engineering in order to calculate the stress of components. The counting is performed in terms of droops. In Figure 4.6, it is illustrated how the rain-flow-counting method is applied. The thick gray line is the depth-of-discharge of the battery, and the thinner colored lines are used for counting the number of cycles for one specific depth-of-discharge level. The colored lines are denoted half cycles. It is seen that each half cycle starts either in a local valley or at a peak. If Figure 4.6 is rotated 90° clockwise it will have a shape similar to a pagoda roof. By letting a rain drop start at each peak and valley, the half cycle belonging to a specific drop, can be obtained by following the drops path down the roof. However, the drop must stop if one of the following conditions are met:

1. It reaches the end of time of the data-set, e.g. half cycle number 1, 2, and 5
2. It runs into a peak / valley, that is higher / deeper than its starting peak / valley, e.g. half cycle number 3
3. It gets into contact with a previous drop, e.g. half cycle number 4 and 6

The amplitude of each half cycle is the difference between the depth-of-discharge at its starting and ending points. Half cycles 1 and 2 therefore both have an amplitude of $DoD_{Bat} = 0.25$.

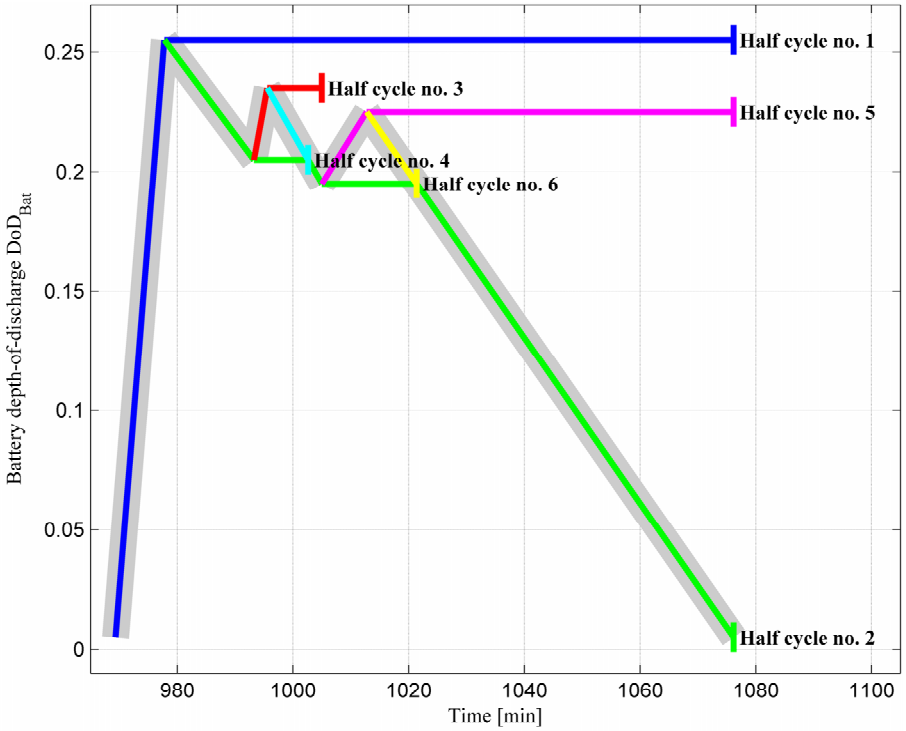

Figure 4.6: Rain-flow-counting method. Depth-of-discharge as a function of the time.

The loss-of-lifetime of a battery is defined by [68]:

$$LoL_{Bat} = \sum_{DoD_{Bat}=0.01}^{DoD_{Bat}=1} \frac{N_{cyc}(DoD_{Bat})}{N_{ctf}(DoD_{Bat})} \quad [-] \tag{4.22}$$

where N_{cyc} $[-]$ Number of full cycles with amplitude DoD_{Bat} that have been counted by using the rain-flow-counting method

It may be noticed that in order to count one full cycle of amplitude DoD_{Bat}, one needs to count two half cycles of amplitude DoD_{Bat}. The end-of-life of the battery with several depth-of-discharge cycles is reached when $LoL_{Bat} = 1$.

4.7 CONCLUSION

It is chosen to use the traditional lead-acid battery due to its simple operation, low cost, availability, and because it is expected that an advantage can be obtained by combining it with an ultracapacitor. A model has been created from data sheet specifications. The model is able to model the terminal voltage, state-of-charge, and lifetime. For the capacity estimation the Peukert equation is used, and for the lifetime calculation the rain-flow counting method is used. The model is only for steady-state purpose, and a dynamic model and laboratory validation are left for future work.

5 Ultracapacitor Modeling

Ultracapacitors are attractive as energy storage devices because they unlike batteries offer a very high efficiency, cycle count, and power density. Their energy density is much better than the traditional electrolytic capacitors, and they can therefore act as a bridge between the high power capacitors and high energy batteries. In this chapter an ultracapacitor is therefore modeled in order to obtain an understanding of its behavior in a system. The ultracapacitor is modeled in both steady-state and dynamic situations.

5.1 Specifications

The ultracapacitor used for the modeling is from Maxwell®. The specifications can be seen in Table 5.1. Because of the high nominal voltage of $V_{UC,max} = 16.2\,\mathrm{V}$ it is understood that several cells are series connected in order to form a module or ultracapacitor bank. Even though it will be denoted "the ultracapacitor".

Manufacture	Maxwell®
Type	BMOD0500 E016
Maximum voltage	$V_{UC,max} = 16.2\,\mathrm{V}$
Capacitance	$C_{UC} = 500\,\mathrm{F}$
Equivalent series resistance	$2.8\,\mathrm{m\Omega}$
Energy density	$3.17\,\mathrm{Wh/kg}$
Power density	$5.4\,\mathrm{kW/kg}$
Volume	$4.7\,\mathrm{L}$
Mass	$5.75\,\mathrm{kg}$

Table 5.1: Data of the used ultracapacitor module.

5.2 Inner Resistance and Equivalent Capacitance

Two important parameters of an ultracapacitor are its inner resistance and capacitance. The inner resistance specifies how much power can be drawn from the ultracapacitor and the capacitance determines how much energy is available. In order to investigate these two parameters the ultracapacitor has been fully charged. At time $t = T_A$ the ultracapacitor is discharged by a constant current of $i_{UC} = 100\,\mathrm{A}$ until a certain voltage is reached at time $t = T_B$. In the meantime the terminal voltage is measured. In Figure 5.1 the ultracapacitor voltage and current can be seen. The current is

negative as it is taken out of the ultracapacitor. It can be seen that at time T_A and T_B the voltage changes immediately when the current either increases or decreases. This is due to the inner resistance. However, the voltage remains constant a few seconds after the current step at T_A even though the current is non-zero, i.e. the basic current equation of a capacitor ($i = C\frac{dv}{dt}$) is not satisfied. It is unknown why this happens, but it is probably due to a failure in the voltage measurement circuit. The inner resistance is therefore calculated at the inverse current step at T_B:

$$R_1 = \left| \frac{v_{UC}(T_{B+}) - v_{UC}(T_{B-})}{i_{UC}(T_{B+}) - i_{UC}(T_{B-})} \right| \quad [\Omega] \tag{5.1}$$

where
v_{UC}	[V]	Ultracapacitor terminal voltage
i_{UC}	[A]	Ultracapacitor terminal current
T_{B-}	[s]	Time just before the inverse current step
T_{B+}	[s]	Time just after the inverse current step

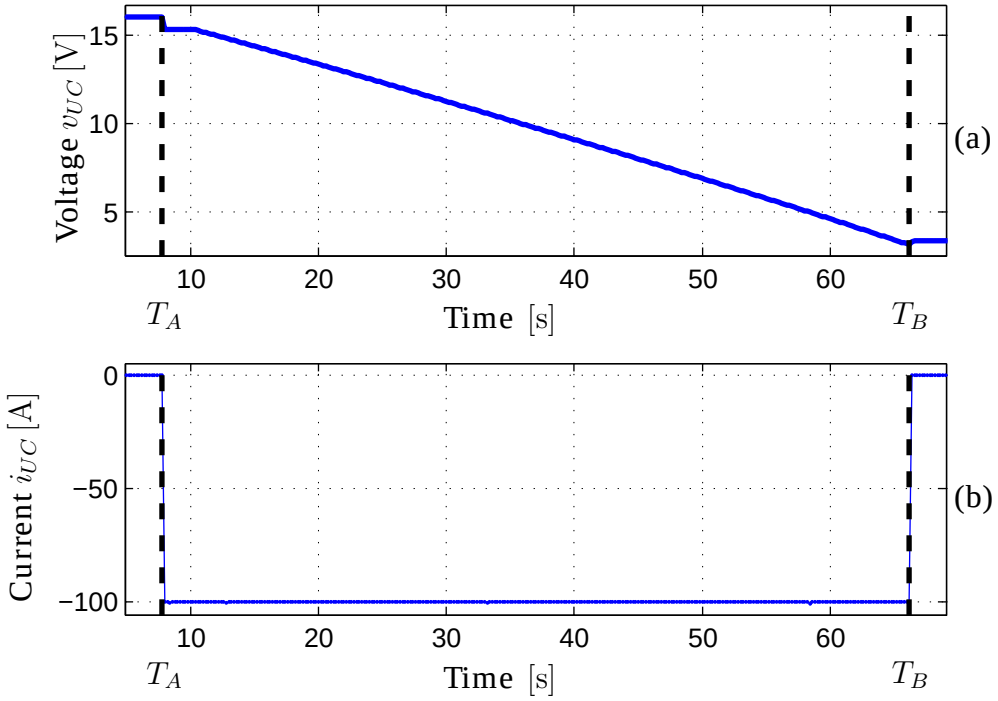

Figure 5.1: Constant discharge of ultracapacitor. (a) Measured voltage. (b) Applied current.

The voltage on the other side of the inner resistance R_1 is therefore given by

$$v_1 = v_{UC} - R_1 i_{UC} \quad [\text{V}] \tag{5.2}$$

During discharge the ultracapacitor can be modeled as in Figure 5.2(a). In this circuit it is assumed that the current i_{UC} is provided by a single equivalent capacitance C_{eq}. This capacitance can be calculated from the derivative of the voltage, i.e.

$$C_{eq} = \frac{i_{UC}}{\dot{v}_1} \quad [\text{F}] \tag{5.3}$$

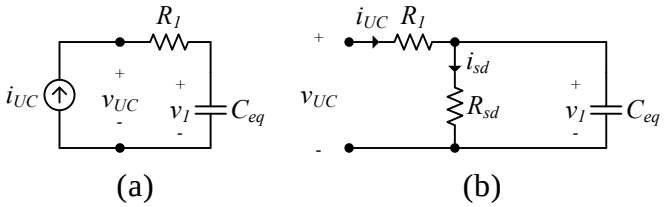

Figure 5.2: Equivalent ultracapacitor circuit modeling. (a) During constant current discharge. (b) During self discharge.

In Figure 5.3 it can be seen that the equivalent capacitance is not constant, but depends on the voltage level v_1. In the same figure it can also be seen that the equivalent capacitance can be approximated by a first order polynomial, i.e.

$$C_{eq} = a_{C_{eq}} v_1 + b_{C_{eq}} \qquad [\mathrm{F}] \tag{5.4}$$

where $a_{C_{eq}}$ Constant
$b_{C_{eq}}$ Constant

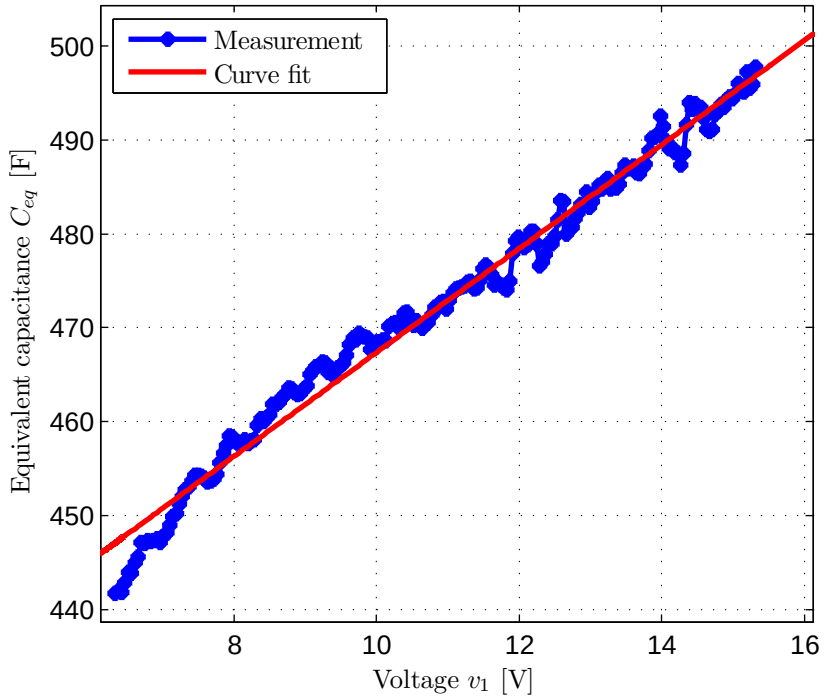

Figure 5.3: Equivalent capacitance of the ultracapacitor during discharge.

5.3 Self Discharge

If the ultracapacitor is the only energy storage device of the fuel cell vehicle it is critical that it can store the energy during the night so it is available when there is a need for it. In order to investigate the self discharge of the ultracapacitor module a long

term test is performed. The ultracapacitor module is charged to its maximum allowed voltage of $V_{UC,max} = 16.2\,\mathrm{V}$. Thereby the charge power supply is disconnected and the open circuit ultracapacitor voltage is measured until it is discharged due to the self discharge. The voltage during self discharge can be seen in Figure 5.4(a). It takes $134\,\mathrm{days}$ before the half of the nominal voltage $\frac{V_{UC,max}}{2} = 8.1\,\mathrm{V}$ is reached. It is noticed that the voltage drops relative fast in the beginning. It is seen that near $t = 100\,\mathrm{days}$, measurements are missing for approximately $5\,\mathrm{days}$. This is due to a power failure in the laboratory, which stopped the data logging.

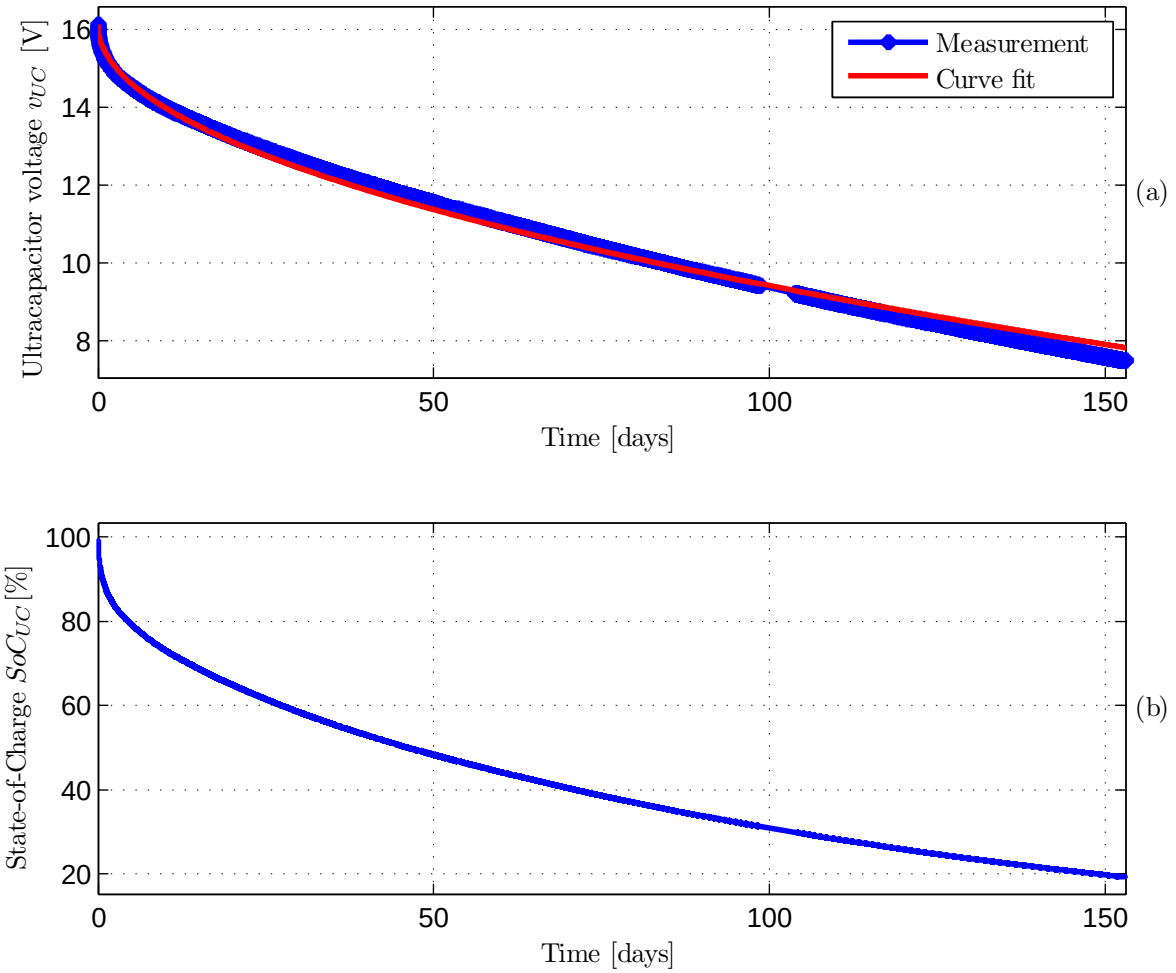

Figure 5.4: Self discharge of ultracapacitor. (a) Voltage. (b) State-of-Charge.

In the specifications of the ultracapacitor in Table 5.1 the nominal capacitance is $C_{UC} = 500\,\mathrm{F}$. However, in Figure 5.3 it is seen that the equivalent capacitance C_{eq} becomes smaller the lower the voltage is. This means that the relative energy of the ultracapacitor drops even faster than expected, i.e. if the capacitance was independent of the voltage. The relative energy, or state-of-charge SoC_{UC}, of the ultracapacitor is defined as

$$SoC_{UC} = \frac{\frac{1}{2}C_{eq}v_{UC}^2}{\frac{1}{2}C_{UC}V_{UC,max}^2} = \frac{C_{eq}v_{UC}^2}{C_{UC}V_{UC,max}^2} \qquad [-] \qquad (5.5)$$

The state-of-charge during self discharge is shown in Figure 5.4(b). Due to the lower equivalent capacitance the state-of-charge after $134\,\text{days}$ is therefore $22.5\,\%$ instead of $25\,\%$. When fully charged it takes approximately $18\,\text{hours}$ to lose $10\,\%$ of the energy.

In [65] the voltage during self discharge are expressed as

$$V = V_0 - m\sqrt{t} \qquad [\text{V}] \tag{5.6}$$

where V [V] Ultracapacitor voltage during self discharge
V_0 [V] Initial voltage at $t = 0\,\text{s}$
m $[\text{V}/\sqrt{\text{s}}]$ Diffusion parameter

The result of applying Equation (5.6) is also shown in Figure 5.4(a). It is seen that the equation is able to describe the ultracapacitor voltage during discharge with an acceptable error. Only in the last third part of the measurement a difference between measurement and curve fit is noticed. However, due to the time depending nature of the equation it is not sufficient for circuit modeling. For example if the ultracapacitor suddenly is charged and afterwards is left in open circuit condition again, this will be difficult to model when using Equation (5.6). Therefore, in [19] a circuit is proposed that is able to model the behavior during self discharge. The circuit is a combination of a resistor in parallel with a series connection of a capacitor and another resistor. However, this circuit is not as accurate as Equation (5.6) [19]. The self discharge has also been investigated in [10], but only for a time period of approximately 6 hours.

The equivalent capacitance in Equation (5.4) depends on the voltage v_1. It will therefore not be problematic if the circuit that is modeling the self discharge behavior also depends on this voltage. During self discharge the ultracapacitor is therefore modeled as in Figure 5.2(b). The time constant during self discharge is formed by the self discharge resistance R_{sd} and the equivalent capacitor C_{eq}. During self discharge no load or source is connected to the ultracapacitor, i.e. $i_{UC} = 0\,\text{A}$. The time constant can therefore be calculated as follows:

$$i_{sd} = \frac{v_{UC}}{R_{sd}} = -C_{eq}\dot{v}_{UC} \qquad [\text{A}] \tag{5.7}$$

$$\Updownarrow$$

$$\tau_{sd} = R_{sd}C_{eq} = -\frac{v_{UC}}{\dot{v}_{UC}} \qquad [\text{s}] \tag{5.8}$$

The self discharge time constant τ_{sd} is shown in Figure 5.5. When fully charged the time constant is relative small, which indicates that the voltage drops quite fast at high voltages. It is seen that the time constant can be approximated to fit a modified Weibull curve, i.e.

$$\tau_{sd} = a_{sd} \cdot e^{-(b_{sd} \cdot v_{UC})^{c_{sd}}} + d_{sd} \qquad [\text{s}] \tag{5.9}$$

where $a_{sd} = 2.0101 \cdot 10^7$ Constant
$b_{sd} = 0.0675$ Constant
$c_{sd} = 16.1625$ Constant
$d_{sd} = 1.1233 \cdot 10^5$ Constant

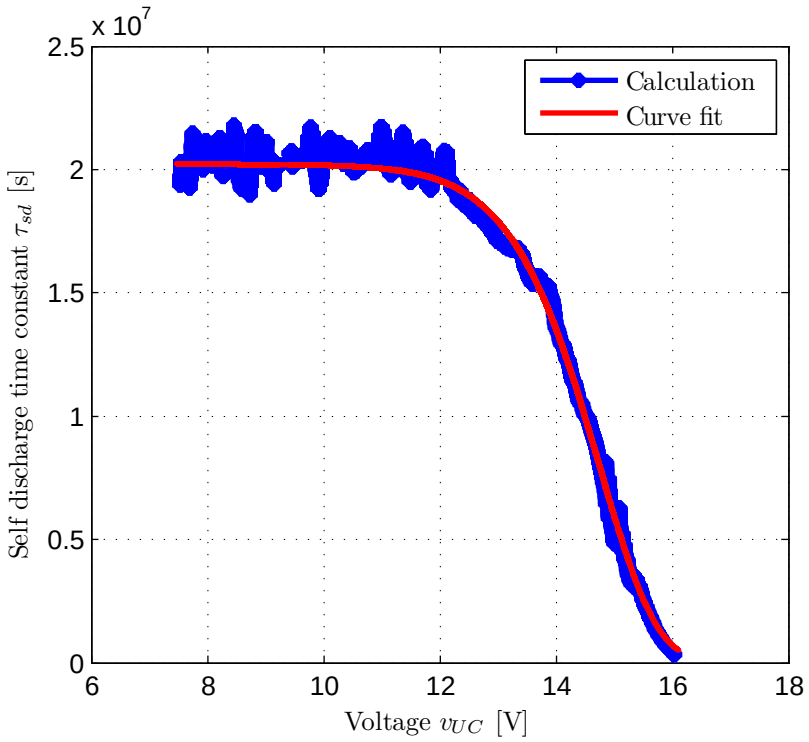

Figure 5.5: Discharge time constant.

The self discharge resistance can now be calculated by solving Equation (5.8), i.e.

$$R_{sd} = \frac{\tau_{sd}}{C_{eq}} \qquad [\Omega] \tag{5.10}$$

5.4 CHARGE RECOVERY

Just after the inverse step at time $t = T_{B+}$ in Figure 5.1 the voltage rises due to the charge recovery. This means that the models in Figure 5.2 are insufficient as "something" needs to charge the equivalent capacitor C_{eq} after the load current i_{UC} has been disconnected. This "something" can be modeled by several RC-circuits as shown in Figure 5.2. The voltage rises with several time constants during the charge recovery. The equivalent capacitance C_{eq} in Figure 5.2 can therefore be replaced by a certain number of RC circuits, in order to model these time constants. Thereby the model in Figure 5.6 is obtained. It is seen that the equivalent capacitor C_{eq} is replaced by k RC circuits. The resistance modeling the self discharge is still present.

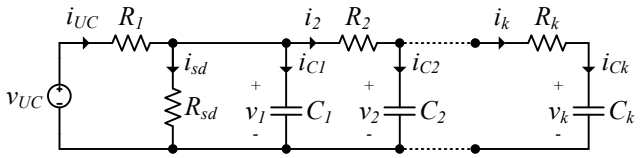

Figure 5.6: Proposed model used for modeling self discharge and charge recovery.

In order to calculate the first capacitor C_1 in Figure 5.6 is it assumed that the current i_2 in Figure 5.6 is constant just before and after the inverse step at time T_B. Due to the fast rise of the voltage the self discharge is neglected. Therefore the ultracapacitor can be modeled as the circuit in Figure 5.7 just before and after the inverse current step. From the two circuit diagrams the capacitor C_1 can be calculated, i.e.

$$i_2(T_{B-}) = I_2 = i_2(T_{B+}) \qquad [\mathrm{A}] \qquad (5.11)$$

$$\Updownarrow$$

$$i_{UC}(T_{B-}) - C_1\dot{v}_1(T_{B-}) = -C_1\dot{v}_1(T_{B+}) \qquad [\mathrm{A}] \qquad (5.12)$$

$$\Updownarrow$$

$$C_1 = \frac{i_{UC}(T_{B-})}{\dot{v}_1(T_{B-}) - \dot{v}_1(T_{B+})} \qquad [\mathrm{F}] \qquad (5.13)$$

This means that the capacitor C_1 can be calculated from the derivative of the voltage v_1 just before and after the inverse step.

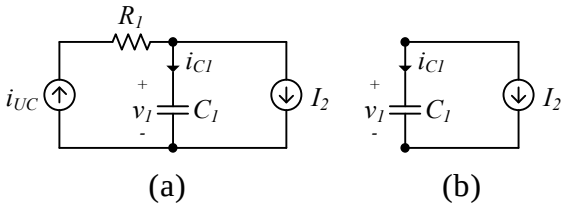

Figure 5.7: Equivalent circuit model at inverse step. (a) Just before the inverse step at time T_{B-}. (b) Just after the inverse step at time T_{B+}.

Self discharge compensation

In Figure 5.8 the voltage of Figure 5.1 is shown after the inverse step at time $t = T_B$. It is seen that the voltage increases for many hours. The self discharge mechanism will therefore affect the voltage. The self discharge current i_{sd} is given by

$$i_{sd} = \frac{v_1}{R_{sd}} \qquad [\mathrm{A}] \qquad (5.14)$$

The charge dissipated in the self discharge resistor R_{sd} during the charge recovery period is therefore

$$q_{sd} = \int_{T_{B+}}^{T_C} i_{sd}dt \qquad [\mathrm{C}] \qquad (5.15)$$

If this charge level is not removed from the equivalent capacitance C_{eq} the compensated voltage of the capacitor C_1 will be

$$v_{1,comp} = v_1 + \frac{q_{sd}}{C_{eq}} \qquad [\mathrm{V}] \qquad (5.16)$$

The compensated voltage $v_{1,comp}$ is also shown in Figure 5.8. It is seen that the charge recovery circuits charge the capacitor C_1 with more than $30\,\mathrm{mV}$.

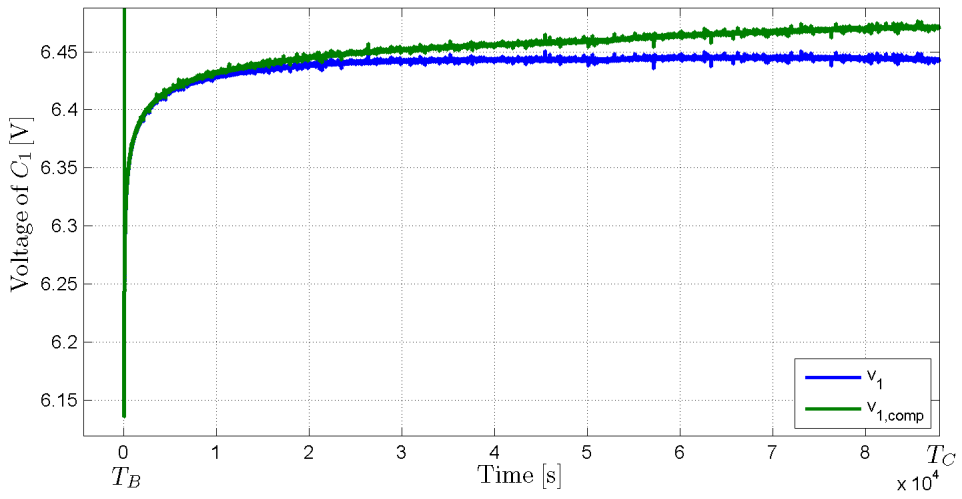

Figure 5.8: Compensated and non-compensated voltage of capacitor C_1 during the charge recovery period.

Time Constant Calculation

The voltage rises with k time constants during the charge recovery time. It is assumed that for each R_iC_i-circuit with time constant τ_i, τ_i is bigger than the time constant τ_{i-1} of $R_{i-1}C_{i-1}$-circuit, i.e. $\tau_1 < \tau_2 \cdots < \tau_k$. It is therefore assumed that for the R_iC_i-circuit in Figure 5.6 the current i_{i+1} is constant, when the R_iC_i-circuit is dominating. The equivalent circuit used for calculating time constant τ_2 is shown in Figure 5.9(a). It is seen that the current contribution of the higher RC-circuits is modeled as a constant current source with current I_3. In Figure 5.9(b) the equivalent circuit model for time constant τ_3 is shown. It is seen that this circuit is obtained by replacing the current source I_3 with a RC-circuit and another current source I_4. However, in order to simplify it is assumed that the current i_2 is almost constant in the time period where the time constant τ_3 is dominating. This means that the voltage slope of capacitor C_2 is equal to the voltage slope of capacitor C_1, i.e.

$$v_2 = v_{1,comp,3} - R_2 I_2 \qquad [\mathrm{V}] \tag{5.17}$$

$$\Downarrow$$

$$\dot{v}_2 = \dot{v}_{1,comp,3} \qquad [\mathrm{V/s}] \tag{5.18}$$

where $v_{1,comp,3}$ [V] Compensated voltage of capacitor C_1 in the interval where time constant 3 τ_3 is dominating

The capacitors C_1 and C_2 therefore behave as they were in parallel. In Figure 5.9(c) it is shown an equivalent circuit diagram for time constant τ_3 when they are in parallel. It is seen that the resistor R_3 is in series with an equivalent resistance $R_{2,cha}$. The equivalent resistance $R_{2,cha}$ is inserted in order to compensate for the moving of capacitor C_2. The equivalent resistance $R_{2,cha}$ can be calculated by using the constraint

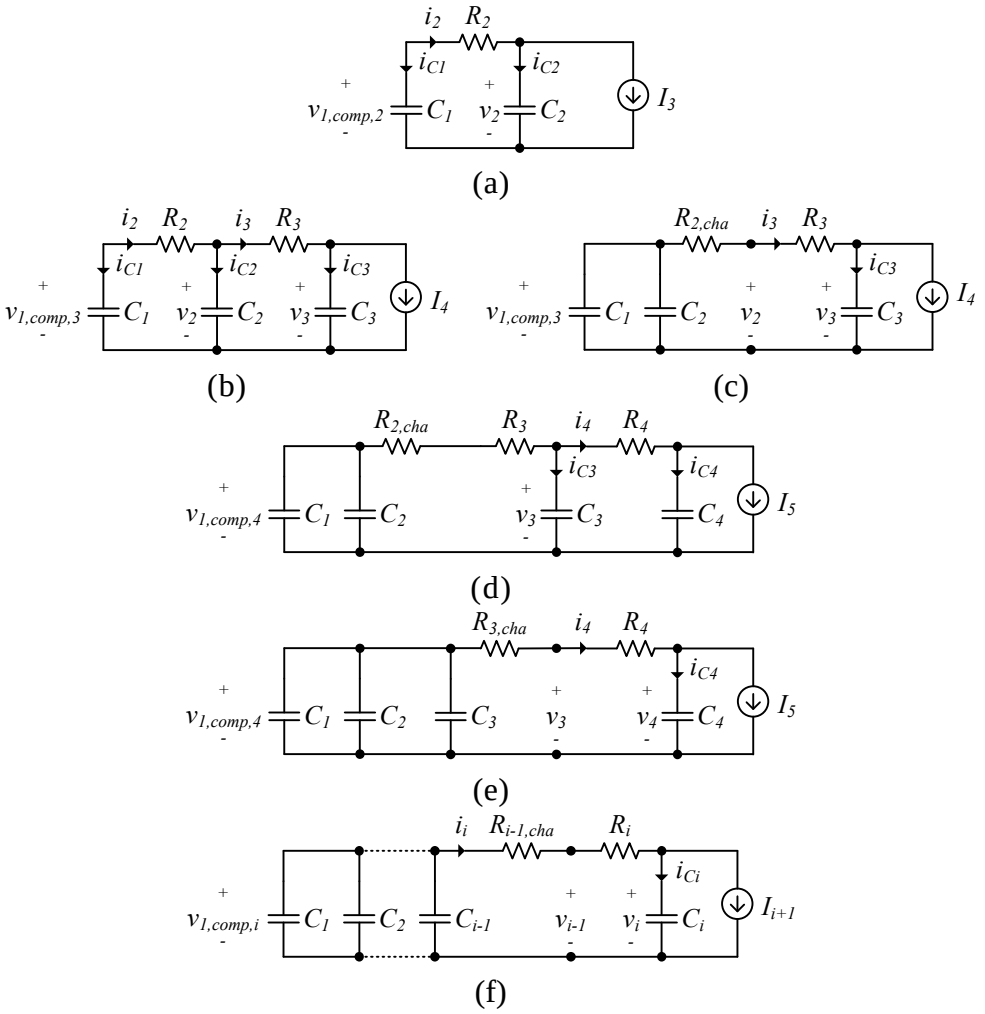

Figure 5.9: Equivalent ultracapacitor circuit modeling during the charge recovery period. (a) Equivalent circuit for time constant τ_2. (b) Equivalent circuit for time constant τ_3. (c) Modified equivalent circuit for time constant τ_3. (d) Equivalent circuit for time constant τ_4. (e) Modified equivalent circuit for time constant τ_4. (f) General structure of equivalent circuit diagrams for time constant τ_i.

that the voltage v_2 of Figure 5.9(b) and (c) should be identical. Therefore:

$$\begin{aligned} v_2 &= v_{1,comp,3} + R_2 C_1 \dot{v}_{1,comp,3} \\ &= v_{1,comp,3} + R_{2,cha}\left(C_1 + C_2\right)\dot{v}_{1,comp,3} \qquad [\mathrm{V}] \end{aligned} \tag{5.19}$$

$$\Updownarrow$$

$$R_{2,cha} = R_2 \frac{C_1}{C_1 + C_2} \qquad [\Omega] \tag{5.20}$$

If the current source I_4 in Figure 5.9(c) is replaced by a RC-circuit and another current source I_5 the equivalent circuit in Figure 5.9(d) is obtained. In order to simplify this circuit is also modified. The modified circuit is seen in Figure 5.9(e). It is seen that it has the same structure as the circuit for the previous time constant in Figure 5.9(c). The equivalent resistance $R_{3,cha}$ is calculated in the same way as the previous equiva-

lent resistance $R_{2,cha}$, i.e.

$$R_{3,cha} = (R_{2,cha} + R_3)\frac{C_1 + C_2}{C_1 + C_2 + C_3} \quad [\Omega] \tag{5.21}$$

For each time constant τ_i this principle can be repeated, i.e. replacing the current source of the previous τ_{i-1}-circuit by a RC-circuit and another current source, and afterwards modifying the circuit by putting all the capacitors to the left of the i^{th} capacitors. In Figure 5.9(f) a general equivalent circuit structure of the i^{th} time constant can be seen. For the i^{th} time constant the equivalent resistor $R_{i-1,cha}$ is therefore

$$R_{i-1,cha} = \begin{cases} 0 & , i = 2 \\ (R_{i-2,cha} + R_{i-1})\frac{\sum_{l=1}^{l=i-2} C_l}{\sum_{l=1}^{l=i-1} C_l} & , i \in [3;k] \end{cases} \quad [\Omega] \tag{5.22}$$

From the general equivalent circuit in Figure 5.9(f) the currents are given by

$$i_i = -\sum_{l=1}^{l=i-1} C_l \dot{v}_{1,comp,i} \quad [\mathrm{A}] \tag{5.23}$$

$$i_{C_i} = C_i \dot{v}_i = i_i - I_{i+1} = -\sum_{l=1}^{l=i-1} C_l \dot{v}_{1,comp,i} - I_{i+1} \quad [\mathrm{A}] \tag{5.24}$$

From Kirchhoff's voltage law one obtains

$$\begin{aligned} v_i &= v_{1,comp,i} - (R_{i-1,cha} + R_i)\, i_i \\ &= v_{1,comp,i} + (R_{i-1,cha} + R_i) \sum_{l=1}^{l=i-1} C_l \dot{v}_{1,comp,i} \quad [\mathrm{V}] \end{aligned} \tag{5.25}$$

$$\Updownarrow$$

$$\dot{v}_i = \dot{v}_{1,comp,i} + (R_{i-1,cha} + R_i) \sum_{l=1}^{l=i-1} C_l \ddot{v}_{1,comp,i} \quad [\mathrm{V/s}] \tag{5.26}$$

When inserting Equation (5.26) in (5.24) the following second order differential equation is obtained:

$$-\frac{I_{i+1}}{\sum_{l=1}^{l=i} C_l} = \frac{(R_{i-1,cha} + R_i)\sum_{l=1}^{l=i-1} C_l C_i}{\sum_{l=1}^{l=i} C_l} \ddot{v}_{1,comp,i} + \dot{v}_{1,comp,i} \quad [\mathrm{V/s}] \tag{5.27}$$

The second order differential equation has a homogeneous solution $v_{1,comp,h}$ and particular solution $v_{1,comp,p}$. The homogeneous solution has the form [38]

$$v_{1,comp,h,i} = a_i + b_i e^{-\frac{1}{\tau_i}(t - t_B)} \quad [\mathrm{V}] \tag{5.28}$$

The time constant τ_i can be determined by solving the characteristic equation, i.e.

$$\begin{aligned} 0 &= \frac{(R_{i-1,cha} + R_i)\sum_{l=1}^{l=i-1} C_l C_i}{\sum_{l=1}^{l=i} C_l} s^2 + s \\ &\Updownarrow \\ s = 0 \quad &\vee \quad -s = \frac{1}{\tau_i} = \frac{\sum_{l=1}^{l=i} C_l}{(R_{i-1,cha} + R_i)\sum_{l=1}^{l=i-1} C_l C_i} \end{aligned} \tag{5.29}$$

The particular solution is given by

$$v_{1,comp,p,i} = c_i(t - t_B) \quad [\mathrm{V}] \tag{5.30}$$

$$c_i = -\frac{I_{i+1}}{\sum_{l=1}^{l=i} C_l} \quad [\mathrm{V/s}] \tag{5.31}$$

The system is therefore given by

$$\begin{aligned} v_{1,comp,i} &= v_{1,comp,h,i} + v_{1,comp,p,i} \\ &= a_i + b_i e^{-\frac{1}{\tau_i}(t-t_B)} + c_i(t - t_B) \quad [\mathrm{V}] \end{aligned} \tag{5.32}$$

$$\dot{v}_{1,comp,i} = -\frac{1}{\tau_i} b_i e^{-\frac{1}{\tau_i}(t-t_B)} + c_i \quad [\mathrm{V/s}] \tag{5.33}$$

$$\ddot{v}_{1,comp,i} = \frac{1}{\tau_i^2} b_i e^{-\frac{1}{\tau_i}(t-t_B)} \quad \left[\mathrm{V/s^2}\right] \tag{5.34}$$

$$c_i = \tau_i \ddot{v}_{1,comp,i} + \dot{v}_{1,comp,i} \quad [\mathrm{V/s}] \tag{5.35}$$

For each n sample it is assumed that the voltage is approximated to be a linear function, i.e. $v_{1,comp,i}[n] = v_{1,comp,i}(T_B)[n] + \dot{v}_{1,comp,i}\,(t - T_B)\,[n]$. The derivative of the voltage $v_{1,comp,i}$ is calculated for each sample n by using least squares in the interval $n - N_{ls,i}$ to $n + N_{ls,i}$, i.e.

$$\underbrace{\begin{bmatrix} v_{1,comp,i}[n - N_{ls,i}] \\ \vdots \\ v_{1,comp,i}[n + N_{ls,i}] \end{bmatrix}}_{\mathbf{Y}} = \underbrace{\begin{bmatrix} 1 & (t[n - N_{ls,i}] - T_B) \\ \vdots & \vdots \\ 1 & (t[n + N_{ls,i}] - T_B) \end{bmatrix}}_{\mathbf{A}} \underbrace{\begin{bmatrix} v_{1,comp,i}(T_B)[n] \\ \dot{v}_{1,comp,i}[n] \end{bmatrix}}_{\mathbf{X}}$$

$$\Updownarrow$$

$$\mathbf{X} = \left(\mathbf{A}^T\mathbf{A}\right)^{-1}\left(\mathbf{A}^T\mathbf{Y}\right) \tag{5.36}$$

$$\Updownarrow$$

$$\dot{v}_{1,comp,i}[n] = \mathbf{X}[2] \tag{5.37}$$

The double derivative is calculated in the same way, i.e.

$$\underbrace{\begin{bmatrix} \dot{v}_{1,comp,i}[n - N_{ls,i}] \\ \vdots \\ \dot{v}_{1,comp,i}[n + N_{ls,i}] \end{bmatrix}}_{\mathbf{Y}} = \underbrace{\begin{bmatrix} 1 & t[n - N_{ls,i}] - T_B \\ \vdots & \vdots \\ 1 & t[n + N_{ls,i}] - T_B \end{bmatrix}}_{\mathbf{A}} \underbrace{\begin{bmatrix} \dot{v}_{1,comp,i}(T_B)[n] \\ \ddot{v}_{1,comp,i}[n] \end{bmatrix}}_{\mathbf{X}}$$

$$\Updownarrow$$

$$\mathbf{X} = \left(\mathbf{A}^T\mathbf{A}\right)^{-1}\left(\mathbf{A}^T\mathbf{Y}\right) \tag{5.38}$$

$$\Updownarrow$$

$$\ddot{v}_{1,comp,i}[n] = \mathbf{X}[2] \tag{5.39}$$

The voltage is sampled with $f_s = 5\,\mathrm{Hz}$. The sampling frequency should be fast enough to capture the fast transients of the ultracapacitor module, but on the other hand it should not be too fast; otherwise the logged data files will be too big, if data is logged

for several hours. The selection of the interval $N_{ls,i}$ used for each R_iC_i-circuit is also a compromise. The interval should be big enough to suppress the influence of the previous $R_{i-1}C_{i-1}$-circuit. However, it should not suppress the response due to the actual R_iC_i-circuit. It has therefore been decided to let $N_{ls,i}$ have the length of two time constants of the previous $R_{i-1}C_{i-1}$-circuit, i.e.

$$N_{ls,i} = 2\tau_{i-1}f_s, \quad i = 2 \dots k \tag{5.40}$$

The derivative and double derivative of $v_{1,comp}$ are now calculated. The constants c_i and τ_i can now be estimated by using least squares method on Equation (5.35). However, the result depends of which part of the data set that is used. That part generated from smaller or higher time constants should therefore not be taken into account. Only data from time $t = T_{start}$ to $t = T_{stop}$ will be included. Therefore, in order to neglect the contribution of smaller time constants, data before two time constants of the previous time constant will not be included. The start time $T_{start,i}$ is therefore

$$T_{start,i} = T_B + 2\tau_{i-1} \qquad [\mathrm{s}] \tag{5.41}$$

The number of RC-circuits k is therefore given by that R_iC_i-circuit that makes $T_{start,i} = T_B + 2\tau_i \geq T_C$. In order to neglect the contribution from higher time constants the stop time T_{stop} is chosen to be the time when the derivative of the compensated voltage $\dot{v}_{comp,i}$ has dropped to $15\,\%$ of its initial value at time $t = T_B$, i.e.

$$0.15 \cdot \dot{v}_{1,comp,i}(T_B) = -\frac{1}{\tau_i} b_i e^{-\frac{1}{\tau_i}(T_{stop,i} - T_B)} + c_i \qquad [\mathrm{V/s}] \tag{5.42}$$

Therefore, from Equation (5.35):

$$\underbrace{\begin{bmatrix} \dot{v}_{1,comp,i}(T_{start,i}) \\ \vdots \\ \dot{v}_{1,comp,i}(T_{stop,i}) \end{bmatrix}}_{\mathbf{Y}} = \begin{cases} \underbrace{\begin{bmatrix} 1 & -\ddot{v}_{1,comp,i}(T_{start,i}) \\ \vdots & \vdots \\ 1 & -\ddot{v}_{1,comp,i}(T_{stop,i}) \end{bmatrix}}_{\mathbf{A}} \begin{bmatrix} c_i \\ \tau_i \end{bmatrix} & , \ i < k \\ \underbrace{\begin{bmatrix} -\ddot{v}_{1,comp,i}(T_{start,i}) \\ \vdots \\ -\ddot{v}_{1,comp,i}(T_{stop,i}) \end{bmatrix}}_{\mathbf{A}} \tau_i & , \ i = k \end{cases} \tag{5.43}$$

$$\Updownarrow$$

$$\begin{bmatrix} c_i \\ \tau_i \end{bmatrix} = \begin{cases} \left(\mathbf{A}^T\mathbf{A}\right)^{-1}\left(\mathbf{A}^T\mathbf{Y}\right) & , \ i < k \\ \begin{bmatrix} 0 \\ \left(\mathbf{A}^T\mathbf{A}\right)^{-1}\left(\mathbf{A}^T\mathbf{Y}\right) \end{bmatrix} & , \ i = k \end{cases} \tag{5.44}$$

For the last time constant τ_k no current source is contributing to the charge recovery. Therefore is the constant c_i equal to zero for $i = k$.

The constants a_i and b_i are also calculated by least squares. From Equation (5.32) one obtains:

$$\underbrace{\begin{bmatrix} \dot{v}_{1,comp,i}(T_{start,i}) - c_i \\ \vdots \\ \dot{v}_{1,comp,i}(T_{stop,i}) - c_i \end{bmatrix}}_{\mathbf{Y}} = \underbrace{\begin{bmatrix} 1 & -\frac{1}{\tau_i} e^{-\frac{1}{\tau_i}(T_{start,i}-T_B)} \\ \vdots & \vdots \\ 1 & -\frac{1}{\tau_i} e^{-\frac{1}{\tau_i}(T_{stop,i}-T_B)} \end{bmatrix}}_{\mathbf{A}} \begin{bmatrix} a_i \\ b_i \end{bmatrix} \tag{5.45}$$

$$\Updownarrow$$

$$\begin{bmatrix} a_i \\ b_i \end{bmatrix} = \left(\mathbf{A}^T\mathbf{A}\right)^{-1}\left(\mathbf{A}^T\mathbf{Y}\right) \tag{5.46}$$

In Figure 5.10 the double derivative, derivative, and the voltage can be seen. The vertical red lines indicates the interval used for the calculation of the parameters a_i, b_i, c_i, and τ_i. The interval used in Figure 5.10(b) is a little more narrow than in Figure 5.10(a). This is because for the $\dot{v}_{1,comp,i}[n]$ calculation samples from $n-N_{ls}$ to $n+N_{ls}$ is required. It is noticed that the estimation only fits the measurements in the specified interval, i.e. from $T_{start,i}$ to $T_{stop,i}$.

RC-Calculation

In the previous section it is shown how the time constants τ_2-τ_k can be calculated. What is left is now to determine the correct value of R_i and C_i that fulfill τ_i. For this purpose the equivalent circuit diagram in Figure 5.11 is made. The measured ultracapacitor current in Figure 5.1(b) is applied to the circuit and the measured voltage v_{UC} in Figure 5.1(a) is compared to the simulated voltage. This is done for each i^{th} RC-circuit. The capacitor C_i is determined by trial-and-error-method. For each C_i the resistance can be calculated from Equation (5.29), i.e.

$$R_i = \tau_i \frac{\sum_{l=1}^{l=i} C_l}{\sum_{l=1}^{l=i-1} C_l C_i} - R_{i-1,cha}, \qquad i \geq 2 \qquad [\Omega] \tag{5.47}$$

The current source I_{i+1} is calculated by using Equation (5.31), i.e.

$$I_{i+1} = -c_i \sum_{l=1}^{l=i} C_l, \qquad i \geq 2 \qquad [\mathrm{A}] \tag{5.48}$$

5.5 Results

The ultracapacitor is fully charged followed by a constant current step until a certain voltage is reached. This is done for three different values of the final voltage. For each laboratory experiment the parameters of the ultracapacitor module are calculated. In Table 5.2 the parameters of the module can be seen for different voltages of v_1. For $v_1 = 10.28\,\mathrm{V}$ the ultracapacitor can be modeled by six time constants, but for lower voltages it is necessary to have seven time constants. At the lowest voltage $v_1 = 3.32\,\mathrm{V}$ the capacitor C_7 is relative big, which means that a relative large amount of voltage is reconstructed at the ultracapacitor terminals, at a relative long time period. For $V_1 = 6.14\,\mathrm{V}$ the capacitor is smaller and less voltage is reconstructed.

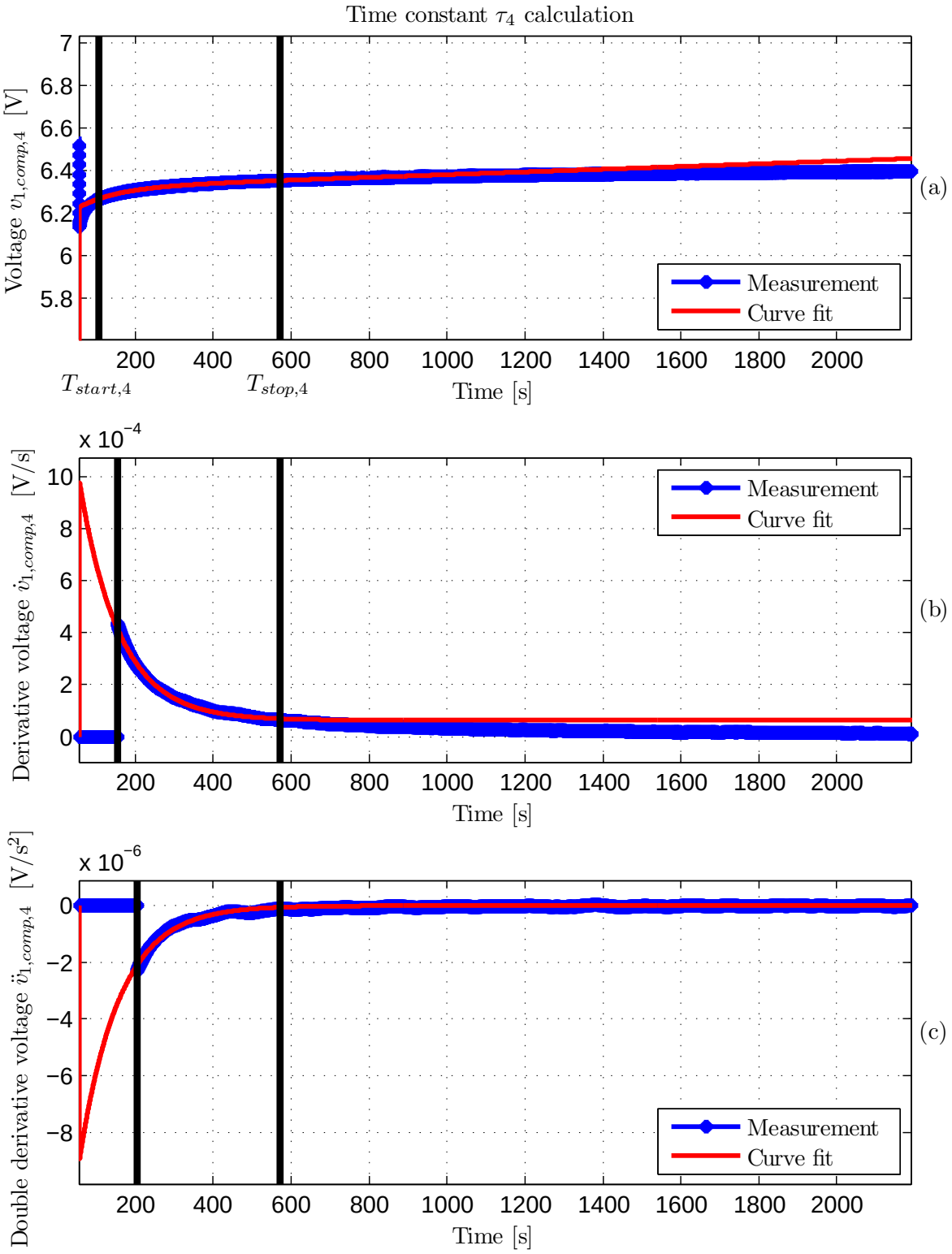

Figure 5.10: Calculation of time constant. (a) Voltage. (b) Derivative voltage. (c) Double derivative voltage.

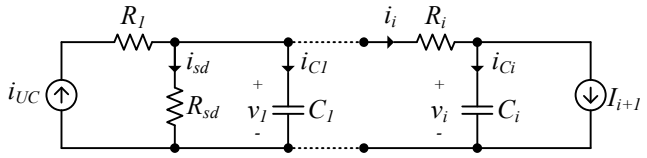

Figure 5.11: Equivalent circuit diagram used for simulation in order to determine the resistance R_i and capacitor C_i.

Parameter	$v_1 = 3.32\,\mathrm{V}$	$v_1 = 6.14\,\mathrm{V}$	$v_1 = 10.28$	Unit
$a_{C_{eq}}$	6.36	5.53	6.81	F / V
$b_{C_{eq}}$	397.9	412.0	394.3	F
C_1	394.4	419.1	454.1	F
R_1	0.002	0.0019	0.002	Ω
C_2	17.4	17.4	18.2	F
R_2	0.321	0.294	0.236	Ω
C_3	4.7	4.9	5.7	F
R_3	5.64	4.76	3.38	Ω
C_4	2.4	2.7	3.7	F
R_4	45.2	33.0	17.3	Ω
C_5	2.2	2.1	2.1	F
R_5	217.6	160.0	95.3	Ω
C_6	3.0	1.7	0.8	F
R_6	$1.02 \cdot 10^3$	818.7	592.6	Ω
C_7	8.5	1.7	-	F
R_7	$4.07 \cdot 10^3$	$5.47 \cdot 10^3$	-	Ω

Table 5.2: Parameters of ultracapacitor module.

In Table 5.2 it can be seen that few of the parameters remain constant with varying voltage. Therefore, in Figure 5.12(a) and (b) the capacitances and resistances are shown relative to the maximum of each parameter, i.e. for C_1 the values are relative to $454.1\,\mathrm{F}$ and for R_4 the values are relative to $45.2\,\Omega$. It can be seen that there is an almost linear relationship between the voltage v_1 and the parameters. This means that in the equivalent circuit model of the ultracapacitor the parameters depend on the actual voltage.

It is chosen to model the parameters by a second order polynomial of the voltage v_1, i.e. $y = av_1^2 + bv_1 + c$. The coefficients for each parameter can be seen in Table 5.3.

Self Discharge

In Figure 5.13 the ultracapacitor voltage response during the self discharge is shown. The measurements are compared to two models denoted advanced and simple, respectively. The advanced model is the model that utilizes the parameters in Table 5.3, and the simple model is the model shown in Figure 5.2(b), which consists of a series resistance R_1, and the voltage depending self discharge resistor R_{sd}, and equivalent capacitor C_{eq} that also depends on the voltage. The measured voltage is the same as shown in Figure 5.4(a). No significant differences between the measurement and the

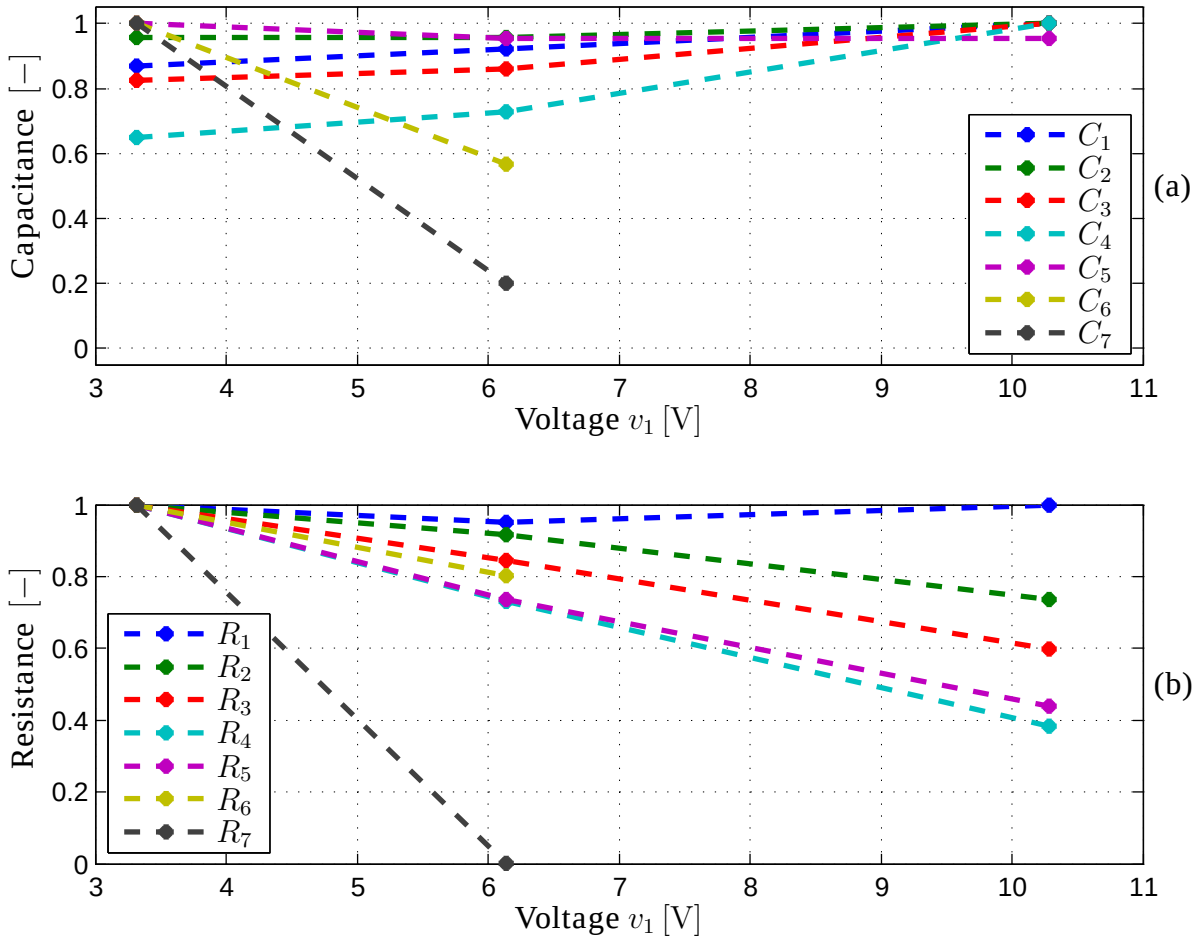

Figure 5.12: Per unit ultracapacitor parameters for different voltage levels. (a) Capacitances. (b) Resistances.

result of the two simulation models are seen.

Charge Recovery

The two models have been applied for three current steps with the same amplitude, but different time durations. After a certain voltage has been reached the current is disabled. The voltage during the constant current discharge can be seen in Figure 5.14(a-c). It is seen that there is coherence between the measurement and the two simulation models. However, as in Figure 5.1 on page 50 a constant voltage is present a few seconds after the current step even though the current is non-zero. This is again assumed to be because of a failure in the voltage measurement circuit. The voltage response during the charge recovery interval is shown in Figure 5.14(d-f). The advanced model is able to follow the voltage measurement in the shown interval. However, because the voltage of the measurement and simulation was not exactly the same, e.g. $\approx 100\,\mathrm{mV}$ in Figure 5.14(e), at the time where the constant current discharge was disabled, there is a voltage offset during the whole charge recovery period. In Figure 5.14(d) the voltage has a peak at approximately half an hour after the inverse current step at $v_{UC} = 10.28\,\mathrm{V}$. Thereafter it begins to drop because of the

Parameter	a	b	c	
C_{eq}	0	6.36	397.9	F
C_1	0	6.36	378.9	F
R_1	0	0	0.002	Ω
C_2	0.0278	-0.2626	17.9660	F
R_2	-0.0006	-0.0035	0.3398	Ω
C_3	0.0176	-0.0953	4.8228	F
R_3	-0.0031	-0.2831	6.6137	Ω
C_4	0.0194	-0.0773	2.4427	F
R_4	0.0767	-5.0520	61.1270	Ω
C_5	0.0051	-0.0837	2.4216	F
R_5	0.6893	-26.9463	299.4640	Ω
C_6	0.0350	-0.7921	5.2440	F
R_6	2.4094	-94.1759	1306.1	Ω
C_7	0.2875	-5.1307	22.3655	F
R_7	206.8965	-3398.6	13073	Ω

Table 5.3: Parameters of ultracapacitor module of the form $y = av_1^2 + bv_1 + c$

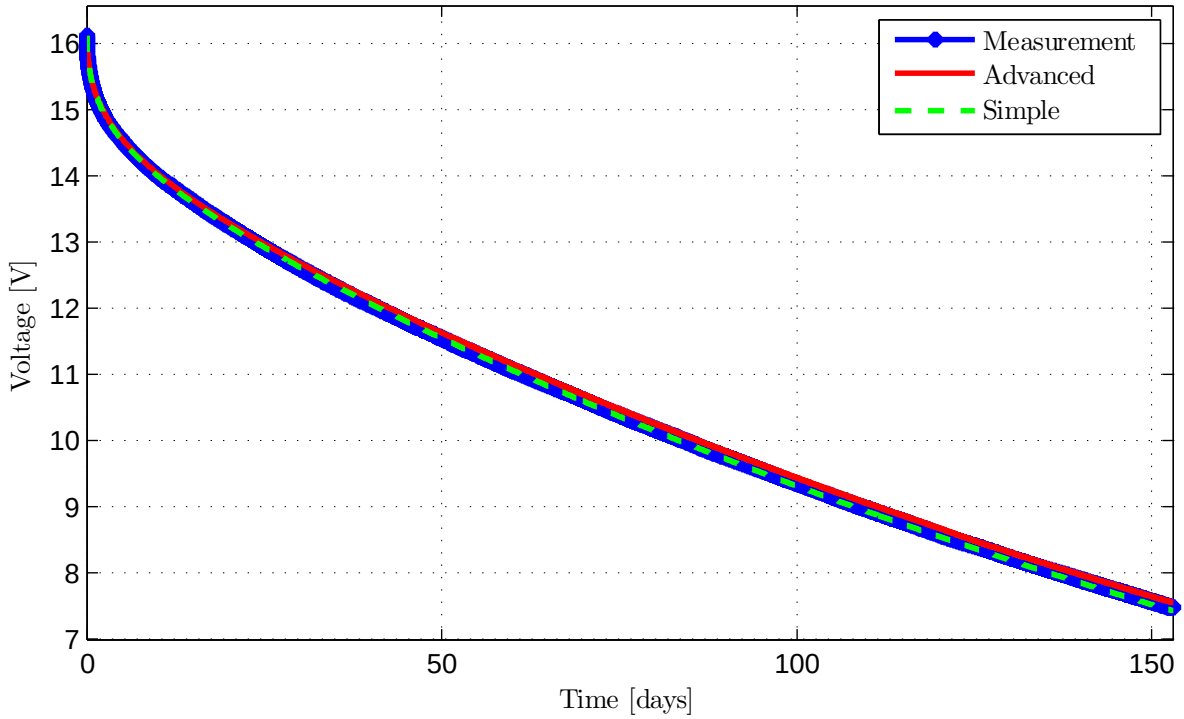

Figure 5.13: Measurement and simulation of ultracapacitor voltage response during self discharge.

self discharge. The voltage measurement drops actually a little faster than the advanced simulation model. This indicates that the rate of self discharge is higher than the experiment in Figure 5.4(a) shows. The difference in self discharge could be due to temperature variations. In Figure 5.14(f) the voltage is still rising after $22\,\text{hours}$. Seven RC-circuits might therefore not be enough to describe the voltage response at such low voltages, i.e. at $3.32\,\text{V}$. However, another experiment has to investigate this. During the constant current discharge the simple model is sufficient, but during the charge recovery period it of course cannot model the rise in voltage as it has no charge recovery circuits implemented. It is only able to model the increase in voltage due the voltage drop across the inner resistance. In Figure 5.14(f) the voltage is measured to be $v_{UC} = 3.92\,\text{V}$ after $22.7\,\text{hours}$. The error between this voltage and the result of the simulations of the advanced and simple models are $1.95\,\%$ and $15.5\,\%$, respectively.

Model Accuracy

In order to assess the accuracy of the advanced and simple model Table 5.4 has been created. Both models are able to model the self discharge with low errors. The result of Ricketts method shown in Figure 5.4(a) provides an error of $4.59\,\%$ after 153 days of self discharge, which however, also is low.

Both the advanced and simple model provide also low errors during the constant current discharge at time $t = T_B$ for all the three constant current discharge tests. The advanced model also gives low error when modeling charge recovery. The simple model has no charge recovery circuit. As the voltage increase caused by the charge recovery becomes higher at low voltages, the relative error also becomes higher at low voltages. This means that the simple model is quite inaccurate for very low voltages.

	Error of advanced model [%]	Error of simple model [%]
After 153 days of self discharge	1.04	0.58
T_B of inverse step at $v_{UC} = 10.28\,\text{V}$	0.18	0.093
T_C of inverse step at $v_{UC} = 10.28\,\text{V}$	0.21	1.42
T_B of inverse step at $v_{UC} = 6.14\,\text{V}$	1.78	1.84
T_C of inverse step at $v_{UC} = 6.14\,\text{V}$	2.26	6.65
T_B of inverse step at $v_{UC} = 3.32\,\text{V}$	0.76	0.53
T_C of inverse step at $v_{UC} = 3.32\,\text{V}$	1.95	15.5

Table 5.4: Voltage error of the advanced and simple models tested during self discharge, constant current discharge, and charge recovery period.

5.6 CONCLUSION

In this chapter a circuit model of an ultracapacitor module has been proposed. The model consists of seven RC-circuits, and a resistor used for modeling the self discharge. Most of the energy of the ultracapacitor is supplied from one capacitor. The six other capacitors model the charge recovery of the ultracapacitor. The voltage due to the charge recovery rises with 6 different time constants, and the energy feed from the charge recovery circuits depend on the actual voltage level. The lower the voltage

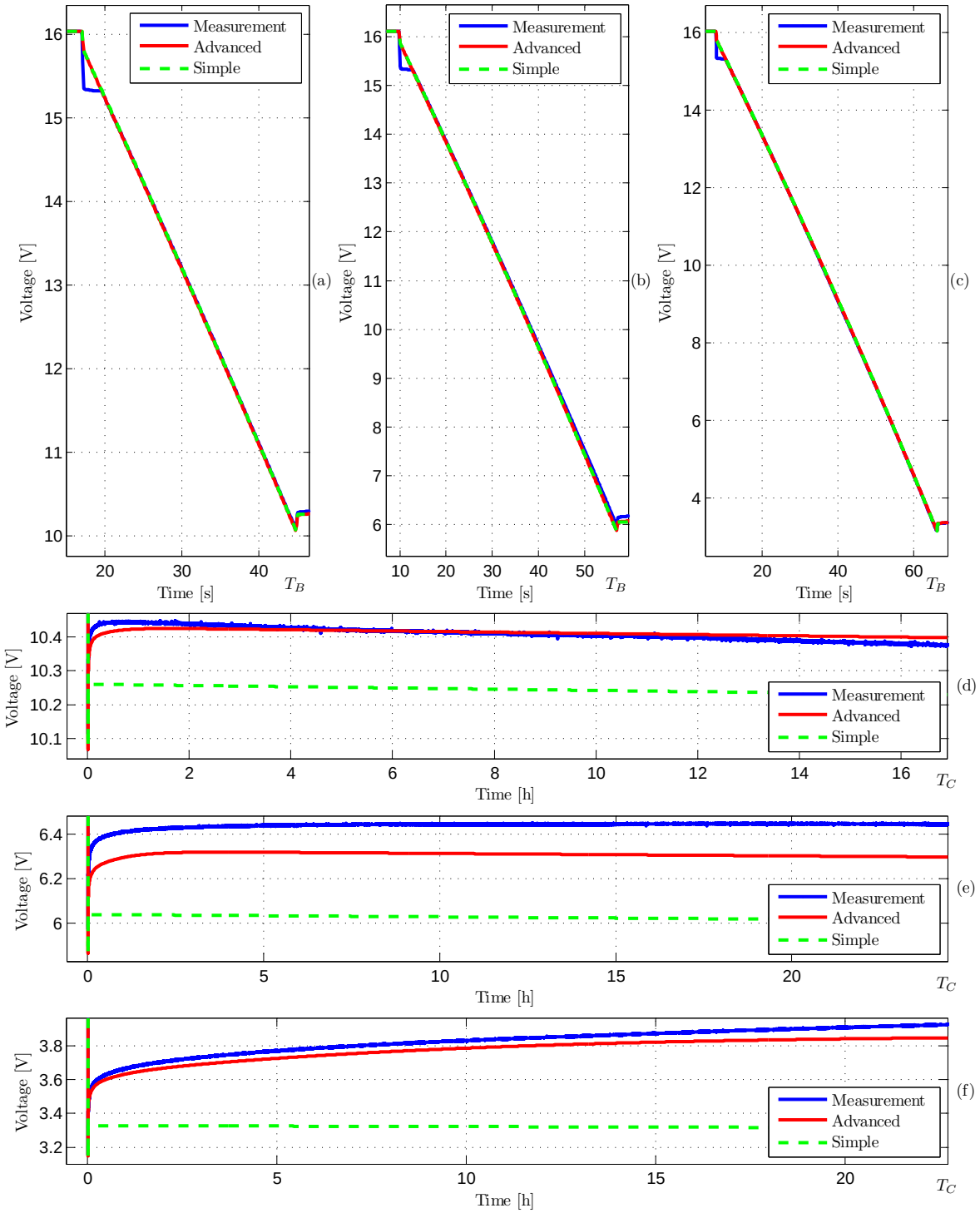

Figure 5.14: Measurement and simulation of ultracapacitor voltage response during constant current discharge and charge recovery period. (a) and (d) Constant current discharge stops at $v_{UC} = 10.28\,\mathrm{V}$. (b) and (e) Constant current discharge stops at $v_{UC} = 6.14\,\mathrm{V}$. (c) and (f) Constant current discharge stops at $v_{UC} = 3.32\,\mathrm{V}$. Subfigures (a,d), (b,e), and (c,f) are from the same experiment / simulation, but shown at different time intervals.

the more energy is supplied from the charge recovery circuits. The self discharge also depends on the actual voltage level. The higher the level the faster the voltage drops due to self discharge. When fully discharged the ultracapacitor losses $10\,\%$ of its energy at approximately 18 hours. The equivalent capacitance of the ultracapacitor also depends on the voltage level, i.e. the lower voltage the lower equivalent capacitance. The self discharge is modeled by a parallel variable leakage resistance. It is shown that the time constant of the self discharge circuit can be approximated successfully by a modified Weibull function of the ultracapacitor voltage. The parameter values of the model are calculated from two different experiments. The first experiment is a long term test where the ultracapacitor is left in open circuit conditions for more than 5 months. This test is used for characterization of the self discharge resistance. The other experiment is a constant current discharge followed by an inverse step, i.e. zero current. The constant current discharge is used to calculate the equivalent capacitance and the inverse current step is used to calculate the RC-circuits of the charge recovery phenomenon. A method to calculate the time constants of the charge recovery circuits has been proposed. The proposed circuit model is able to model both the transient behavior and the slow behavior due to self discharge and charge recovery when the ultracapacitor is discharged. However, in order to complete the model the ultracapacitor should also be investigated in charging mode. This is left for future work. During the measurements the temperature was not controlled. It is therefore also left for future work to investigate how the circuit parameters depend on the temperature.

6 Fuel Cell Converter

The fuel cell voltage and efficiency depend on the power drawn from the fuel cell. The converter interfacing the fuel cell to the bus voltage should therefore be able to handle a wide range of input voltage and provide a high efficiency in the whole power area. In this chapter a fuel cell converter will therefore be presented. The modes of operation are described and analytical expression of the efficiency are derived and verified experimentally. In Appendix C steady-state equations and transfer functions are derived and current controllers are designed and verified.

6.1 TOPOLOGY

Many converters suitable for fuel cells have been presented in literature [39, 44, 47, 50, 56, 57, 64, 80, 83, 84, 95]. If the bus voltage is between the upper and lower boundaries of the fuel cell, the fuel cell converter should be able to both buck and boost the voltage. A non-inverting buck-boost converter has been chosen due to its combination of the well known buck and boost converters [30, 64, 67, 74, 86].

The equivalent circuit diagram of the non-inverting buck-boost converter can be seen in Figure 6.1. The non-inverting buck-boost converter consists of the inductor L, output filter capacitor C_o, the active switches Q_3 and Q_4, and the freewheeling diodes D_1 and D_2. In order to increase the efficiency the converter has been implemented with synchronous rectifiers (switch Q_1 and Q_2, respectively) which bypass the current through the freewheeling diodes D_1 and D_2.

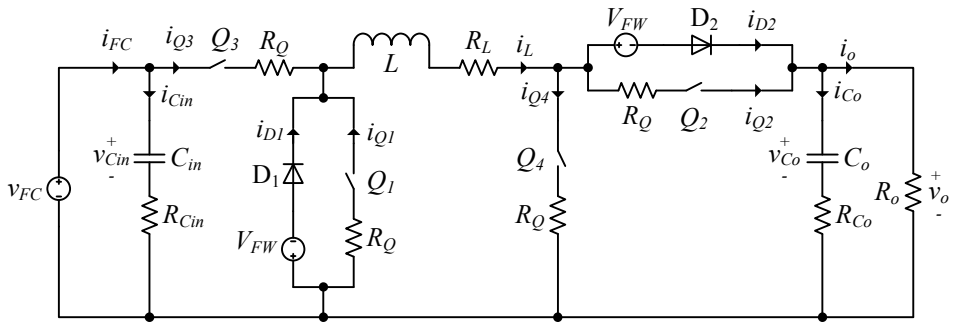

Figure 6.1: Equivalent circuit diagram of the non-inverting buck-boost converter.

In the equivalent circuit model in Figure 6.1 the non-ideal model of each component is included. It is seen that the inductor is modeled as an ideal inductor L with a series resistance R_L. The capacitors C_{in} and C_o are modeled as ideal capacitors with equivalent series resistances $R_{C_{in}}$ and R_{C_o} respectively. The switches Q_1 Q_2, Q_3, and

Q_4 are modeled as ideal switches with a series resistance R_Q. The diodes D_1 and D_2 are modeled as ideal diodes in series with a constant forward voltage source V_{FW}.

The fuel cell is very sensitive to ripple current and voltage as this will reduce the lifetime [15, 32, 46, 90]. The converter is therefore implemented with an input filter capacitor C_{in} in order to reduce the current discontinuity caused by switch Q_3 when this is switching.

Modes of Operation

Basically the converter can be operated in three modes, i.e. buck-mode, boost-mode, and buck-boost-mode. Each mode is divided into two sub modes. In the switch modes with an odd index number the switch Q_2 is not utilized in order to protect for negative inductor currents. See Section 9.2 on page 128 for further details. This gives six different modes which are given by:

Buck-mode This mode can be used when the input voltage is higher than the output voltage.

- **Switch-mode 1** Q_2 and Q_4 are constantly turned off. The output voltage or current of the converter are controlled by switching Q_1 and Q_3 on and off opposite of each other.
- **Switch-mode 2** The difference between this mode and switch-mode 1 is that Q_2 is constantly turned on instead of off.

Boost-mode This mode can be used when the input voltage is lower than the output voltage.

- **Switch-mode 3** Q_3 is constantly turned on and Q_1 and Q_2 are constantly turned off. The output voltage or current of the converter are controlled by switching Q_4.
- **Switch-mode 4** The difference between this mode and switch-mode 3 is that switch Q_2 is turned on and off opposite of switch Q_4 instead of being constantly turned off.

Buck-boost-mode This mode can be used when the input voltage is either higher or lower than the input voltage, i.e. the buck-boost-mode can be utilized in the whole power and voltage spectrum of the fuel cell.

- **Switch-mode 5** In this mode Q_2 is constantly turned off, and Q_1 is operated opposite of the pair (Q_3, Q_4), i.e. when Q_1 conducts Q_3 and Q_4 are non-conducting, and vice versa. By controlling how long time Q_3 and Q_4 should conduct in one switch period, i.e. controlling the duty cycle, the converter can either buck or boost the voltage.
- **Switch-mode 6** The difference between this mode and switch-mode 5 is that instead of being constantly turned off switch Q_2 is conducting when Q_1 is conducting.

The disadvantage of the buck-boost-mode is that the inductor current is higher in this mode than if the converter was operated in buck or boost-mode. The switching losses are also higher in this mode because all four switches must be turned on and off in every switching period [43].

In Figure 6.2 the inductor currents and gate-signals are seen in the six switch modes. In one switching period of interval T_s two dead time intervals each of time T_{DT} are applied. In the interval DT_s the inductor current is rising and in the interval $(1-D)\,T_s$ the inductor current is falling.

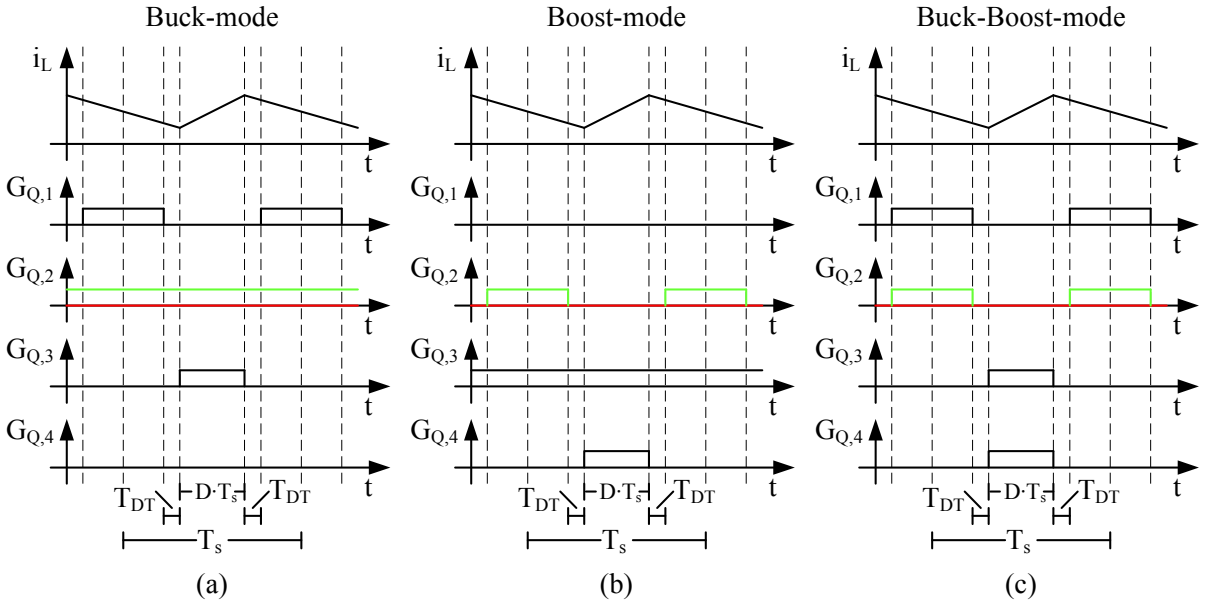

Figure 6.2: Inductor current and gate signals due to the operation modes of the non-inverting buck-boost converter. (a) Buck-mode. Red line of G_{Q_2}: Switch-mode 1. Green line of G_{Q_2}: Switch-mode 2. (b) Boost-mode. Red line of G_{Q_2}: Switch-mode 3. Green line of G_{Q_2}: Switch-mode 4. (c) Buck-Boost-mode. Red line of G_{Q_2}: Switch-mode 5. Green line of G_{Q_2}: Switch-mode 6.

6.2 Efficiency

Often the power electronics of a hybrid system are assumed to have a constant efficiency, independent of the actual current and voltage levels. This is an assumption that might lead to wrong conclusions as the efficiency depends on the states or conditions of the power electronics [7], e.g. if the efficiency of a DC/DC converter is in the range from $80\,\%$ at full load to $99\,\%$ at partial load, the total loss highly depends on whether the converter is operated most of the time at high or low power levels. Of course, if the efficiency is very high in the whole area of operating, the deviations will be smaller.

In order to investigate how the converter affects the efficiency of the whole system it is necessary to be able to calculate the efficiency of the converter due to different voltage and current levels. The efficiency will only be investigated in buck-mode and boost-mode as it is not desirable to operate the converter in buck-boost-mode.

RMS-Currents

The peak-peak inductor current ripple is given by

$$\Delta I_{L,pp} = \begin{cases} \frac{(V_{FC}-V_o-V_{FW}-R_L I_L)}{L f_s} D & \text{Switch-mode 1} \\ \frac{(V_{FC}-V_o-2R_L I_L)}{L f_s} D & \text{Switch-mode 2} \\ \frac{(V_{FC}-V_o-V_{FW}-R_L I_L)}{L f_s} (1-D) & \text{Switch-mode 3} \\ \frac{(V_{FC}-V_o-2R_L I_L)}{L f_s} (1-D) & \text{Switch-mode 4} \end{cases} \quad [\mathrm{A}] \qquad (6.1)$$

The RMS-currents of the components inside the converter are derived from the waveforms of the converter in buck-mode and boost-mode, which are shown in Figure 6.3 and Figure 6.4, respectively.

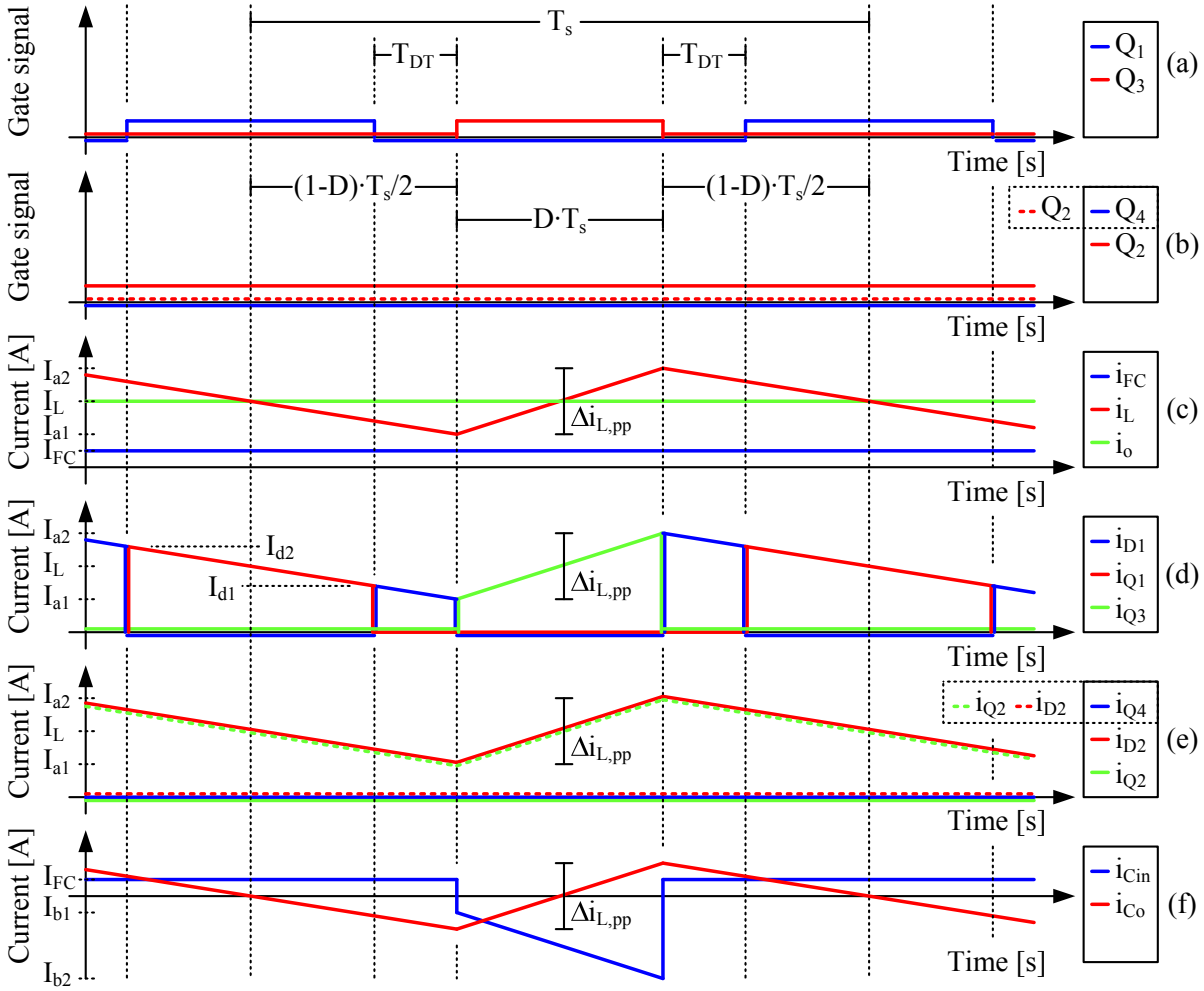

Figure 6.3: Steady-state curves of the non-inverting buck-boost converter in buck-mode, switch-mode 1 and switch-mode 2 (dashed lines). (a) Gate signals of switch Q_1 and Q_3. (b) Gate signals of switch Q_2 and Q_4. (c) Current of the fuel cell i_{FC}, inductor i_L, and output i_o. (d) Current of diode D_1 i_{D_1}, switch Q_1 i_{Q_1}, and switch i_{Q_3}. (e) Current of diode D_2 i_{D_2}, switch Q_2 i_{Q_2}, and switch Q_4 i_{Q_4}.

In order to simplify the calculation of the RMS-current the following variables are introduced:

$$\begin{aligned} I_{a_1} &= I_L - \tfrac{\Delta I_{L,pp}}{2} \quad , \quad I_{a_2} = I_L + \tfrac{\Delta I_{L,pp}}{2} \\ I_{b_1} &= I_{FC} - I_{a_1} \quad , \quad I_{b_2} = I_{FC} - I_{a_2} \\ I_{c_1} &= I_{a_1} - I_o \quad , \quad I_{c_2} = I_{a_2} - I_o \\ I_{d_1} &= I_{a_1} + \tfrac{\Delta I_{L,pp} D_{DT}}{1-D} \quad , \quad I_{d_2} = I_{a_2} - \tfrac{\Delta I_{L,pp} D_{DT}}{1-D} \end{aligned} \tag{6.2}$$

The variables are valid in both buck-mode and boost-mode and are also shown graphically in Figure 6.3 and Figure 6.4.

From Figure 6.3 and 6.4 the RMS-currents of the converter in buck-mode and boost-mode can be seen in Table 6.1 [23]:

$$
\begin{array}{lcll}
I_{C_{in},rms} & = & \begin{cases} \sqrt{\frac{1}{3}\left(I_{b_1}^2 + I_{b_1}I_{b_2} + I_{b_2}^2\right)D + I_{FC}^2\left(1-D\right)} & \text{Buck-mode} \\ \frac{\Delta I_{L,pp}}{2\sqrt{3}} & \text{Boost-mode} \end{cases} \\
I_{C_o,rms} & = & \begin{cases} \frac{\Delta I_{L,pp}}{2\sqrt{3}} & \text{Buck-mode} \\ \sqrt{\frac{1}{3}\left(I_{b_1}^2 + I_{b_1}I_{b_2} + I_{b_2}^2\right)D + I_{FC}^2\left(1-D\right)} & \text{Boost-mode} \end{cases} \\
I_{Q_1,rms} & = & \begin{cases} \sqrt{\frac{1}{3}\left(I_{d_1}^2 + I_{d_1}I_{d_2} + I_{d_2}^2\right)\left(1-D-2D_{DT}\right)} & \text{Buck-mode} \\ 0 & \text{Boost-mode} \end{cases} \\
I_{Q_2,rms} & = & \begin{cases} 0 & \text{Switch-mode 1} \\ \sqrt{\frac{1}{3}\left(I_{a_1}^2 + I_{a_1}I_{a_2} + I_{a_2}^2\right)} & \text{Switch-mode 2} \\ 0 & \text{Switch-mode 3} \\ \sqrt{\frac{1}{3}\left(I_{d_1}^2 + I_{d_1}I_{d_2} + I_{d_2}^2\right)\left(1-D-2D_{DT}\right)} & \text{Switch-mode 4} \end{cases} \\
I_{Q_3,rms} & = & \begin{cases} \sqrt{\frac{1}{3}\left(I_{a_1}^2 + I_{a_1}I_{a_2} + I_{a_2}^2\right)D} & \text{Buck-mode} \\ \sqrt{\frac{1}{3}\left(I_{a_1}^2 + I_{a_1}I_{a_2} + I_{a_2}^2\right)} & \text{Boost-mode} \end{cases} \\
I_{Q_4,rms} & = & \begin{cases} 0 & \text{Buck-mode} \\ \sqrt{\frac{1}{3}\left(I_{a_1}^2 + I_{a_1}I_{a_2} + I_{a_2}^2\right)D} & \text{Boost-mode} \end{cases} \\
I_{D_1,rms} & = & \begin{cases} \sqrt{\frac{1}{3}\left(I_{a_1}^2 + I_{a_1}I_{d_1} + I_{d_1}^2 \ldots \right. \\ \left. +I_{a_2}^2 + I_{a_2}I_{d_2} + I_{d_2}^2\right)D_{DT}} & \text{Buck-mode} \\ 0 & \text{Boost-mode} \end{cases} \\
I_{D_2,rms} & = & \begin{cases} \sqrt{\frac{1}{3}\left(I_{a_1}^2 + I_{a_1}I_{a_2} + I_{a_2}^2\right)} & \text{Switch-mode 1} \\ 0 & \text{Switch-mode 2} \\ \sqrt{\frac{1}{3}\left(I_{a_1}^2 + I_{a_1}I_{a_2} + I_{a_2}^2\right)\left(1-D\right)} & \text{Switch-mode 3} \\ \sqrt{\frac{1}{3}\left(I_{a_1}^2 + I_{a_1}I_{d_1} + I_{d_1}^2 \ldots \right. \\ \left. +I_{a_2}^2 + I_{a_2}I_{d_2} + I_{d_2}^2\right)D_{DT}} & \text{Switch-mode 4} \end{cases} \\
I_{L,rms} & = & \sqrt{\frac{1}{3}\left(I_{a_1}^2 + I_{a_1}I_{a_2} + I_{a_2}^2\right)} &
\end{array}
$$

Table 6.1: Calculation of RMS-currents in buck-mode in Figure 6.3 and boost-mode in Figure 6.4 [23].

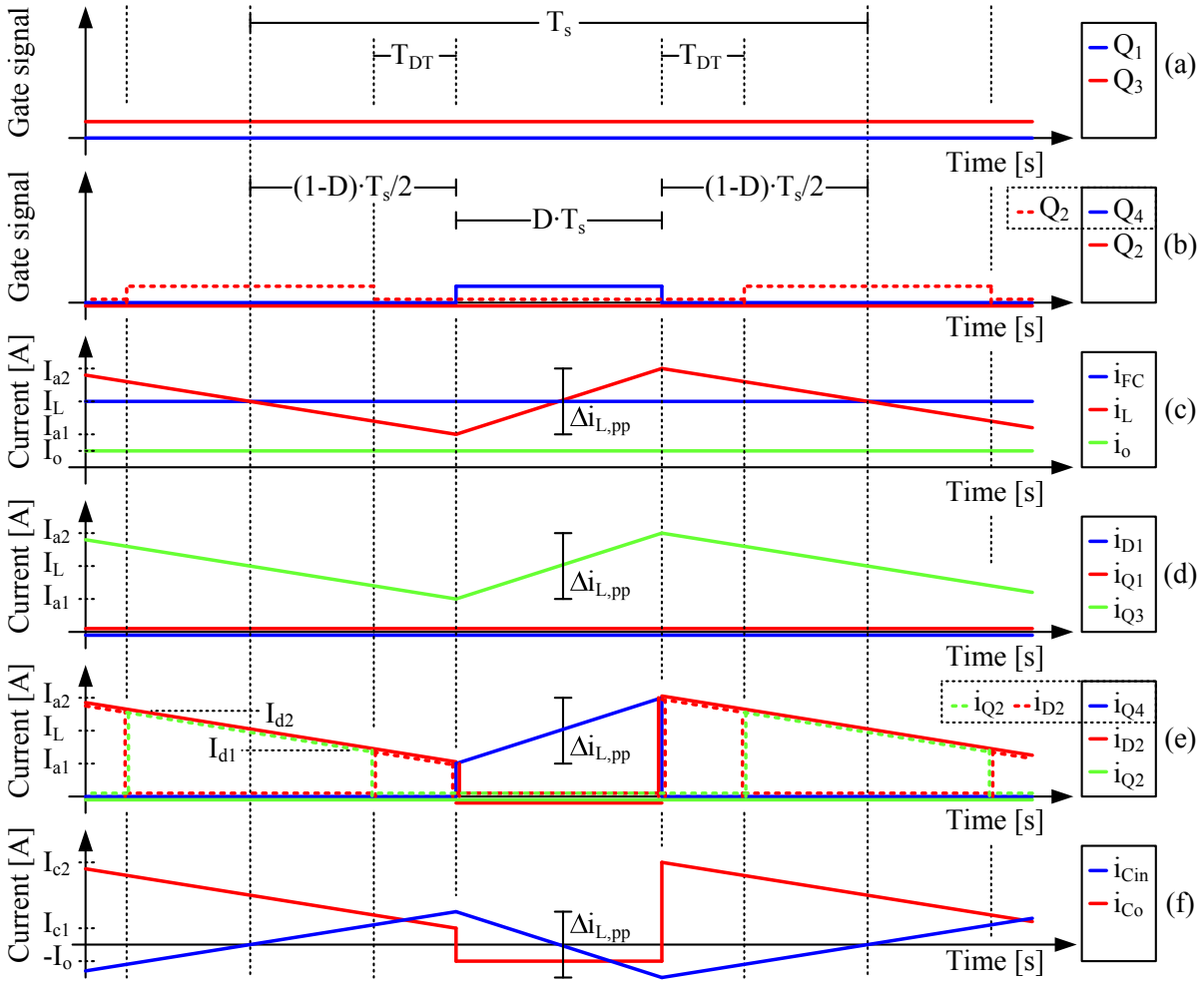

Figure 6.4: Steady-state curves of the non-inverting buck-boost converter in boost-mode, switch-mode 3 and switch-mode 4 (dashed lines). (a) Gate signals of switch Q_1 and Q_3. (b) Gate signals of switch Q_2 and Q_4. (c) Current of the fuel cell i_{FC}, inductor i_L, and output i_o. (d) Current of diode D_1 i_{D_1}, switch Q_1 i_{Q_1}, and switch i_{Q_3}. (e) Current of diode D_2 i_{D_2}, switch Q_2 i_{Q_2}, and switch Q_4 i_{Q_4}.

Power Consumption

The power losses in each component of the equivalent circuit diagram in Figure 6.1 are calculated by using the RMS-current in Table 6.1. The power loss calculations can be seen in Table 6.2. It is seen that for the switches the turn-on and turn-off losses have also been included in the power loss calculation. In order to simplify the core loss of the inductor has not been included.

The output power is given by the summation of the individual losses calculated in Table 6.2 subtracted from the input power, i.e.

$$P_o = P_{FC} - P_{C_{in}} - P_{C_o} - P_{D_1} - P_{D_2} - P_L - P_{Q_1} - P_{Q_2} - P_{Q_3} - P_{Q_4} \quad [\mathrm{W}] \quad (6.3)$$

The converter efficiency is therefore given by

$$\eta_{Con,FC} = \frac{P_o}{P_{FC}} \quad [-] \quad (6.4)$$

$$
\begin{aligned}
P_{C_{in}} &= R_{C_{in}} I_{C_{in}}^2 \\
P_{C_o} &= R_{C_o} I_{C_o}^2 \\
P_{Q_1} &= \begin{cases} R_Q I_{Q_1,rms}^2 + \frac{1}{2} f_s V_{FC} \left(T_{rise} I_{d_2} + T_{fall} I_{d_1} \right) & \text{Buck-mode} \\ R_Q I_{Q_1,rms}^2 & \text{Boost-mode} \end{cases} \\
P_{Q_2} &= \begin{cases} R_Q I_{Q_2,rms}^2 & \text{Buck-mode} \\ R_Q I_{Q_2,rms}^2 & \text{Switch-mode 3} \\ R_Q I_{Q_2,rms}^2 + \frac{1}{2} f_s V_{FC} \left(T_{rise} I_{d_2} + T_{fall} I_{d_1} \right) & \text{Switch-mode 4} \end{cases} \\
P_{Q_3} &= \begin{cases} R_Q I_{Q_3,rms}^2 + \frac{1}{2} f_s V_{FC} \left(T_{rise} I_{a_1} + T_{fall} I_{a_2} \right) & \text{Buck-mode} \\ R_Q I_{Q_3,rms}^2 & \text{Boost-mode} \end{cases} \\
P_{Q_4} &= \begin{cases} R_Q I_{Q_4,rms}^2 & \text{Buck-mode} \\ R_Q I_{Q_4,rms}^2 + \frac{1}{2} f_s V_{FC} \left(T_{rise} I_{a_1} + T_{fall} I_{a_2} \right) & \text{Boost-mode} \end{cases} \\
P_{D_1} &= V_{FW} I_{D_1,rms} \\
P_{D_2} &= V_{FW} I_{D_2,rms} \\
P_L &= R_L I_{L,rms}^2
\end{aligned}
$$

Table 6.2: Power losses calculation of the components inside the converter.

In the efficiency calculation the losses due to drivers, measurements, computation, etc., are not included, as it is assumed that these are negligible.

Power Loss Analysis

The power consumption of the converter is analyzed for two cases of the output voltage when the fuel cell is applied to the converter. The parameters of the converter can be seen in Table 6.3.

The power consumption inside the converter can be seen in Figure 6.5. An electronic load is connected to the load side of the converter and a power supply is connected to the input side. The input voltage follows the polarization curve of the fuel cell shown in Figure 3.2 on page 31 when 65 cells are assumed to be series connected. The output voltage is controlled to $V_o = 30\,\mathrm{V}$ in Figure 6.5(a) and $V_o = 48\,\mathrm{V}$ in Figure 6.5(b). As the input voltage decreases when the input power increases is Figure 6.5(a) in buck-mode and Figure 6.5(b) is in boost-mode. Generally it can be seen that the highest output voltage provides the highest efficiency. This is because the resistive losses are lower for higher voltages due to the lower RMS-currents of the converter. It is also seen that at the lowest power level, i.e. $P_{FC} = 100\,\mathrm{W}$ the efficiency is lowest. This is because the synchronous rectifier Q_2 is disabled in this situation because the current level is below the threshold level of the protection circuit.

Description	Symbol	Value
Max. input voltage	$V_{FC_{max}}$	65 V
Min. input voltage	$V_{FC_{min}}$	35 V
Rated input power	$P_{FC_{rat}}$	1000 W
Max. output voltage	$V_{o_{max}}$	48 V
Min. output voltage	$V_{o_{min}}$	30 V
Switching frequency	f_s	25 kHz
Dead time	T_{DT}	800 ns
Inductance	L	200 μH
Inductor resistance	R_L	8 mΩ
Input capacitor	C_{in}	2.35 mF
ESR of C_{in}	$R_{C_{in}}$	9.35 mΩ
Output capacitor	C_o	4.7 mF
ESR of C_o	R_{C_o}	4.66 mΩ
Diode forward voltage drop	V_{FW}	0.6 V
On-resistance of switches	R_Q	2.05 mΩ
Rise time of switches	T_{rise}	36 ns
Fall time of switches	T_{fall}	10 ns

Table 6.3: Fuel cell converter specifications and parameters.

Therefore the diode D_2 carries all the current. The protection circuit is explained in Section 9.2 on page 128. Even though the synchronous rectifiers of switch Q_1 and Q_2 are utilized a relative large amount of the power is lost in the diodes D_1 in buck-mode (Figure 6.5 (a)) and D_2 in boost-mode (Figure 6.5 (b)). This power consumption can be reduced by lowering the dead-time of the pairs (Q_1,Q_3) and (Q_2,Q_4). At higher power levels the main contributor of the power consumption is the inductor due to higher current levels.

The converter efficiency has been measured for different input powers and output voltages. The input voltage of the converter is the voltage characteristic of the fuel cell, i.e. the higher power the lower input voltage. The converter input power is varied between 100 W to 1000 W for an output voltage of 30 V, 36 V, 42 V, 48 V, and 54 V. The converter will therefore operate both in buck and boost mode. The results can be seen in Figure 6.6. The measurements in Figure 6.6(b) coincide well with the theoretic efficiency calculation in Figure 6.6(a).

6.3 CONCLUSION

A non-inverting buck-boost converter has been presented. Operation modes have been explained and analytical expressions of the RMS-currents and efficiency have been derived. Steady-state equations and transfer functions are derived in Appendix C. The converter has an efficiency at full load of approximately 98%, in both buck-mode and boost-mode. At low loads the efficiency is low, as one of the synchronous rectifiers then cannot be utilized, due to reverse current protection.

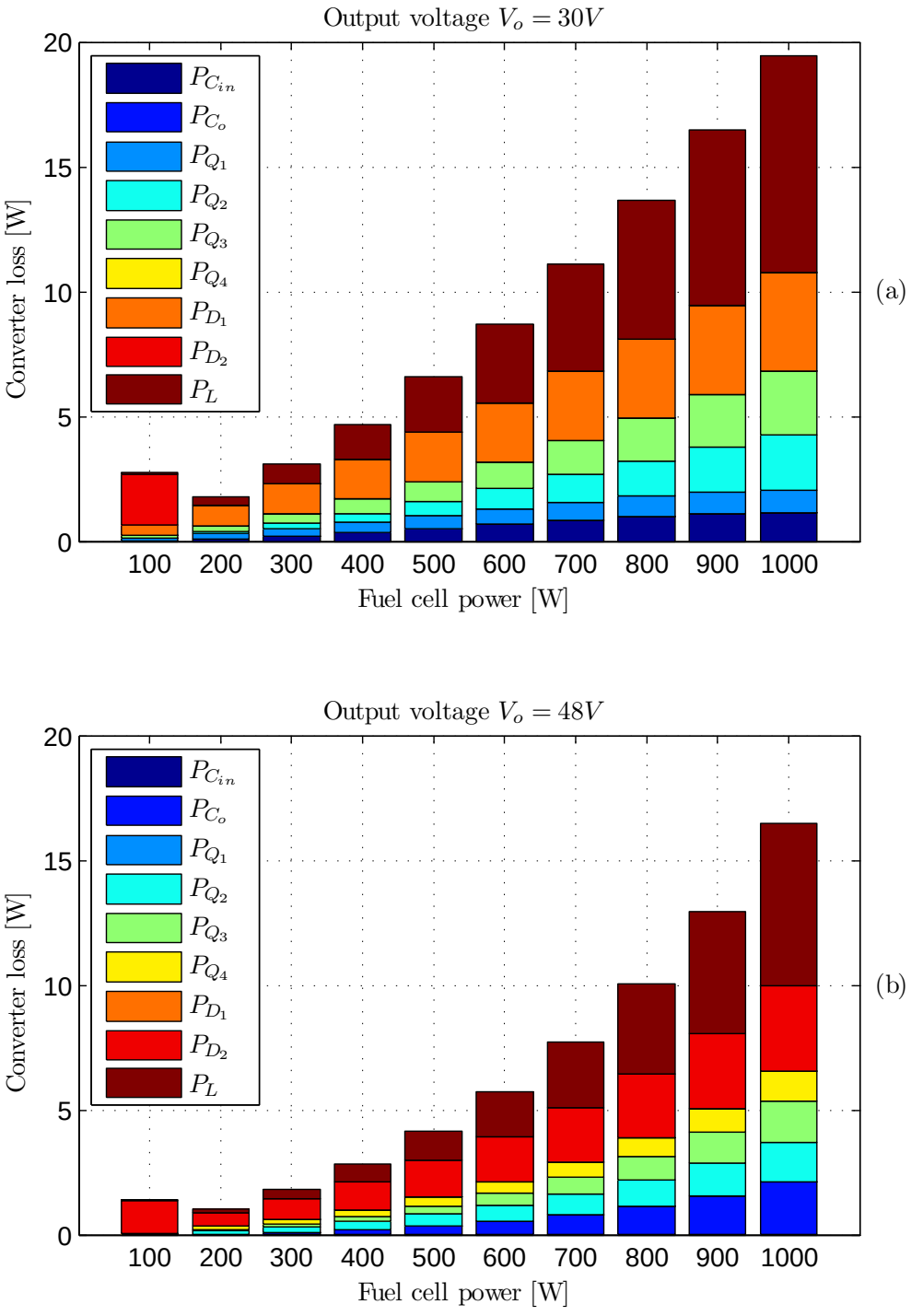

Figure 6.5: Loss inside the converter. (a) Output voltage $V_o = 30\,\mathrm{V}$. (b) Output voltage $V_o = 48\,\mathrm{V}$.

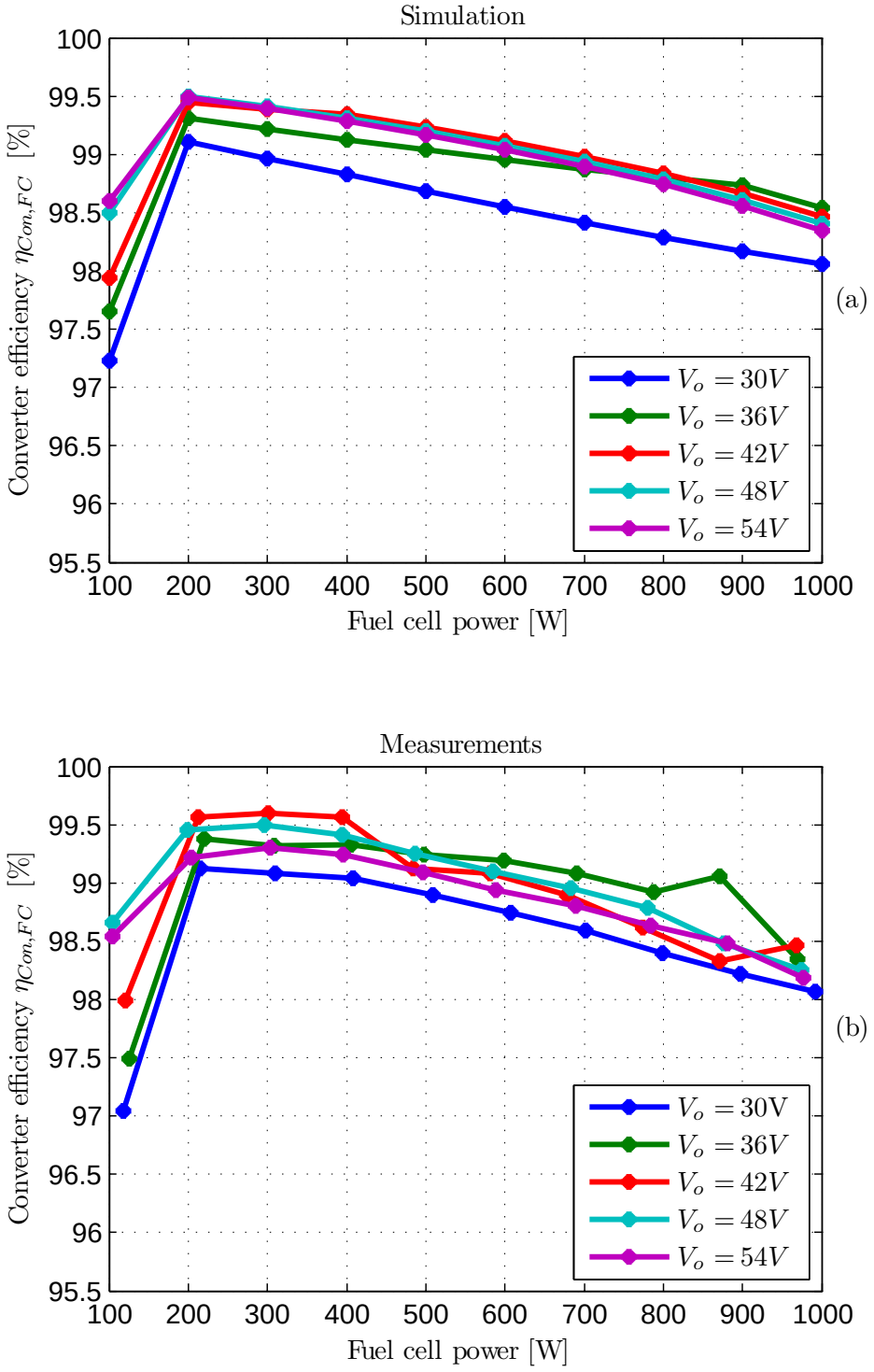

Figure 6.6: Efficiency of the converter for different input powers and output voltages. (a) Simulation results. (b) Experimental results.

7 Drive System

In this chapter the drive system is modeled. The drive system is here defined as the electric machines, which are used for propulsion, and the inverters which supply the machines. The models are used for calculating the power transferred through the electric machines and inverters.

7.1 Electric Machine

As for the case of the fuel cell and battery, many types of electric machines exist. The most suitable machine for the propulsion of a vehicle is a trade of among several parameters, but the machine should perform well in all or most of the following items [11, 93, 96]:

- High torque and power density
- High torque at low speed for acceleration and climbing
- High intermittent torque for short durations
- A wide speed range with sufficient torque capability
- A high efficiency in the whole area of the torque-speed-curve, in both motor and generator mode
- High reliability and robustness
- Low cost

Due to the requirement of high efficiency and reliability, usually only AC-motors are considered as DC-motors suffer from these issues. Three types of AC-machines are here considered for the propulsion. The small review is based on [11, 85, 88, 93, 96].

Induction Machine - IM This machine is a well known and proven technology, which is widely available. It has a high reliability, can operate in a hostile environment, requires low maintenance, and has low cost. The drawback of this machine is a low efficiency and low power factor.

Permanent Magnet Synchronous Machine - PMSM This machine is also a proven technology. The PMSM has a high torque / power density, a high efficiency, and easily removal of heat due to the lack of rotor currents. Due to the magnets inside the rotor this machine is more expensive to manufacture than the IM, the magnets can be destroyed due to over currents or too high temperature, and an uncontrolled rectification can take place if the speed becomes too high. Because of the magnets this machine also has a short constant power region, which means that it might be necessary to use field weakening in order to obtain a high speed.

Switched Reluctance Machine - SRM This machine has a simple and robust construction, and is therefore relatively cheap to produce. The SRM has a long constant power region, but suffers from high acoustic noise, high torque ripple, and a poor power factor which results in high inverter current ratings.

Due to the surroundings where the truck will operate, i.e. parks, and cemeteries, etc., it is important that the machine is silent, which eliminates the SRM. The GMR Truck is a low speed vehicle, which means that it is not necessary with a long constant power region. Due to the high load capability (up to $1000\,\mathrm{kg}$) and the requirement of being able to climb steep roads ($15\,\%$ slope) a high torque is required in the whole speed range. These issues and the fact that the physical space is limited in the truck favors the PMSM when compared to the IM. It is assumed that the fuel cell stack will be more costly than the electric machines. For this reason it is important with a high efficiency, in order to decrease the fuel cell power rating. The high efficiency again favors the PMSM, and therefore this is selected.

Modeling

AC machines are often modeled in the dq-reference frame, which rotates with the velocity of the stator field. Thereby the sinusoidal currents, voltages, and flux linkages become constant, which is simpler. The dq-model of a PMSM is given by [62]:

$$v_d = R_s i_d + L_d \frac{di_d}{dt} - \omega_e L_q i_q \quad [\mathrm{V}] \tag{7.1}$$

$$v_q = R_s i_q + L_q \frac{di_q}{dt} + \omega_e L_d i_d + \omega_e \lambda_{pm} \quad [\mathrm{V}] \tag{7.2}$$

$$\tau_e = \frac{3}{2}\frac{P}{2}\left(\lambda_{pm} i_q + (L_d - L_q)\, i_d i_q\right) \quad [\mathrm{Nm}] \tag{7.3}$$

$$\tau_e = J_s \frac{d\omega_s}{dt} + B_v \omega_s + \mathbf{sign}(\omega_s)\tau_c + \tau_s \quad [\mathrm{Nm}] \tag{7.4}$$

$$p_{EM} = \frac{3}{2}\left(v_d i_d + v_q i_q\right) \quad [\mathrm{W}] \tag{7.5}$$

$$p_s = \omega_s \tau_s \quad [\mathrm{W}] \tag{7.6}$$

$$\omega_e = \frac{P}{2}\omega_s \quad [\mathrm{rad/s}] \tag{7.7}$$

where	v_d	[V]	D-axis voltage
	v_q	[V]	Q-axis voltage
	i_d	[A]	D-axis current
	i_q	[A]	Q-axis current
	p_{EM}	[W]	Electric power of the machine
	τ_e	[Nm]	Electromechanical torque
	τ_s	[Nm]	Shaft torque
	ω_e	[rad/s]	Electric angular velocity
	ω_s	[rad/s]	Shaft angular velocity
	R_s	[Ω]	Phase resistance
	L_d	[H]	D-axis inductance
	L_q	[H]	Q-axis inductance
	B_v	[Nms/rad]	Viscous friction coefficient
	τ_c	[Nm]	Coulomb friction
	λ_{pm}	[Vs/rad]	Flux linkage of the permanent magnet
	P	[−]	Number of poles

The dq-model in Equation (7.1)- (7.7) includes resistive loss and mechanical loss. The core loss, which becomes higher at high speeds are neglected in order to simplify.

Efficiency

The efficiency is defined as

$$\eta_{EM} = \begin{cases} \frac{p_s}{p_{EM}} & p_s \geq 0 \\ \frac{p_{EM}}{p_s} & p_s < 0 \end{cases} \qquad [-] \tag{7.8}$$

In order to investigate the efficiency, the theoretic efficiency of a motor with parameters in Table 7.1 is calculated.

Stator resistance	R_s	$9.62\,\mathrm{m\Omega}$
D-axis inductance	L_d	$28.7\,\mu\mathrm{H}$
Q-axis inductance	L_q	$47.2\,\mu\mathrm{H}$
Permanent magnet flux linkage	λ_{pm}	$9.71\,\mathrm{mWb}$
Poles	P	12
Moment of inertia	J_s	$18.2 \cdot 10^{-3}\,\mathrm{kgm^2}$
Viscous friction coefficient	B_v	$1 \cdot 10^{-3}\,\mathrm{Nms/rad}$
Coulomb friction	τ_c	$0.1\,\mathrm{Nm}$

Table 7.1: Parameters of PMSM used for efficiency investigation.

The efficiency contour of the machine with the parameters in Table 7.1 is shown in Figure 7.1. The efficiency is calculated when using $I_d = 0$ control. This control property does not utilize the reluctance torque due the difference in the inductances in the d-axis and q-axis, but this control property is simpler. It is seen that the efficiency increases with higher shaft angular velocity and torque. However, if the core losses were taken into account, the efficiency would probably be lower at high speed, as they are proportional with the speed squared [82].

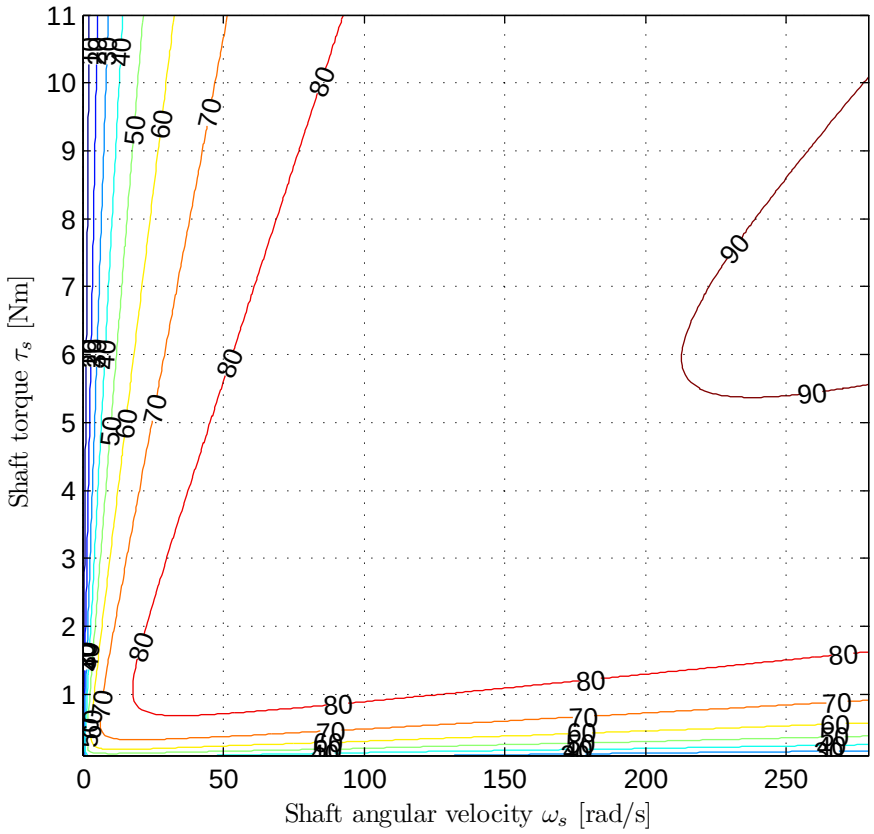

Figure 7.1: Efficiency plot of a PMSM for $I_d = 0$ control. The labels in the contour lines displays the efficiency in %.

The maximum efficiency of the PMSM used for illustration is $\eta_{EM} = 90.4\,\%$. At the maximum speed $\omega_{s,max} = 279\,\mathrm{rad/s}$ and torque $\tau_{s,max} = 11\,\mathrm{Nm}$ the machine has a power factor angle of $\phi_{EM}\left(\tau_{s,max}, \omega_{s,max}\right) = 0.53\,\mathrm{rad}$ and efficiency of $\eta_{EM}\left(\tau_{s,max}, \omega_{s,max}\right) = 0.90$.

7.2 INVERTER

A circuit diagram of the inverter can be seen in Figure 7.2. The inverter transmits power between the electric machine (with phase voltages v_A, v_B, and v_C) and the bus by turning on and off the switches Q_{A+}, Q_{A-}, Q_{B+}, Q_{B-}, Q_{C+}, and Q_{C-}. The switches are assumed to be of type MOSFET with on-resistance $R_{Q,Inv}$. The diodes in parallel of each switch are creating a path for the motor currents during the dead-time, i.e. when both switches in one branch are non-conducting in order to avoid a shoot-through.

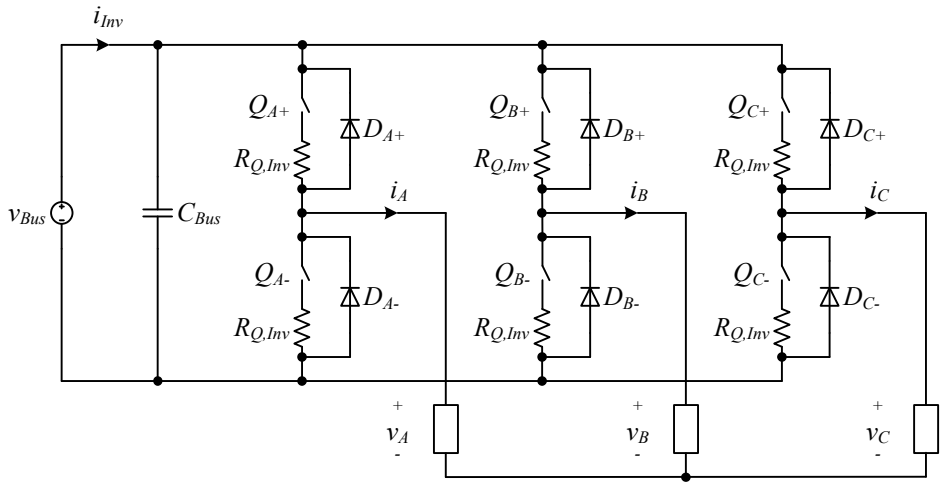

Figure 7.2: Circuit diagram of inverter.

Voltage Modeling

The inverter inverts the DC bus voltage to three phase AC voltages and currents, which are given by

$$v_A = \hat{V}_p \sin(\omega_e t + \phi_{EM}) \quad [\mathrm{V}] \tag{7.9}$$

$$v_B = \hat{V}_p \sin(\omega_e t + \frac{2\pi}{3} + \phi_{EM}) \quad [\mathrm{V}] \tag{7.10}$$

$$v_C = \hat{V}_p \sin(\omega_e t - \frac{2\pi}{3} + \phi_{EM}) \quad [\mathrm{V}] \tag{7.11}$$

$$i_a = \hat{I}_p \sin(\omega_e t) \quad [\mathrm{A}] \tag{7.12}$$

$$i_B = \hat{I}_p \sin(\omega_e t + \frac{2\pi}{3}) \quad [\mathrm{A}] \tag{7.13}$$

$$i_C = \hat{I}_p \sin(\omega_e t - \frac{2\pi}{3}) \quad [\mathrm{A}] \tag{7.14}$$

where $\hat{V}_p$ [V] Peak phase voltage
$\hat{I}_p$ [A] Peak phase current
ϕ_{EM} [rad] Power factor angle
ω_e [rad/s] Fundamental angular velocity

Many modulation methods that can do the DC / AC conversion exist. A simple method is the sinusoidal modulation. When using this method the peak phase voltage is given by [53]

$$\hat{V}_p = m_i \frac{V_{Bus}}{2} \quad [\mathrm{V}] \tag{7.15}$$

where m_i $[-]$ Modulation index

Loss Modeling

The losses of an inverter are given by the switches and diodes. The diode losses are usually divided into a resistive loss and a loss due to the forward voltage drop. Besides a resistive and forward voltage loss the loss of the switches are also characterized

by turn on and turn off loss. In order to simplify only the resistive loss of the switches are considered. The resistive loss of an inverter when using sinusoidal modulation technique is given by [29]

$$p_{Inv,Q} = R_{Q,Inv}\left(\frac{3}{4} + \frac{2m_i}{\pi}\cos\left(\phi_{EM}\right)\right)\hat{I}_p^2 \qquad [\mathrm{W}] \qquad (7.16)$$

where $R_{Q,Inv}$ $[\Omega]$ Switch on resistance

The output power of the inverter is the motor input power p_{EM}. The inverter loss is modeled in Equation (7.16). The inverter input power and efficiency are therefore

$$p_{Inv} = v_{Bus} i_{Inv} = p_{EM} + p_{Inv,Q} \qquad [\mathrm{W}] \qquad (7.17)$$

$$\eta_{Inv} = \begin{cases} \frac{p_{EM}}{p_{Inv}} & p_{EM} \geq 0 \\ \frac{p_{Inv}}{p_{EM}} & p_{EM} < 0 \end{cases} \qquad [-] \qquad (7.18)$$

7.3 CONCLUSION

The permanent magnet synchronous machine is chosen as electric machine due to its high power density and efficiency. The machine has been modeled in the dq-frame. For the inverter the traditional hard switching three leg inverter is used. It is modeled under the sinusoidal modulation technique, and only the resistive loss of the switches is taken into account due to simplicity.

Part III

Fuel Cell Truck

8 Design

In the two previous parts of this thesis the load of the GMR Truck has been analyzed and the essential components in a FCSPP have been modeled. This chapter will therefore combine these two parts and investigate different designs of a FCSPP for the FC Truck. Different configurations of combining the energy storage device(s) and the fuel cell stack to a common bus voltage will be investigated. As the system at least contains two power sources, it is necessary to divide the power sufficiently between the units. An energy management strategy and charging strategy will therefore also be presented. The different designs will be compared in terms of volume, mass, efficiency, and battery lifetime.

8.1 System Overview

The main components of the FC Truck can be seen in Figure 8.1. When comparing with the original power system of the GMR Truck shown in Figure 2.4 on page 17, it is seen that the body frame is reused, i.e. a new power system has therefore been connected to the original gear-boxes.

In order to size the components of the system it is necessary to know the power requirements of the vehicle. Figure 8.1 therefore also shows the power flow between the units. It is seen that power flows to or from the electric machines (EM) to a common bus through two inverters (Inv). The energy from the hydrogen storage is fed to the bus through the fuel cell stack (FC). Power is also flowing to or from the battery (Bat) and / or ultracapacitors (UC).

Bus Power

Besides the shaft power $p_{s,R}$ and $p_{s,L}$, the power system must also provide power for the light p_{Light}, balance-of-plant of the fuel cell system p_{BoP}, the auxiliary devices p_{Aux}, and the heater p_{Heat}. From Table 1.2 on page 6 the light consumption is specified to be $P_{Light} = 170\,\mathrm{W}$. The balance-of-plant consumption is the supply power of the units required to make the fuel cell stack operate, e.g. air blower, hydrogen valves, control system, and communication. In [4] the efficiency and balance-of-plant loss of a $2\,\mathrm{kW}$ HTPEM system is investigated. The paper only considers the loss of the air blower, as this is the most significant contribution of loss. From the paper it can be extracted that the loss is $102\,\mathrm{W}$ when the fuel cell operates at $2100\,\mathrm{W}$. The required air flow depends on the produced power of the fuel cell. However, for simplicity it is assumed that the loss is direct proportional to the fuel cell stack power p_{FC}. Therefore

$$p_{BoP} = 0.05 p_{FC} \qquad [\mathrm{W}] \tag{8.1}$$

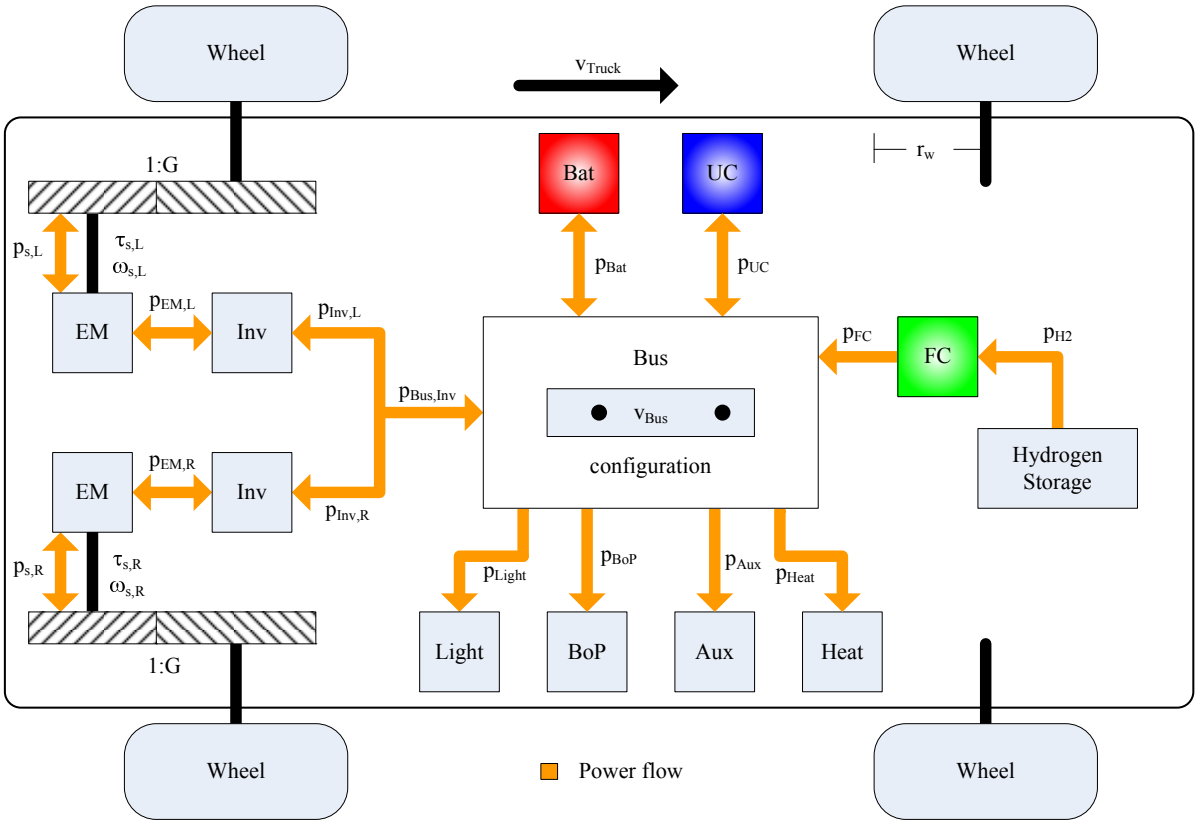

Figure 8.1: System overview and power flow of power system.

The auxiliary loads include the vehicle computer, drivers, control panel, etc. It is assumed that the load of the auxiliary devices is $p_{Aux} = 50\,\mathrm{W}$ when the truck is being used.

The fuel cell stack is operated above $100\,^{\circ}\mathrm{C}$ which means that it needs to be heated-up before it can produce power. In [5] different heating strategies have been investigated. A relatively fast method for heating is to blow hot air into the stack. The time it takes to heat-up the stack depends on several parameters, e.g. temperature of the hot air, isolation, flow rate, etc. In [5] it is shown that it takes approximately $T_{Heat} = 6\,\mathrm{min}$ before a $1\,\mathrm{kW}$ fuel cell stack has reached $100\,^{\circ}\mathrm{C}$ when $P_{Air} = 1200\,\mathrm{W}$ of hot air is blowing into the stack. If it is assumed that the device that converts the power from the bus to hot air has an efficiency of $80\,\%$ the heating power of the device is $P_{Heat,\,1\mathrm{kW}} = \frac{P_{Air}}{0.8} = 1500\,\mathrm{W}$. As for the balance-of-plant power it is assumed that the heating power also is proportional to the fuel cell power rating $P_{FC,rat}$, i.e.

$$p_{Heat} = \frac{p_{Heat,1\,\mathrm{kW}}}{1000\,\mathrm{W}} P_{FC,rat} = 1.5 P_{FC,rat} \qquad [\mathrm{W}] \tag{8.2}$$

The heating power in Equation (8.2) must therefore be applied for $T_{Heat} = 6\,\mathrm{min}$ before the fuel cell stack has the proper temperature. In order to reduce the energy requirement of the energy storage device, it would be preferable that the fuel cell stack could be heated catalytic [5]. However, an energy storage device is still needed for the propulsion during the heating period since a delay of $T_{Heat} = 6\,\mathrm{min}$ cannot be accepted.

It has later in [3] been shown, that a resistive heater was able to heat-up a $1\,\mathrm{kW}$ fuel cell stack in $800\,\mathrm{s}$. The resistive heater has a resistor with a total resistance of $R_{Heat} = 2.5\,\Omega$, which is connected to a $48\,\mathrm{V}$ battery package. This means that the following amount of energy is transfered from the bus to the heater:

$$E_{Heat} = \frac{(48\,\mathrm{V})^2}{2.5\,\Omega} \cdot 800\,\mathrm{s} = 205\,\mathrm{Wh} \tag{8.3}$$

From the previous case in [5] the energy of the hot air is

$$E_{Air} = P_{Air} T_{Heat} = 120\,\mathrm{Wh} \tag{8.4}$$

Even though the heating time of the two cases is not the same, and the setups also are different a rough estimate of the efficiency of the heater is

$$\eta_{Heater} = \frac{E_{Heat}}{E_{Air}} = 59\,\% \tag{8.5}$$

This is lower than the $80\,\%$, which is assumed above. However, the heating device in [3] is a prototype, and it is believed that its efficiency can be improved by optimization. Therefore it is assumed that the $80\,\%$ is not unrealistic.

8.2 Bus Voltage

Selection of the DC bus voltage is a quite essential decision to make, as it affects many devices of the drive system, i.e. the electrical machine, the choice of power electronic topologies, the configuration of input sources, etc. Basically it is a decision between whether to use a high or low voltage bus. Both solutions have pros and cons. Several parameters have influence on the decision, e.g. cost, availability, safety, efficiency, volume and weight.

The battery voltage of the electrical system of automobile manufacturers has changed from $6\,\mathrm{V}$ to $12\,\mathrm{V}$ in the mid 1955 [58]. The $12\,\mathrm{V}$ architecture is still used today, but the load power of the electric systems of a car is much higher today than in the fifties. Therefore a new system based on a $36\,\mathrm{V}$ battery voltage is considered. The $36\,\mathrm{V}$ battery packages are charged at $42\,\mathrm{V}$ level, and for this reason the system is called the 42V PowerNet [9, 33].

For the inverters and motors many standard components exist for the $230\,\mathrm{V}$ and $400\,\mathrm{V}$ levels, which will make one of those levels appropriate. A high bus voltage will also demand thin wires when compared to a low bus voltage. However, the GMR Truck is a relatively low power application which means that it probably would be difficult to find a fuel cell, battery, and ultracapacitor that suit to these high voltage levels. Due to safety reasons it is chosen to use the 42V PowerNet system. The $42\,\mathrm{V}$ system has minimum and maximum continuous voltage of $30\,\mathrm{V}$ and $48\,\mathrm{V}$, respectively. The system is described in "ISO 21848: Road vehicles - Electrical and electronic equipment for a supply voltage of 42 V - Electrical loads".

8.3 Configurations

An energy storage device can be connected to the fuel cell stack in many ways [31, 55]. A simple configuration is to directly connect two devices in parallel, e.g. fuel

cell / battery, fuel cell / ultracapacitor, or battery / ultracapacitor. However, in this way the power drawn of each device cannot be controlled, but is passively determined by the impedance of the devices. The impedance depends on many parameters, e.g. temperature, state-of-charge, health, and point of operation. Each device might therefore be operated at an inappropriate condition with respect to lifetime and efficiency. The voltage characteristics also have to match perfectly of the two devices, and only a fraction of the range of operation of the devices can be utilized, e.g. in a fuel cell / battery configuration the fuel cell must provide almost the same power all the time due to the fixed voltage of the battery, and in a battery / ultracapacitor configuration only a few percentage of the energy capability of the ultracapacitor can be used. This is again due to the nearly constant voltage of the battery. By introducing DC / DC converters one can select the voltage rating of the devices more flexible, and the power of each device can be controlled.

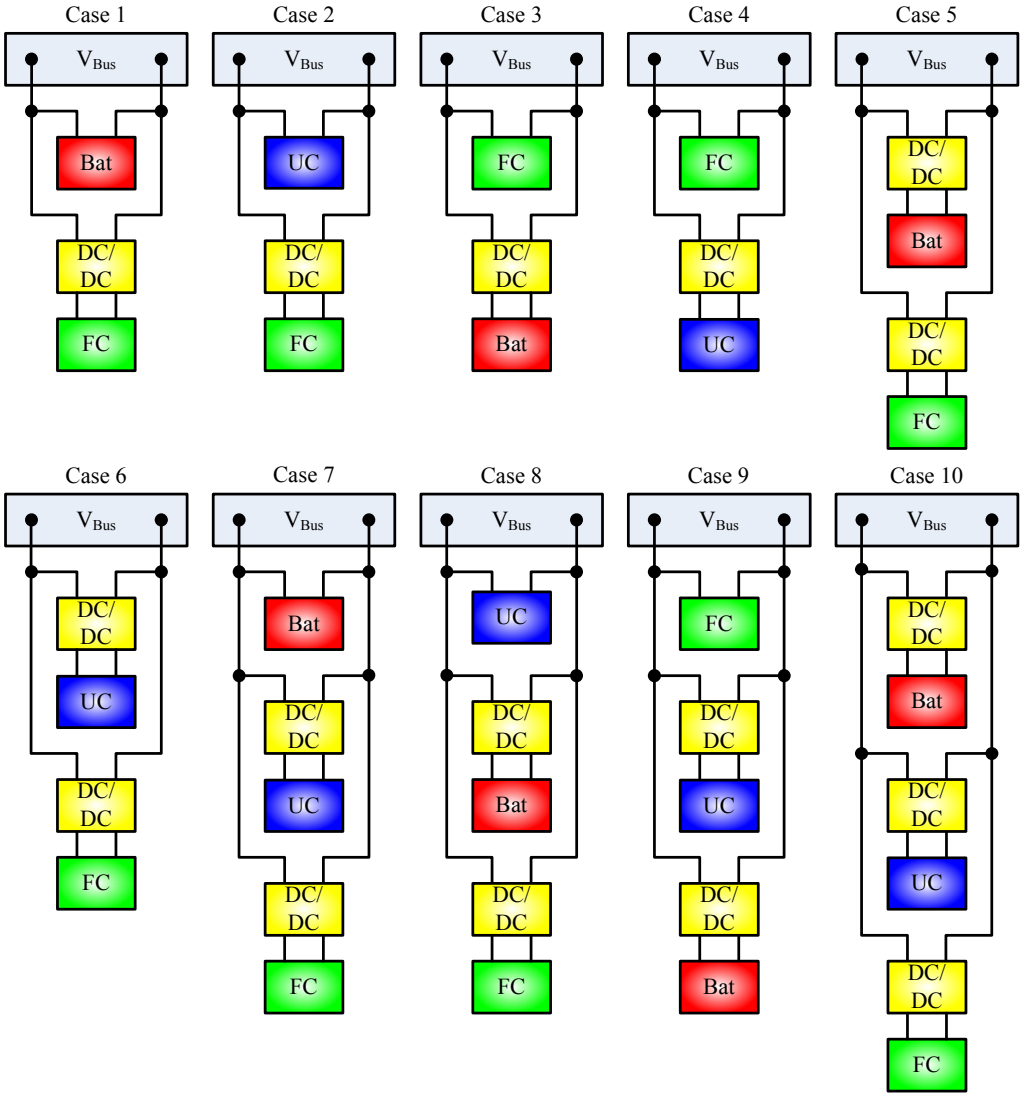

Figure 8.2: Ten cases of connecting the fuel cell and energy storage device(s) to a common bus.

In Figure 8.2 ten cases of connecting the fuel cell and energy storage device(s) to a

common bus are shown. In case 1 and 7 the battery is connected directly to the bus. In case 2 and 8 the ultracapacitor is connected directly to the bus. In case 3, 4 and 9 the fuel cell is connected directly to the bus and in case 5, 6 and 10 all the units are connected to the bus through DC/DC converters, and the bus is therefore kept at a fixed value.

In Table 8.1 the span of the bus voltage can be seen due to the devices connected to it. Fuel cells and ultracapacitors have a wide voltage variation. Therefore it is chosen to use the whole range of the 42V PowerNet standard, i.e. from $30\,\mathrm{V}$ to $48\,\mathrm{V}$, when the devices are directly on the bus, in order to utilize as much power or energy as possible. It is desired to investigate if it has any affect to keep the bus voltage at a fixed level. A voltage level of $42\,\mathrm{V}$ has been chosen due to the name of the standard.

The voltage variation will affect the VA rating of the inverters and DC/DC converters, i.e. for the same power at the minimum bus level the current will be different of the four situations in Table 8.1. In case 7, 8, 9 and 10 both a battery and ultracapacitor are parts of the system. For these configurations one might take advantage of the high efficiency and power capability of the ultracapacitor and the high energy capacity of the battery [69, 73].

	FC at bus	Bat at bus	UC at bus	Fixed bus
$V_{Bus,max}$ [V]	48	42	48	42
$V_{Bus,min}$ [V]	30	30	30	42

Table 8.1: Maximum and minimum bus voltage depending on the device connected to it.

8.4 Modeling and Parameter Calculation

The properties and characteristics of the fuel cell, battery, and ultracapacitor described in part II will be used for the modeling of the whole system. However, the voltage, power, and energy rating might not necessarily suit the required ratings of the devices in Figure 8.2. Therefore, the units will be scaled in a series and parallel structure to fit the requirements. The series parallel structure can be seen in Figure 8.3. Each cell, block or module is connected in N_s series cells, blocks, or modules, and therefore creating one string. N_p strings are thereby put in parallel. Each cell, block, or module has a voltage v_{Base} and current i_{Base}. This means that the terminal voltage v is given by the sum of the series connected cells, blocks, or modules, i.e. $v = N_s v_{Base}$, and that the current entering the terminals i is the sum of the parallel connected strings, i.e. $i = N_p i_{Base}$.

In the figure it is noticed that the direction of the currents only is valid for the battery and ultracapacitor, as a positive current of the fuel cell is defined as the current leaving the fuel cell, and not the current entering it, as for the case of the battery and ultracapacitor.

For each unit, i.e. fuel cell, battery, or ultracapacitor, it has been chosen to scale that unit to the same voltage level for all the 10 cases in Figure 8.2. This means that sometimes it is necessary to either buck or boost the voltage, as the voltage of one unit might be higher or lower than the bus voltage. For the battery and ultracapacitor it

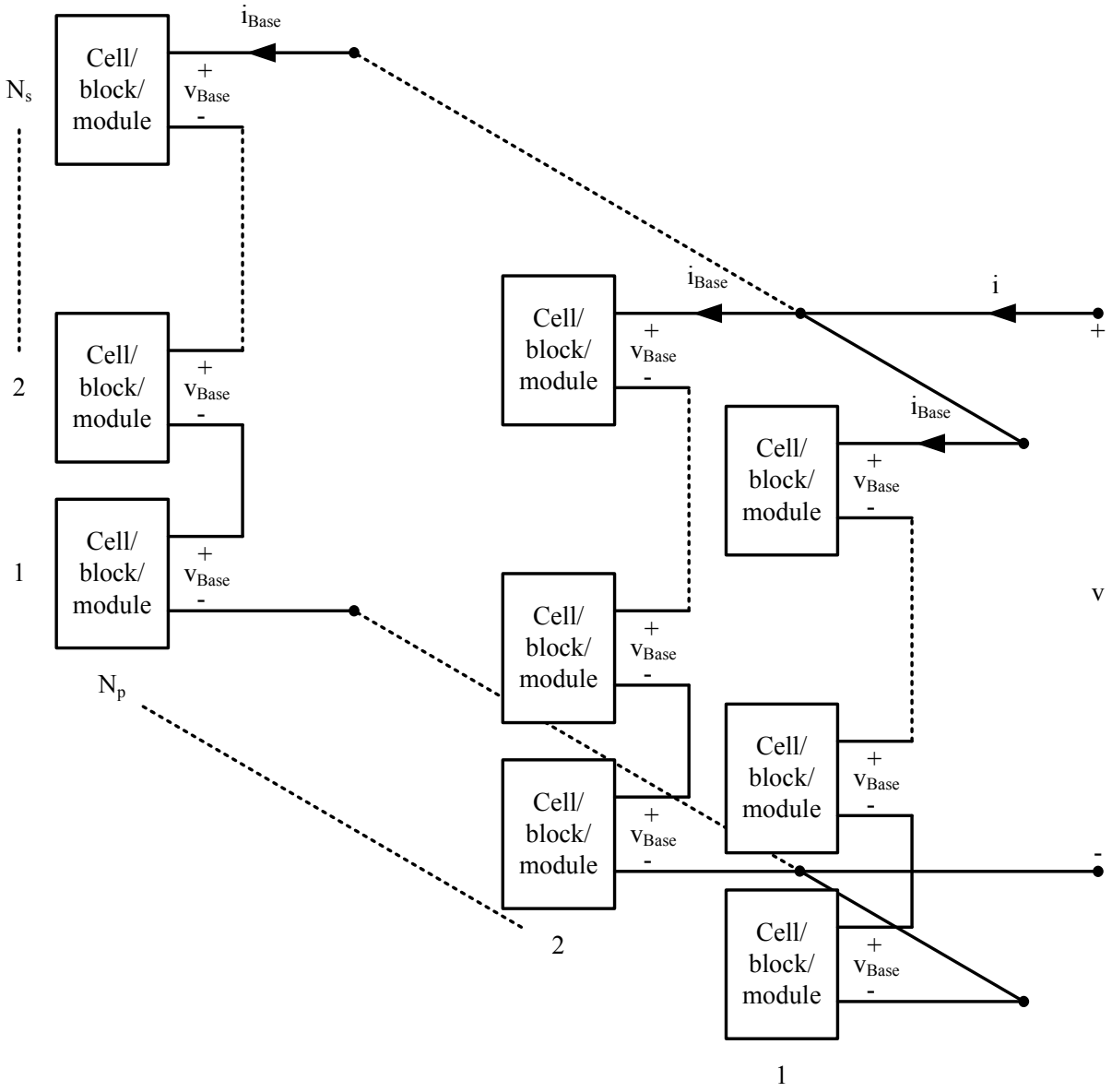

Figure 8.3: Series parallel structure used for modeling the fuel cell stack, battery, and ultracapacitor.

is therefore necessary to be able to buck or boost the voltage in both directions of the power flow.

Fuel Cell

In order to calculate the proper number of units in series and parallel the base values of the device are repeated in Table 8.2.

Base open circuit voltage	$V_{FC,oc,Base}$	$0.922\,\mathrm{V}$
Base nominal voltage	$V_{FC,nom,Base}$	$0.516\,\mathrm{V}$
Base nominal power	$P_{FC,nom,Base}$	$15.4\,\mathrm{W}$
Base resistance	$R_{FC,Base}$	$5.6\,\mathrm{m\Omega}$
Specific power	SP_{FC}	$131.4\,\mathrm{W/kg}$
Power density	PD_{FC}	$62.2\,\mathrm{W/L}$

Table 8.2: Fuel cell base values used for scaling.

The mass and volume density is calculated from the data of the fuel cell stack in Table 9.1 on page 126 as this stack uses the same cells.

For all the configurations in Figure 8.2 the fuel cell will have an open circuit voltage of $V_{FC,oc} = V_{Bus,max}$ (FC at bus) $= 48\,\mathrm{V}$. The number of series connected cells is therefore

$$N_{FC,s} = \frac{V_{FC,oc}}{V_{FC,oc,Base}} \approx 52 \tag{8.6}$$

The nominal fuel cell voltage is therefore $V_{FC,nom} = N_{FC,s} V_{FC,nom,Base} = 26.8\,\mathrm{V}$ which is less than the minimum allowed voltage level of the 42V PowerNet system. The fuel cell can therefore only provide the nominal power when it is behind a DC/DC converter, i.e. case 1, 2, 5, 6, 7, 8, and 10. The number of parallel cells depends on the required nominal fuel cell power $P_{FC,rat}$, i.e.

$$N_{FC,p} = \frac{P_{FC,rat}}{N_{FC,s} P_{FC,nom,Base}} \qquad [-] \tag{8.7}$$

It is noticed that in the calculation of the number of parallel strings $N_{FC,p}$ in Equation (8.7) the number $N_{FC,p}$ can easily be a float or below 1, depending on the power level. For the given cell used for the modeling, the number of course needs to be an integer if it should be realized in practice. However, it is assumed that the cells can be delivered with different areas, e.g. a half area results in the half nominal power and current, and the double area provides the double nominal power and current. For very low power levels it might not be practically feasible to produce a fuel cell stack with a relatively high voltage level. In the same way the area of a low-voltage fuel cell stack will be unrealistic big for very high power levels. However, these issues are neglected.

The fuel cell stack model consists of $N_{FC,s}$ cells in series and $N_{FC,p}$ strings in parallel. The fuel cell model in Chapter 3 is based on a single cell. Therefore in order to reuse this model, the fuel cell stack is simulated as a single base cell. The base fuel cell current is therefore

$$i_{FC,Base} = \frac{i_{FC}}{N_{FC,p}} \qquad [\mathrm{A}] \tag{8.8}$$

For the ten cases of configuration in Figure 8.2 it is chosen not to investigate the direct parallel structure, e.g. the fuel cell terminals connected to the ultracapacitor terminals, and maximum one unit can therefore be connected directly to the bus without using a DC/DC converter. For this reason, the current of each device can always be controlled. If it is assumed that current of the fuel cell is controlled in a sufficient slow manner, and that the fuel cell always has the proper hydrogen and air flow, and temperature (except during heating), the fuel cell can be considered to operate in steady-state at all times. For this reason there is no need for the dynamic model created by using electrochemical impedance spectroscopy, and the fuel cell can therefore be modeled properly by using the model in Figure 3.1 on page 30, which can provide the polarization curve.

The internal fuel cell base voltage is from Equation (3.4) therefore

$$v_{FC,int,Base} = V_{FC,oc,Base} - a_{FC}\log\left(\frac{i_{FC,Base}+I_n}{b_{FC}}\right) + a_{FC}\log\left(\frac{I_n}{b_{FC}}\right) \quad [\mathrm{V}] \tag{8.9}$$

where $I_n = 0.01\,\mathrm{A}$ Fuel crossover and internal currents
$a_{FC} = 0.0318\,\mathrm{V}$ Constant
$b_{FC} = 0.72\,\mathrm{V}$ Constant

The fuel cell base voltage $v_{FC,Base}$, stack voltage v_{FC}, and power p_{FC} are therefore

$$v_{FC,Base} = v_{FC,int,Base} - R_{FC,Base}i_{FC,Base} \quad [\mathrm{V}] \tag{8.10}$$
$$v_{FC} = N_{FC,s}v_{FC,Base} \quad [\mathrm{V}] \tag{8.11}$$
$$p_{FC} = v_{FC}i_{FC} \quad [\mathrm{W}] \tag{8.12}$$

The hydrogen mass flow and power is from Equation (3.6) and Equation (3.7) repeated here:

$$\dot{m}_{H2} = N_{FC,s}\frac{M_{H2,mol}}{2F}i_{FC} \quad [\mathrm{kg/s}] \tag{8.13}$$
$$p_{H2} = \dot{m}_{H2}HHV_{H2} \quad [\mathrm{W}] \tag{8.14}$$

where $F = 96485$ [C/mol] Faraday's constant
$\dot{m}_{H2}$ [kg/s] Mass flow of hydrogen
$N_{FC,s}$ [−] Number of series connected fuel cells
$M_{H2,mol} = 0.00216$ [kg/mol] Hydrogen molar mass
i_{FC} [C/s] Fuel cell current
p_{H2} [W] Power of hydrogen
HHV_{H2} [J/kg] Higher heating value of hydrogen

Battery

The battery will also be put in a series parallel structure. The battery base values are therefore repeated in Table 8.3.

The battery pack consists of $N_{Bat,s} = 3$ series connected blocks. This means that the maximum and minimum battery voltage is

$$V_{Bat,max} = N_{Bat,s}V_{Bat,max,Base} = 41.4\,\mathrm{V} \tag{8.15}$$
$$V_{Bat,min} = N_{Bat,s}V_{Bat,min,Base} = 31.5\,\mathrm{V} \tag{8.16}$$

Base maximum voltage	$V_{Bat,max,Base}$	$13.8\,\mathrm{V}$
Base minimum voltage	$V_{Bat,min,Base}$	$10.5\,\mathrm{V}$
Base maximum power	$P_{Bat,max,Base}$	$1988\,\mathrm{W}$
Base $10\,\mathrm{h}$ capacity	$Q_{Bat,10,Base}$	$37\,\mathrm{Ah}$
Base $20\,\mathrm{h}$ discharge current	$I_{Bat,20,Base}$	$2\,\mathrm{A}$
Base nominal resistance	$R_{Bat,nom,Base}$	$11.6\,\mathrm{m\Omega}$
Base mass	$M_{Bat,Base}$	$14.5\,\mathrm{kg}$
Base volume	$V_{Bat,Base}$	$6.4\,\mathrm{L}$

Table 8.3: Battery base values used for scaling.

In order to fulfill the power and energy requirements, the $N_{Bat,s}$ series connected battery blocks will be connected in $N_{Bat,p}$ parallel strings. As for the case with the fuel cell it is assumed that the number $N_{Bat,p}$ can be of any value greater than zero; also values below 1. The battery will also be simulated in its base form. The base battery current is therefore

$$i_{Bat,Base} = \frac{i_{Bat}}{N_{Bat,p}} \qquad [\mathrm{A}] \tag{8.17}$$

The base open circuit voltage $v_{Bat,oc,Base}$, base voltage $v_{Bat,Base}$, and battery voltage are

$$v_{Bat,oc,Base} = \left(V_{Bat,max,Base} - V_{Bat,min,Base}\right) SoC_{Bat} + V_{Bat,min,Base} \qquad [\mathrm{V}] \tag{8.18}$$

$$v_{Bat,Base} = v_{Bat,oc,Base} + R_{Bat,Base} i_{Bat,Base} \qquad [\mathrm{V}] \tag{8.19}$$

$$v_{Bat} = N_{Bat,s} v_{Bat,Base} \qquad [\mathrm{V}] \tag{8.20}$$

The state-of-charge calculation is also done on the base battery block:

$$k = a_k |i_{Bat,Base}| + b_k \qquad [-] \tag{8.21}$$

$$i_{Bat,eq,Base} = \begin{cases} -\frac{Q_{Bat,10,Base}}{T_{Bat,20}} \left(\frac{|i_{Bat,Base}|}{I_{Bat,20,Base}}\right)^k & i_{Bat,Base} < 0\,\mathrm{A} \\ \eta_{Bat,cha} i_{Bat,Base} & i_{Bat,Base} \geq 0\,\mathrm{A} \end{cases} \qquad [\mathrm{A}] \tag{8.22}$$

$$SoC_{Bat} = 1 + \int \frac{i_{Bat,eq,Base}}{Q_{Bat,10,Base} 3600\,\mathrm{s/h}} dt \qquad [-] \tag{8.23}$$

where a_k = 0.0024 Constant
b_k = 1.1519 Constant
$\eta_{Bat,cha}$ = 0.84 Charging efficiency

Ultracapacitor

Ultracapacitors are generally only operated to half of their nominal voltage in order to limit the current requirements of the power electronics. In Chapter 5 it was shown that the charge recovery phenomenon is most significant at low voltage levels. It is chosen to limit the minimum voltage level of the ultracapacitor to the half of the nominal, i.e. $V_{UC,min} = V_{UC,max}/2$. This means that the simple ultracapacitor model, also presented in Chapter 5, is sufficient, as it is able to model the self discharge and capacitance as

Base maximum voltage	$V_{UC,max,Base}$	$16.2\,\mathrm{V}$
Base minimum voltage	$V_{UC,min,Base}$	$8.1\,\mathrm{V}$
Base internal resistance	$R_{UC,Base}$	$2\,\mathrm{m\Omega}$
Base equivalent minimum capacitance	$C_{eq,min,Base}$	$449.4\,\mathrm{F}$
Base equivalent maximum capacitance	$C_{eq,max,Base}$	$500.9\,\mathrm{F}$
Base mass	$M_{UC,Base}$	$5.75\,\mathrm{kg}$
Base volume	$V_{UC,Base}$	$4.7\,\mathrm{L}$

Table 8.4: Ultracapacitor base values used for scaling.

good as the advanced model, which consists of seven RC-circuits used for modeling the charge recovery. The ultracapacitor base values are repeated in Table 8.4.

The maximum ultracapacitor voltage is $V_{UC,max} = V_{Bus,max}$ (UC at bus) $= 48\,\mathrm{V}$. The number of series connected ultracapacitor modules is therefore

$$N_{UC,s} = \frac{V_{UC,max}}{V_{UC,max,Base}} \approx 3 \tag{8.24}$$

In Table 5.1 on page 49 the power density is specified to be $5.4\,\mathrm{kW/kg}$. This means that the peak power is $M_{Bat,Base} \cdot 5.4\,\mathrm{kW/kg} = 31.1\,\mathrm{kW}$. However, as for the battery it is chosen to be conservative. The maximum power is therefore calculated at the minimum voltage. The maximum and minimum ultracapacitor voltages depend on the configuration, i.e.

$$V_{UC,max} = \begin{cases} V_{Bus,max} = 48\,\mathrm{V} & \text{Case } 2,8 \\ N_{UC,s}V_{UC,max,Base} = 48.6\,\mathrm{V} & \text{Case } 4,6,7,9,10 \end{cases} \quad [\mathrm{V}] \tag{8.25}$$

$$V_{UC,min} = \begin{cases} V_{Bus,min} = 30\,\mathrm{V} & \text{Case } 2,8 \\ \frac{V_{UC,max}}{2} = 24.3\,\mathrm{V} & \text{Case } 4,6,7,9,10 \end{cases} \quad [\mathrm{V}] \tag{8.26}$$

The maximum base power is therefore

$$P_{UC,max,Base} = \frac{\left(\frac{V_{UC,min}}{N_{UC,s}}\right)^2}{4R_{UC,Base}} = \begin{cases} 12.5\,\mathrm{kW} & \text{Case } 2,8 \\ 8.2\,\mathrm{kW} & \text{Case } 4,6,9,10 \end{cases} \tag{8.27}$$

From Table 5.3 on page 65 the minimum and maximum equivalent capacitances are given by

$$C_{eq,min,Base} = a_{C_{eq}}V_{UC,min,Base} + b_{C_{eq}} = 449.4\,\mathrm{F} \tag{8.28}$$

$$C_{eq,max,Base} = a_{C_{eq}}V_{UC,max,Base} + b_{C_{eq}} = 500.9\,\mathrm{F} \tag{8.29}$$

where $a_{C_{eq}} = 6.36$ Constant
$b_{C_{eq}} = 397.9$ Constant

As for the fuel cell and battery, the ultracapacitor is also simulated as a base module. The base current $i_{UC,Base}$ and voltage $v_{UC,Base}$ are therefore

$$i_{UC,Base} = \frac{i_{UC}}{N_{UC,p}} \quad [\mathrm{A}] \tag{8.30}$$

$$v_{UC,Base} = \frac{v_{UC}}{N_{UC,s}} \quad [\mathrm{V}] \tag{8.31}$$

The equivalent capacitance, self discharge time constant, and self discharge resistance are also calculated per base cell

$$C_{eq,Base} = a_{C_{eq}} v_{UC,Base} + b_{C_{eq}} \quad [\mathrm{F}] \tag{8.32}$$

$$\tau_{sd,Base} = a_{sd} \cdot e^{-\left(b_{sd} v_{UC,Base}\right)^{c_{sd}}} + d_{sd} \quad [\mathrm{s}] \tag{8.33}$$

$$R_{sd,Base} = \frac{\tau_{sd,Base}}{C_{eq,Base}} \quad [\Omega] \tag{8.34}$$

where $a_{sd} = 2.0101 \cdot 10^7$ Constant
$b_{sd} = 0.0675$ Constant
$c_{sd} = 16.1625$ Constant
$d_{sd} = 1.1233 \cdot 10^5$ Constant

The ultracapacitor base voltage $v_{UC,Base}$ is therefore calculated as follows

$$i_{sd,Base} = \frac{v_{UC,1,Base}}{R_{sd,Base}} \quad [\mathrm{A}] \tag{8.35}$$

$$i_{eq,Base} = i_{UC,Base} - i_{sd,Base} = C_{eq,Base} \frac{dv_{UC,1,Base}}{dt} \quad [\mathrm{A}] \tag{8.36}$$

$$v_{UC,Base} = v_{UC,1,Base} + R_{UC,Base} i_{UC,Base} \quad [\mathrm{V}] \tag{8.37}$$

DC/DC Converters

Due to the fixed amount of series connected cells, blocks, and modules, i.e. $N_{FC,s} = 52$, $N_{Bat,s} = 3$, and $N_{UC,s} = 3$, it is necessary to be able to both buck and boost the voltage, depending on the actual voltage of the bus and the given device. The battery and ultracapacitor can handle both positive and negative currents, and therefore the DC / DC converter of these units should be able to buck and boost the voltage for both directions of the power flow.

In order to simplify the same converter topology will be used for the fuel cell stack, battery, and ultracapacitor. The circuit diagram of the converter can be seen in Figure 8.4.

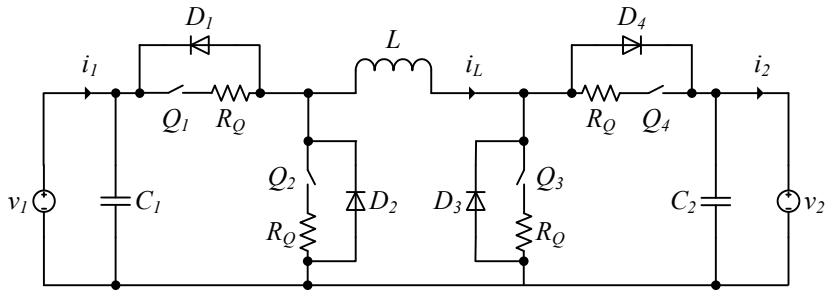

Figure 8.4: Circuit diagram of bi-directional non-inverting buck-boost converter.

In Chapter 6 it is shown that the losses are proportional to the current level (except at low current levels where the synchronous rectifiers could not be used, due to the reverse current protection). The total loss of the converter is the accumulation of the loss in each individual component. In Chapter 6 it was also shown that the loss in each

component also is proportional with the current level. Therefore, in order to simplify the loss of the converter can be modeled by a single component, which is chosen in such a way, that the loss of this component has the same value as the loss of all the components added together.

In Appendix D it has been shown that the relationship between the power of source 1 P_1, of source 2 P_2, and power loss of the switches P_Q is given by

$$\underbrace{V_2 I_2}_{P_2} = \underbrace{V_1 I_1}_{P_1} - \underbrace{2 R_Q I_2^2}_{P_Q} \quad [\mathrm{W}] \tag{8.38}$$

This means that the efficiency is

$$\eta_{Con} = \begin{cases} \frac{P_2}{P_1} & I_2 \geq 0 \\ \frac{P_1}{P_2} & I_2 < 0 \end{cases} \quad [-] \tag{8.39}$$

The converter VA-rating is the multiplication of the maximum voltage and current at each side of the converter, i.e.

$$P_{Con,rat} = \max \left(\begin{bmatrix} \max(v_1) \max(|i_1|) \\ \max(v_2) \max(|i_2|) \end{bmatrix} \right) \quad [\mathrm{VA}] \tag{8.40}$$

Fuel Cell Converter

The fuel cell converter will be designed with an efficiency of $\eta_{con,FC,rat} = 0.95$ at the nominal fuel cell power $P_{FC,nom}$ and minimum bus voltage $V_{Bus,min}$. Therefore from Equation (8.38):

$$P_{Bus,FC,rat} = \eta_{Con,FC,rat} P_{FC,nom} \quad [\mathrm{W}] \tag{8.41}$$

$$I_{Bus,FC,rat} = \frac{P_{Bus,FC,rat}}{V_{Bus,min}} \quad [\mathrm{A}] \tag{8.42}$$

$$P_{Con,Q,FC,rat} = P_{FC,nom,rat} - P_{Bus,FC,rat} \quad [\mathrm{W}] \tag{8.43}$$

$$R_{Q,Con,FC} = \frac{P_{Con,Q,FC,rat}}{2 I_{Bus,FC,rat}^2} \quad [\Omega] \tag{8.44}$$

The fuel cell converter should be able to handle both the maximum voltage and current on both sides on the converter. The power rating is therefore

$$P_{Con,FC,rat} = \max \left(\begin{bmatrix} V_{Bus,max} \max(i_{Bus,FC}) \\ V_{FC,oc} \max(i_{FC}) \end{bmatrix} \right) \quad [\mathrm{VA}] \tag{8.45}$$

Battery Converter

The battery converter will be designed with an efficiency of $\eta_{con,Bat,rat} = 0.95$ at the maximum battery discharge power and minimum bus voltage. Therefore from Equation (8.38):

$$P_{Bat,Bus,rat} = \eta_{Con,Bat,rat} \min(p_{Bat}) \quad [\mathrm{W}] \tag{8.46}$$

$$P_{Con,Q,Bat,rat} = P_{Bat,Bus,rat} - \min(p_{Bat}) \quad [\mathrm{W}] \tag{8.47}$$

$$I_{Bat,rat} = \frac{\min(p_{Bat})}{V_{Bat,min}} \quad [\mathrm{A}] \tag{8.48}$$

$$R_{Q,Con,Bat} = \frac{P_{Con,Q,Bat,rat}}{2 I_{Bat,rat}^2} \quad [\Omega] \tag{8.49}$$

The battery is modeled in such a way that a positive current charges the battery and a negative current discharge it. With this sign convention the battery is therefore the source number 2 in Figure 8.4 and the bus is source 1. Therefore the minimum battery power is used for the calculation of the switch resistance $R_{Q,Con,Bat}$. Due to the sign convention the minimum battery power is therefore negative.

The battery converter power rating is

$$P_{Con,Bat,rat} = \max\left(\begin{bmatrix} V_{Bat,max}\max\left(|i_{Bat}|\right) \\ V_{Bus,max}\max\left(|i_{Bus,Bat}|\right) \end{bmatrix}\right) \quad [\text{VA}] \quad (8.50)$$

Ultracapacitor Converter

The ultracapacitor converter will also be designed with an efficiency of $\eta_{con,UC,rat} = 0.95$ at the maximum battery discharge power and minimum bus voltage. Therefore from Equation (8.38):

$$P_{UC,Bus,rat} = \eta_{Con,UC,rat}\min\left(p_{UC}\right) \quad [\text{W}] \quad (8.51)$$

$$P_{Con,Q,UC,rat} = P_{UC,Bus,rat} - \min\left(p_{UC}\right) \quad [\text{W}] \quad (8.52)$$

$$I_{UC,rat} = \frac{\min\left(p_{UC}\right)}{V_{UC,min}} \quad [\text{A}] \quad (8.53)$$

$$R_{Q,Con,UC} = \frac{P_{Con,Q,UC,rat}}{2I_{UC,rat}^2} \quad [\Omega] \quad (8.54)$$

The ultracapacitor converter power rating is

$$P_{Con,UC,rat} = \max\left(\begin{bmatrix} V_{UC,max}\max\left(|i_{UC}|\right) \\ V_{Bus,max}\max\left(|i_{Bus,UC}|\right) \end{bmatrix}\right) \quad [\text{VA}] \quad (8.55)$$

Electric Machine

Due to the permanent magnet the maximum speed is limited by the available bus voltage. In Table 8.1 where the bus voltage is shown for different cases the minimum bus voltage is either $V_{Bus,min} = 30\,\text{V}$ or $V_{Bus,min} = 42\,\text{V}$. Two different machines will therefore be designed.

The electric machine should provide a continuous torque of $\tau_{s,rat} = 11\,\text{Nm}$ at $\omega_{s,rat} = 279\,\text{rad/s}$. It is chosen to use the same mechanical parameters as for the case in Chapter 7. The electromechanical torque and electric angular velocity at the maximum shaft speed and torque is therefore

$$\tau_{e,rat} = B_v\omega_{s,rat} + \tau_c + \tau_{s,rat} = 11.4\,[\text{Nm}] \quad (8.56)$$

$$\omega_{e,rat} = \frac{P}{2}\omega_{s,rat} = 1674\,\text{rad/s} \quad (8.57)$$

where	$B_v = 1\cdot10^{-3}\,\text{Nms/rad}$	Viscous friction coefficient
	$\tau_c = 0.1\,\text{Nm}$	Coulomb torque
	$P = 12$	Number of poles

The machine should be able to deliver this electromechanical torque at the minimum bus voltage $V_{Bus,min}$. The power factor angle from the previous case is used

again, i.e. $\phi_{EM,rat} = 0.53\,\text{rad}$. At the minimum bus level, the maximum peak phase voltage from Equation (7.15) is (when using sinusoidal modulation technique):

$$\hat{V}_{p,rat} = \frac{V_{Bus,min}}{2} \quad [\text{V}] \tag{8.58}$$

Therefore, when using $I_d = 0$ control the d and q-axis voltages are

$$V_{d,rat} = -\sin(\phi_{EM,rat})\hat{V}_{p,rat} \quad [\text{V}] \tag{8.59}$$

$$V_{q,rat} = \cos(\phi_{EM,rat})\hat{V}_{p,rat} \quad [\text{V}] \tag{8.60}$$

The machine used for illustration in Chapter 7 has an efficiency of $\eta_{EM,rat} = 0.9$ at the nominal point of operation. The machine is therefore designed to have this efficiency at that point. Again, when using the $I_d = 0$ property, the rest of the motor parameters can be calculated by manipulating Equation (7.1)-(7.7):

$$I_{q,rat} = \frac{\tau_{s,rat}\omega_{s,rat}}{\frac{3}{2}V_{q,rat}\eta_{EM,rat}} \quad [\text{A}] \tag{8.61}$$

$$\lambda_{pm} = \frac{2}{3}\frac{2}{P}\frac{\tau_{e,rat}}{I_{q,rat}} \quad [\text{Wb}] \tag{8.62}$$

$$R_s = \frac{V_{q,rat} - \omega_{e,rat}\lambda_{pm}}{I_{q,rat}} \quad [\Omega] \tag{8.63}$$

$$L_q = \frac{-V_{d,rat}}{\omega_{e,rat}I_{q,rat}} \quad [\text{H}] \tag{8.64}$$

Inverter

It is chosen to design the inverter with an efficiency $\eta_{Inv,rat} = 0.95$, at the same point of operation as the electric machine, i.e. at the minimum bus voltage $V_{Bus,min}$. At this point of operation the input power is

$$P_{EM,rat} = \frac{3}{2}\left(V_{d,rat}I_{d,rat} + V_{q,rat}I_{q,rat}\right) \quad [\text{W}] \tag{8.65}$$

The inverter loss is therefore from Equation (7.18):

$$P_{Inv,Q,rat} = \frac{1 - \eta_{Inv,rat}}{\eta_{Inv,rat}}P_{EM,rat} \quad [\text{W}] \tag{8.66}$$

From Equation (7.15) the modulation index at the minimum bus voltage

$$m_{i,rat} = \frac{2\hat{V}_{p,rat}}{V_{Bus,min}} \quad [-] \tag{8.67}$$

When using $I_d = 0$ control the peak phase current is equal to the q-axis current, i.e. $\hat{I}_{p,rat} = I_{q,rat}$. The switch resistance R_Q that will provide an efficiency of $\eta_{Inv,rat} = 0.95$ at the minimum bus voltage and maximum torque and speed of the motor is from Equation (7.16):

$$R_{Q,Inv} = \frac{P_{Inv,Q,rat}}{\left(\frac{3}{4} + \frac{2m_{i,rat}}{\pi}\cos(\phi_{EM,rat})\right)\hat{I}_{p,rat}^2} \quad [\Omega] \tag{8.68}$$

The inverter VA-rating is the maximum of the DC and AC side, i.e.

$$P_{Inv,rat} = \max\left(\begin{bmatrix} 3 \overbrace{\frac{V_{Bus,max}}{2\sqrt{2}}}^{\text{max phase RMS}} & \frac{\max(\hat{I}_p)}{\sqrt{2}} \\ V_{Bus,max} & \max(|i_{Inv}|) \end{bmatrix}\right) \quad [\text{VA}] \tag{8.69}$$

8.5 Energy Management Strategy

The energy management strategy (EMS) is very important as it is responsible for distributing the power between the different units. A good EMS should provide high system efficiency, high performance, and protect the components. Different energy management strategies have been proposed for fuel cell / battery / ultracapacitor hybrid systems [7, 26, 45, 79]. Due to the many different configurations a simple energy management strategy is desired, which can be used for all the cases. Figure 8.5 is presenting the system level block diagram of the applied EMS. The input to the EMS is the power of the two inverters $p_{Inv,R}$ and $p_{Inv,L}$, the power to the light p_{Light}, the balance-of-plant power p_{BoP}, power to the auxiliary devices p_{Aux}, the fuel cell stack heater p_{Heat}, and the requested charging power of the battery $p_{Bus,Bat,charge}{}^*$ and ultracapacitors $p_{Bus,UC,charge}{}^*$. The output of the EMS is the fuel cell stack bus power $p_{Bus,FC}$, battery bus power $p_{Bus,Bat}$, and ultracapacitor bus power $p_{Bus,UC}$.

The bus load power is defined as

$$p_{Bus,Load} = p_{Aux} + p_{BoP} + p_{Light} + p_{Heat} + p_{Inv,L} + p_{Inv,R} \quad [\text{W}] \tag{8.70}$$

In the ideal case the fuel cell stack should be able to provide power to the load $p_{Bus,Load}$, and to charge the energy storage devices with their requested charging powers. However, due to the relatively low dynamic properties of fuel cell system, the desired fuel cell bus power contribution $p_{Bus,FC}{}^*$ is settled by a low-pass filter (Block "FC-LP-filter" in Figure 8.5) with bandwidth $f_{LP,FC}$. The fuel cell stack itself has a relatively fast response, as shown in Figure 3.7 on page 37, were a current step and inverse current step where applied to the fuel cell. In Figure 3.7(b) the time constant is approximately $50\,\text{ms}$. However, this is in a laboratory setup with sufficient hydrogen and oxygen supply. In a mobile application there will be no air cylinders, but the fuel cell will use the oxygen from the surrounding air. A fan is therefore controlling the required air flow to the cathode side. In Figure 3.4 on page 34 it is seen that the impedance of the fuel cell becomes more resistive at low frequencies when the air stoichiometry is reduced. This means a weak air supply results in high fuel cell impedance, which is undesirable. The bandwidth of the low pass filter therefore depends on the bandwidth of the fan. In [78] a $5\,\text{kW}$ fuel cell system is described. The air mass flow of that system has a time constant of approximately $0.25\,\text{s}$. The bandwidth of the air mass flow system is therefore $0.64\,\text{Hz}$. The fuel cell power should change with a frequency that is significantly lower. It is therefore chosen to use $f_{LP,FC} = 10\,\text{mHz}$.

Depending on the connection to the bus, the desired fuel cell stack power $p_{FC}{}^*$ can be calculated. In order to insure that the fuel cell does not deliver more power than its power rating $P_{FC,rat}$ or lower than zero power, the "Saturation" block in Figure 8.5 is utilized. If the fuel cell is heating-up, it cannot provide power, i.e. $p_{FC} = 0$. In this

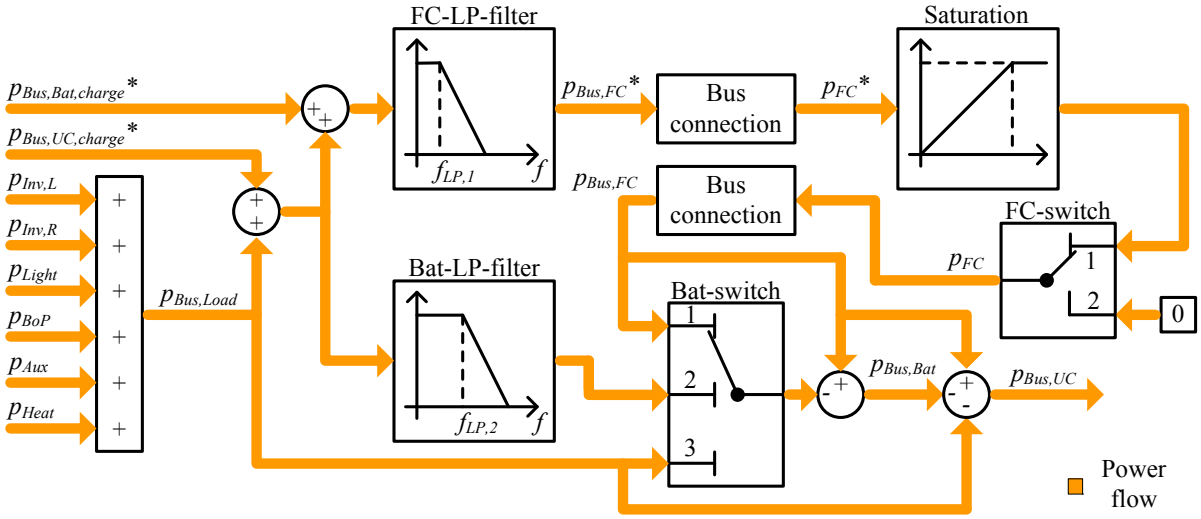

Figure 8.5: System level block diagram of energy management strategy.

situation the switch "FC-switch" in Figure 8.5 therefore is in position 2. During normal operation it is in position 1.

The switch "Bat-switch" in Figure 8.5 is used to divide the bus power between the battery and ultracapacitors. When the ultracapacitors are the only energy storage device, the switch is in position 1. Thereby the battery bus power contribution is zero, and the ultracapacitors therefore provide that part of the load power that the fuel cell is not able to deliver. When the battery is the only energy storage device, the switch is in position 3. Thereby the ultracapacitor bus power contribution becomes zero, and the battery provides the difference between the fuel cell bus power and bus load power. When both the battery and ultracapacitors are presented the switch is in position 2. In this situation, the battery contribution is also determined by a low-pass filter (Block "Bat-LP-filter" in Figure 8.5). This filter has a higher bandwidth $f_{LP,Bat}$ than $f_{LP,FC}$ of the fuel cell filter. However, the bandwidth is chosen sufficiently low, so that the load power due to the short term accelerations and braking of the vehicle is fed to the ultracapacitors. In this way the battery assists the fuel cell stack with the base part of the load power, and the ultracapacitors take care of the peak powers. It may be understood, that if the fuel cell power rating is sufficiently high, the battery in this situation is only utilized during the heating-up of the fuel cell stack. However, if the fuel cell stack power rating is very small, the battery will be the main source of energy to the electric machines, and the only function of the fuel cell is to charge the battery and ultracapacitors during standstill. The choice of cut-off frequency is a trade-off between the sizing of the battery and ultracapacitor. If the frequency is too low, the energy requirement of the ultracapacitor might be too big, and if the frequency is too high the power requirement of the battery becomes too big. By trial-and-error method it turns out, that $f_{LP,Bat} = 20\,\mathrm{mHz}$ provides a sufficient balance between the power and energy distribution of the battery and ultracapacitor.

In Figure 8.6(a) the fuel cell, battery, and ultracapacitor contribution to the load power is shown for case 7 with a fuel cell power rating of $P_{FC,rat} = 2500\,\mathrm{W}$, where both the battery and ultracapacitor are present. It is seen that the fuel cell provides the base power, the battery delivers the power requirement of low frequency, and the

ultracapacitors handle the fast peak powers. Therefore, in this way the ultracapacitors act as a high-pass filter. In Figure 8.6(b) the state-of-charge of the battery is shown. Due to the heating requirement in the start of the plot, i.e. from time $420\,\mathrm{min}$ the load power is high. As the battery in this situation should provide the power, the state-of-charge drops quite fast. At time $426\,\mathrm{min}$ the fuel cell has reached the correct temperature, and therefore it starts to produce power. The fuel cell power rating is sufficient for the shown example, so the battery can be charged while the truck is being used. The ultracapacitor voltage can be seen in Figure 8.6(c). When the truck is in passive mode the ultracapacitor is fully charged.

The proposed energy management strategy shares ideas with the one presented in [1], where a diesel generator, battery, and ultracapacitor hybrid are investigated. In that work the diesel generator is operated at the point where it has the highest efficiency, and the ultracapacitor is also acting as a high pass filter. However, if a fuel cell is operated at the point of maximum efficiency only a small fraction of the power capability is used. Therefore, in order to utilize as much of the nominal power as possible, the fuel cell should try to follow the load. Therefore the "FC-LP-filter" is used.

Charging Strategy

In Figure 8.5 it is shown how the load power is divided between the fuel cell stack, battery, and ultracapacitors. When the state-of-charge of the battery is 1, and the ultracapacitor voltage is below its reference voltage, the fuel cell charges them, provided by availability of extra power. The battery is charged with the current level $2I_{Bat,10}$.

$$p_{Bus,Bat,charge}{}^{*} = \begin{cases} 2I_{Bat,10}v_{Bat} & SoC_{Bat} < 1 \\ 0 & SoC_{Bat} \geq 0 \end{cases} \quad [\mathrm{W}] \tag{8.71}$$

The 10 hour current depends on the number of parallel strings, i.e.

$$I_{Bat,10} = N_{Bat,p}\frac{Q_{Bat,10,Base}}{10\,\mathrm{h}} \quad [\mathrm{A}] \tag{8.72}$$

Due to the health of the ultracapacitors, it is of high importance that they are not overcharged. When the vehicle is used, i.e. active, the ultracapacitors have to capture the braking energy, which means that they should not be fully charged. When the vehicle is active, it is chosen to charge the ultracapacitors to a value between the maximum and minimum voltage, so there is a buffer of equal size for the energy due to braking and accelerating. The ultracapacitor voltage reference is therefore:

$$v_{UC}^{*} = \begin{cases} \frac{V_{UC,max}+V_{UC,min}}{2} & \text{Truck active} \\ V_{UC,max} & \text{Truck inactive} \end{cases} \quad [\mathrm{V}] \tag{8.73}$$

When the truck is inactive the ultracapacitor is charged to the maximum voltage. Thereby the ultracapacitor is fully utilized and an extra buffer is provided for the self discharging

When the ultracapacitors are charged by the fuel cell, the maximum charging power will be the rated fuel cell power $P_{FC,rat}$. For the configurations with both a battery and ultracapacitor, the battery will provide the base power to the loads when

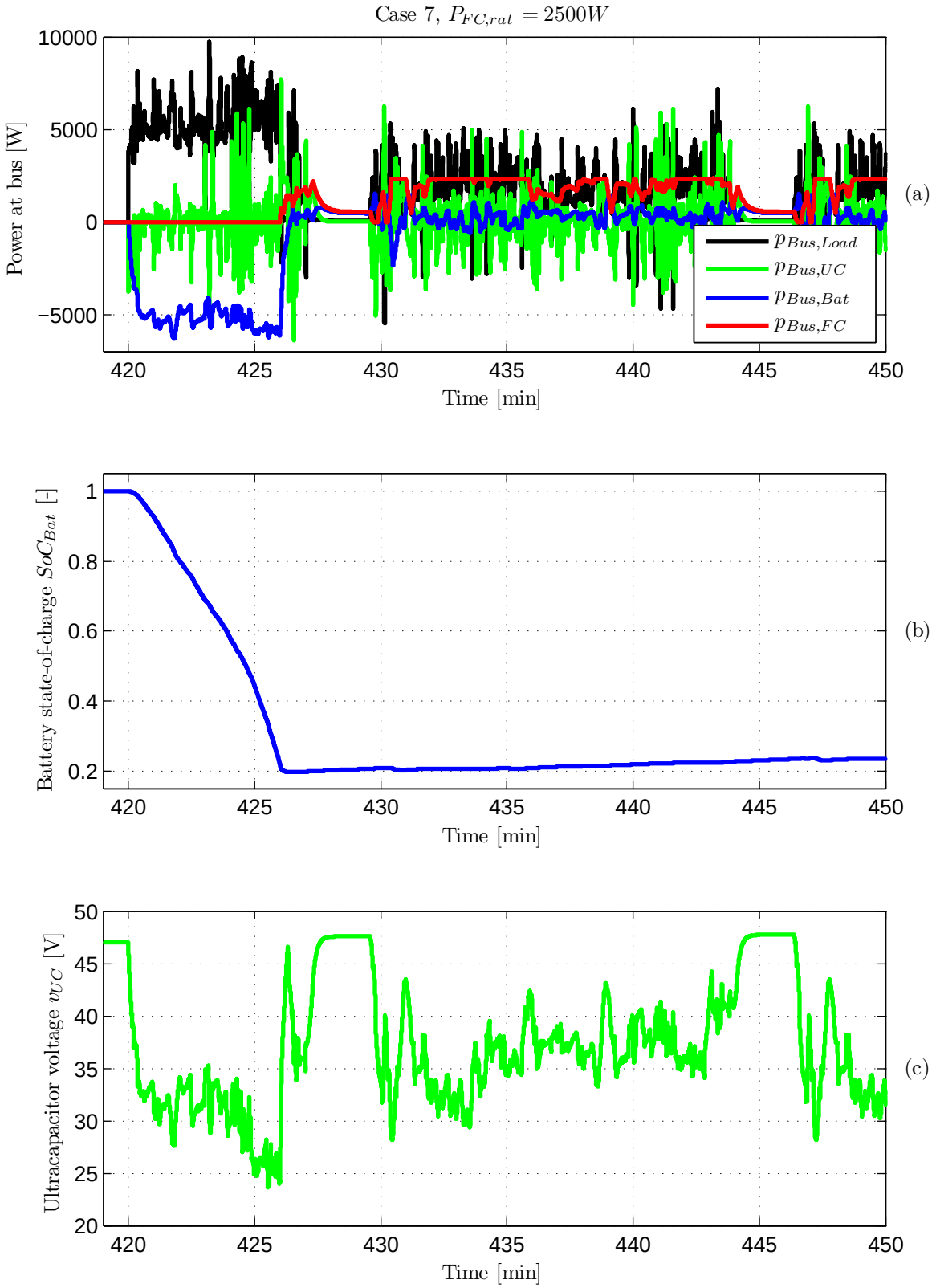

Figure 8.6: Results of applying energy management strategy when both a battery and ultracapacitor acts as energy storage devices. (a) Bus powers. (b) State-of-charge of battery. (c) Ultracapacitor voltage.

the fuel cell is heating-up. In order to reduce the stress of the battery, it is in this situation therefore decided not to charge the ultracapacitors. The charging power is therefore

$$P_{Bus,UC,charge} = \begin{cases} 0 & \text{Heating required} \\ P_{FC,rat} & \text{No heating required} \end{cases} \quad [\text{W}] \qquad (8.74)$$

The proposed energy management strategies in Figure 8.5 suggest that the fuel cell and battery are operated in a smooth way. However, in order to insure that the ultracapacitors are not overcharged, it might be necessary to disconnect them when the voltage approaches $V_{UC,max}$. Thereby the fuel cell or battery will be operated in a discontinuous way, which is not desirable. In order to avoid an abrupt change of power of the fuel cell and battery, the ultracapacitor should stop "asking" for charging power before it reaches the reference voltage v_{UC}^*. The equivalent capacitance of the combination of the series and parallel structure of the ultracapacitor base module is when fully charged given by

$$C_{eq} = \frac{N_{UC,p}}{N_{UC,s}} C_{eq,max,Base} \quad [\text{F}] \qquad (8.75)$$

If it is neglected that the capacitance depends on the actual voltage, the energy that needs to be put into a capacitor with voltage v_{UC} before it is charged to v_{UC}^* is given by

$$E_{UC,charge} = \frac{1}{2} C_{eq} {v_{UC}^*}^2 - \frac{1}{2} C_{eq} {v_{UC}}^2 \quad [\text{J}] \qquad (8.76)$$

Due to the lowpass filters in front of the fuel cell and battery, they will still provide power a few time constants after an inverse step has been applied. This energy should therefore be exactly enough to charge the ultracapacitor to the desired voltage. After the inverse step the output of the lowpass filters is exponentially falling. The energy of this falling power is the initial power times the time constant. Therefore from Equation (8.76), the required charge power at the inverse step should be

$$P_{UC,charge,req} = \begin{cases} \frac{E_{UC,charge}}{\tau_{LP,FC}} & \text{Case 2, 4, and 6} \\ \frac{E_{UC,charge}}{\tau_{LP,Bat}} & \text{Case 7, 8, 9, and 10} \end{cases} \quad [\text{W}] \qquad (8.77)$$

where $\tau_{LP,FC}$ [s] Time constant of the FC-LP-filter
$\tau_{LP,Bat}$ [s] Time constant of the Bat-LP-filter

The ultracapacitor should therefore stop "asking" for power when the power calculated in Equation (8.77) becomes smaller than the actual fuel cell power p_{FC}. The requested ultracapacitor charging power at the bus is therefore

$${p_{Bus,UC,charge}}^* = \begin{cases} P_{Bus,UC,charge} & P_{UC,charge,req} > p_{FC} \\ 0 & |P_{UC,charge,req}| \leq p_{FC} \\ -P_{Bus,UC,charge} & P_{UC,charge,req} < -p_{FC} \end{cases} \quad [\text{W}] \qquad (8.78)$$

Due to the charging energy in Equation (8.76) the requested ultracapacitor charging power at the bus in Equation (8.78) can also be negative. This is useful when the

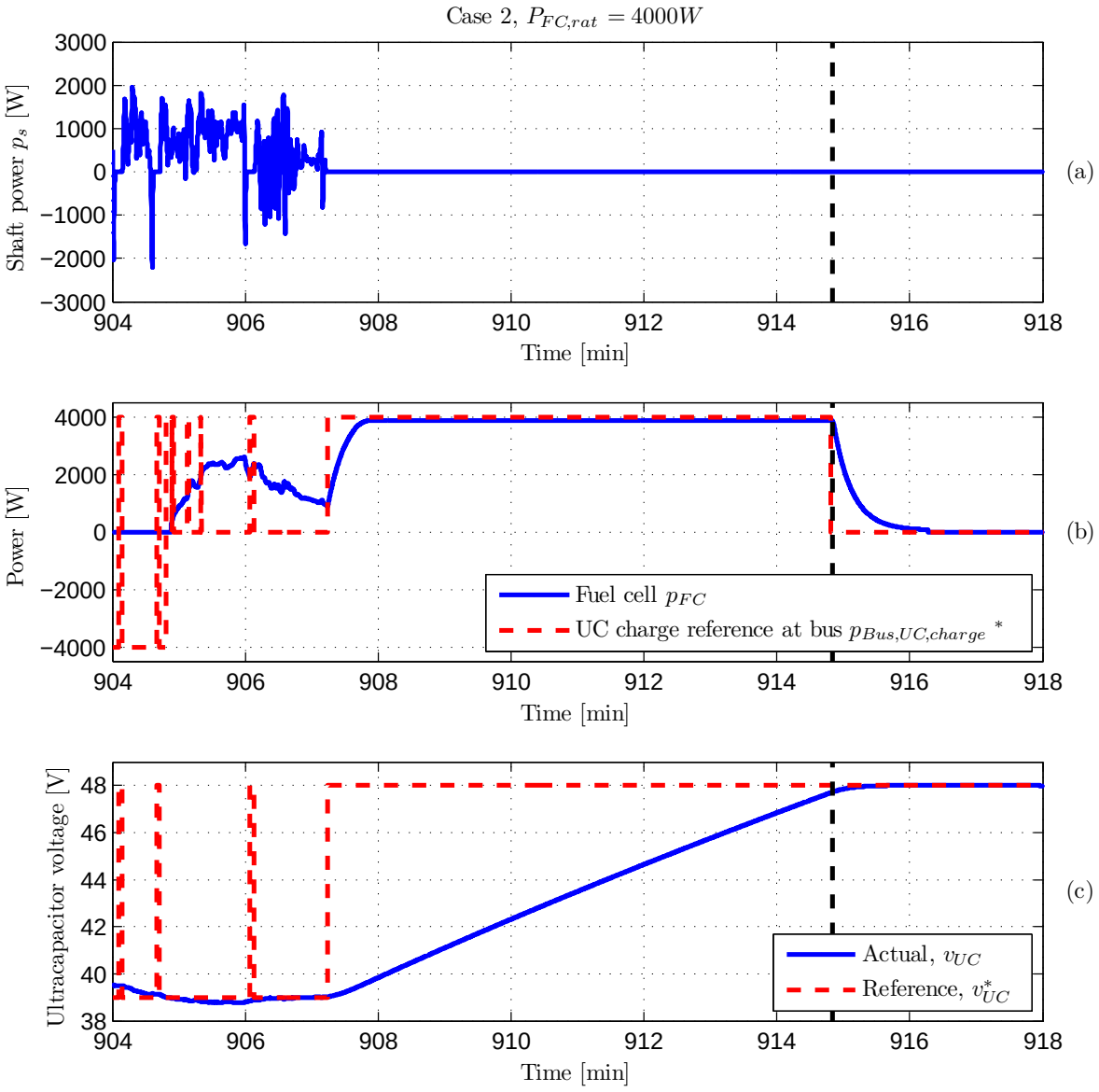

Figure 8.7: Charging strategy for ultracapacitor. Case 2, $P_{FC,rat} = 4000\,\mathrm{W}$. (a) Shaft power. (b) Fuel cell power and ultracapacitor charge reference power at the bus. (c) Actual and reference ultracapacitor voltage.

ultracapacitor voltage is higher than the desired; as the voltage then can be brought down to the desired value faster, so braking energy is not wasted.

In Figure 8.7 it is seen how the charging strategy is applied. It is seen that when the shaft power in Figure 8.7(a) becomes zero, i.e. the truck is passive, the ultracapacitor reference voltage becomes high. In Figure 8.7(b) it is seen that the ultracapacitor charge power at the bus $p_{Bus,UC,charge}{}^{*}$ is high when the actual ultracapacitor voltage v_{UC} is lower than the reference v_{UC}^{*}. It is negative when the actual voltage is higher than the reference, and zero when the required charging power in Equation (8.77) $P_{UC,charge,req}$ is below the actual fuel cell power p_{UC}. At time $t \approx 914.8\,\mathrm{min}$ at the black dashed line it is seen that the charge reference power for the ultracapacitor becomes zero in Figure 8.7(b). As the shaft power in Figure 8.7(a) is zero also, an inverse step is applied to the fuel cell filter "FC-LP-filter". This results in the exponential shape of the fuel cell power in Figure 8.7(b). In Figure 8.7(c) it is seen that the energy due to the exponential fall, is exactly enough to complete the charging of the ultracapacitor.

8.6 Design Strategy

The ten cases of configurations shown in Figure 8.2 will be investigated for different fuel cell stack power ratings. For each case the number of parallel strings of the battery, ultracapacitor or both must be calculated. The number should have a sufficient size, so both the energy and power requirement are fulfilled [75, 89].

Battery Sizing

The maximum power capability of the battery pack is

$$P_{Bat,max} = N_{Bat,s} N_{Bat,p} P_{Bat,max,Base} \quad [\mathrm{W}] \tag{8.79}$$

The minimum allowed state-of-charge of the battery is $SoC_{Bat,min} = 0.2$. If a simulation is performed with a given number $N_{Bat,p}$ it can be verified if the power and energy requirements are fulfilled. If the minimum state-of-charge min (SoC_{Bat}) is less than the required $SoC_{Bat,min}$ or if the maximum discharge power $|\min(p_{Bat})|$ is bigger than the maximum discharge power $P_{Bat,max}$, the battery package is too small, and the number $N_{Bat,p}$ should therefore be increased. This number is denoted $N_{Bat,p,under}$ as it is under the required number. If both requirements on the other hand are fulfilled the number is too big, and should therefore be reduced. This number of parallel strings is therefore denoted $N_{Bat,p,over}$ as it is over the required number $N_{Bat,p}$. The next number for iteration is therefore between the two extremes, i.e.

$$N_{Bat,p} = \frac{N_{Bat,p,under} + N_{Bat,p,over}}{2} \quad [-] \tag{8.80}$$

This procedure is repeated until the calculated number $N_{Bat,p}$ converges to the minimum value where both the energy and power requirements are satisfied, i.e. if

$$0.01 > \frac{N_{Bat,p,over} - N_{Bat,p,under}}{N_{Bat,p}} \tag{8.81}$$

If the inequality in Equation (8.81) is not satisfied, a new iteration will be carried out.

Ultracapacitor Sizing

The maximum power capability of the ultracapacitor is

$$P_{UC,max} = N_{UC,s} N_{UC,p} P_{UC,max,Base} \quad [\mathrm{W}] \tag{8.82}$$

The minimum allowed ultracapacitor voltage, which depends on the configuration of the system, is given in Equation (8.26). As for the battery a simulation is performed with a given number $N_{US,p}$. If this number results in, that either the minimum voltage $\min(v_{UC})$ is below $V_{UC,min}$ or if the maximum power $|\min(p_{UC})|$ is higher than $P_{UC,max}$, the number is denoted $N_{UC,p,under}$. If both requirements are fulfilled it is denoted $N_{UC,p,over}$. The number for the next iteration is calculated in the same way as for the battery, i.e.

$$N_{UC,p} = \frac{N_{UC,p,under} + N_{UC,p,over}}{2} \quad [-] \tag{8.83}$$

The procedure is repeated until the number $N_{UC,p}$ is converged to the smallest number possible, that satisfies the energy and power requirements, i.e. if

$$0.01 > \frac{N_{UC,p,over} - N_{UC,p,under}}{N_{UC,p}} \tag{8.84}$$

When both the battery and ultracapacitor are present in the system, the iterations are performed in two steps in order to make sure that the numbers $N_{Bat,p}$ and $N_{UC,p}$ converges. Therefore for the first step, the number $N_{UC,p}$ is kept to a fixed value, and the number $N_{Bat,p}$ is calculated as described above. When the number $N_{Bat,p}$ converges to the right value, the simulation program is locked with this number, and the program is then searching for the number of the ultracapacitor $N_{UC,p}$ until this number converges.

Design Procedure

A Matlab® / Simulink® design program has been created which is able to design the FCSPP. The procedure of the design program can be seen in Figure 8.8. First one of the ten cases of configurations is selected. Thereby the parameters of the electric machine and inverter are calculated, and afterwards the rated fuel cell stack power $P_{FC,rat}$ is chosen. The parameters of the DC / DC converter, i.e. $R_{Q,Con,FC}$, $R_{Q,Con,Bat}$, and $R_{Q,Con,UC}$, depend on the voltage and current rating of the input and output sides of the converters. These are calculated from a previous simulation result. A new simulation is now performed. The procedure of the simulation is seen on the right in Figure 8.8. The shaft torque τ_s and angular velocity ω_s is applied to the vehicle model, which depends on the chosen configuration of the power system. By using the proposed energy management and charging strategies, the shaft power p_s, i.e. the multiplication of the shaft torque and angular velocity, is directed through the different subsystems of the FC Truck. The outputs of the simulation are the necessary voltages, currents, powers, and state-of-charge of the system. If the chosen configuration contains a battery, it can from the simulated state-of-charge and power of the battery be decided if the number of parallel battery strings is too low, too high, or sufficient. If the configuration contains an ultracapacitor the required number of parallel strings is

calculated from the power and voltage of the ultracapacitor. If the number of parallel strings has not converged yet, a new iteration is performed, i.e. calculate converter parameters from simulation result -> execute a new simulation -> calculate number of parallel strings. When the number of parallel strings converges, the power ratings of the components can be calculated, and the results are stored in a file. The design procedure can now be repeated for another rated fuel cell stack power or another type of configuration.

8.7 Simulation Results

For each combination of the ten cases of configurations and the fuel cell power ratings the different units are sized. For each (i_{case}, $P_{FC,rat}$) combination the total volume, mass, system efficiency, and battery lifetime will therefore be calculated.

Mass and Volume

The total mass and volume of the FCSPP is the mass and volume of the individual components, i.e. the motors, inverters, fuel cell, DC/DC converters, energy storage devices, and hydrogen storage. In Table 8.5 some key parameters used to calculate mass and volume are listed.

Description	Symbol	Value
Fuel cell specific power	SP_{FC}	$131.4\,\mathrm{W/kg}$
Fuel cell power density	PD_{FC}	$62.2\,\mathrm{W/L}$
Battery specific power	SP_{Bat}	$137.1\,\mathrm{W/kg}$
Battery power density	PD_{Bat}	$310.6\,\mathrm{W/L}$
Power electronic specific power	SP_{PE}	$6.8\,\mathrm{kW/kg}$
Power electronics power density	PD_{PE}	$4.9\,\mathrm{kW/L}$
Electric machine specific power [34]	SP_{EM}	$1\,\mathrm{kW/kg}$
Electric machine power density [34]	PD_{EM}	$3.5\,\mathrm{kW/L}$
Hydrogen storage specific energy [49]	SE_{HS}	$1.5\,\mathrm{kWh/kg}$
Hydrogen storage energy density [49]	ED_{HS}	$1.2\,\mathrm{kWh/L}$

Table 8.5: Key numbers used for calculating mass and volume. The specific power and power density of the fuel cell and power electronics are calculated in Chapter 9.

From Equation (8.27) the specific power and power density of the ultracapacitor are

$$SP_{UC} = \frac{P_{UC,max,Base}}{M_{UC,Base}} = \begin{cases} 2.17\,\mathrm{kW/kg} & \text{Case } 2,8 \\ 1.43\,\mathrm{kW/kg} & \text{Case } 4,6,9,10 \end{cases} \tag{8.85}$$

$$PD_{UC} = \frac{P_{UC,max,Base}}{V_{UC,Base}} = \begin{cases} 2.66\,\mathrm{kW/L} & \text{Case } 2,8 \\ 1.74\,\mathrm{kW/L} & \text{Case } 4,6,9,10 \end{cases} \tag{8.86}$$

The energy of the hydrogen can be calculated by integrating the power of the hydrogen p_{H2} from the time where the driving cycle begins until it is finish and the energy storage devices are fully recharged, i.e.

$$E_{H2} = \int \frac{p_{H2}}{3600\,\mathrm{s/h}} dt \qquad [\mathrm{Wh}] \tag{8.87}$$

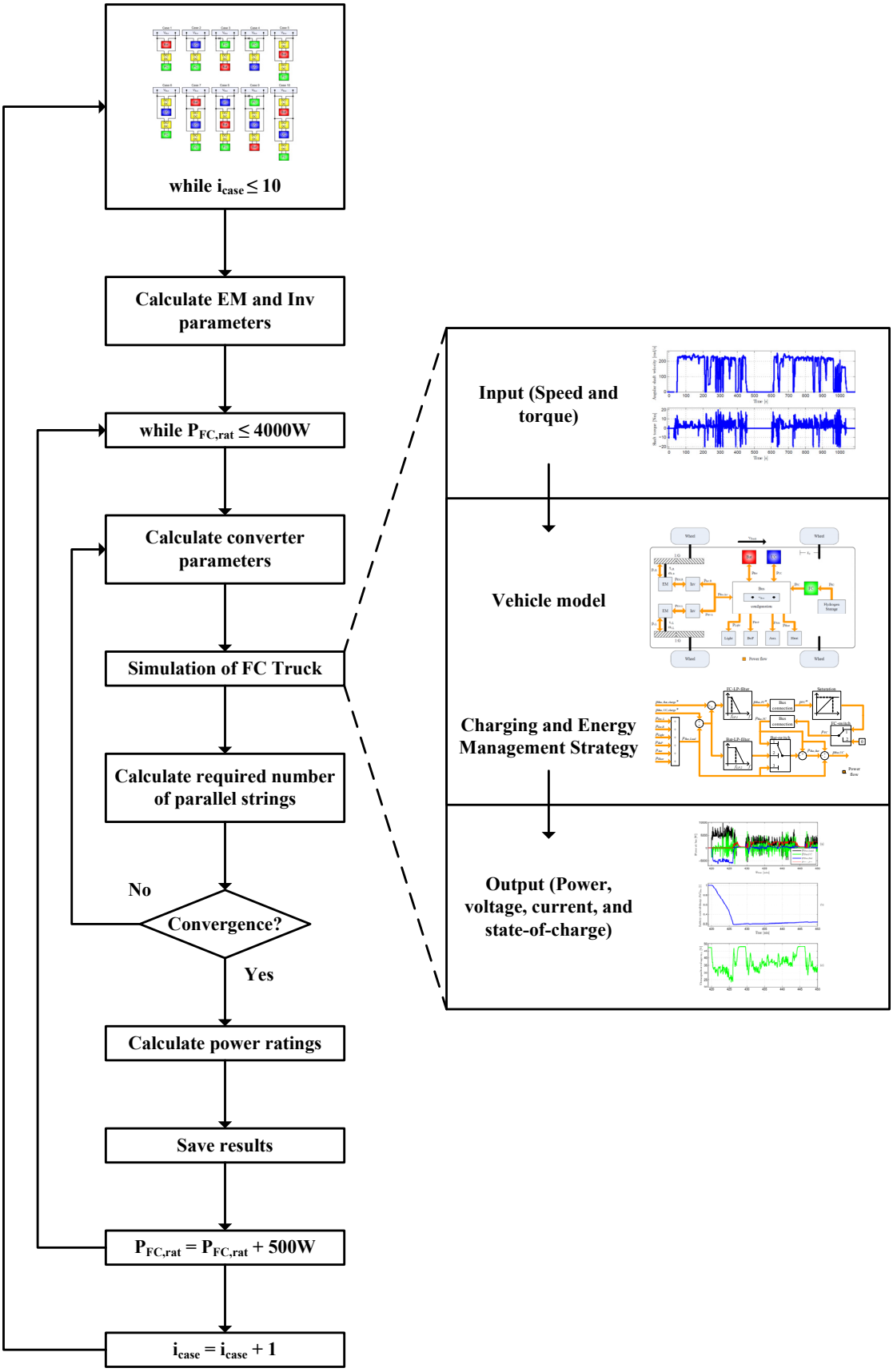

Figure 8.8: Flow chart of design procedure for the FCSPP.

The system volume and mass are therefore

$$V_{sys} = 2\frac{P_{EM,rat}}{PD_{EM}} + \frac{P_{FC,nom}}{PD_{FC}} + \frac{P_{Bat,max}}{PD_{Bat}} + \frac{P_{UC,max}}{PD_{UC}} + \frac{E_{H2}}{SE_{HS}} + \frac{2P_{Inv,rat} + P_{Con,FC,rat} + P_{Con,Bat,rat} + P_{Con,UC,rat}}{PD_{PE}} \quad [\mathrm{L}] \quad (8.88)$$

$$M_{sys} = 2\frac{P_{EM,rat}}{SP_{EM}} + \frac{P_{FC,nom}}{SP_{FC}} + \frac{P_{Bat,max}}{SP_{SP_{Bat}}} + \frac{P_{UC,max}}{SP_{UC}} + \frac{E_{H2}}{SE_{HS}} + \frac{2P_{Inv,rat} + P_{Con,FC,rat} + P_{Con,Bat,rat} + P_{Con,UC,rat}}{PS_{PE}} \quad [\mathrm{kg}] \quad (8.89)$$

These two equations are general for all the ten cases of configurations, and therefore some of the parameters are zero, e.g. in case 1 there is no ultracapacitor included, so $P_{UC,max}$ and $P_{Con,FC,UC,rat}$ are zero when calculating the system volume and mass for case 1.

In Figure 8.9 and Figure 8.10 the mass and volume are shown for the different configurations and fuel cell power ratings. It is seen that the system will be quite heavy and bulky when an ultracapacitor is the only energy storage device, i.e. case 2, 4, and 6. At low fuel cell power ratings the mass and volume is so high that it probably will not be practical feasible. In the design procedure it was assumed that the system mass of the FCSPP will not be bigger than the original battery package of the GMR Truck at $174\,\mathrm{kg}$. However, if the truck should be able to carry the mass of the ultracapacitors for low fuel cell power ratings it will require a bigger amount of power to the motors, which will require more energy, which again will require more storage capacity and the system will therefore be even bigger and heavier.

Except of the cases with pure ultracapacitor, i.e. case 2, 4, and 6, it is from the two figures seen that there are minor differences in the system mass and volume for the different configurations. This is due to the high specific power and power density of the power electronics. What matters is instead the fuel cell power rating, as this has much bigger influence on the system volume and mass.

Due to the heating requirement of the fuel cell there is a minimum amount of energy that must be provided by the energy storage device(s). This minimum energy requirement increases when the fuel cell power rating increases because of the assumption that the energy required for heating is proportional to the fuel cell power rating. This means that for all the configurations there is a threshold where it does not help to increase the fuel cell power rating as it will just increase the energy requirement of the energy storage device(s). This is illustrated in Figure 8.11(a) and Figure 8.12(a) where the mass and volume distribution for case 1 is shown. It is seen that for $P_{FC,rat} = 500\,\mathrm{W}$ the mass and volume of the battery M_{Bat} and V_{Bat}, respectively are very big, and the mass and volume of the fuel cell is quite small. Increasing the fuel cell power rating also increases the mass and volume of the fuel cell M_{FC} and V_{FC}, respectively, but the mass and volume of the battery are reduced even more, and the system mass and volume are therefore reduced. However, for fuel cell power ratings higher than $P_{FC,rat} = 2500\,\mathrm{W}$ it is seen that both the mass and volume of the battery and fuel cell increases, and therefore the system mass and volume also increases. In Figure 8.11(b) and Figure 8.12(b) it is seen that it does not help much on the system mass and volume to introduce an ultracapacitor. It can be seen that the

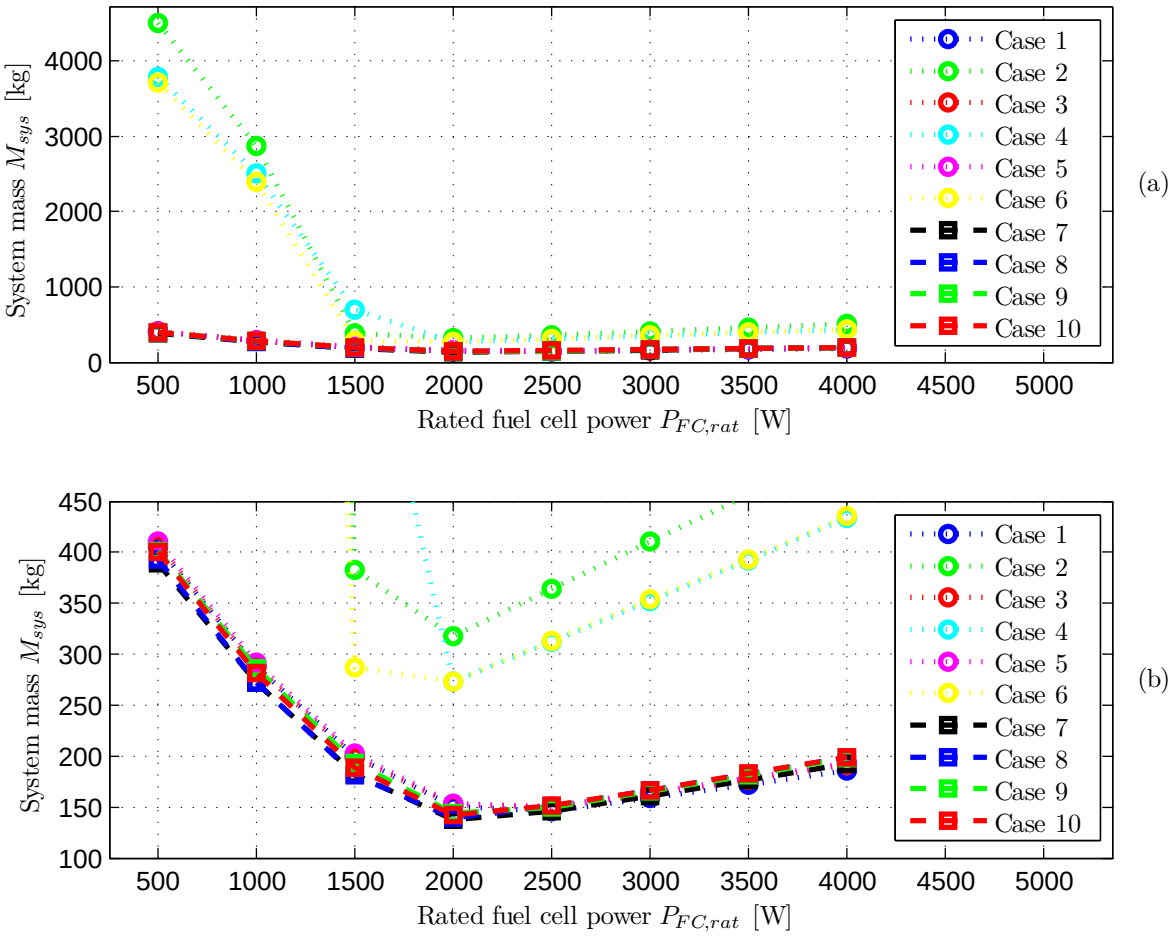

Figure 8.9: System mass of FCSPP. (b) Zoom.

mass and volume of the ultracapacitor M_{UC} and V_{UC}, respectively, actually increases a little bit when the fuel cell power rating increases. This is due to the energy management strategy, where the fuel cell is operated in a smooth manner. Therefore, when one is braking the ultracapacitor has to handle both the braking energy, but also the energy from the fuel cell in a short period, until it is directed to the battery. A more sophisticated energy management strategy might be able to handle this issue. The third biggest contributor of the system mass and volume is the hydrogen storage M_{HS}. The mass and volume of the power electronics M_{PE} and V_{PE}, respectively, and electric machines M_{EM} and V_{EM}, respectively, hardly can be noticed.

System Efficiency

The energy delivered to the shaft is also obtained by integrating the power. Therefore

$$E_s = \int \frac{p_s}{3600\,\mathrm{s/h}} dt \qquad [\mathrm{Wh}] \tag{8.90}$$

The total efficiency of the FCSPP is therefore the ratio of the energy of the shafts

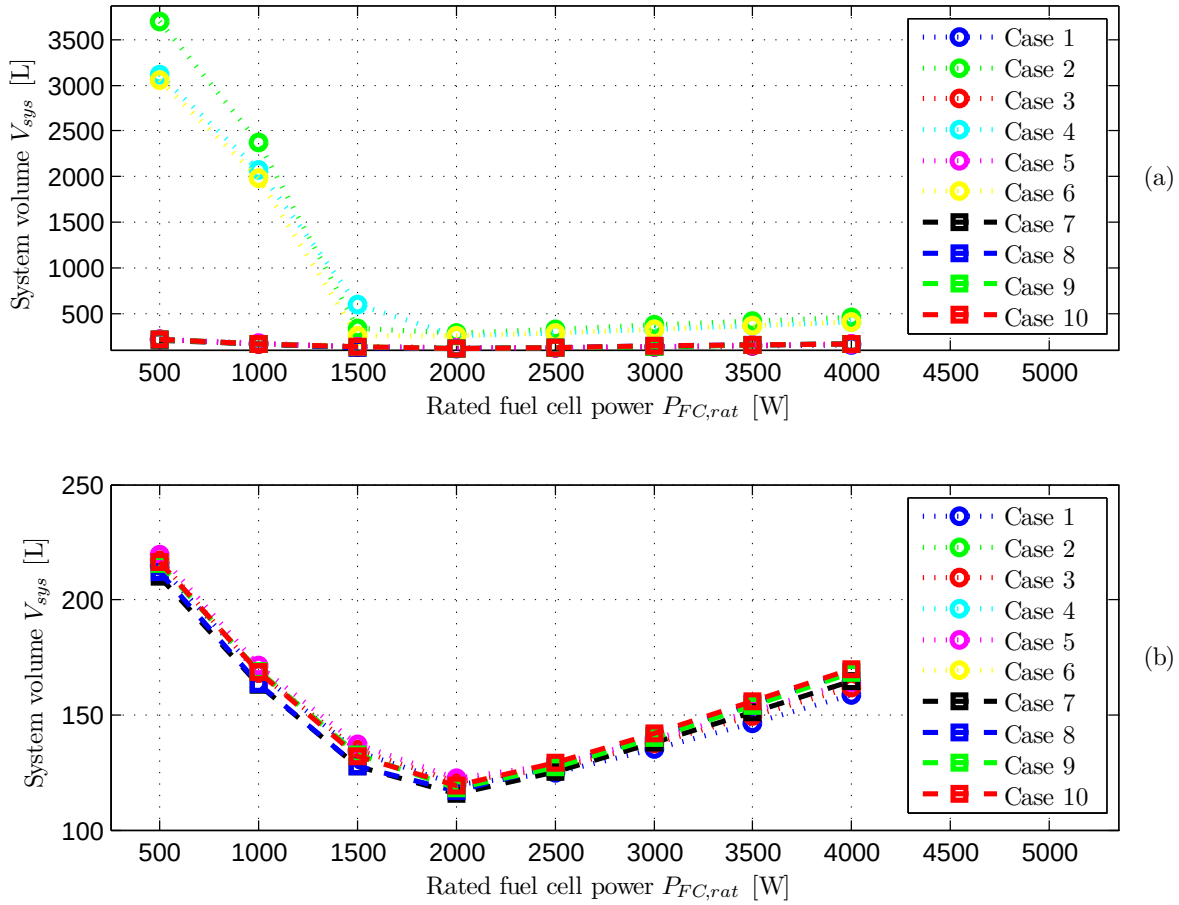

Figure 8.10: System volume of FCSPP. (b) Zoom.

relative to the consumed hydrogen energy, i.e.

$$\eta_{sys} = \frac{2E_s}{E_{H2}} \qquad [-] \tag{8.91}$$

The multiplication of two is due to the two motors of the truck. In Figure 8.13 the system efficiency of the ten cases of configurations for different fuel cell power ratings are seen. It is noticed that generally the efficiency is lower when the fuel cell power is low. There are two reasons for this. The first is because the fuel cell then is operating at its maximum or rated power all the time, where it has the lowest efficiency, and the second reason is that it takes longer time to recharge the energy storage device(s), which means that the power consumption of the auxiliary devices becomes dominating. The configurations where the battery is the only energy storage device provide the lowest efficiency, i.e. case 1, 3, and 5. The system efficiency is improved if the energy storage devices consist of both a battery and an ultracapacitor, i.e. case 7, 8, 9, and 10. However, the highest efficiency is obtained if the ultracapacitor is the only energy storage device, i.e. case 2, 4, and 6. Despite of the relatively high self discharge rate when fully charged the high efficiency of the ultracapacitor results therefore also in the highest system efficiency. For the three choices of energy storage devices, i.e. pure battery, pure ultracapacitor, or a combination of both, it is also seen that the ef-

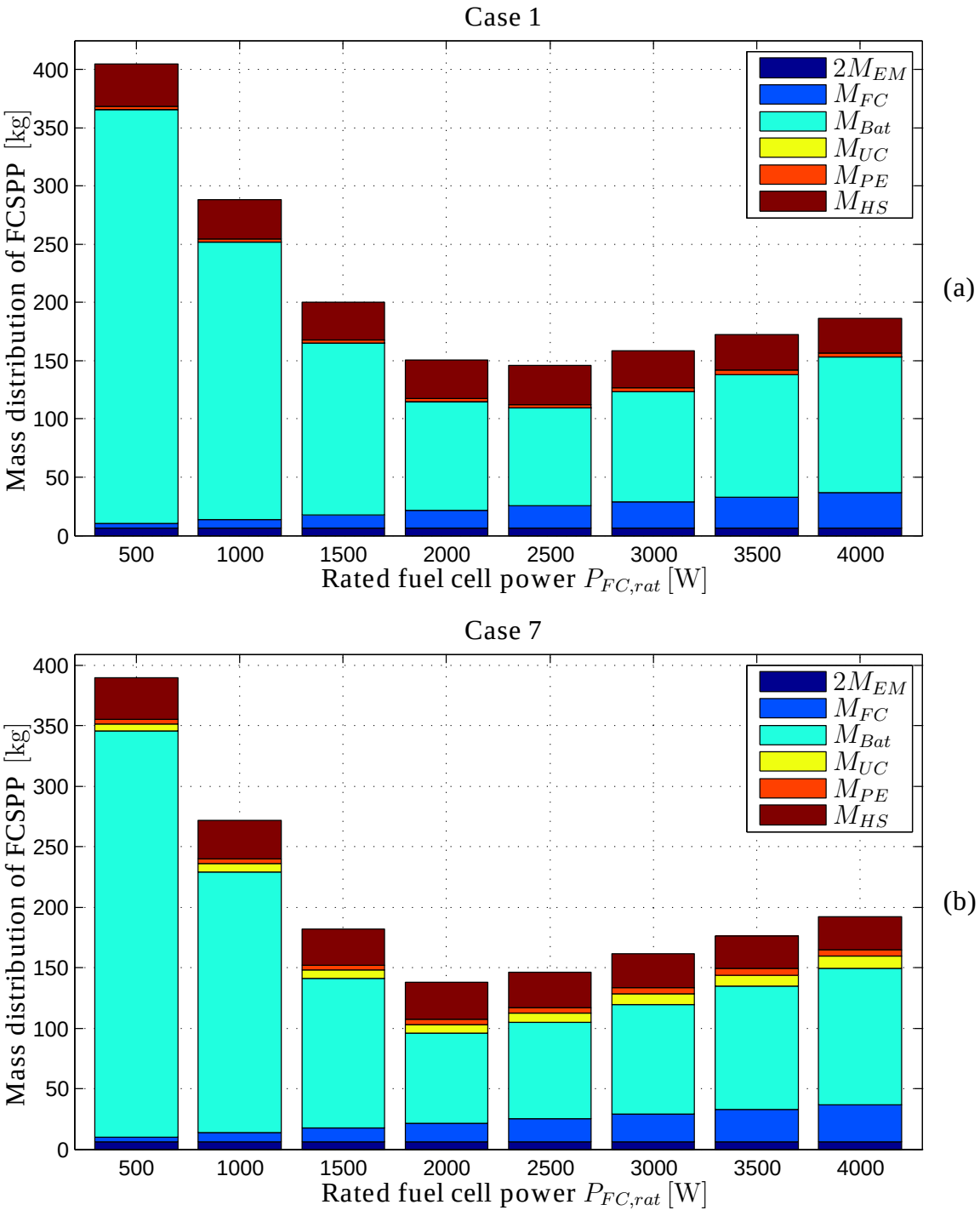

Figure 8.11: Mass distribution of FCSPP. (a) Case 1, pure battery. (b) Case 7, battery and ultracapacitor.

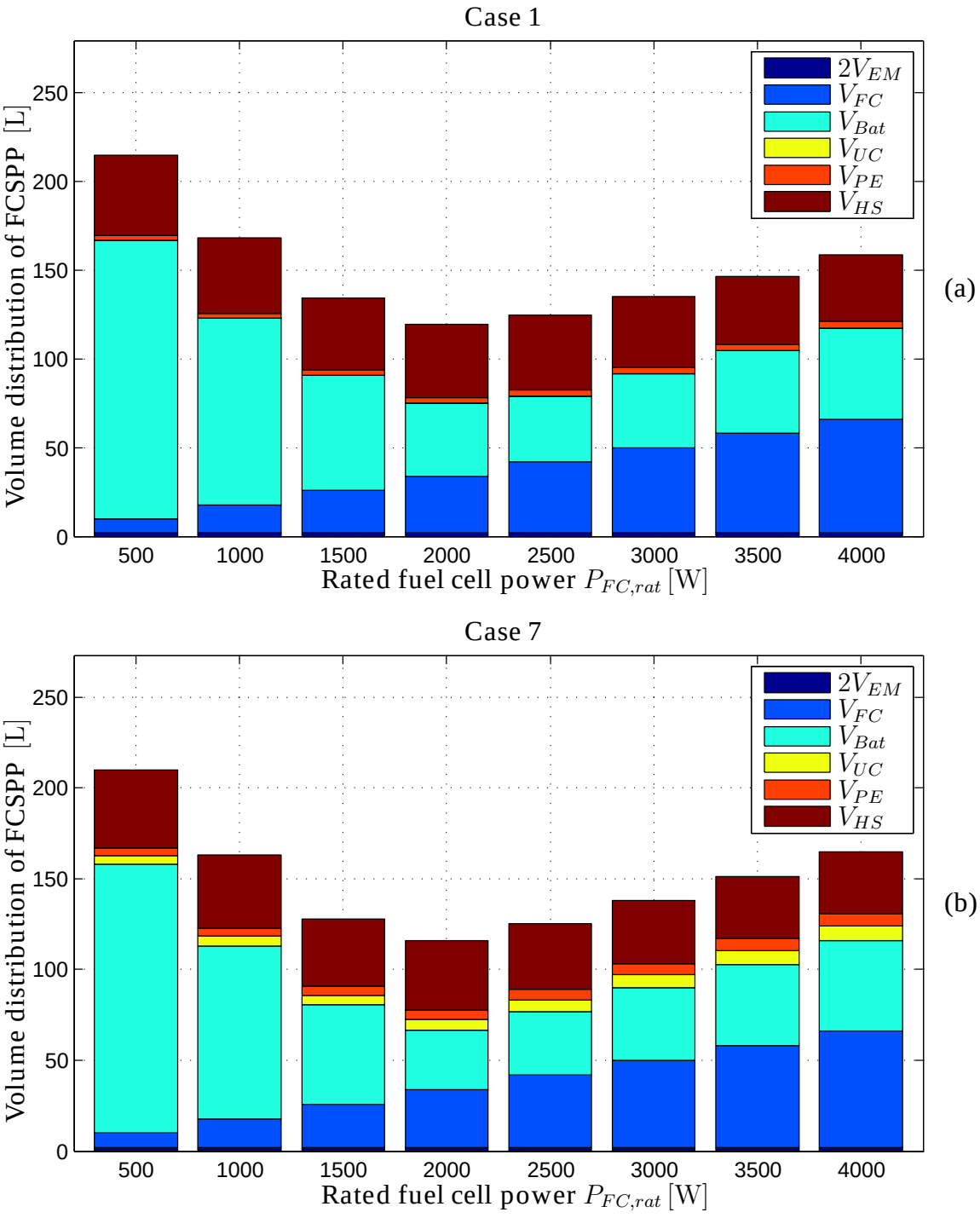

Figure 8.12: Volume distribution of FCSPP. (a) Case 1, pure battery. (b) Case 7, battery and ultracapacitor.

ficiency is highest when the fuel cell is directly on the bus. This is because the "path" from the fuel cell to the loads is shorter, as there is no loss providing DC / DC converter between the fuel cell and the bus. However, the main reason for the higher efficiency when the fuel cell is directly connected to the bus voltage is, that the minimum allowed bus voltage of the 42V PowerNet is $V_{Bus,min} = 30\,\mathrm{V}$, which is higher than the nominal voltage of the fuel cell $V_{FC,nom} = 26.8\,\mathrm{V}$. When the fuel cell is directly on the bus, the fuel cell therefore cannot be operated at its rated power, as the bus voltage otherwise will be lower than allowed. The full potential of the fuel cell is therefore not utilized, but it is operated at a higher point of efficiency, which also will give higher system efficiency.

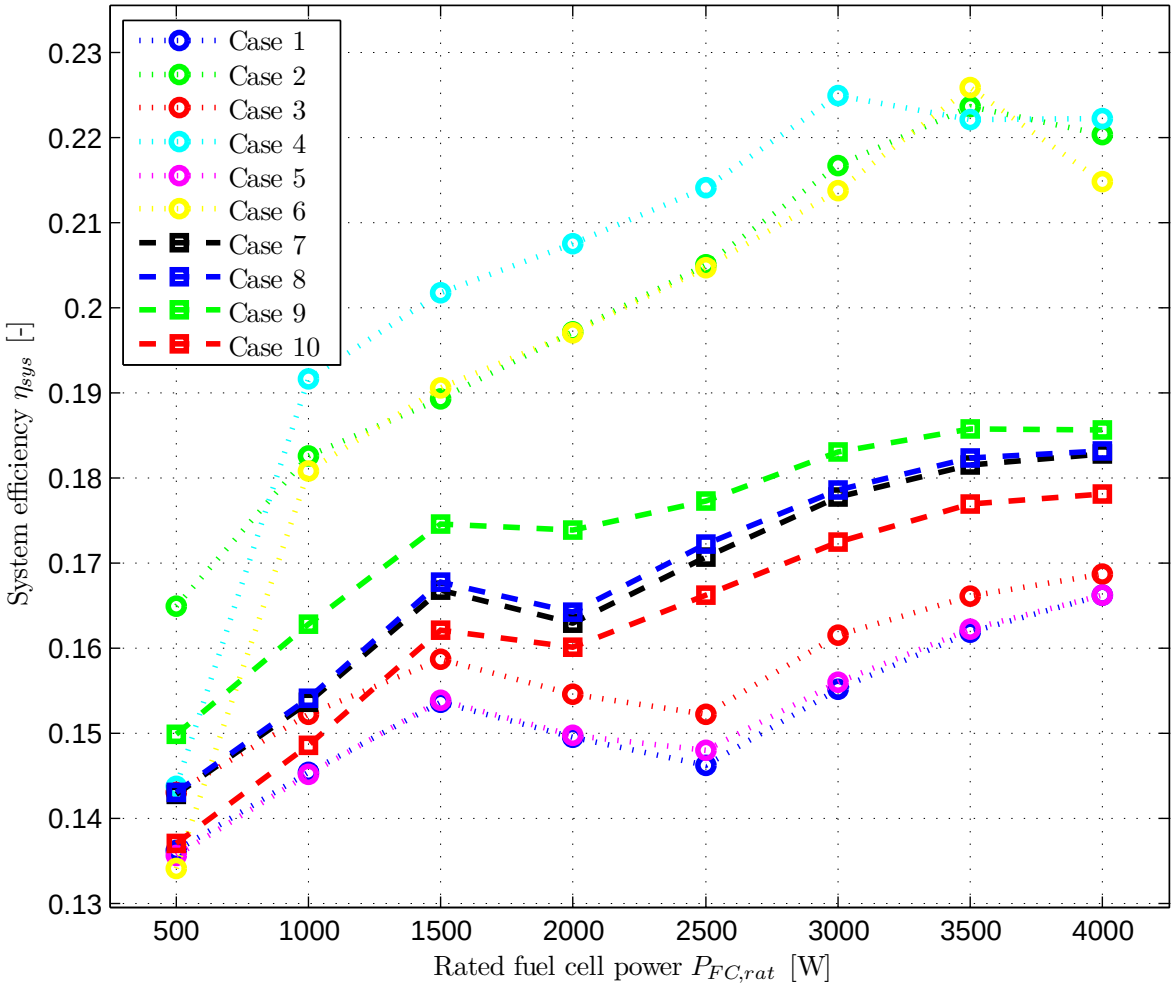

Figure 8.13: System efficiency for the ten cases of configuration with different fuel cell power ratings.

In order to investigate how the fuel cell power rating effects the efficiency of the system, the energy loss of each device is shown in Figure 8.14 for case 1 and 7. The energy delivered to the shafts, $2E_s$ is also shown in the plot in order to compare the loss relative to the useful consumption. If all the contributions of energy of each bar are added together, the result will be the total energy of the hydrogen E_{H2}, which in

the end provides the energy for all the losses.

It is seen that most of the power is lost inside the fuel cell. However, the higher power rating of the fuel cell, the less is lost in the fuel cell, as the time where it operates at full power (with lowest efficiency) then becomes shorter. In Figure 8.14(a) it is seen that a relatively high amount of energy is wasted in the battery. In Figure 8.14(b) it is seen that the loss in the battery is reduced by utilizing ultracapacitors. For both cases it is seen that the energy loss due to the auxiliary devices are becoming smaller the higher fuel cell power rating. This is because the higher fuel cell power, the faster the energy storage devices can be recharged, and thereby the constant power loss due to the auxiliary devices are not present so long time.

From Figure 8.11 it was seen that the minimum battery mass is obtained for a fuel cell power rating of $P_{FC,rat} = 2500\,\mathrm{W}$ for case 1, and $P_{FC,rat} = 2000\,\mathrm{W}$ for case 7. When investigating the energy distribution for the same two cases in Figure 8.14, it is noticed that for the fuel cell power rating that provided the lowest battery mass, i.e. $P_{FC,rat} = 2500\,\mathrm{W}$ for case 1 and $P_{FC,rat} = 2000\,\mathrm{W}$ for case 7, the energy loss in the battery is biggest also. This is because of the Peukert equation. For the same terminal current of the battery, the more Ah is "lost" the smaller the Ah-rating of the battery is. If the Ah-rating of the battery on the other hand is very big, the amount of charging energy needed to compensate for the drawn current is smaller.

Battery Lifetime

The last thing to compare is the battery lifetime, which is calculated for the cases which contain a battery. The results are shown in Figure 8.15. It is seen that the battery lifetime generally is low. It is also seen that combining a battery and ultracapacitor increases the battery lifetime.

To better understand Figure 8.15 a histogram for case 1 and 7, for two different fuel cell power ratings are shown in Figure 8.16. For the low fuel cell power rating it is for both cases of configurations seen that the battery only contains a few deep cycles and shallow cycles. However, when the fuel cell power rating is increased the battery becomes smaller due to the lower energy requirement (until a certain point). This means that for the case where the battery is the only energy storage device the load powers due to the accelerations and decelerations of the truck becomes bigger relative to the battery capacity $Q_{Bat,10}$. Therefore, they now affect the depth-of-discharge curve of the battery, which affects the battery lifetime. Even though these shallow cycles have low amplitude, they are reducing the lifetime because they are repeated many times. In Figure 8.16(d) the advantages of combining an ultracapacitor with a battery clearly can be seen. Even though the battery approximately has the same size as in Figure 8.16(b), the battery in this configuration does not see all the shallow cycles as they are directed to the ultracapacitor. It may be noticed that the data sheet did not contain any information regarding the lifetime for cycles less than $DoD_{Bat} = 0.2$. For cycles below this amplitude the cycles-to-failure is based on extrapolations of the (DoD_{Bat}, $N_{Bat,ctf}$)-curve. It is therefore not sure that the very small cycles will affect the battery lifetime. In [8] the lifetime is for example modeled by an exponential function, which means that the battery should be able to handle more shallow cycles with this exponential model, than the model used in this work, i.e. a fourth order polynomial. If the small cycles can be neglected, the battery lifetime will not be improved by

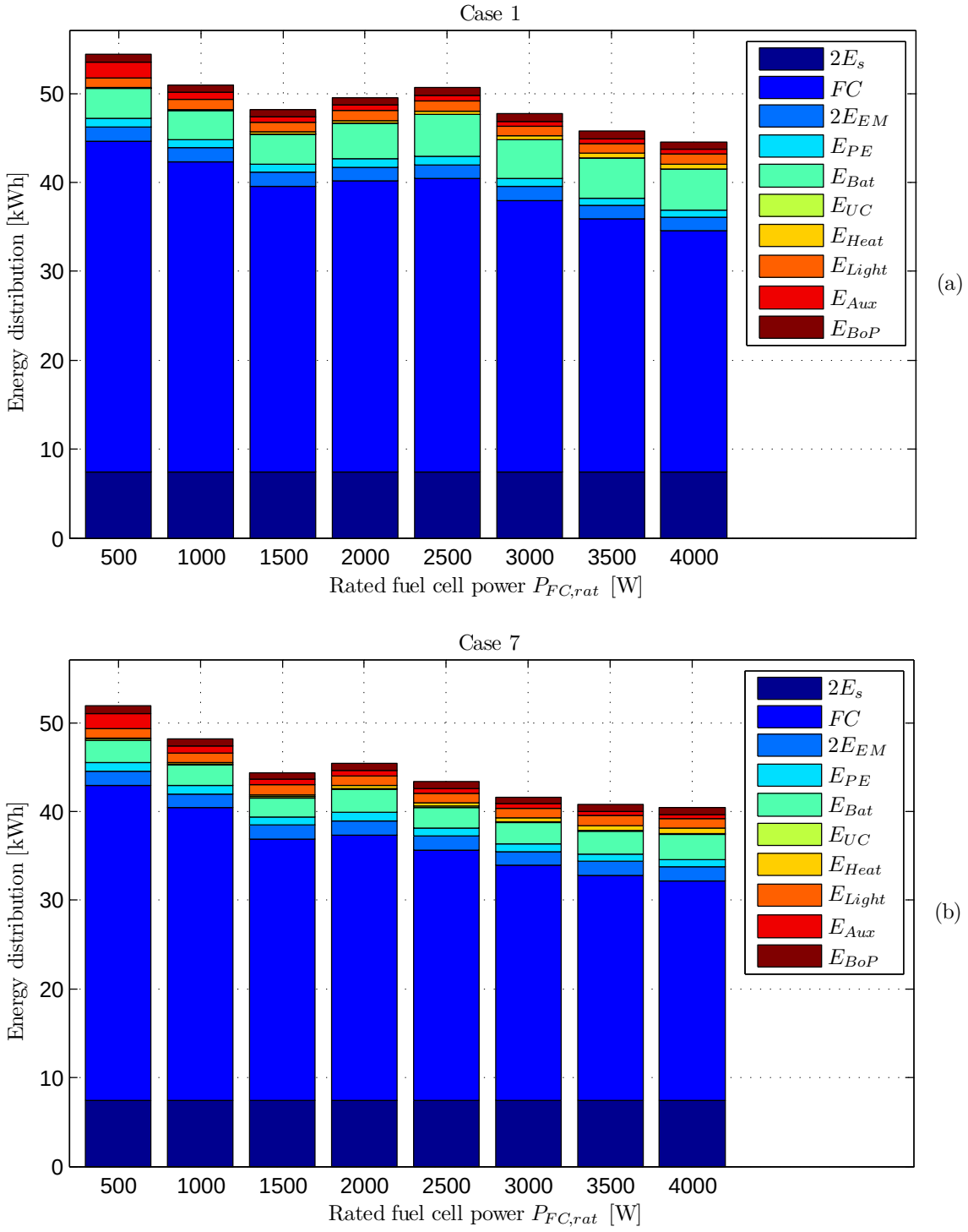

Figure 8.14: Energy distribution for different fuel cell power ratings. (a) Case 1. (b) Case 7.

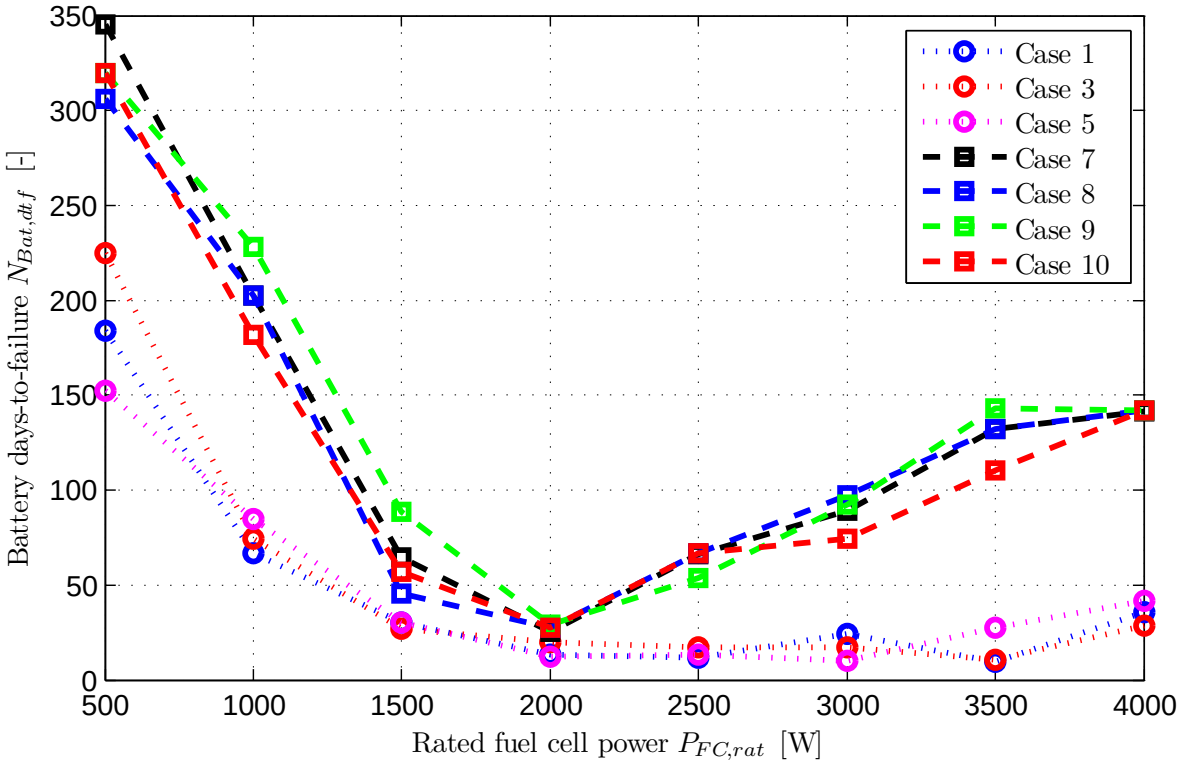

Figure 8.15: Days-to-failure of battery.

adding ultracapacitors. However, more investigation of the battery lifetime is therefore necessary.

The used driving cycle consists of one short driving cycle which is repeated many times. Therefore, the battery is discharged to only a few depth-of-discharge values. In the design procedure it is strived to minimize the rating of the battery and / or ultracapacitor. This provides a small and light system volume and mass, but as it has been shown, minimizing the battery has not a positive effect on the system efficiency and battery lifetime. Therefore it have in [71] been investigated what will happen if the battery or ultracapacitor is overrated, i.e. they have a bigger energy capacity than needed. It turns out that overrating the battery has a very positive effect on the battery lifetime, without making the system too big or heavy.

8.8 System Selection

Ten different configurations have been compared for 8 different fuel cell power ratings, and the most appropriate system should therefore be selected for implementation. The best system of course depends on which parameters are important, e.g. mass, volume, efficiency, lifetime, cost, maintenance, etc. In this research only volume, mass, efficiency, and battery lifetime have been considered. The original GMR Truck had a battery package with a five hour capacity of $E_5 = 36\,\mathrm{V} Q_5 = 6.48\,\mathrm{kWh}$, a volume of $76.2\,\mathrm{L}$, and mass of $174\,\mathrm{kg}$. The FC Truck is designed to deliver $2E_s = 7.4\,\mathrm{kWh}$ to the motor shafts over a time interval of eight hours. This is even more energy than the original GMR Truck was able to deliver, but in the beginning of the thesis it was also

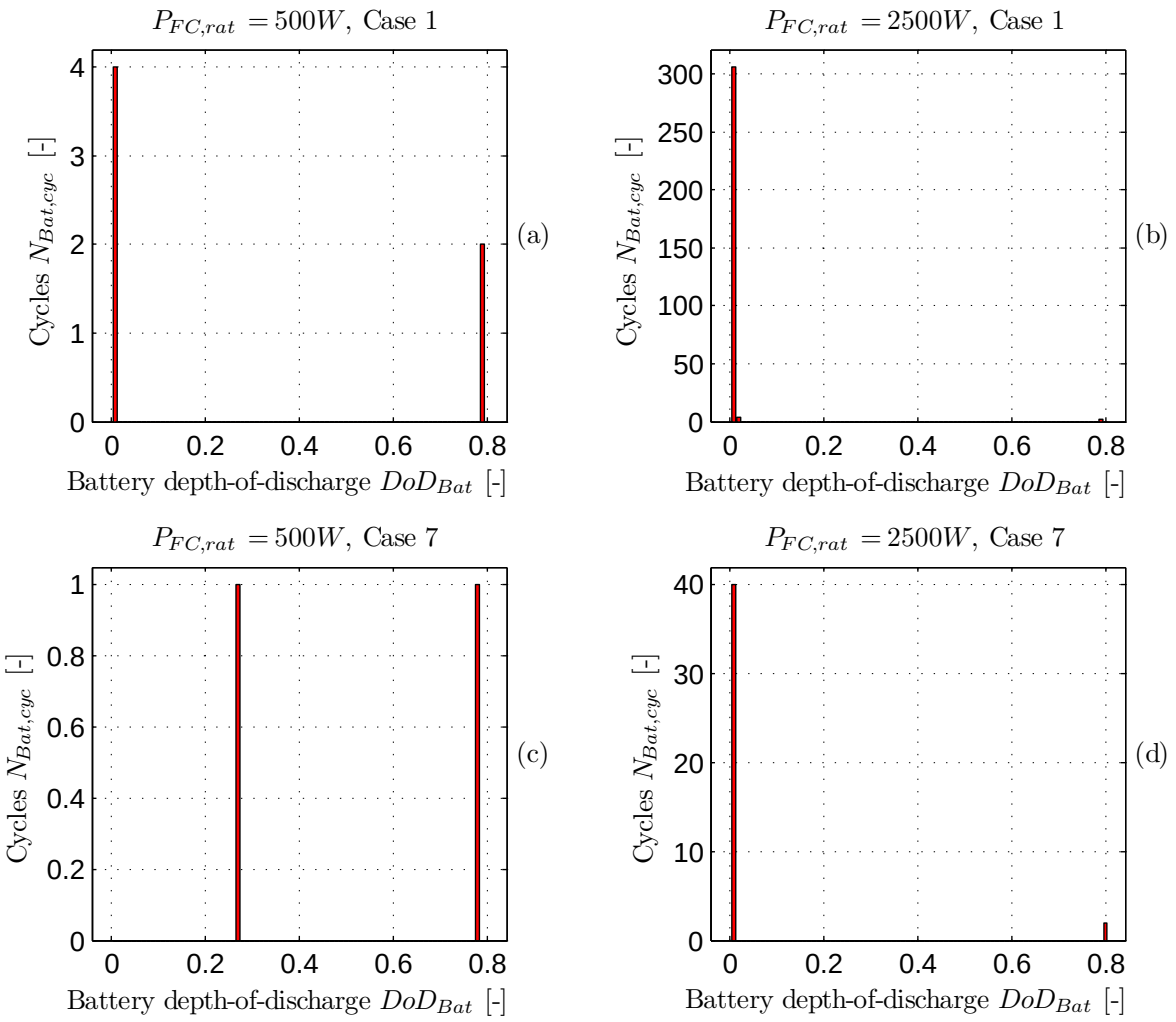

Figure 8.16: Cycles versus depth-of-discharge. (a) Case 1, $P_{FC,rat} = 500\,\mathrm{W}$. (b) Case 1, $P_{FC,rat} = 2500\,\mathrm{W}$. (c) Case 7, $P_{FC,rat} = 500\,\mathrm{W}$. (d) Case 7, $P_{FC,rat} = 2500\,\mathrm{W}$.

stated that the performance of the FC Truck should be better than the original GMR Truck. If the system mass should be less than $174\,\mathrm{kg}$ it is from Figure 8.9(b) seen that only case 1, 3, 5, 7, 8, 9, and 10 for a fuel cell power rating of $2000\,\mathrm{W} \leq P_{FC,rat} \leq 3000\,\mathrm{W}$ are able to satisfy this criteria. For the system volume it is in Figure 8.10 however seen, that none of the configurations are able to provide a system volume below $76.2\,\mathrm{L}$ due to the high volume of the battery, fuel cell, and hydrogen storage. A liquid fuel, e.g. methanol or another type of battery might be able to reduce the system volume, but this is left for future work. For the possibilities left, i.e. case 1, 3, 5, 7, 8, 9, and 10 for $2000\,\mathrm{W} \leq P_{FC,rat} \leq 3000\,\mathrm{W}$, it is in Figure 8.13 and 8.15 seen that the pure battery solutions, i.e. case 1, 3, and 5, have both the lowest system efficiency and battery lifetime. For this reason these three cases should be omitted, which means that only case 7, 8, 9, and 10 for a fuel cell power rating of $2000\,\mathrm{W} \leq P_{FC,rat} \leq 3000\,\mathrm{W}$ are left. In Figure 8.13 and 8.15 it is also seen that $P_{FC,rat} = 3000\,\mathrm{W}$ provides a higher efficiency and battery lifetime than the two other fuel cell power ratings. The "best" solution is therefore either case 7, 8, 9, or 10 for a fuel cell power rating of $P_{FC,rat} = 3000\,\mathrm{W}$. Case

8 has the second highest efficiency and the highest battery lifetime. Case 9 has the highest efficiency and second highest battery lifetime. The preferred solution is therefore one of these two cases for a fuel cell power rating of $P_{FC,rat} = 3000\,\mathrm{W}$. However, it is strongly highlighted that this assessment is based on the pure lifetime modeling of the battery. If it turns out that the shallow cycle has none or less influence than approximated, the conclusion might be different.

8.9 Conclusion

In this chapter a method to design a FCSPP for the FC Truck has been presented. A model of the FC Truck has been created in Matlab® / Simulink®. The model consists of the models of each item, i.e. a model of the fuel cell, electric machines, inverters, energy storage devices, and DC / DC converters. The input to the fuel cell truck model is the driving cycle presented earlier. The driving cycle consists of the shaft angular velocity and torque of the electric machines. The fuel cell system should also provide power to other loads on the FC Truck, these loads are the light, auxiliary devices, balance-of-plant of the fuel cell system, and a heater used for heating the fuel cell stack. These extra loads are also included in the fuel cell truck model. Three different scenarios of energy storage devices have been considered, i.e. pure battery, pure ultracapacitor, and both units combined. It is chosen to comply to the 42V PowerNet standard, which provides limitations of the bus voltage.

Ten different configurations of connecting a fuel cell and an energy storage device to a common bus have been investigated for different fuel cell power ratings. In some of the configurations a given device, i.e. the fuel cell stack or battery package, is connected to the bus directly or through a DC / DC converter.

An energy management strategy that sufficiently divides the load power between the fuel cell and energy storage device(s) has been proposed. The energy management strategy uses low pass filters to insure that the power of the fuel cell (and also battery when an ultracapacitor is present) is smooth, so the stress is reduced. When a battery and ultracapacitor are combined the ultracapacitor acts as a high pass filter, which handles all the peak powers due to accelerations and decelerations. A charging strategy has also been proposed, which charges the energy storage devices when the fuel cell can provide the necessary power.

A design procedure of sizing the energy storage devices is presented. The energy storage devices have to fulfill both an energy requirement and a power requirement. The program calculates the minimum required number of parallel strings that is necessary in order to fulfill the energy and power requirements. This is done in an iterative process where a simulation of the FC Truck is performed, parameters are thereby calculated, and a new simulation is executed. This is repeated until the parameters converge. A system has been designed for ten cases of configurations for different fuel cell power ratings.

The system volume, mass, efficiency, and battery lifetime have been calculated for each combination of the ten configurations and fuel cell power ratings. Due to the relatively long and energy consuming required heating of the fuel cell stack, the energy requirement of the energy storage device(s) is so big, that it will not be feasible to use an ultracapacitor as the only energy storage device, as the system simply will be too big and heavy, even though a pure ultracapacitor solution provides the highest

system efficiency of the different configurations. In turns of system mass and volume no significant improvement is obtained by combining a battery with an ultracapacitor, again due to the relatively high energy requirement.

Increasing the fuel cell power rating also increases the system efficiency. A higher fuel cell power rating also reduces the energy requirement of the energy storage devices, but only until a certain point. A relatively large amount of energy is lost in the battery, which results in a low efficiency when the battery is the only energy storage device. Adding an ultracapacitor improves the efficiency.

Increasing the fuel cell power rating has a positive effect on the system mass and volume (until a certain point) and efficiency. However, it does not have a positive effect on the battery lifetime when the battery is the only energy storage device, as all the partial cycles reduce the lifetime. Combining the battery with an ultracapacitor improves the lifetime significant, as the ultracapacitor is able to handle the partial cycles. However, the data sheet of the battery provides no information regarding the lifetime of partial cycles, and these are therefore based on extrapolations. The battery lifetime at partial cycles must therefore be investigated before it can be concluded that the lifetime are improved by adding ultracapacitors.

8.10 DISCUSSION

In the design method the fuel cell power is given, and the rating of the energy storage device(s) is then calculated, based on the energy and power requirements. In this research it is strived to minimize the rating of the energy storage devices, e.g. the battery is designed to have a minimum state-of-charge of $SoC_{Bat,min} = 0.2$. When the fuel cell power rating is increased the energy requirement of the energy storage device is decreased (until a certain point of the fuel cell power rating, due to the increased energy requirement for the heating). It turns out that the partial cycles are critical for the battery lifetime. The energy storage devices therefore cannot be rated due to the energy and power requirement alone, and the battery lifetime should therefore be included in the procedure of selecting the proper battery rating.

As already mentioned the data sheet of the used battery contains huge uncertainties of the cycle-to-failure for partial cycles below a depth-of-discharge of $DoD_{Bat} = 0.2$. The effect of these shallow cycles should therefore be investigated. The lead-acid battery also suffers from a low lifetime in general. In [54] the cycle-to-failure of a NiMH has been specified to $N_{ctf} = 8 \cdot 10^5$ for a depth-of-discharge of $DoD_{Bat} = 0.05$, and $N_{ctf} = 1400$ for $DoD_{Bat} = 1$. In [48] the cycles-to-failure have been specified to $N_{ctf} = 3000$ for a depth-of-discharge of $DoD_{Bat} = 0.82$ and $DoD_{Bat} = 0.6$ for a NiMH and LiIon battery, respectively. For $N_{ctf} = 40 \cdot 10^3$ the depth-of-discharge is $DoD_{Bat} = 0.15$ for the NiMH and $DoD_{Bat} = 0.1$ for the LiIon. These values are much better than for the lead-acid, and these batteries should therefore be taken into account. However, these batteries are more expensive than the lead-acid batteries, and therefore cost should also be included.

Another argument of including the cost is because of the power electronics. The power electronics have a high power density and efficiency when compared to most of the other components of the FCSPP. This means that the effect of having a DC / DC converter or not, hardly can be seen. In order to assess the influence of the power electronics, the cost should therefore also be included, e.g. the VA-rating of an inverter

is higher when the fuel cell stack or ultracapacitor is connected directly at the bus, than if the bus voltage is kept at a fixed level.

9 Implementation

In this chapter the implementation of the FCSPP in the FC Truck is described. A fuel cell converter that is able to both buck and boost the voltage is used, which means that it also should transit between the two modes in a sufficient manner. Different methods are therefore investigated.

9.1 Overview

Due to the many partners involved in the consortium, the different tasks were carried out in parallel and not in a sequential order. Therefore the construction of the system and collection of components were carried out before the analysis in the previous chapter was finish. This means that some of the ratings, e.g. fuel cell power, battery capacity, and bus voltage, are different than the analysis in the previous chapter suggests.

In Figure 9.1 it is seen how the components are placed in the truck. Two inverters are supplying the two motors of PMSM-type. The inverters are connected directly across a $48\,\mathrm{V}$-battery package, but the fuel cell is connected to the battery package through a DC/DC converter. The battery package consists of four series connected lead-acid battery blocks, which are in parallel with four $16.2\,\mathrm{V}$ ultracapacitor modules. The fuel cell system is controlled by the vehicle controller which is placed just above the stack. The fuel cell converter and vehicle controller are exchanging data through a RS-232 connection. The fuel cell converter measures the fuel cell voltage and current and transmits them to the vehicle controller. The fuel cell voltage and current are used by the vehicle controller to control the fuel cell stack. The vehicle controller sends enable signals to the fuel cell converter, telling the fuel cell converter if it can draw a current or not. When the fuel cell converter is allowed to draw a current, the vehicle controller also tells the fuel cell converter the maximum current allowed. This is useful during the start-up and shut-down procedure [3]. The inverters are operating alone, i.e. no data are exchanged between the inverters and the vehicle controller or fuel cell converter. It is therefore the job of the fuel cell converter to make sure that the proper amount of fuel cell power is directed to the inverters, and thereby to the motors. The fuel cell converter is also charging the battery package when the fuel cell can provide the necessary power.

Fuel Cell Stack

The blue fuel cell stack is from the company Serenergy®. At the front end it is seen how the heater is connected to the stack. The heater is simply a thin wire connected across the battery terminals. To the heater is also attached a blower. The blower has

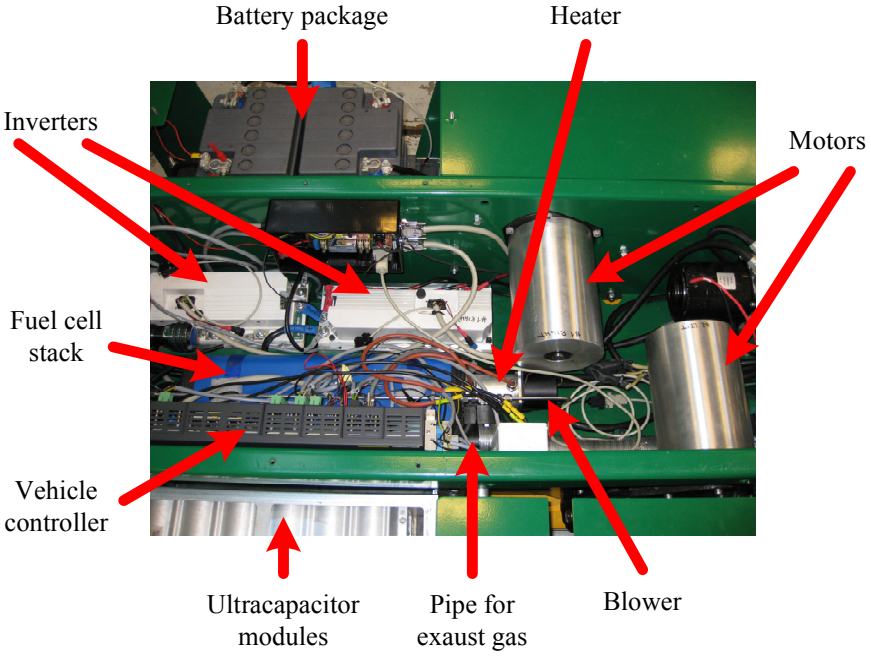

Figure 9.1: GMR FC Truck.

two purposes. The first purpose is to blow the hot air into the stack during heating, and the other purpose is to supply the stack cathode side with air, i.e. oxygen, during normal operation of the fuel cell. Right next to the heater and blower a pipe for exhaust gas is connected. As the temperature for a HTPEM is above $100\,^{\circ}\mathrm{C}$ the exhaust gas is not water, but steam.

The specifications of the fuel cell stack can be seen in Table 9.1. The specific power of the module is $SP_{FC} = \frac{P_{FC,nom}}{M_{FC}} = 131.4\,\mathrm{W/kg}$ and the power density is $PD_{FC} = \frac{P_{Fc,nom}}{V_{FC,nom}} = 62.2\,\mathrm{W/L}$. These values where used in the previous chapter to calculate the system mass and volume.

Manufacturer	Serenergy®
Type	Serenus 166 Air C
Nominal power	$P_{FC,nom} = 920\,\mathrm{W}$
Volume	$V_{FC} = 14.8\,\mathrm{L}$
Mass	$M_{FC} = 7\,\mathrm{kg}$

Table 9.1: Data of the used fuel cell stack.

Inverter

Next to the fuel cell stack the two inverters are placed. The inverters are from Semikron® and they have a built-in Texas Instruments® LF2406A DSP, current sensors, DC-link voltage sensors, DC-link capacitors, protection against short circuit, over current, over voltage, and over temperature, i.e. they have all the required hardware, and they should therefore only be programmed. The specifications can be seen in Table 9.2.

Manufacture	Semikron®
Type	SKAI 6001MD10-1450L
Maximum bus voltage	$V_{Bus,max} = 80\,\mathrm{V}$
Maximum phase RMS current ($< 20\,\mathrm{s}$)	$I_{p,max} = 400\,\mathrm{A}$
Volume	$V_{Inv} = 6.9\,\mathrm{L}$
Mass	$M_{Inv} = 5\,\mathrm{kg}$

Table 9.2: Data of the used inverters.

When using sinusoidal modulation technique the maximum RMS phase voltage is $V_{p,max}\frac{V_{Bus,max}}{2\sqrt{2}} = 28.3\,\mathrm{V}$. This means that the VA-rating of the inverter is $P_{Inv,max} = 3\hat{V}_{p,max}I_{p,max} = 33.96\,\mathrm{kVA}$. The specific power SP_{Inv} and power density PD_{Inv} of the inverter are therefore

$$SP_{Inv} = \frac{P_{Inv,max}}{M_{Inv}} = 6.8\,\mathrm{kW/kg} \tag{9.1}$$

$$PD_{Inv} = \frac{P_{Inv,max}}{V_{Inv}} = 4.9\,\mathrm{kW/L} \tag{9.2}$$

Motors

Rotor and stator are bought as frameless motor kit. However, the motor kit is made for a bus voltage of $340\,\mathrm{V}$, and therefore the stator has been rewound to suit the $48\,\mathrm{V}$ bus level, and afterwards it has been put into a motor frame. The position of the machines is obtained by a sensor bearing. The specifications of the frameless motor kit are shown in Table 9.3.

Bus voltage	$340\,\mathrm{V}$
Line-line inductance	$0.98\,\mathrm{mH}$
Line-line resistance	$0.12\,\Omega$
Maximum speed	$8300\,\mathrm{rpm}$
Nominal speed	$5950\,\mathrm{rpm}$
Maximum continuous torque	$6.53\,\mathrm{Nm}$
Stall torque	$13.06\,\mathrm{Nm}$
Poles	8

Table 9.3: Specifications of frameless motor kit (original parameters and not the parameters of the modified stator).

9.2 Fuel Cell Converter

The fuel cell converter is of the same topology treated in Chapter 6. Its circuit diagram can be seen in Figure 9.2.

The converter realization can be seen in Figure 9.3. The converter is inserted in a box with transparency walls. The converter consists of two layers. The bottom layer is the physical implementation of the equivalent circuit diagram in Figure 6.1. The top layer consists of several units, e.g. a supply board that provides voltages of different levels, a measurement board that measures the required voltages and currents,

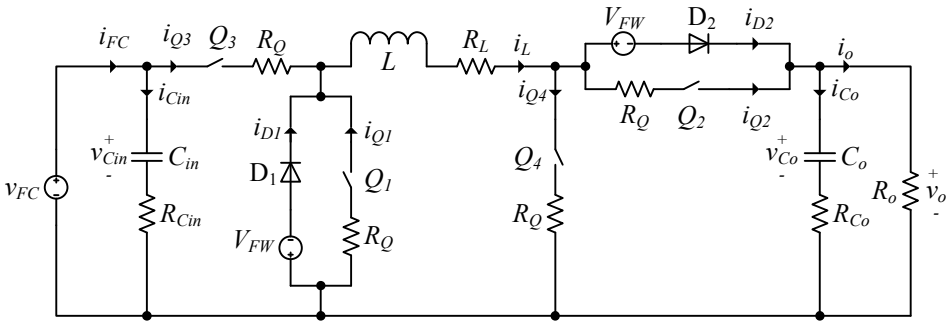

Figure 9.2: Equivalent circuit diagram of the non-inverting buck-boost converter.

a protection board that protects against reverse and over currents. The whole converter is controlled by a floating point DSP from Texas Instruments® (F28335). The DSP is mounted on a board from Spectrum Digital®, which provides the necessary input/output pins, connectors, etc. In Figure 9.3 a white LabView® box is also shown. However, this box is not a part of the converter, but is only used for data acquisition.

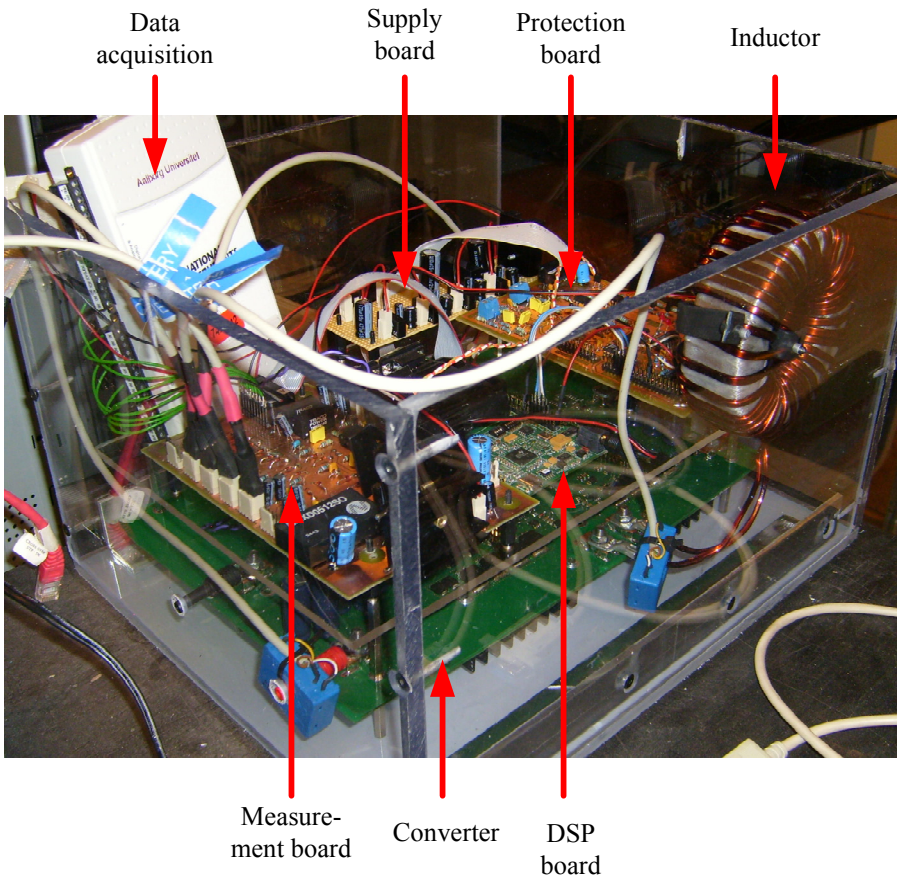

Figure 9.3: Practical realization of the fuel cell converter.

Protection

The converter has three kinds of hardware protection circuits, i.e.

1) Over current The fuel cell is very sensitive to over currents. If the input current (fuel cell current) is bigger than its nominal current, the fuel cell is disconnected.

2) Shoot-through Dead-time is included in the PWM signals from the DSP in order to avoid that an upper and lower switch conduct at the same time. However, as an extra protection a comparator circuit has been implemented. If a shoot-through is detected all switches are turned into open states.

3) Reverse current flow If the synchronous rectifier of the boost-diode switch Q_2 is turned on the current through it can be negative if the converter is operated in discontinuous mode. If the current between inductor and output capacitor is below $3\,\mathrm{A}$ the synchronous rectifier of the boost-diode will therefore be forced into open-state.

Transition

If the converter is operating in buck-mode, and needs to increase either the output voltage or current it will increase the duty cycle D_{Q_3} of switch Q_3. However, sometimes the duty cycle will go into saturation, i.e. $D_{Q_3} = 1$. In the same way, if the converter is operating in boost-mode, and it suddenly needs to decrease the output voltage or current, it will decrease the duty cycle D_{Q_4} of switch Q_4. However, this switch will also soon turn into saturation, i.e. $D_{Q_4} = 0$. For the two cases the converter therefore needs to change the state. This is illustrated in Figure 9.4(a) where a transition-method is inserted between the buck-mode and boost-mode. The transition method is therefore a "gate-way" between the two modes. In the figure it is seen that the transition between the intermediate transition method and either the buck-mode or boost-mode is implemented as a hysteresis controller with a gab of $D_{Q_3} = 0.05$ and $D_{Q_4} = 0.05$. This is to avoid continuously shifting between the modes.

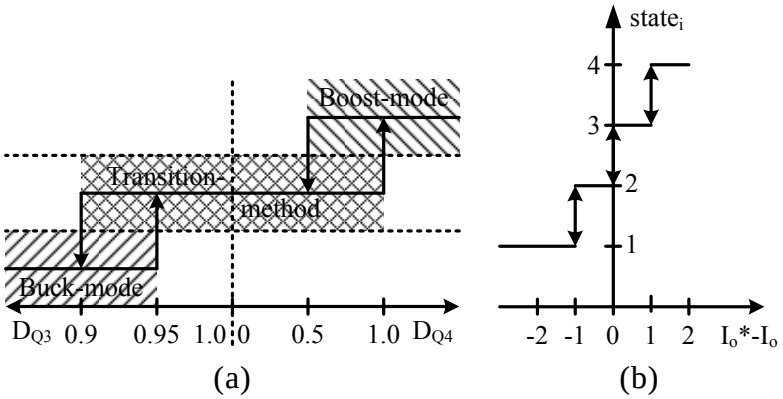

Figure 9.4: Selection of switch-mode. (a) "Hysteresis" control of transitions. (b) State variable $state_i$ dependency of output current error.

The duty cycle alone is not enough to decide if a transition should be made, e.g. if a duty cycle of $D_{Q_3} = 0.97$ exactly results in the correct output voltage or current there is no need to change to boost-mode. In order to asses if the converter is operating in the correct mode, the output current error $I_o^* - I_o$ is investigated. In Figure 9.4(b) it is seen how the output current error is divided into a variable $state_i$ which can have

four different values, i.e.

$$state_i = \begin{cases} 1 & & I_o^* - I_o & < & -1\,\mathrm{A} \\ 2 & -1\,\mathrm{A} \leq & I_o^* - I_o & < & 0\,\mathrm{A} \\ 3 & 0\,\mathrm{A} \leq & I_o^* - I_o & < & 1\,\mathrm{A} \\ 4 & 1\,\mathrm{A} \leq & I_o^* - I_o & & \end{cases} \quad [-] \tag{9.3}$$

A simple method to transit between buck-mode and boost-mode is to apply the buck-boost-mode in between, as this mode both can buck and boost the voltage. However, in [12, 13, 43] this has been demonstrated to cause high transients. Instead the authors have proposed a method where a specific pattern of buck-mode and boost-mode is applied between the buck-mode and buck-boost-mode and between the boost-mode and buck-boost-mode. The method provides very low transients, but the method utilizes the buck-boost-mode which results in lower efficiency, if the converter reaches steady-state in this mode.

In [60, 61] a combination of buck-mode and boost-mode is also proposed. In the transition from buck-mode to boost-mode the duty cycle of the buck switch is clamped to $96\,\%$. This results in low transient, but also a lower efficiency. The control of the duty cycles of the buck and boost switches was implemented in the traditional analog way. However, it is believed that improvement can be obtained by utilizing digital controllers.

Even though the transitions between buck-mode and boost-mode already have been investigated in other research, this issue still needs to be handled. Three transition methods will therefore be investigated here

Transition method 1 This method only transits if the error is big, i.e. $state_i \in \{1, 4\}$. This method is very simple, but lacks from the fact, that within the error interval of $state_i \in \{2, 3\}$ the current cannot be controlled.

Transition method 2 The buck-boost-mode can both buck and boost the current. Therefore, in order to avoid that there is a gab where the current cannot be controlled, this mode is introduced.

Transition method 3 The converter is acting both in buck-mode and boost-mode at the same time, i.e. when the converter is operating in buck-mode, the boost-switch Q_4 starts to switch before the duty cycle of switch Q_3 reaches $D_{Q_3} = 1$. In the same way, when the converter is operating in boost-mode, the switch Q_3 starts to switch before the duty cycle of switch Q_4 turns into saturation.

Discontinuity

In order to obtain a fast transition from e.g. buck-mode to boost-mode a transition can be made immediately. However, if the duty cycle of the buck-switch Q_3 is lower than $D_{Q,3} = 1$ before the transition is made a significant higher voltage will be present across the inductor, which will lead to high oscillations. In Figure 9.5 it is shown how voltages and currents behave when the duty cycle of switch Q_3 turns into saturation, i.e. $D_{Q,3} = 1$. The converter is operating in buck-mode with an input voltage of $v_{FC} = 40\,\mathrm{V}$ and output voltage of $V_o = 34\,\mathrm{V}$. The load is a resistor. Due to a sudden high current request, the controller increases the duty cycle. In Figure 9.5(a,c) the current controller increases the duty cycle until it reaches $D_{Q,3} = 0.95$. At this time the duty cycle is instantly clamped to $D_{Q,3} = 1$. It is seen that this causes high oscillations of the output voltage v_o and inductor current i_L.

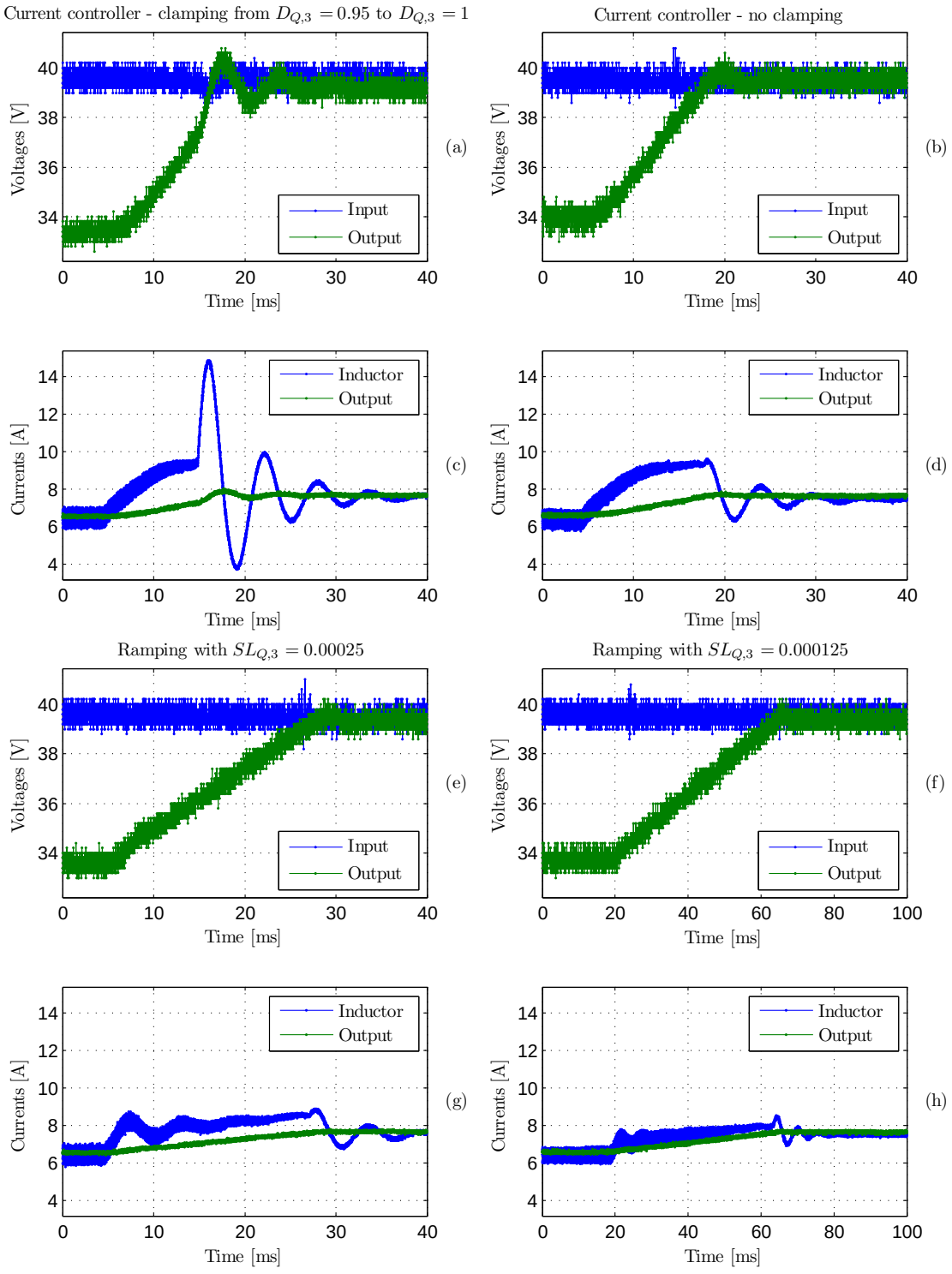

Figure 9.5: Input voltage v_{FC}, output voltage v_o, inductor current i_L, and output current i_o due to the discontinuous operation switch Q_3. (a) and (c) current controller determines the duty cycle. When it reaches $D_{Q,3} = 0.95$ it is clamped to $D_{Q,3} = 1$. (b) and (d) current controller determines the duty cycle of switch Q_3. (e) and (g) The duty cycle is ramped with a slope of $SL_{Q,3} = 0.00025$. (f) and (h) Duty cycle is ramped with slope $SL_{Q,3} = 0.000125$.

In Figure 9.5(c,d) there is no clamping, and the current controller increases the duty cycle until it reaches $D_{Q,3} = 1$. It is seen that the oscillations are smaller than with clamping. However, due to the fastness of the current controller, oscillations of the output voltage and inductor current are still present. Instead of letting the current controller decide the fastness of the duty cycle, the duty cycle is ramped-up with a certain slope $SL_{Q,3}$. In Figure 9.5(e,g) the duty cycle is increased with slope $SL_{Q,3} = 0.00025$, and in Figure 9.5(f,h) the slope is $SL_{Q,3} = 0.000125$. It is seen that there are almost no oscillations of the output voltage, and the oscillations of the inductor current are significant smaller. However, due to the lower slope of the duty cycle, it takes longer time before $D_{Q,3} = 1$ is obtained, i.e. the bandwidth of the output current controller is reduced.

Control structure

As the battery package determines the bus voltage, the fuel cell converter controls the current that is fed into the bus from the fuel cell stack. The general control structure can be seen in Figure 9.6. An inductor reference current i_L^* is calculated from the output reference current i_o^* by using the steady-state equations which are derived in Appendix C, i.e.

$$i_L^* = \begin{cases} i_o^* & \text{Buck-mode} \\ \frac{i_o^*}{1-D} & \text{Boost-mode or buck-boost-mode} \end{cases} \quad [\text{A}] \qquad (9.4)$$

The inductor reference current is calculated from the steady-state duty cycle D. Therefore, the inductor reference current should be updated with a lower frequency than the duty cycle. The transition from buck-mode to boost-mode and vice versa can result in oscillations of the inductor current, and thereby also the duty cycle. The oscillations should therefore have been sufficiently suppressed before the reference inductor current is updated. At every switching period the duty cycle is updated. It is chosen to update the inductor reference current every LoopcountMax$= 450$ for transition method 1 and 3, and for every LoopcountMax$= 1000$ for transition method 2. This corresponds to an update interval of $T_{update} = 18\,\text{ms}$ and $T_{update} = 40\,\text{ms}$, respectively. The update interval is longer for transition method 2, as the buck-boost-mode is inserted between the buck-mode and boost-mode. The shift to or from the buck-boost-mode causes a high change of the inductor current, and therefore it needs longer time to settle down.

The control of the fuel cell converter is implemented in an interrupt function that is executed at $f_s = 25\,\text{kHz}$. The overall structure of the flow-chart of this interrupt function can be seen in Figure 9.7. At every switching period an interrupt is generated. In the beginning of the interrupt routine the inductor current is sampled. Afterwards, at every LoopcountMax switching periods, the current from the fuel cell converter to the bus is calculated, i.e.

$$i_{FC,Bus} = \begin{cases} i_L & \text{Buck-mode} \\ \frac{i_L}{1-D} & \text{Boost-mode or buck-boost-mode} \end{cases} \quad [\text{A}] \qquad (9.5)$$

The state variable $state_i$ is thereby calculated, and the new switch-mode and reference inductor current can be calculated. Finally the duty cycle that results in the desired inductor current is calculated.

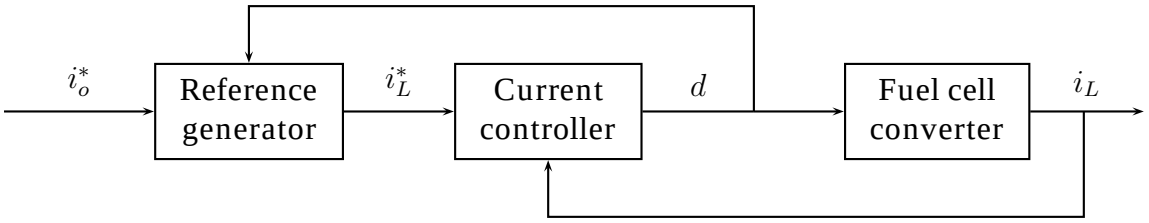

Figure 9.6: Fuel cell converter control structure.

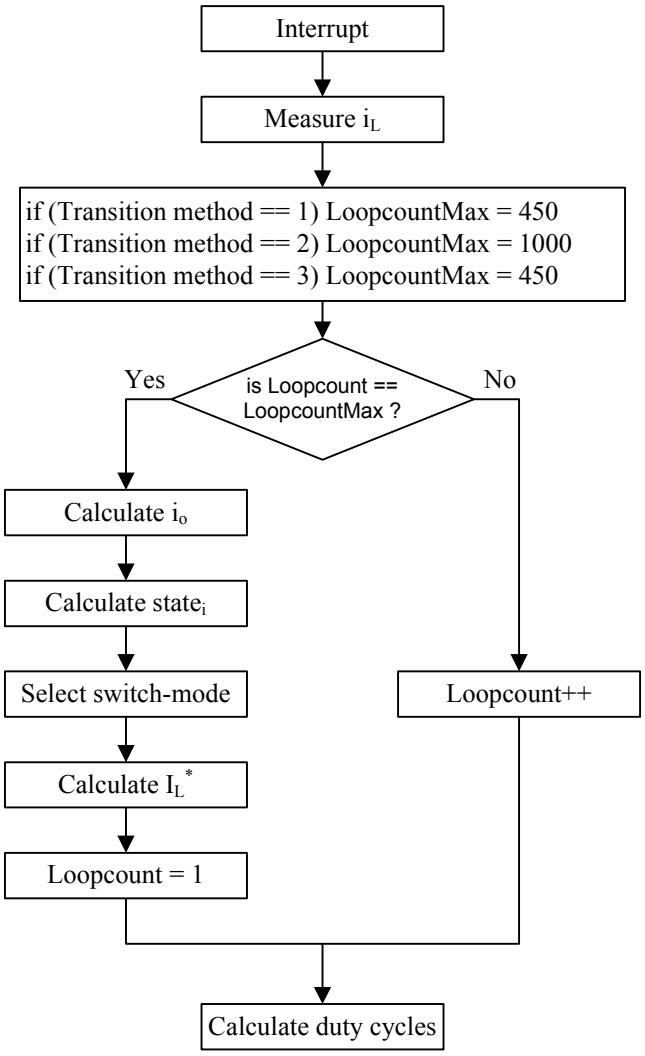

Figure 9.7: Flow chart of interrupt function.

Ramping of Duty Cycles

In order to avoid big oscillations due to the fast rise or fall of the duty cycles the duty cycles are either ramped up or down when a transition is going to take place. In Figure 9.8 it is seen how the duty cycles of switch Q_3 and Q_4 behaves before, during, and after a transition from buck-mode to boost-mode and vice versa. The duty cycles are shown for all three transition methods. For transition method 1 it is in Figure 9.8(a) seen that the duty cycle of switch Q_3 is ramped-up with slope SL_{Q3} so that it reaches $D_{Q3} = 1$ exactly at the time where the switch-mode and inductor reference current are updated. In this way the duty cycle is not clamped and the converter changes to boost-mode. After that time instant the duty cycle of switch Q_4 is under the control of the inductor current controller. In the same way the duty cycle of switch Q_4 is ramped-down in Figure 9.8(d) so it reaches $D_{Q4} = 0$ at the update time interval. After the update time interval the duty cycle of switch Q_3 is determined by the inductor current controller.

For transition method 2 and 3 it is in Figure 9.8(b-c) seen that the duty cycle of switch Q_3 is ramped-up with slope SL_{Q3}, so it reaches $D_{Q3} = 0.975$ at the update time interval. At that time instant the converter changes to buck-boost-mode for transition method 2. Therefore the duty cycles of switch Q_3 and Q_4 become equal until the next update interval where the converter changes to boost-mode. For transition method 3 it is in Figure 9.8(c) seen that when the duty cycle of switch Q_3 reaches $D_{Q3} = 0.975$ the duty cycle of switch Q_4 starts to rise due to the output of the inductor current controller. When the duty cycle of switch Q_3 reaches $D_{Q3} = 1$ the converter is in traditional boost-mode. For the boost-mode to buck-mode it is in Figure 9.8(f) seen that the duty cycle of switch Q_4 is ramped-down to $D_{Q4} = 0.025$. At that instant switch Q_3 begins to become active and there is again a small time interval where both switch Q_3 and Q_4 are operating individually.

Due to the results of the slopes in Figure 9.5 the maximum slope has been set to $SL_{max} = 0.00025$. The algorithm for calculating the slopes of switch Q_3 and Q_4 for the three transition is shown in Figure 9.9.

Results

In Figure 9.10 transition method 1 has been implemented. In Figure 9.10(a,c) the transition from buck-mode to boost-mode is shown. It is seen that the output voltage and current increase nice and smoothly without oscillations. At time $80\,\mathrm{ms}$ where the transition takes place, there is a little oscillation of the inductor current. In Figure 9.10(b,d) the converter changes from boost-mode to buck-mode. Due to some oscillations of the inductor current at the time the transition takes place, the output voltage and current does not change as smoothly as for the shift from buck-mode to boost-mode. However, the transition can be made more smoothly by modifying either the update time interval T_{update} or slope SL_{Q4}.

The results of applying transition method 2 are seen in Figure 9.11. In the buck-boost-mode the inductor current is relatively big which means that the output voltage drops when the converter changes from buck-mode or boost-mode to buck-boost-mode as it takes some time to build up the inductor current. In the same way when going from buck-boost-mode to buck-mode or boost-mode the energy in the inductor is released for the output load, which means that the voltage rises significant. In

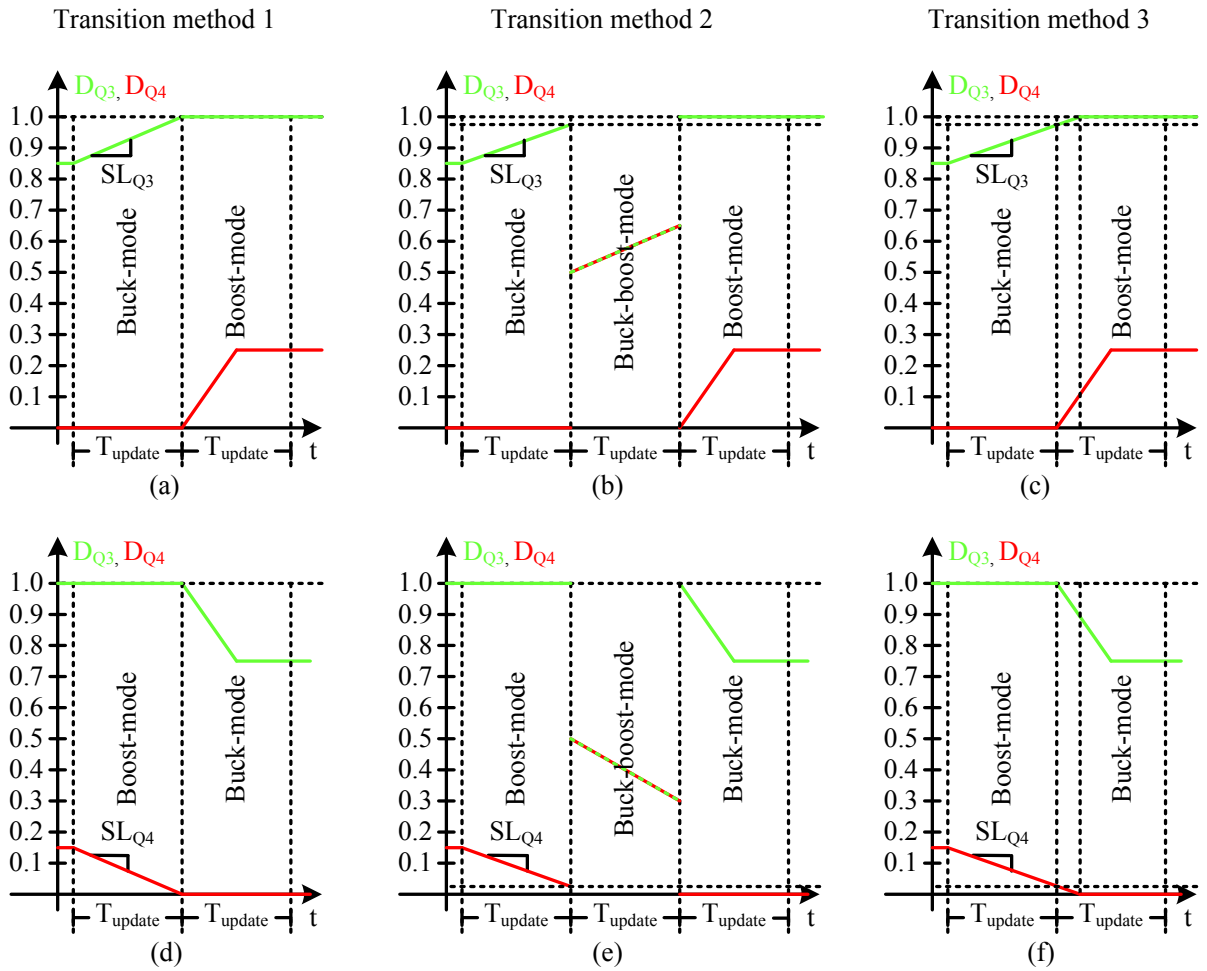

Figure 9.8: Ramping of duty cycles. Green line: duty cycle of switch Q_3. Red lines: duty cycle of switch Q_4. The duty cycle values are only for illustration of the principle. (a) Transition from buck-mode to boost-mode for transition method 1. (b) Transition from buck-mode to boost-mode for transition method 2. (c) Transition from buck-mode to boost-mode for transition method 3. (d) Transition from boost-mode to buck-mode for transition method 1. (e) Transition from boost-mode to buck-mode for transition method 2. (f) Transition from boost-mode to buck-mode for transition method 3.

Figure 9.11(a,c) it is seen that it requires two update intervals of duration $T_{update} = 40\,\mathrm{ms}$ each in order to transit from buck-mode to boost-mode. However, going from boost-mode to buck-mode requires in Figure 9.11(b,d) only one update interval.

In Figure 9.11 the transitions due to transition method 3 are shown. It is seen that the output voltage and inductor current are changing smoothly for both cases of transition. The transition from boost-mode to buck-mode is even more smoothly than in transition method 1.

In Figure 9.13 the currents and gate voltages are shown when transition method 3 is applied. The figure is shown for two cases: when the input voltage is bigger than the output voltage, and when the input voltage is smaller than the output voltage. In Figure 9.13(a) the inductor and output currents are shown and in Figure 9.13(c) the

if transition method 1

$$SL_{Q3} = \frac{1 - D_{Q3}}{\text{LoopcountMax}} \tag{9.6}$$

if $SL_{Q3} > SL_{max}$

$$SL_{Q3} = SL_{max} \tag{9.7}$$

if $(D_{Q3} + SL_{Q3} \cdot \text{LoopcountMax}) \geq 0.95$

$$SL_{Q3} = \frac{0.945 - D_{Q3}}{\text{LoopcountMax}} \tag{9.8}$$

end

end

$$SL_{Q4} = \frac{0 - D_{Q4}}{\text{LoopcountMax}} \tag{9.9}$$

if $SL_{Q4} < -SL_{max}$

$$SL_{Q4} = -SL_{max} \tag{9.10}$$

if $(D_{Q4} + SL_{Q4} \cdot \text{LoopcountMax}) \leq 0.05$

$$SL_{Q4} = \frac{0.055 - D_{Q4}}{\text{LoopcountMax}} \tag{9.11}$$

end

end

else

if $D_{Q3} < 0.975$

$$SL_{Q3} = \frac{0.98 - D_{Q3}}{\text{LoopcountMax}} \tag{9.12}$$

else

$$SL_{Q3} = \frac{1 - D_{Q3}}{\text{LoopcountMax}} \tag{9.13}$$

end

if $SL_{Q3} > SL_{max}$

$$SL_{Q3} = SL_{max} \tag{9.14}$$

end

if $D_{Q4} > 0.025$

$$SL_{Q4} = \frac{0.0245 - D_{Q4}}{\text{LoopcountMax}} \tag{9.15}$$

else

$$SL_{Q4} = \frac{0 - D_{Q4}}{\text{LoopcountMax}} \tag{9.16}$$

end

if $SL_{Q4} < -SL_{max}$

$$SL_{Q4} = -SL_{max} \tag{9.17}$$

end

end

Figure 9.9: Algorithm for calculating slopes of switch Q_3 and Q_4.

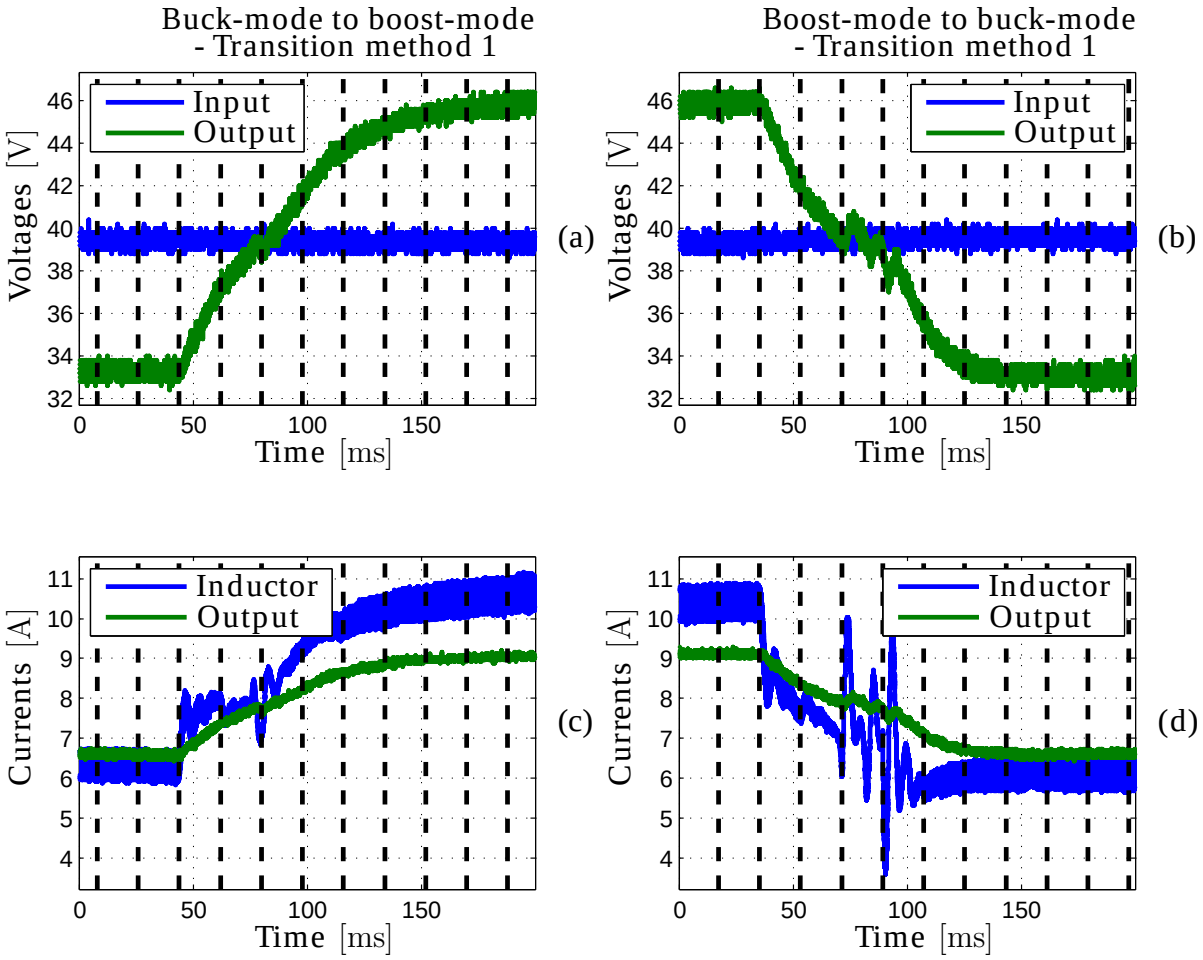

Figure 9.10: Transition method 1. The vertical black dashed lines are the update-time intervals. (a) Voltages during transition from buck-mode to boost-mode. (b) Voltages during transition from boost-mode to buck-mode. (c) Currents during transition from buck-mode to boost-mode. (d) Currents during transition from boost-mode to buck-mode.

gate voltages are shown when the input voltage is bigger than the output voltage. It is seen that when only switch Q_3 is applied the inductor current increases slightly because the input voltage is a little bigger than the output voltage. When switch Q_4 also is applied the current increases even more. In Figure 9.13(b,d) the input voltage is smaller than the output voltage. Therefore the inductor current in Figure 9.13 decreases when only switch Q_3 is applied. It is noticed that the duty cycle of switch Q_4 is bigger in this situation than in Figure 9.13 (c) where the input voltage is bigger than the output voltage.

From the plots of the three transition methods it is clear that transition method 2, which includes the buck-boost-mode, is not appropriate as it provides a high inductor current and is relatively slowly to transits between two switch modes. Transition method 3, where the buck-mode and boost-modes float into each other, provides the smoothest transitions, and it also has no dead-band like transition method 1, where the converter either is in buck-mode or boost-mode, which means that the current can

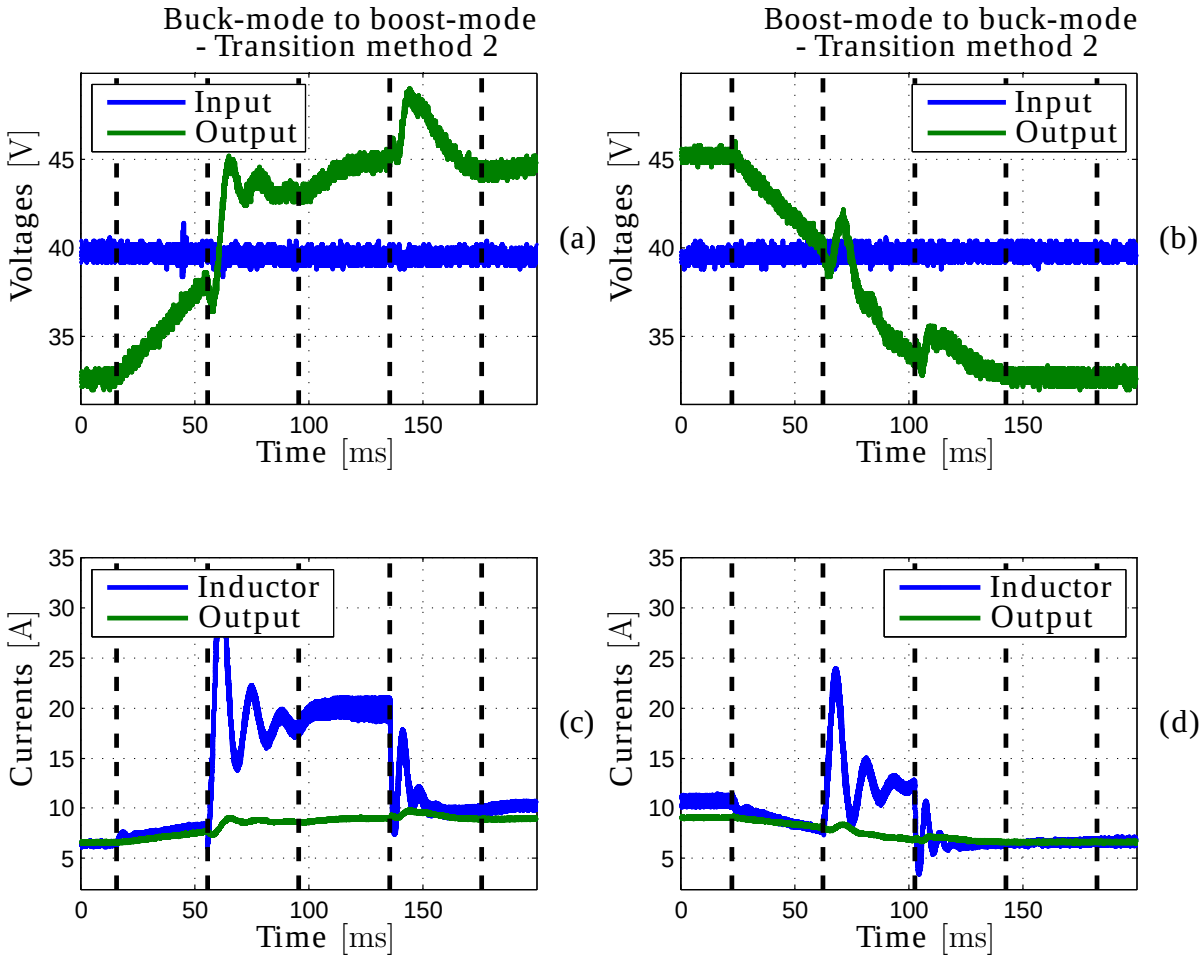

Figure 9.11: Transition method 2. The vertical black dashed lines are the update-time intervals. (a) Voltages during transition from buck-mode to boost-mode. (b) Voltages during transition from boost-mode to buck-mode. (c) Currents during transition from buck-mode to boost-mode. (d) Currents during transition from boost-mode to buck-mode.

be controlled at all values.

After this work has been carried out the work in [42] has been published. In the paper it is stated that the transients were due to the time delay that exists from the controller's PWM pulse to the switch actual changes state. The time delay was therefore compensated and the transients were reduced significantly. The method was applied on a voltage controller, where the input voltage was changed either below or above the output voltage, which were controlled to a fixed value. In this research it is the output current that is controlled, and not the voltage. For this reason the method presented here and the method of [42] cannot be compared directly. However, the compensation technique of [42] might be applied to the current control structure in this work also. The results of [42] seem to be very promising and the method has the advantage that it only uses pure buck-mode or boost-mode, and no combination of them. Therefore the switching losses should be very low.

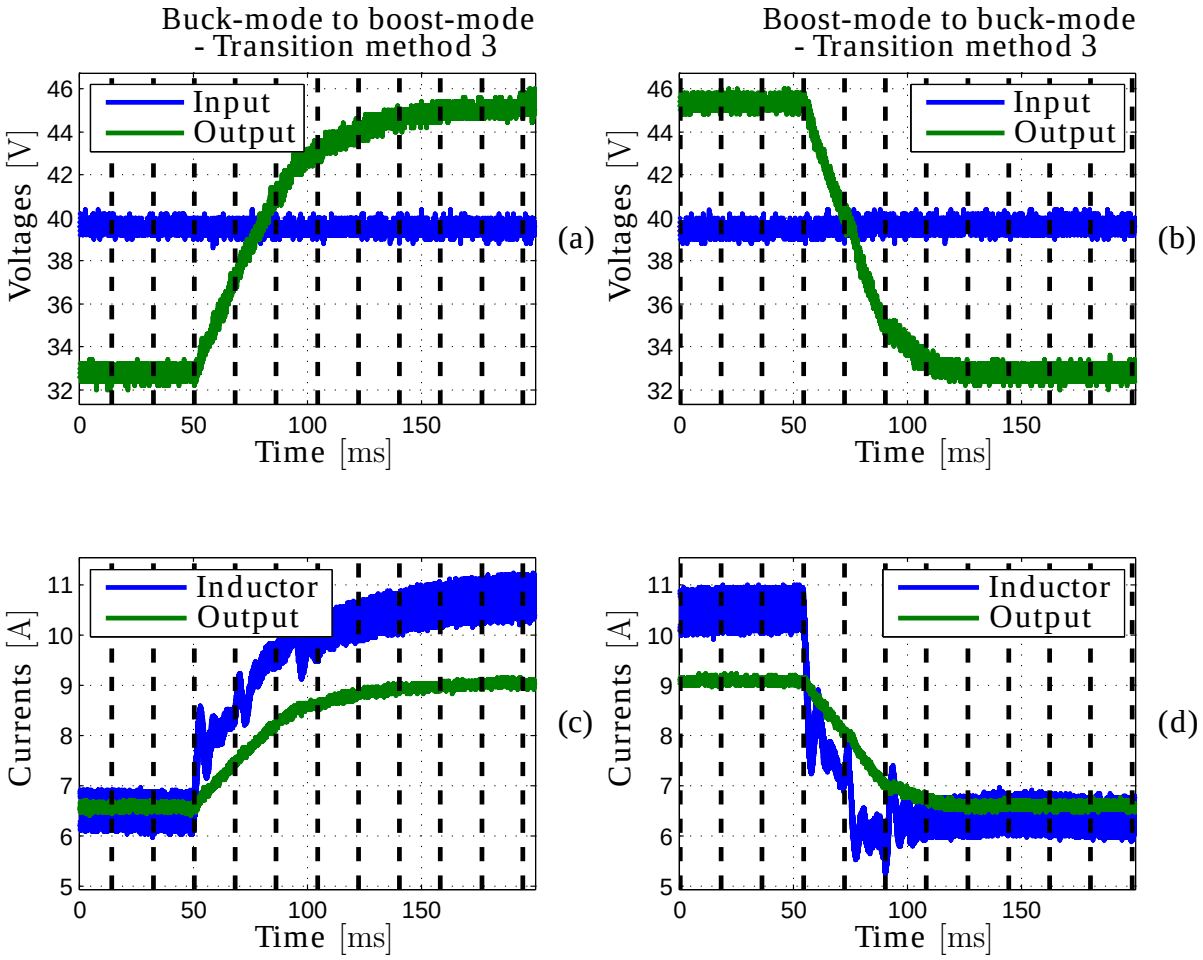

Figure 9.12: Transition method 3. The vertical black dashed lines are the update-time intervals. (a) Voltages during transition from buck-mode to boost-mode. (b) Voltages during transition from boost-mode to buck-mode. (c) Currents during transition from buck-mode to boost-mode. (d) Currents during transition from boost-mode to buck-mode.

Oscillations

When the converter is operated in buck-mode the switch Q_4 should be applied in the whole switching period in order to reduce the loss of diode D_2. However, in order to avoid reverse power flow the switch Q_4 is disconnected by hardware if the current through it is below $3\,\mathrm{A}$. When the switch Q_4 is disconnected the output voltage drops by the voltage across the diode D_2. Therefore the output current decreases. The current controller will therefore increase the duty cycle in order to increase the inductor current so the output current error is minimized. When the current through switch Q_4 becomes bigger than $3\,\mathrm{A}$ switch Q_4 will be applied by hardware again. Due to the lack of the voltage drop across diode D_2 the output current will then increase. The controller will therefore reduce the duty cycle in order to minimize the output current error. When the current through switch Q_4 becomes below $3\,\mathrm{A}$ switch Q_4 will be disconnected by hardware again. This scenario will therefore repeat itself and create oscillations of the output current and voltage which is undesirable.

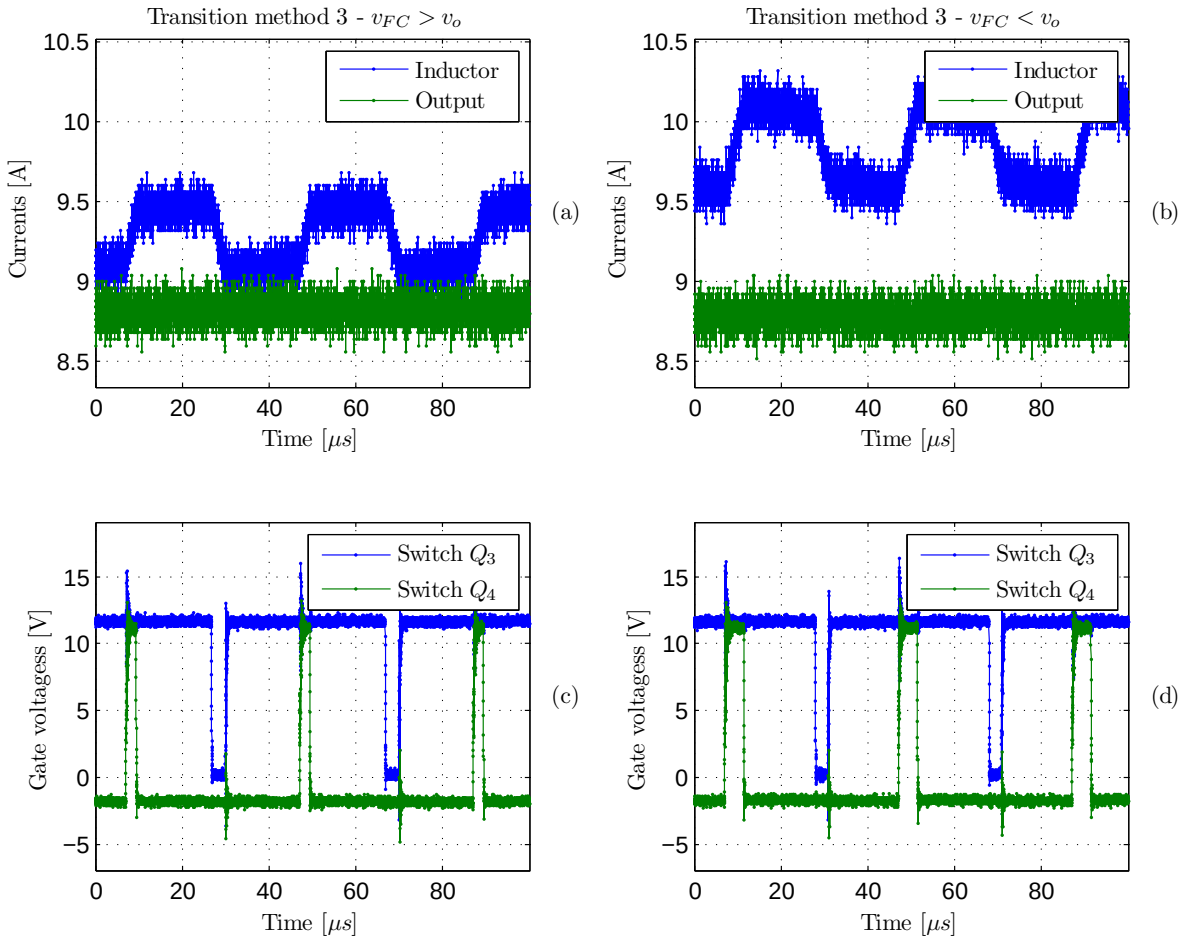

Figure 9.13: Current and gate voltage due to transition method 3. (a) Inductor and output currents when the input voltage is bigger than the output voltage. (b) Inductor and output currents when the input voltage is smaller than the output voltage. (c) Gate voltages of switch Q_3 and Q_4 when the input voltage is bigger than the output voltage. (d) Gate voltages of switch Q_3 and Q_4 when the input voltage is smaller than the output voltage.

A simple method to avoid these oscillations is by software to increase the current limit of when switch Q_4 can be utilized. The drawback of this method is that all the current will flow through the diode D_2 when the current is below the limit. This will therefore give higher loss than if the synchronous rectifier switch Q_4 is utilized. It is therefore desirable that switch Q_4 could be used for low currents also.

In order to take advantage of switch Q_4 at low current levels a method is proposed. If the inductor reference current is around $3\,\mathrm{A}$, e.g. $5\,\mathrm{A}$, a higher temporary reference current is inserted. The temporary reference current insures that a sufficient temporary steady-state inductor current is obtained so the switch Q_4 is applied all the time. The temporary reference inductor current makes sure that the transition from the temporary reference current to the actual reference inductor current occurs with such small natural oscillations of the inductor current that the hardware protection circuit not is triggered.

By trial-and-error-method it turns out that a temporary reference inductor current of $i^*_{L,temp} = 8\,\mathrm{A}$ should be applied for $40\,\mathrm{ms}$ or 1000 switching periods.

In Figure 9.14 a step in the output reference current is performed. The currents and voltages are shown with and without the temporary high inductor reference current. In Figure 9.14(a) it is seen how the inductor current oscillates. In Figure 9.14(c) the input and output voltages are shown. Because the load is a resistor the output voltage also oscillates due to the oscillations of the output current.

In Figure 9.14(b,d) the temporary high inductor reference current is applied when the same step of the output current is performed. It is seen how the inductor current is boosted in the temporary period of $40\,\mathrm{ms}$. After that it drops to the appropriate steady-state value. When it drops it does not fall below the threshold current of $3\,\mathrm{A}$ of the hardware protection circuit, and therefore does the current not start to oscillate. Because of the temporary high inductor current, the output current and voltage are also boosted to values higher than the requested steady-state values. It is seen that the output voltage has a peak in the temporary period of approximately $6\,\mathrm{V}$ higher than its final value. Depending on the load this peak voltage might be too high, and the interval of the temporary high inductor reference current might therefore be reduced.

9.3 Status of Implementation

At the current moment the different parts of the FC Truck have been tested individually with success. However, the overall test, i.e. everything put together, has failed. The fuel cell converter provided so much EMI that the inverters were not able to operate satisfactory, and the start-up procedure where the vehicle controller and fuel cell converter should share information in a certain order needs also to be debugged.

9.4 Conclusion

In this chapter issues regarding implementation of the fuel cell shaft power pack are described. The FC Truck is implemented with two PMSMs, which are controlled by two inverters. The inverters are connected to a $48\,\mathrm{V}$ lead-acid battery package, which thereby determines the bus voltage. A $1\,\mathrm{kW}$ HTPEMFC stack is connected to the bus through a non-inverting buck-boost converter. Three different methods to transit between buck-mode and boost-mode are proposed. A method where both the buck-mode and boost-mode are applied on the same time, but independent of each other provides the smoothest transition. At low currents the protection circuit of reverse currents can make the inductor current start to oscillate. A method has been proposed that makes it possible to operate at low current intervals without oscillations of the inductor current. Each individual component has been tested with success, but debugging is still needed in order to make the whole system work together.

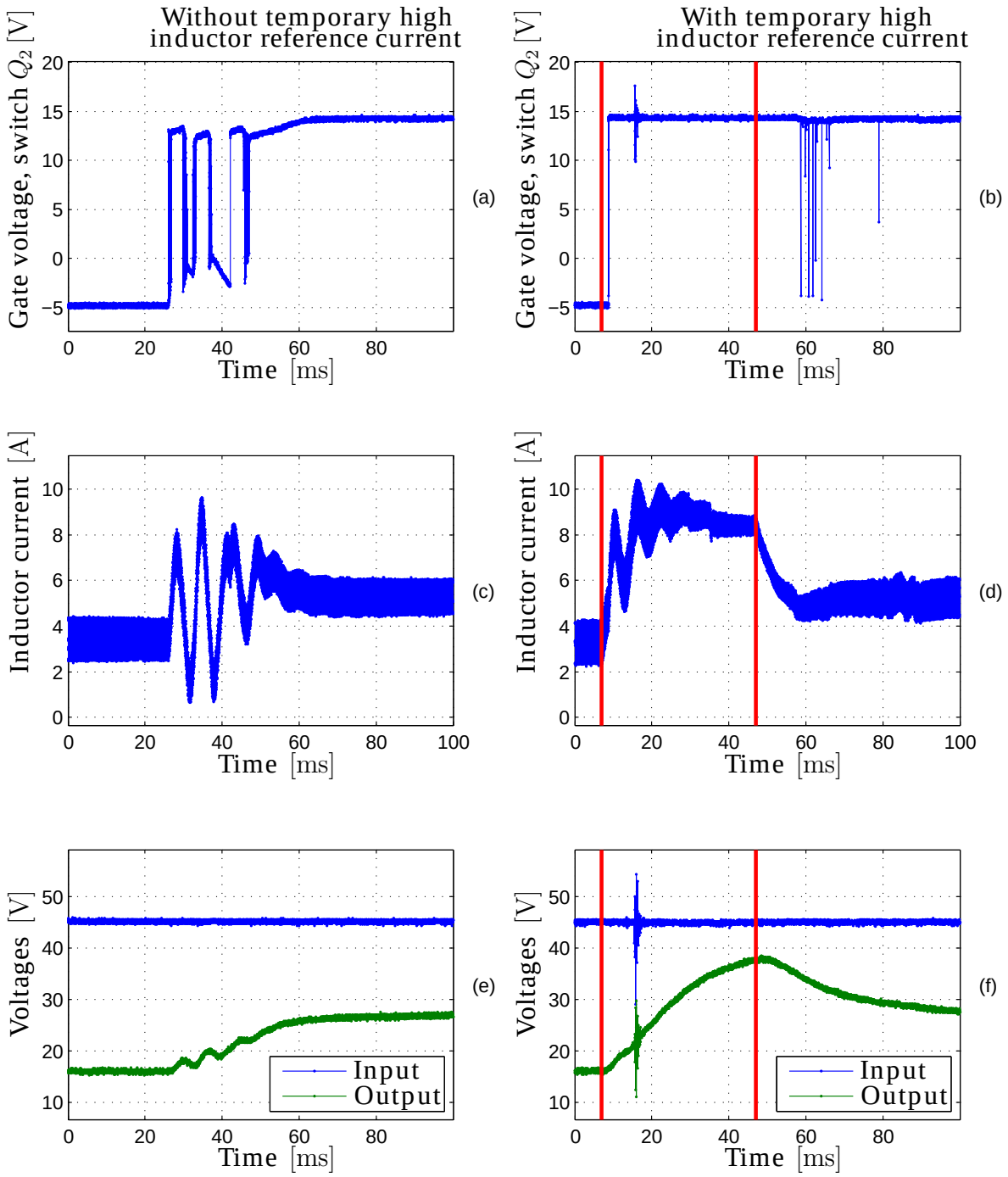

Figure 9.14: Step of output current with and without the temporary high inductor reference current. The red vertical lines indicate that the controller is updated. (a) Gate voltage of switch Q_2 without temporary high inductor reference current. (b) Gate voltage of switch Q_2 with temporary high inductor reference current. (c) Inductor current without temporary high inductor reference current. (d) Inductor current with temporary high inductor reference current. (e) Input and output voltages without temporary high inductor reference current. (f) Input and output voltages with temporary high inductor reference current.

Part IV

Conclusion, Contributions, and Future Work

10 Conclusion

10.1 Preliminaries

This PhD thesis is about designing and implementation of a fuel cell shaft power pack (FCSPP) for a fuel cell truck, which originally was powered by lead-acid batteries. The FCSPP includes a fuel cell stack, fuel storage, energy storage device, electric machine, power electronics, and the necessary control. The purpose by replacing the original lead-acid battery package with a FCSPP is to increase the hours and area of operation of the truck, to avoid the long charging time of the original battery package, to avoid a frequently change of the battery package, and the desire of an electric outlet for electric tools.

The load profile of the truck is analyzed by a simulation model and field measurements. The field measurements did not indicate that the original battery package was insufficient for the actual usage of the truck. Therefore a new driving cycle based on the field measurements were created in order to obtain a more demanding load profile.

10.2 Modeling

A steady-state and dynamic model of a High Temperature Proton Exchange Membrane Fuel Cell (HTPEMFC) is presented. The dynamic model is created by using electrochemical impedance spectroscopy. It is able to model the dynamic behavior of a fuel cell, but only in a certain point of operation. The model can be improved by making the parameters depend on the actual state of the fuel cell.

A steady-state model of a lead-acid battery block is also presented, which is able to model the voltage, state-of-charge level, and lifetime. The lifetime is calculated by using rain-flow-counting method. The battery model is based on data sheet specifications.

An ultracapacitor module has also been modeled. The self discharge, capacitance, and charge recovery depend strongly on the actual charge level. The self discharge is relatively high when fully charged but becomes less significant with lower voltage. The capacitance drops linearly with the voltage, i.e. the lower voltage the lower capacitance. At high voltage levels the charge recovery is not significant, but at lower voltages levels the increase in voltage due to charge recovery becomes higher. A model that consists of seven RC-circuits has been developed, and a systematic method to obtain the parameters is presented. Each of the seven RC elements depends on the actual voltage level.

If the voltage of the fuel cell does not fit to the bus voltage it is advantageous to insert a DC / DC converter in between. As it sometimes is necessary to step-down the

voltage and sometimes to boost the voltage, the non-inverting buck-boost converter has been investigated. A detailed model has been created which takes the parasitic into account. Transfer functions and analytic expressions of the efficiency have been derived. The converter has an efficiency of $98\,\%$ at nominal power.

A permanent magnet synchronous machine (PMSM) is used for propulsion due to its higher power density and efficiency. The machine is controlled by an inverter. The PMSM is modeled in the traditional dq-reference frame, and the inverter is modeled by taking the losses of the switches into account.

10.3 DESIGN

Ten different configurations of combining the fuel cell with an energy storage device to a common bus voltage have been investigated. The energy storage device is either a battery, ultracapacitor, or a combination of both. It is chosen to apply to the 42V PowerNet standard, which specifies the upper and lower limits of the bus voltage.

An energy management strategy and charging strategy which can be applied for all ten cases of configurations have been proposed. The energy management strategy divides the load power to the energy storage device(s) in such a way that the fuel cell is operated smoothly without any discontinuity. When both a battery and ultracapacitor are present the ultracapacitor acts as a high pass filter for the load power, and it therefore takes care of both the positive and negative peak powers. The charging strategy insures that the ultracapacitor is charged to the desired reference without overcharging it. This is done in a way so the fuel cell and battery power are not interrupted.

A design procedure has been proposed which calculates the proper number of parallel strings of the energy storage device(s). The design procedure is integrated in a design program which has been created in a Matlab® / Simulink® environment. The design program is executed in an iterative process until a converging is obtained. The ten cases of configurations are evaluated for different fuel cell power ratings. For all the different configurations and fuel cell power ratings the system mass, volume, efficiency, and battery lifetime are compared.

Due to the voltage limits of the 42V PowerNet standard results indicate that it not is appropriate to connect a fuel cell or ultracapacitor directly at the bus, as the full potential of these two units therefore cannot be utilized, and the system therefore becomes bigger and heavier. However, from an efficiency point of view it is advantages to connect the fuel cell directly to the bus as the efficiency of a fuel cell is higher when the drawn fuel cell power decreases.

Due to a heating period of the fuel cell of 6 minutes where the energy storage device must provide power both for the heating unit and electric machines, it is not appropriate to use ultracapacitors as the only energy storage device, as the system will be too big and heavy because of the limited energy density of these devices. For the same reason it does not help the system mass and volume to combine ultracapacitors with a battery package. However, combining the battery and ultracapacitor has a positive effect on the system efficiency.

Increasing the fuel cell power rating decreases the energy requirement of the energy storage device until a certain point. When a battery is included the partial load cycles therefore have a significant negative effect on the battery lifetime. Combining a

battery with ultracapacitors improves apparently the battery lifetime, as the ultracapacitors then takes care of the shallow cycles. However, there is a big uncertainty of the number of cycle-to-failure for depth-of-discharge levels below $20\,\%$ for the used battery, and further investigation of the battery lifetime is therefore necessary.

10.4 Implementation

Because it is necessary to operate the fuel cell converter in either buck-mode or boost-mode, it is also necessary to transit between these two modes in a smooth and effective manner. Three methods have been investigated. A method where the converter is operated in both buck-mode and boost-mode at the same time provides the smoothest transitions with minor oscillations.

At low current levels the inductor current can start to oscillate due to a reverse current protection circuit. A method has been proposed which makes it possible to avoid the oscillations at low current levels, without decreasing the efficiency.

11 Scientific Contributions

During this PhD project the following are considered as contributions:

Fuel cell modeling A new type of the PEM fuel cells, i.e. the HTPEMFC, has been modeled by using electrochemical impedance spectroscopy, and an equivalent electric circuit diagram has been proposed. At the time where the work were carried out, mainly the low temperature type (LTPEMFC) of the PEM fuel cells have been investigated.

Ultracapacitor modeling A systematic method to obtain parameters of an ultracapacitor module has been presented, and a model has been proposed. The time constant of the self discharge resistance is modeled by a modified Weibull function. The ultracapacitor model is able to simulate the charge recovery for more than 16 h, and the loss in voltage due to the self discharge can be modeled for more than 150 days.

Design of fuel cell systems A systematic method has been proposed for designing a fuel cell system. The iterative process of the design method and the detailed modeling of the different components, are considered as a contribution, as it designs the system "to the limit". In the evaluation of the system structure, the battery lifetime is taken into account, which also is a contribution.

Fuel cell converter Detailed transfer functions and analytic expressions of the non-inverting buck-boost converter have been derived. Different methods to transit between buck-mode and boost-mode have been investigated, and a method to avoid oscillations at low current levels has been proposed.

12 Future Work

There are still many steps that must be investigated before the "optimal" fuel cell shaft power pack can be designed. An obvious parameter when selecting the most suitable system is of course the cost and it should be included in the comparison of the different configurations.

A simple way to connect different devices is to put them in parallel, e.g. a battery in parallel with a fuel cell without having DC/DC converters in between. The power flow becomes then more complicated to model, as it depends on the instantaneous impedance of each device. The parallel structures should therefore be included.

In this study the lead-acid battery were used, but it might not be the best choice for a fuel cell application. Other types of batteries should be considered also. For each battery type one can also select if the battery should be rated for high power, high energy, or if it should be a compromise in between. In the same way other fuel cell systems should be considered, e.g. on-board reforming or LTPEMFC. Both are considered to affect the start-up time, which probably will decrease the energy requirement of the energy storage device.

The energy management strategy in this work is relatively simple, and other strategies could be considered, as the direction of power flow has a big impact on the sizing, efficiency, and lifetime. As the lead-acid battery, the fuel cells also suffer from low lifetime. The fuel cell power rating will therefore probably have a huge influence on the total system cost when maintenance cost is included also.

It is pointed out that ultracapacitors might have a positive effect on the battery lifetime, as they can handle all the partial cycles of low energy. However, the used battery lifetime model was based on extrapolations, as the battery data sheet did not contain information regarding the lifetime due to cycles of low amplitude. The battery lifetime due to shallow cycles should therefore be investigated.

Bibliography

[1] C. R. Akli, X. Roboam, B. Sareni, and A. Jeunesse. Energy management and sizing of a hybrid locomotive. *Proc. of European Conference on Power Electronics and Applications (EPE)*, pages 1 – 10, September 2007.

[2] S. J. Andreasen, J. L. Jespersen, E. Schaltz, and S. K. Kær. Characterisation and modelling of a high temperature pem fuel cell stack using electrochemical impedance spectroscopy. *Fuel Cells*, 4:463 – 473, January 2009.

[3] Søren Juhl Andreasen. Design and control of high temperature pem fuel cell system. *PhD Thesis, Aalborg University*, October 2009.

[4] Søren Juhl Andreasen, Leanne Ashworth, Ian Natanael Menjón Remón, and Søren Knudsen Kær. Directly connected series coupled htpem fuel cell stacks to a li-ion battery dc bus for a fuel cell electrical vehicle. *International journal of hydrogen Energy*, 33(23):7137 – 7145, December 2008.

[5] Søren Juhl Andreasen and Søren Knudsen Kær. Modelling and evaluation of heating strategies for high temperature polymer electrolyte membrane fuel cell stacks. *International Journal of Hydrogen Energy*, 33(17):4655 – 4664, September 2008.

[6] Søren Juhl Andreasen and Søren Knudsen Kær. Dynamic model of the high temperature proton exchange membrane fuel cell stack temperature. *Journal of Fuel Cell Science and Technology*, 6(4):1 – 8, November 2009.

[7] Jennifer Bauman and Mehrdad Kazerani. A comparative study of fuel-cell-battery, fuel-cell-ultracapacitor, and fuel-cell-battery-ultracapacitor vehicles. *IEEE Transactions on Vehicular Technology*, 57(2):760 – 769, March 2008.

[8] Henrik Bindner, Tom Cronin, Per Lundsager, James F. Manwell, Utama Abdulwahid, and Ian Baring-Gould. Lifetime modelling of lead acid batteries. *Risø Report*, April 2005.

[9] Wolfgang Bremer. International standard for future automotive 42 v supply voltages (powernet). *Journal of Power Sources*, 116(1 - 2):73 – 78, July 2003.

[10] H. El Brouji, J. M. Vinassa, O. Briat, N. Bertrand, and E. Woirgard. Ultracapacitors self discharge modelling using a physical description of porous electrode impedance. *Proc. of IEEE Vehicle Power and Propulsion Conference (VPPC)*, September 2008.

[11] G. Brusaglino, V. Ravello, N. Schofield, and D. Howe. Advanced drives for electrically propelled vehicles. *IEE Colloquium on Electrical Machine Design for All-Electric and Hybrid-Electric Vehicles*, pages 4/1 – 4/12, 1999.

[12] Arindam Chakraborty, Alireza Khaligh, and Ali Emadi. Combination of buck and boost modes to minimize transients in the output of a positive buck-boost converter. *Proc. of IEEE Industrial Electronics Conference (IECON)*, pages 2372 – 2377, November 2006.

[13] Arindam Chakraborty, Alireza Khaligh, Ali Emadi, and Arthur Pfaelzer. Digital combination of buck and boost converters to control a positive buck-boost converter. *Proc. of IEEE Power Electronics Specialists Conference (PESC)*, pages 1 – 6, June 2006.

[14] H. L. Chan and D. Sutanto. A new battery model for use with battery energy storage systems and electric vehicles power systems. *Proc. of IEEE Power Engineering Society Winter Meeting*, 1:470 – 475, January 2000.

[15] Woojin Choi, Jo. W. Howze, and Prasad Enjeti. Development of an equivalent circuit model of a fuel cell to evaluate the effects of inverter ripple current. *Journal of Power Sources*, October 2005.

[16] Thomas Christen and Martin W. Carlen. Theory of ragone plots. *Journal of Power Sources*, 91:210 – 216, March 2000.

[17] F. V. Conte. Battery and battery management for hybrid electric vehicles: a review. *Elektrotechnik and Informationstechnik*, 123:424 – 431, October 2006.

[18] Brian Cook. Introduction to fuel cells and hydrogen technology. *Engineering Science and Education Journal*, 11(6):205–216, December 2002.

[19] Yasser Diab, Pascal Venet, Hamid Gualous, and Gerard Rojat. Self-discharge characterization and modeling of electrochemical capacitor used for power electronics applications. *IEEE Transactions on Power Electronics*, 24(2):510 – 517, February 2009.

[20] Dennis Doerffel and Suleiman Abu Sharkh. A critical review of using the peukert equation for determining the remaining capacity of lead-acid and lithium-ion batteries. *Journal of Power Sources*, 155(2):395 – 400, April 2006.

[21] Mehrdad Ehsani, Yimin Gao, Sebastien E. Gay, and Ali Emadi. *Modern Electric, Hybrid Electric, and Fuel Cell Vehicles - Fundamentals, Theory, and Design*. CRC Press LLC, first edition, 2005. ISBN 0-8493-3154-4.

[22] Michael W. Ellis, Michael R. Von Sparkovsky, and Douglas J. Nelson. Fuel cell systems: Efficient, flexible energy conversion for the 21st century. *Proceedings of the IEEE*, 89(12):1808–1818, December 2001.

[23] Robert W. Erikson and Dragan Maksimovic. *Fundamentals of power electronics*. Kluwer, second edition, 2000. ISBN 0-7923-7270-0.

[24] Handbook for gel-vrla-batteries, part 2: Installation, commissioning and operation, December 2003.
`http://www.sonnenschein.org/PDF%20files/GelHandbookPart2.pdf`.

[25] Application: Innovation consortium fuel cell shaft power packs (fc-spp).

[26] Andre Augusto Ferreira, Jose Antenor Pomilio, Giorgio Spiazzi, and Leonardo de Araujo Silva. Energy management fuzzy logic supervisory for electric vehicle power supplies system. *IEEE Transactions on Power Electronics*, 23(1):107 – 115, January 2008.

[27] Alexandru Forrai, Hirohito Funato, Yukihiro Yanagita, and Yoshitsugu Kato. Fuel-cell parameter estimation and diagnostics. *IEEE Transactions on Energy Conversion*, 20(3):668–675, September 2005.

[28] Gene F. Franklin, J. David Powell, and Michael Workman. *Digital Control of Dynamic Systems*. Addison Wesley Longman, Inc., third edition, 1997. ISBN 0-201-82054-4.

[29] A. Fratta and F. Scapino. Modeling inverter losses for circuit simulation. *Proc. of IEEE Power Electronics Specialists Conference (PESC)*, 1:4479–4485, June 2004.

[30] Mark Gaboriault and Andrew Notman. A high efficiency, non-inverting, buck-boost dc-dc converter. *Proc. of IEEE Applied Power Electronics Conference and Exposition (APEC)*, 3:1411 – 1415, February 2004.

[31] L. Gao, Z. Jiang, and R. A. Dougal. Performance of power converters in hybrid fuel cell / battery power sources. *Proc. of Power Electronics Specialists Conference (PESC)*, 3:2018 – 2022, June 2004.

[32] Randall S. Gemmen. Analysis for the effect of inverter ripple current on fuel cell operating condition. *Journal of Fluids Engineering*, 125(3):576 – 585, May 2003.

[33] Alfons Graf. Semiconductors in the 42v powernet. *Proc. of 42V Automotive Systems Conference*, September 17-18 2001.

[34] V. Hassani and R. Fessler. Department of energy's ee technical team roadmap for advanced power electronics and electric machines, April 2004.

[35] A. G. Hombrados, L. Gonzalez, M. A. Rubio, W. Agila, E. Villanueva, D. Guinea, E. Chinarro, B. Moreno, and J.R. Jurado. Symmetrical electrode mode for pemfc characterisation using impedance spectroscopy. *Journal of Power Sources*, 151:25 – 31, October 2005.

[36] M. Usman Iftikhar, D. Riu, F. Druart, S. Rosini, Y. Bultel, and N. Retiere. Dynamic modeling of proton exchange membrane fuel cell using non-integer derivatives. *Journal of Power Sources*, May 2006.

[37] Jesper Lebæk Jespersen, Erik Schaltz, and Søren Knudsen Kær. Electrochemical characterization of a polybenzimidazole-based high temperature proton exchange membrane unit cell. *Journal of Power Sources*, 191(2):289 – 296, June 2009.

[38] Erwin Kreyszig. *Advanced Engineering Mathematics*. John Wiley & Sons, eighth edition, 1999. ISBN 0-471-15496-2.

[39] Jih-Sheng Lai. A high-performance v6 converter for fuel cell power conditioning system. *Proc. of IEEE Vehicle Power and Propulsion Conference (VPPC)*, pages 624–630, September 2005.

[40] James Larminie and Andrew Dicks. *Fuel Cell Systems Explained*. John Wiley & Sons, second edition, 2003. ISBN 0-470-84857-x.

[41] M. A. Laughton. Fuel cells. *Engineering Science and Education Journal*, 11(1):7–16, January / February 2002.

[42] Young-Joo Lee, Alireza Khaligh, and Ali Emadi. A compensation technique for smooth transitions in a noninverting buck-boost converter. *IEEE Transactions on Power Electronics*, 24(4):1002 – 1016, April 2009.

[43] Young-Joo Lee, Alireza Khaligh, and Ali Emadi. Digital combination of buck and boost converters to control a positive buck-boost converter and improve the output transients. *IEEE Transactions on Power Electronics*, 24(5):1267 – 1279, May 2009.

[44] G. Lefevre, J. P. Ferrieux, J. Barbaroux, P. Boggetto, and P. Charlat. A new dc-ac converter for portable fuel cell applications. *Proc. of European Conference on Power Electronics and Applications (EPE)*, September 2003.

[45] A. Lidozzi and L. Solero. Power balance control of multiple-input dc-dc power converter for hybrid vehicles. *Proc. of IEEE International Symposium on Industrial Electronics*, 2(2):1467 – 1472, May 2004.

[46] C. Liu, T. Nergaard, L. Leslie, J. Ferrell, X. Huang; T. Shearer, J. Reichl, J. Lai, and John Bates. Power balance control and voltage conditioning for fuel cell converter with multiple sources. *Proc. of IEEE Power Electronics Specialists Conference (PESC)*, 4:2001–2006, June 2002.

[47] Changrong Liu, Amy Johnson, and Jih-Sheng Lai. A novel three-phase high-power soft-switched dc / dc converter for low-voltage fuel cell applications. *IEEE Transactions on Industrial Applications*, 41(6):1691–1697, November / December 2005.

[48] Tony Markel and Andrew Simpson. Plug-in hybrid electric vehicle energy storage system design. *Proc. of Advanced Automotive Battery Conference*, May 2006.

[49] Tony Markel, Matthew Zolot, Keith B. Wipke, and Ahmad A. Pesaran. Energy storage system requirements for hybrid fuel cell vehicles. *Proc. of Advanced Automotive Battery Conference*, June 2003.

[50] J. Marshall and M. Kazerani. Design of an efficient fuel cell vehicle drivetrain, featuring a novel boost converter. *Proc. of IEEE Conference of Industrial Electronics Society (IECON)*, November 2005.

[51] Ni Meng, M. K.H. Leung, D. Y. C. Leung, and K. Sumathy. Prospect of proton exchange membrane fuel cells (pemfc) for transportation. *Proc. of World Renewable Energy Congress (WREC)*, August / September 2004.

[52] Joeri Van Mierlo, Peter Van den Bossche, and Gaston Maggetto. Models of energy sources for ev and hev: fuel cells, batteries ultracapacitors, flywheels and engine-generators. *Journal of Power Sources*, 128(1):76 – 89, March 2004.

[53] Ned Mohan, Tore M. Underland, and William P. Robbins. *Power electronics*. John Wiley, third edition, 2003. ISBN 0-471-22693-9.

[54] Thierry Montanie. Electric energy storage evaluation for urban rail vehicles. *Proc. of European Conference on Power Electronics and Applications (EPE)*, September 2003.

[55] R. M. Moore, K. H. Hauer, S. Ramaswamy, and J. M. Cunningham. Energy utilization and efficiency analysis for hydrogen fuel cell vehicles. *Journal of Power Sources*, 159(2):1214 – 1230, September 2006.

[56] Gerry Moschopoulos and Praveen Jain. Single-stage zvs pwm full-bridge converter. *IEEE Transactions on Aerospace and Electronic Systems*, 39(4):1122 – 1133, October 2003.

[57] Abdellah Narjiss, Daniel Depernet, Frédéric Gustin, Daniel Hissel, and Alain Berthon. Design and control of a fuel cell dc/dc converter for embedded applications. *Proc. of European Conference on Power Electronics and Applications (EPE)*, September 2007.

[58] Paul R. Nicastri and Henry Huang. Jump starting 42v powernet vehicles. *IEEE Aerospace and Electronic Systems Magazine*, 15(8):25 – 31, August 2000.

[59] Ryan O'Hayre, Suk-Won Cha, Whitney Colella, and Fritz B. Prinz. *Fuel Cell Fundamentals*. John Wiley & Sons, first edition, 2006. ISBN 0-471-74148-5.

[60] Rajarshi Paul and Dragan Maksimovic. Analysis of pwm nonlinearity in non-inverting buck-boost power converters. *Proc. of IEEE Power Electronics Specialists Conference (PESC)*, pages 3741–3747, June 2008.

[61] Rajarshi Paul and Dragan Maksimovic. Smooth transition and ripple reduction in 4-switch non-inverting buck-boost power converter for wcdma rf power amplifier. *Proc. of IEEE International Symposium on Circuits and Systems (ISCAS)*, pages 3266 – 3269, June 2008.

[62] P. D. Chandana Perera. *Sensorless control of Permament Magnet synchronous Motor Drives*. Aalborg University, second edition, 2002. ISBN 87-89179-41-2.

[63] Jan Hovald Petersen. *Teknologiudredning ved FC-SPP projektet - Billagsmappe 2*. Hydrogen Innovation & Research Center, HIRC, Marts 2006.

[64] Haibo Qiao, Yicheng Zhang, Yongtao Yao, and Li Wei. Analysis of buck-boost converters for fuel cell electric vehicles. *Proc. of IEEE International Conference on Vehicular Electronics and Safety (ICVES)*, pages 109 – 113, December 2006.

[65] B. W. Ricketts and C. Ton-That. Self-discharge of carbon-based supercapacitors with organic electrolytes. *Journal of Power Sources*, 89(1):64 – 69, July 2000.

[66] K. J. Runtz and M. D. Lyster. Fuel cell equivalent circuit models for passive mode testing and dynamic mode design. *Proc. of Canadian Conference on Electrical and Computer Engineering*, pages 794–797, May 2005.

[67] Biranchinath Sahu and Gabriel A. Rincón-Mora. A low voltage, dynamic, noninverting, synchronous buck-boost converter for portable applications. *IEEE Transactions on Power Electronics*, 19(2):443 – 452, March 2004.

[68] Dirk Uwe Sauer and Heinz Wenzl. Comparison of different approaches for lifetime prediction of electrochemical systems - using lead acid batteries as example. *Journal of Power Sources*, 176(2):477–483, February 2008.

[69] Erik Schaltz, Søren Juhl Andreassen, and Peter Omand Rasmussen. Design of propulsion system for a fuel cell vehicle. *Proc. of European Conference on Power Electronics and Applications (EPE)*, September 2007.

[70] Erik Schaltz, Jesper Lebæk Jespersen, and Peter Omand Rasmussen. Development of a 400 w high temperature pem fuel cell power pack: Equivalent circuit modeling. *Proc. of Fuel Cell Seminar*, November 2006.

[71] Erik Schaltz, Alireza Khaligh, and Peter Omand Rasmussen. Influence of battery/ultracapacitor energy-storage sizing on battery lifetime in a fuel cell hybrid electric vehicle. *IEEE Transactions on Vehicular Technology*, 58(8):3882 – 3891, October 2009.

[72] N. Schofield, H.T. Yap, J. Van Mierlo, G. Maggetto, and P. Van den Bossche. A state-of-the-art review and database of fuel cells and their application in electric vehicles useful for education needs. *Proc. of European Conference on Power Electronics and Applications (EPE)*, September 2003.

[73] Roberto M. Schupbach, Juan C. Balda, Matthew Zolot, and Bill Kramer. Design methodogy of a combined battery-ultracapacitor energy storage unit for vehicle power management. *Proc. of IEEE Power Electronics Specialist Conference (PESC)*, 1:88–93, June 2003.

[74] Jaw-Kuen Shiau, Chun-Jen Cheng, and Ching-En Tseng. Stability analysis of a non-inverting synchronous buck-boost power converter for a solar power management system. *Proc. of IEEE International Conference on Sustainable Energy Technologies (ICSET)*, pages 263 – 268, November 2008.

[75] Godfrey Sikha and Branko N. Popov. Performance optimization of a battery-capacitor hybrid system. *Journal of Power Sources*, 143(1):130 – 138, July 2004.

[76] Luca Solero, Alessandro Lidozzi, and Josè Antenor Pomilio. Design of multiple-input power converter for hybrid vehicles. *IEEE Transactions on Power Electronics*, 20(5):1007–1016, September 2005.

[77] Antoni Szumanowski and Yuhua Chang. Battery management system based on battery nonlinear dynamics modeling. *IEEE Transactions on Vehicular Technology*, 57(3):1425 – 1432, May 2008.

[78] M. Tekin, D. Hissel, M. C. Pera, and J. M. Kauffmann. Energy management strategy for embedded fuel cell system using fuzzy logic. *Proc. of IEEE International Symposium on Industrial Electronics*, 1:501 – 506, May 2004.

[79] Phatiphat Thounthong, Stephane Rael, and Bernard Davat. Energy management of fuel cell / battery / supercapacitor hybrid power source for vehicle applications. *Journal of Power Sources*, 193(1):376 – 385, August 2009.

[80] Maja Harfman Todorovic, Leonardo Palma, and Prasad N. Enjeti. Design of a wide input range dc-dc converter with a robust power control scheme suitable for fuel cell power conversion. *IEEE Transactions on Industrial Electronics*, 55(5): 1247 – 1255, March 2008.

[81] F. Trinidad, C. Gimeno, J. Gutierrez, R. Ruiz, J. Sainz, and J. Valenciano. The vrla modular wound design for 42 v mild hybrid systems. *Journal of Power Sources*, 116(1 - 2):128 – 140, July 2003.

[82] Naomitsu Urasaki, Tomonobu Senjyu, and Katsumi Uezato. An accurate modeling for permanent magnet synchronous motor drives. *Proc. of Applied Power Electronics Conference and Exposition (APEC)*, 1:387 – 392, February 2000.

[83] R.-J. Wai and C.-Y. Lin. High-efficiency, high-step-up dc-dc converter for fuel-cell generation system. *IEE Proceedings - Electric Power Applications*, 152(5):1371–1378, September 2005.

[84] Chien-Ming Wang, Yen-Nien Wang, Chia-Hao Yang, and Alain Berthon. A new zvs-pwm full-bridge step-up / down converter. *Proc. of Industrial Electronics Society Conference (IECON)*, 1:908 – 913, November 2004.

[85] J. Wang, Z. P. Xia, B. Taylor, and D. Howe. Supercapacitor-based torque booster for downsized ice vehicle. *Proc. of International Conference on Power Electronics, Machines and Drives (PEMD)*, 1:55 – 60, March / April 2004.

[86] Robert S. Weissbach and Kevin M. Torres. A noninverting buck-boost converter with reduced components using a microcontroller. *Proc. of IEEE SoutheastCon*, pages 79 – 84, March / April 2001.

[87] S. S. Williamson, A. Khaligh, S. C. Oh, and A. Emadi. Impact of energy storage device selection on the overall drive train efficiency and performance of heavy-duty hybrid vehicles. *Proc. of IEEE Vehicle Power and Propulsion Conference (VPPC)*, September 2005.

[88] Sheldon S. Williamson, Srdjan M. Lukic, and Ali Emadi. Comprehensive drive train efficiency analysis of hybrid electric and fuel cell vehicles based on motor-controller efficiency modeling. *IEEE Transactions on Power Electronics*, 21(3):730 – 740, May 2006.

[89] Ying Wu and Hongwei Gao. Optimization of fuel cell and supercapacitor for fuel-cell electrical vehicles. *IEEE Transactions on Vehicular Technology*, 55(6):1748–1755, November 2006.

[90] Kong Xin and Ashwin M. Khambadkone. Dynamic modelling of fuel cell with power electronic current and performance analysis. *Proc. of International Conference on Power Electronics and Drive Systems (PEDS)*, 1:607 – 612, November 2003.

[91] H. T. Yap, N. Schofield, and C. M. Bingham. Hybrid energy / power sources for electric vehicle traction system. *Proc. of Power Electronics, Machines and Drives conference (PEMD)*, 1(1):61–66, March 2004.

[92] Xiaozi Yuan, Jian Colin Sun, Mauricio Blanco, Haijiang Wang, Jiujun Zhang, and David P. Wilkinson. Ac impedance diagnosis of a 500 w pem fuel cell stack: Part i: Stack impedance. *Journal of Power Sources*, June 2006.

[93] Mounir Zeraoulia, Mohamed El Hachemi Benbouzid, and Demba Diallo. Electric motor drive selection issues for hev propulsion systems: A comparative study. *IEEE Transactions on Vehicular Technology*, 55(6):1756 – 1764, November 2006.

[94] Jianlu Zhang, Jiujun Zhang, Yanghua Tang, Chaojie Song, Titichai Navessin, Zhiqing Shi, Datong Song, Haijiang Wang, David P. Wilkinson, Zhong-Sheng Liu, and Steven Holdcroft. High temperature pem fuel cells. *Journal of Power Sources*, June 2006.

[95] Xuancai Zhu, Dehong Xu, Guoqiao Shen, Danji Xi, K. Mino, and H. Umida. Current-fed dc / dc converter with reverse block igbt for fuel cell distributing power system. *Proc. of Industry Applications Society Annual Meeting (IAS)*, 3:2043 – 2048, October 2005.

[96] Z. Q. Zhu and David Howe. Electrical machines and drives for electric, hybrid, and fuel cell vehicles. *Proceedings of the IEEE*, 95(4):746 – 765, April 2007.

Part V

Appendices

A Publications of the Author

1. **Erik Schaltz**, Jesper Lebæk Jespersen and Peter Omand Rasmussen, "Development of a 400 W High Temperature PEM Fuel Cell Power Pack: Equivalent Circuit Modeling", Proc. of Fuel Cell Seminar, USA, 2006.
2. **Erik Schaltz**, Søren Juhl Andreasen and Peter Omand Rasmussen, "Design of Propulsion System for a Fuel Cell Vehicle", Proc. of European Conference on Power Electronics and Applications (EPE), 2007.
3. **Erik Schaltz**, Peter Omand Rasmussen and Alireza Khaligh, "Non-Inverting Buck-Boost Converter for Fuel Cell Applications", Proc. of Industrial Electronics Society Conference (IECON), pp. 855-860, 2008.
4. **Erik Schaltz**, Alireza Khaligh and Peter Omand Rasmussen, "Investigation of Battery / Ultracapacitor Energy Storage Rating for a Fuel Cell Hybrid Electric Vehicle", Proc. of Vehicle Power and Propulsion Conference (VPPC), pp. 1-6, 2008.
5. **Erik Schaltz**, Peter Omand Rasmussen, "Design and Comparison of Power Systems for a Fuel Cell Hybrid Electric Vehicle", Proc. of IEEE Industrial Applications Society Annual Meeting (IAS), pp. 1-8, 2008.
6. **Erik Schaltz**, Peter Omand Rasmussen and Alireza Khaligh, "Influence of Battery / Ultracapacitor Energy-Storage Sizing on Battery Lifetime in a Fuel Cell Hybrid Electric Vehicle", Transactions on Vehicular Technology, vol. 58, no. 8, pp. 3882-3891, October, 2009.
7. Jesper Lebæk Jespersen, **Erik Schaltz** and Søren Knudsen Kær, "Electrochemical characterization of a polybenzimidazole-based high temperature proton exchange membrane unit cell", Journal of Power Sources, vol. 91, no. 2, pp. 289-296, June, 2009.
8. Zhihao Li, Omer Onar, Alireza Khaligh and **Erik Schaltz**, "Design, control and power management of a battery / ultra-capacitor hybrid system for small electric vehicles", Proc. of Society of Automotive Engineering (SAE), pp. 1-8, 2009.
9. Zhihao Li, Omer Onar, Alireza Khaligh and **Erik Schaltz**, "Design and Control of a Multiple Input DC / DC Converter for Battery / Ultra-capacitor Based Electric Vehicle Power System", Proc. of IEEE Applied Power Electronis Conference and Exposition (APEC), pp. 591-596, USA, 2009.
10. Søren Juhl Andreasen, Jesper Lebæk Jespersen, **Erik Schaltz** and Søren Knudsen Kær, "Characterisation and Modelling of a High Temperature PEM Fuel Cell Stack using Electrochemical Impedance Spectroscopy", Fuel Cells '09, pp. 463-473, 2009.

B Drive Train Modeling of the GMR Truck

In this appendix the drive train of the original lead-acid powered GMR Truck is modeled. The drive train consists of the electric machines, the gear-boxes, and the wheels. The models are necessary in order to calculate the power flow between the terminals of the electric machine and the wheels of the truck.

B.1 Battery

The batteries of the original GMR Truck are of type FT 06 180 1 and are from Exide Technologies®. The specifications of the batteries can be seen in Table B.1.

Battery voltage	6 V
5 h capacity	180 Ah
20 h capacity	210 Ah
Mass	29 kg
Volume	12.7 L
Cycles (EN 60 254-1 / IEC 254-1)	900 cycles

Table B.1: Specifications of the lead-acid batteries used in the GMR Truck.

B.2 Electric Machine

The GMR Truck is equipped with two separately excited motors from CFR in Italy (Type: 151-SB-NV-O, Code: MRD.0307.01).

Motor Data

The details of the motor can be seen in Table B.2.

Modeling

A separately excited DC machine may be split into an electrical and mechanical part. The electrical part is given by

$$v_a = R_a i_a + L_a \frac{di_a}{dt} + \text{sign}(i_a) V_b + e_a \quad [\text{V}] \tag{B.1}$$

$$e_a = k_\phi \omega_s \quad [\text{V}] \tag{B.2}$$

$$v_f = R_f i_f + L_f \frac{di_f}{dt} \quad [\text{V}] \tag{B.3}$$

Rated shaft power	$P_{s,nom}$	$2\,\mathrm{kW}$
Rated armature voltage	$V_{a,nom}$	$36\,\mathrm{V}$
Rated armature current	$I_{a,nom}$	$70\,\mathrm{A}$
Rated shaft speed	$n_{s,nom}$	$2000\,\mathrm{rpm}$
Rated shaft torque	$\tau_{s,nom}$	$9.5\,\mathrm{Nm}$
Minimum field current	$I_{f,min}$	$4\,\mathrm{A}$
Rated field current	$I_{f,nom}$	$8\,\mathrm{A}$
Maximum field current	$I_{f,max}$	$15\,\mathrm{A}$

Table B.2: Specifications of the DC motors of the GMR Truck.

where	v_a	$[\mathrm{V}]$	Armature voltage
	R_a	$[\Omega]$	Armature resistance
	i_a	$[\mathrm{A}]$	Armature current
	L_a	$[\mathrm{H}]$	Armature inductance
	V_b	$[\mathrm{V}]$	Voltage drop across the brushes
	e_a	$[\mathrm{V}]$	Back emf
	k_ϕ	$[\mathrm{V}\cdot\mathrm{s/rad}]$	Machine constant
	ω_s	$[\mathrm{rad/s}]$	Shaft angular velocity
	R_f	$[\Omega]$	Field winding resistance
	i_f	$[\mathrm{A}]$	Field winding current
	L_f	$[\mathrm{H}]$	Field winding inductance

The mechanical part is given by

$$\tau_e = J_s\frac{d\omega_s}{dt} + B_v\omega_s + \text{sign}(\omega_s)\tau_c + \tau_s \qquad [\mathrm{Nm}] \qquad \text{(B.4)}$$

$$= k_\phi i_a \qquad [\mathrm{Nm}] \qquad \text{(B.5)}$$

where	τ_e	$[\mathrm{Nm}]$	Electromechanical torque
	J_s	$[\mathrm{kg}\cdot\mathrm{m}^2]$	Shaft moment of inertia
	B_v	$[\mathrm{Nm}\cdot\mathrm{s/rad}]$	Viscous friction coefficient
	τ_c	$[\mathrm{Nm}]$	Coulomb torque
	τ_s	$[\mathrm{Nm}]$	Shaft torque

Motor Parameter Determination

Several experiments have been done on the motors in order to calculate the electric and mechanical machine parameters in Equation (B.1)-(B.5).

Armature Resistance and Brush Voltage Drop

A current is applied to the armature terminals of the machine and the terminal voltage is measured. No excitation current or shaft load is applied, i.e. the velocity is zero. Therefore Equation (B.1) in steady-state is reduced to

$$V_a = R_a I_a + \text{sign}(I_a)V_b \qquad [\mathrm{V}] \qquad \text{(B.6)}$$

This is a first order polynomial, which also can be seen from the measurements in Figure B.1. From the measurement points a curve fit can be made. The resistance R_a

is then the slope of the curve fit graph and V_b is the value where the armature current is zero.

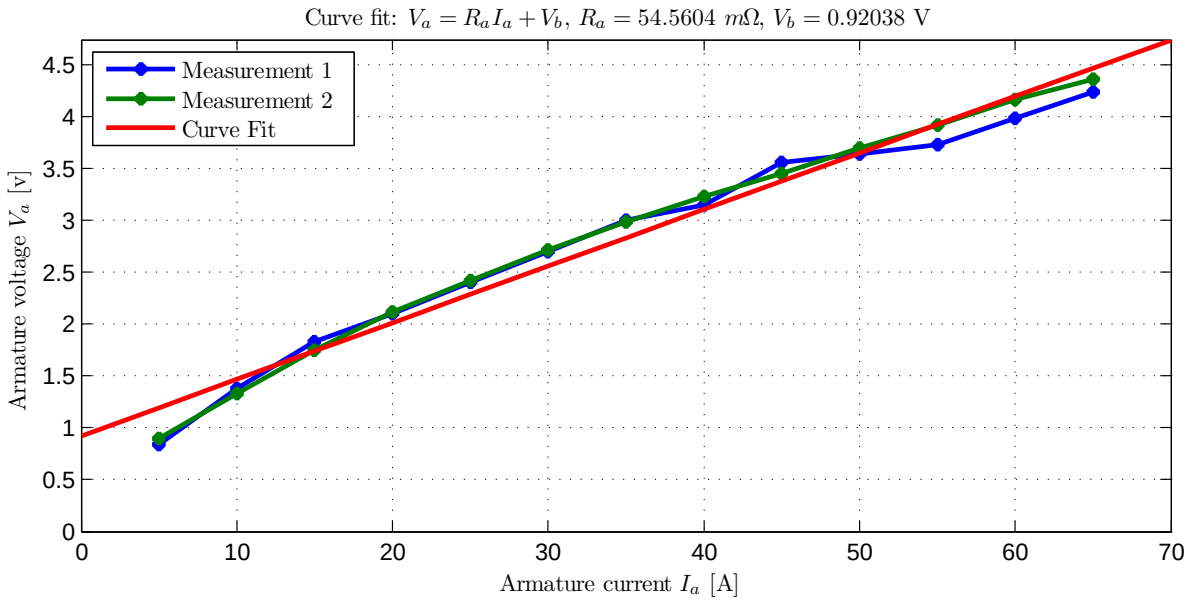

Figure B.1: Armature voltage versus armature current.

Field Winding Resistance

The experiment performed to calculate the field winding resistance is similar to the previous. A current is applied to the field winding and the field winding voltage is measured. No armature current or load shaft is applied. In steady-state Equation (B.3) is reduced to

$$V_f = R_f I_f \qquad [\mathrm{V}] \tag{B.7}$$

The measurement can be seen in Figure B.2.

Machine Constant

In this experiment the machine is driven as a generator by another machine. A constant current is applied to the field winding and the open circuit back-emf is measured at the armature terminals. In this situation Equation (B.1) is reduced to

$$V_a = E_a = k_\phi \omega_s \qquad [\mathrm{V}] \tag{B.8}$$

In Figure B.3(a) the linear relationship between the induced voltage and shaft velocity can be seen. If the speed n_s is converted to angular velocity, i.e. $\omega_s = \frac{2\pi}{60} n_s$, the field constant k_ϕ is the slope of the (ω_s, E_a)-curve. However, as it may be understood from Figure B.3(a) the machine constant depend on the field winding current. For each field winding current the belonging machine constant is calculated. The result is shown in Figure B.3(b). It is seen that the machine constant k_ϕ can be described by a second order polynomial, i.e.

$$k_\phi = \mathrm{sign}(I_f) a_{k_\phi} I_f^2 + b_{k_\phi} + \mathrm{sign}(I_f) c_{k_\phi} \qquad [\mathrm{Vs/rad}] \tag{B.9}$$

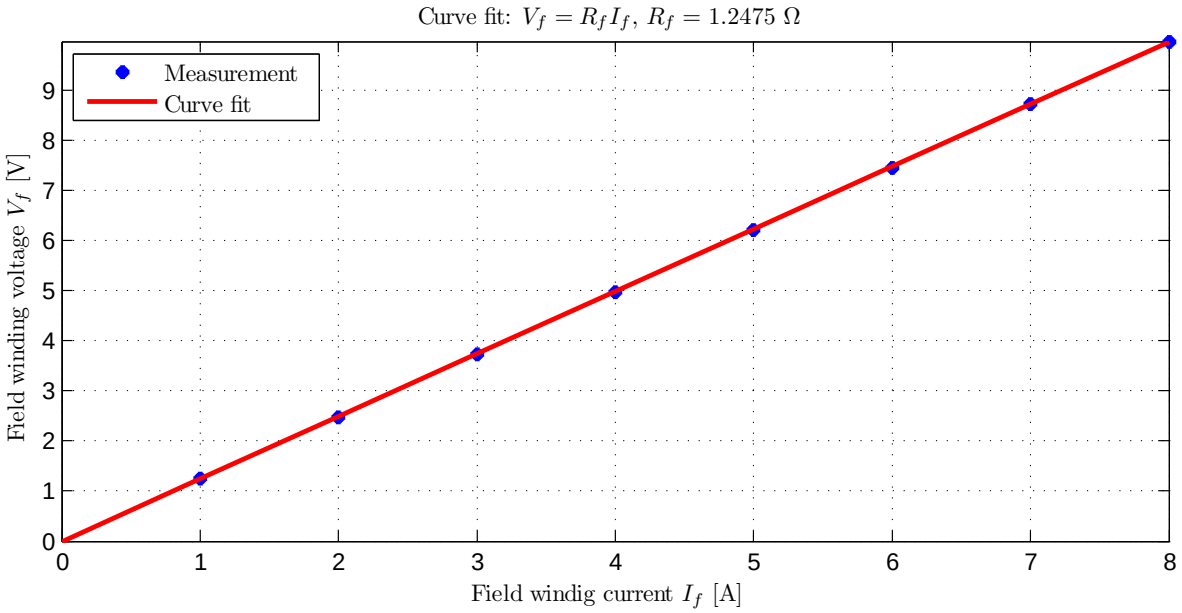

Figure B.2: Field winding voltage versus field winding current.

Viscous Friction Coefficient and Coulomb Torque

The machine is driven in motor-mode but without a shaft load, i.e. $\tau_s = 0\,\mathrm{Nm}$. The armature current, field winding current, and shaft velocity is measured. In steady-state Equation (B.4) is reduced to

$$\tau_e = B_v\omega_s + \mathrm{sign}(\omega_s)\tau_c \qquad [\mathrm{Nm}] \qquad \text{(B.10)}$$

This is a first order polynomial where the viscous friction coefficient is the slope of the (ω_s, τ_e)-curve and the coulomb torque is the offset. The friction coefficient and coulomb torque can be calculated from the measurements shown in Figure B.4.

Shaft Inertia

Again the machine is driven in motor-mode without any load. When the speed has reached steady-state the armature supply is disconnected and the induced voltage at the terminals is measured. In this situation the electromechanical torque is zero and Equation (B.4) is therefore given by

$$0 = J_s\frac{d\omega_s}{dt} + B_v\omega_s + \tau_c \qquad [\mathrm{Nm}] \qquad \text{(B.11)}$$

In Laplace this can be expressed as

$$\begin{aligned} 0 &= J_s\left(s\Omega_s(s) - \omega_s(t=0)\right) + B_v\Omega_s + \frac{1}{s}\tau_c \\ &\Updownarrow \\ \Omega_s(s) &= \frac{1}{s+\frac{B_v}{J_s}}\omega_s(t=0) - \frac{1}{s}\frac{\frac{1}{J_s}}{s+\frac{B_v}{J_s}}\tau_c \end{aligned} \qquad \text{(B.12)}$$

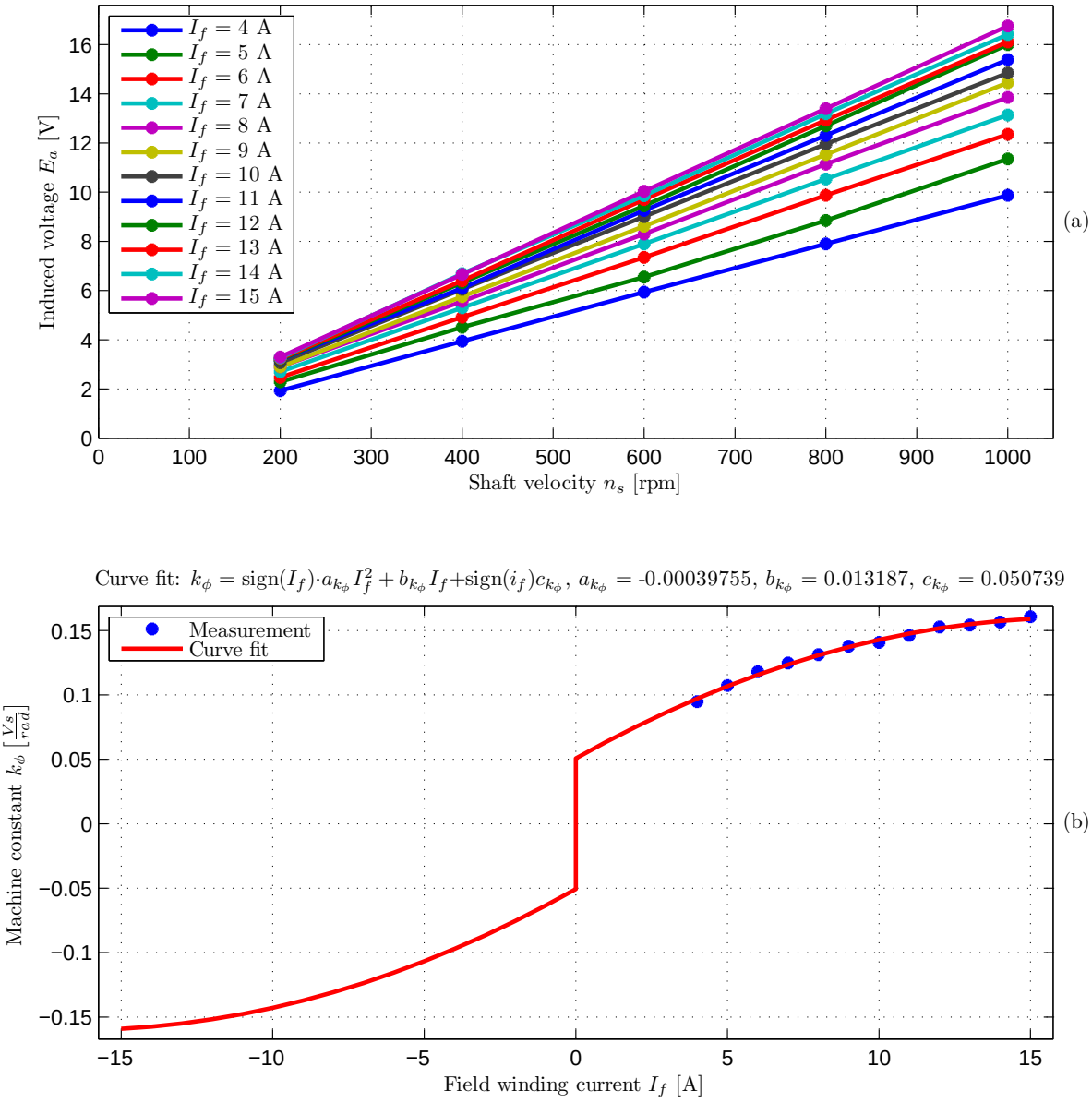

Figure B.3: Determination of machine constant k_ϕ. (a) Back-emf versus shaft velocity for different field winding currents. (b) Machine constant as a function of the field winding current.

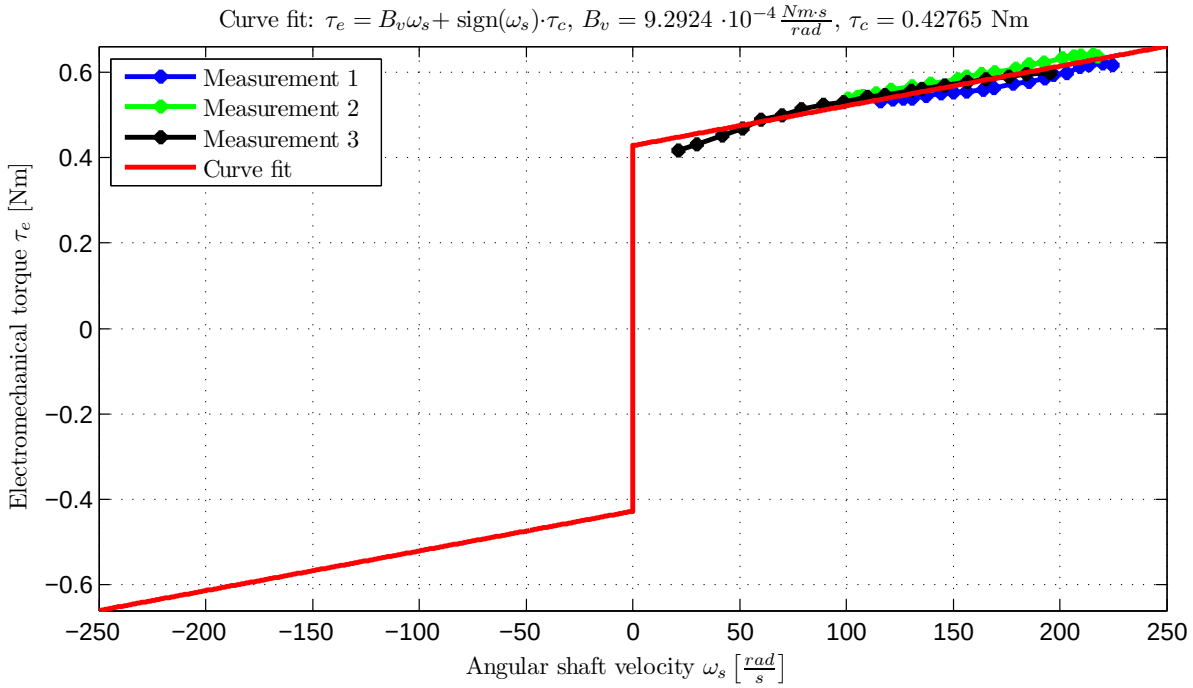

Figure B.4: Electromechanical torque versus the angular shaft velocity in no-load.

By taking the inverse Laplace the inertia can be calculated, i.e.

$$\omega_s = e^{-\frac{B_v}{J_s}t}\left(\omega_s(t=0) + \frac{\tau_c}{B_v}\right) - \frac{\tau_c}{B_v} \qquad [\text{rad/s}] \tag{B.13}$$

$$\Updownarrow$$

$$J_s = -\frac{B_v}{\log\left(\omega_s + \frac{\tau_c}{B_v}\right) - \log\left(\omega_s(t=0) + \frac{\tau_c}{B_v}\right)}t \qquad \left[\text{kg}\cdot\text{m}^2\right] \tag{B.14}$$

The measurement used for calculating the shaft inertia can be seen in Figure B.5.

Summary of Electric Machine Parameters

The calculated parameters are shown in table B.3.

Efficiency

In motor-mode the input power is a contribution of the armature power P_a and the field winding power P_f. The core losses are neglected. By using Equation (B.1)-(B.5) the input power can be written as

$$\begin{aligned} P_{in} &= \underbrace{V_a I_a}_{P_a} + \underbrace{V_f I_f}_{f} = \underbrace{R_a I_a^2 + V_b I_a + k_\phi \omega_s I_a}_{P_a} + \underbrace{R_f I_f^2}_{P_f} \\ &= \underbrace{R_a I_a^2 + V_b I_a + R_f I_f^2}_{P_{Loss}} + \tau_e \omega_s \qquad [\text{W}] \end{aligned} \tag{B.15}$$

For each of the values of the shaft torque τ_s and angular velocity ω_s the electromechanical torque is given by Equation (B.5). The only unknown of the power loss calculation

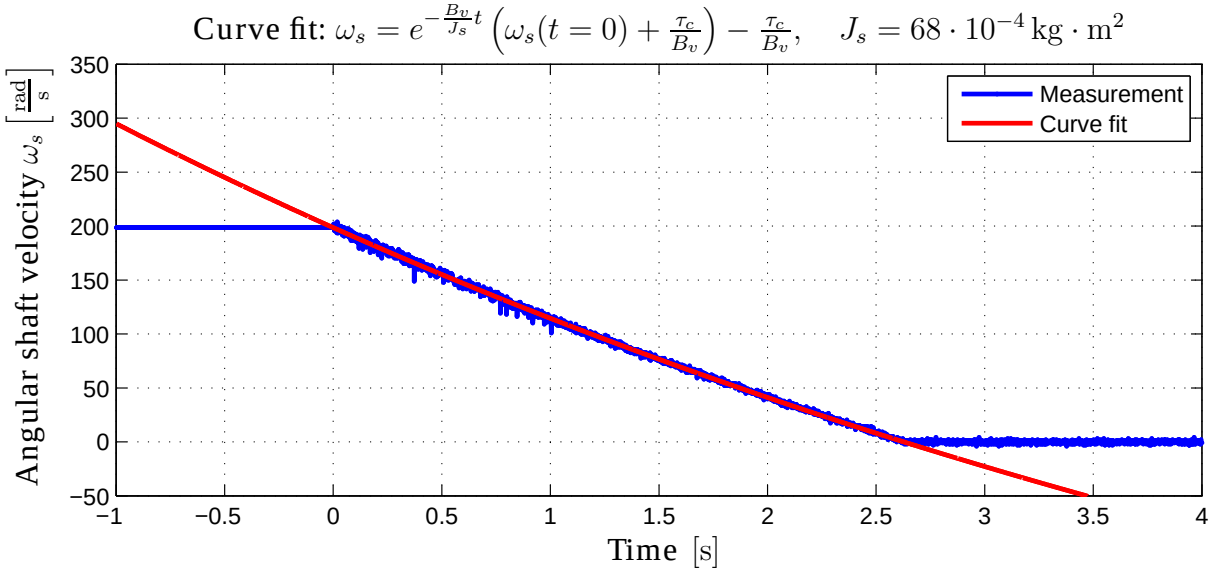

Figure B.5: Angular shaft velocity when applying an inverse step.

Armature resistance	R_a	$54.6\,\mathrm{m\Omega}$ at $20\,^\circ\mathrm{C}$
Brush voltage drop	V_b	$0.92\,\mathrm{V}$
Constant	a_{k_ϕ}	-0.00039755
Constant	b_{k_ϕ}	0.0132
Constant	b_{k_ϕ}	0.0507
Machine constant	k_ϕ	$\mathrm{sign}(i_f)a_{k_\phi}i_f^2 + b_{k_\phi}i_f + \mathrm{sign}(i_f)c_{k_\phi}$
Field winding resistance	R_f	$1.248\,\Omega$ at $20\,^\circ\mathrm{C}$
Shaft moment of inertia	J_s	$68 \cdot 10^{-4}\,\mathrm{kg \cdot m^2}$
Viscous coefficient	B_v	$9.3 \cdot 10^{-4}\,\mathrm{Nm \cdot s/rad}$
Coulomb torque	τ_c	$0.43\,\mathrm{Nm}$

Table B.3: Motor parameters.

in Equation (B.15) are the armature and field winding currents, I_a and I_f respectively. The armature current indirectly depends on the field winding current. In order to maximize the efficiency it is therefore necessary to chose a field winding current that minimizes the power loss P_{Loss} in Equation (B.15), i.e.

$$I_f = \min\left(P_{Loss}\right) \qquad [\mathrm{A}] \tag{B.16}$$

In motor mode the efficiency is

$$\eta = \frac{P_s}{P_{in}} = \frac{\tau_s \omega s}{P_{Loss} + \tau_e \omega_s} \qquad [-] \tag{B.17}$$

The efficiency of the machine in motor-mode for different shaft torques and speeds can be seen in Figure B.6. It can be seen the maximum efficiency is $\eta_{max} \approx 77\,\%$ when the shaft speed and torque are at their nominal values, i.e. $n_{s,nom} = 2000\,\mathrm{rpm}$ and $\tau_{s,nom} = 9.5\,\mathrm{Nm}$.

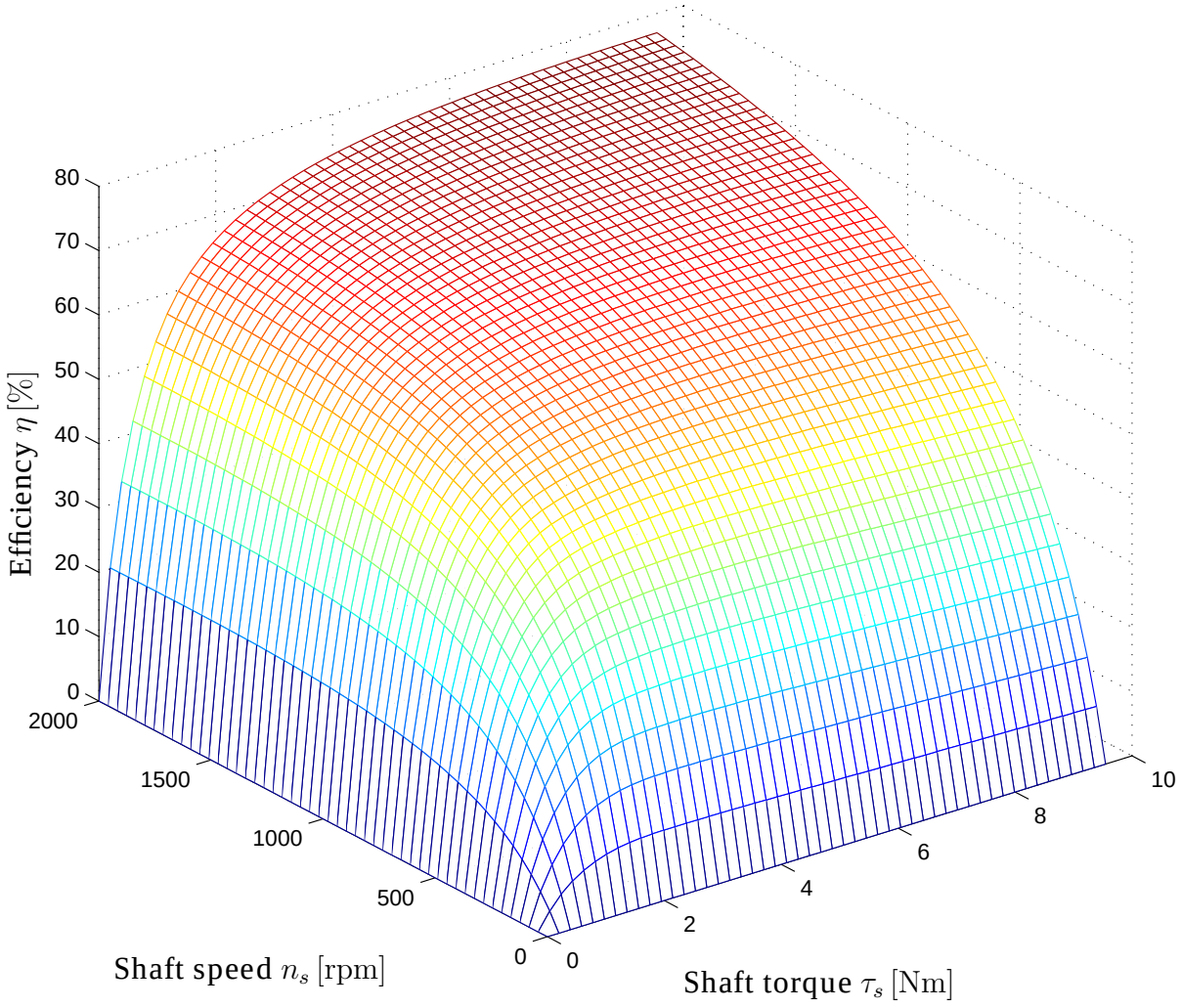

Figure B.6: Theoretical efficiency of the DC motor of the GMR Truck.

B.3 GEAR-BOXES

The electric machines have been modeled in the previous section. This means that when the terminal voltage and the currents of the armature and field winding are known the shaft torque and angular velocity of the electric machine can be calculated. The output power of the electric machines is directed to the wheels through two gear-boxes. In order to be able to calculate how much of the power that actual is transferred to the wheels it is also necessary to model the gear-boxes.

Modeling

The gear-box consist of a small cogwheel (cogwheel 1) that is connected to the motor shaft and a bigger cogwheel (cogwheel 2) that is connected to the wheel of the truck. In Figure B.7(a)-(c) the free body diagram of cogwheel 1, cogwheel 2, and the wheel is shown. It is seen that for each device the input torque have to overcome the torque due to the moment of inertia, viscous friction torque, and coulomb torque in order to produce an output torque. From the free body diagrams the following equations can

be written

$$\tau_s = J_{cw_1}\frac{d\omega_s}{dt} + B_{v,cw_1}\omega_s + \text{sign}(\omega_s)\tau_{c,cw_1} + r_1 f_{cw} \quad [\text{Nm}] \tag{B.18}$$

$$r_2 f_{cw} = J_{cw_2}\frac{d\omega_w}{dt} + B_{v,cw_2}\omega_w + \text{sign}(\omega_w)\tau_{c,cw_2} + \tau_2 \quad [\text{Nm}] \tag{B.19}$$

$$\tau_2 = J_w\frac{d\omega_w}{dt} + B_{v,w}\omega_w + \text{sign}(\omega_w)\tau_{c,w} + \tau_w \quad [\text{Nm}] \tag{B.20}$$

where

τ_s	$[\text{Nm}]$	Shaft torque
τ_2	$[\text{Nm}]$	Torque between cogwheel 2 and the wheel
τ_w	$[\text{Nm}]$	Wheel torque
ω_s	$[\text{rad/s}]$	Shaft angular velocity
ω_w	$[\text{rad/s}]$	Wheel angular velocity
J_{cw_1}	$[\text{kgm}^2]$	Moment of inertia of cogwheel 1
J_{cw_2}	$[\text{kgm}^2]$	Moment of inertia of cogwheel 2
J_w	$[\text{kgm}^2]$	Moment of inertia of the wheel
B_{v,cw_1}	$[\text{Nms/rad}]$	Coulomb friction coefficient of cogwheel 1
B_{v,cw_2}	$[\text{Nms/rad}]$	Coulomb friction coefficient of cogwheel 2
B_w	$[\text{Nms/rad}]$	Coulomb friction coefficient of the wheel
r_1	$[\text{m}]$	Radius of cogwheel 1
r_2	$[\text{m}]$	Radius of cogwheel 2
f_{cw}	$[\text{N}]$	Force between cogwheel 1 and 2
τ_{c,gw_1}	$[\text{Nm}]$	Coulomb torque of cogwheel 1
τ_{c,gw_2}	$[\text{Nm}]$	Coulomb torque of cogwheel 2
$\tau_{c,w}$	$[\text{Nm}]$	Coulomb torque of the wheel

At the intersection between cogwheel 1 and 2 it is assumed that the power is transferred without loss, i.e.

$$r_1 f_{cw}\omega_s = r_2 f_{cw}\omega_w \quad [\text{W}] \tag{B.21}$$

$$\Updownarrow$$

$$G = \frac{\omega_s}{\omega_w} = \frac{r_2}{r_1} \quad [-] \tag{B.22}$$

When manipulating Equation (B.18)-(B.22) one obtains

$$\tau_s = \underbrace{\left(J_{cw_1} + \frac{J_{cw_2} + J_w}{G^2}\right)}_{J^s_{gw}}\frac{d\omega_s}{dt} + \underbrace{\left(B_{v,cw_1} + \frac{B_{v,cw_1} + B_{v,cw_2}}{G^2}\right)}_{B^s_{v,gw}}\omega_s + \text{sign}(\omega_s)\underbrace{\left(\tau_{c,cw_1} + \frac{\tau_{c,cw_2} + \tau_{c,cw_2}}{G}\right)}_{\tau^s_{c,gw}} + \tau^s_w \quad [\text{Nm}] \tag{B.23}$$

$$\tau_w = G\tau^s_w \quad [\text{Nm}] \tag{B.24}$$

where	J^s_{gw}	$[\mathrm{kgm}^2]$	Equivalent moment inertia of the gear-box and wheel seen from the shaft
	$B^s_{v,gw}$	$[\mathrm{Nms/rad}]$	Equivalent viscous frictions coefficient of the gear-box and wheel seen from the shaft
	$\tau^s_{c,gw}$	$[\mathrm{Nm}]$	Equivalent coulomb torque of the gear-box and wheel seen from the shaft
	$G = 15$	$[-]$	Gear ratio
	τ_w	$[\mathrm{Nm}]$	Wheel torque
	τ^s_w	$[\mathrm{Nm}]$	Wheel torque seen from the shaft

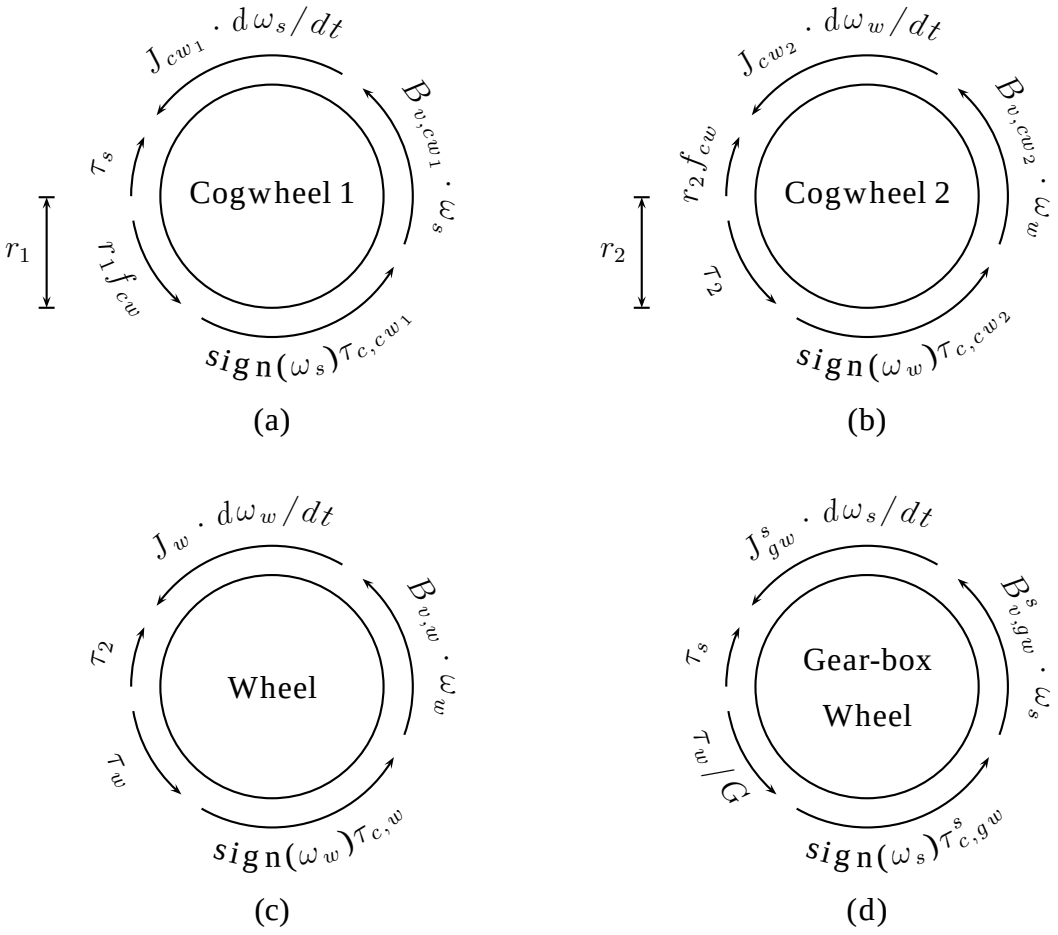

Figure B.7: Modeling of gear-box. (a) Free body diagram of cogwheel 1. (b) Free body diagram of cogwheel 2. (c) Free body diagram of wheel. (d) Shaft-to-wheel free body diagram.

Parameter Determination

In order to determine the parameters of the gear-boxes is one of the electric machines connected to its belonging gear-box and the wheel is spinning in free air.

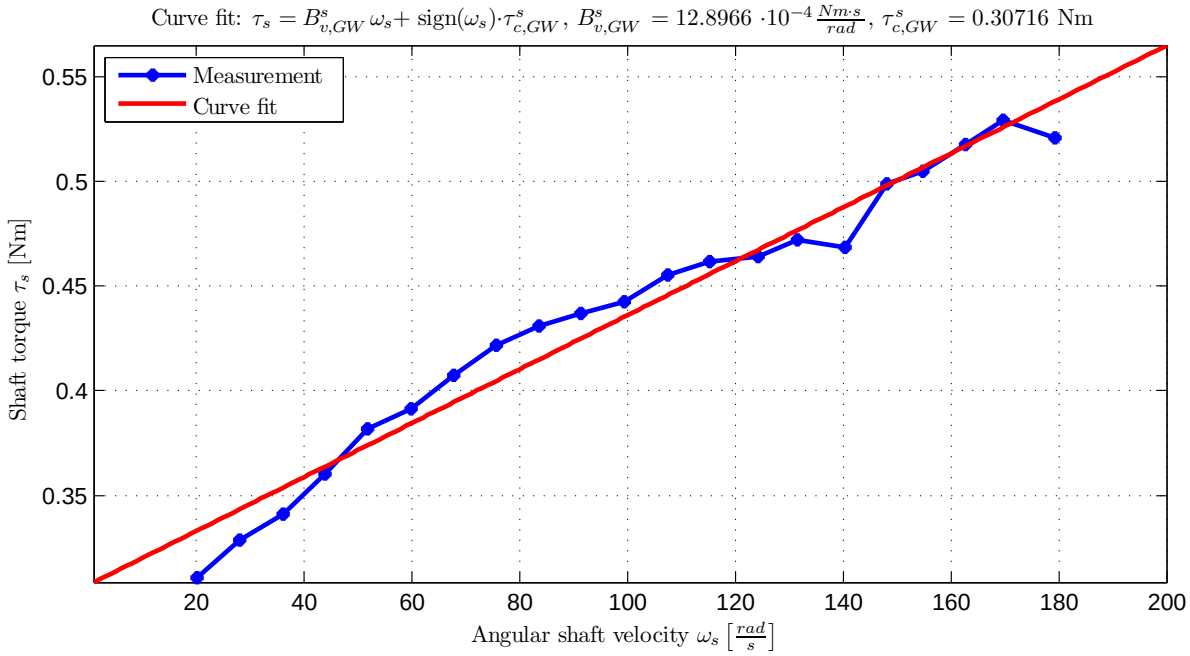

Figure B.8: Shaft torque and angular velocity in no-load.

Viscous Friction Coefficient and Coulomb Torque

This experiment is performed in the same manner as for the experiment carried out to calculate the viscous friction coefficient and coulomb torque of the electric machine. A field current and an armature voltage are applied. If the electromechanical torque is big enough to overcome the sticktion friction the wheel will start to rotate. By manipulating Equation (B.4) and (B.5) the shaft torque in steady-state can be calculated as follows

$$\tau_s = k_\phi I_a - B_v \omega_s - \text{sign}(I_f)\tau_c \qquad [\text{Nm}] \qquad \text{(B.25)}$$

If no wheel torque is applied, i.e. the wheel is rotating in free air, the steady-state shaft torque from Equation (B.23) is reduced to

$$\tau_s = B^s_{v,gw}\omega_s + \text{sign}(\omega_s)\tau^s_{c,gw} \qquad [\text{Nm}] \qquad \text{(B.26)}$$

The shaft torque versus the shaft angular velocity are shown in Figure B.8. The viscous friction coefficient and the coulomb torque can be calculated by identifying the slope and offset of the graph.

Moment of Inertia

The moment of inertia of the gear and wheel J^s_{gw} is calculated in the same way as for the moment of inertia of the shaft. When a steady-state shaft speed is obtained the armature supply is disconnected and the back-emf is measured so the angular shaft speed can be calculated. The result can be seen in Figure B.9.

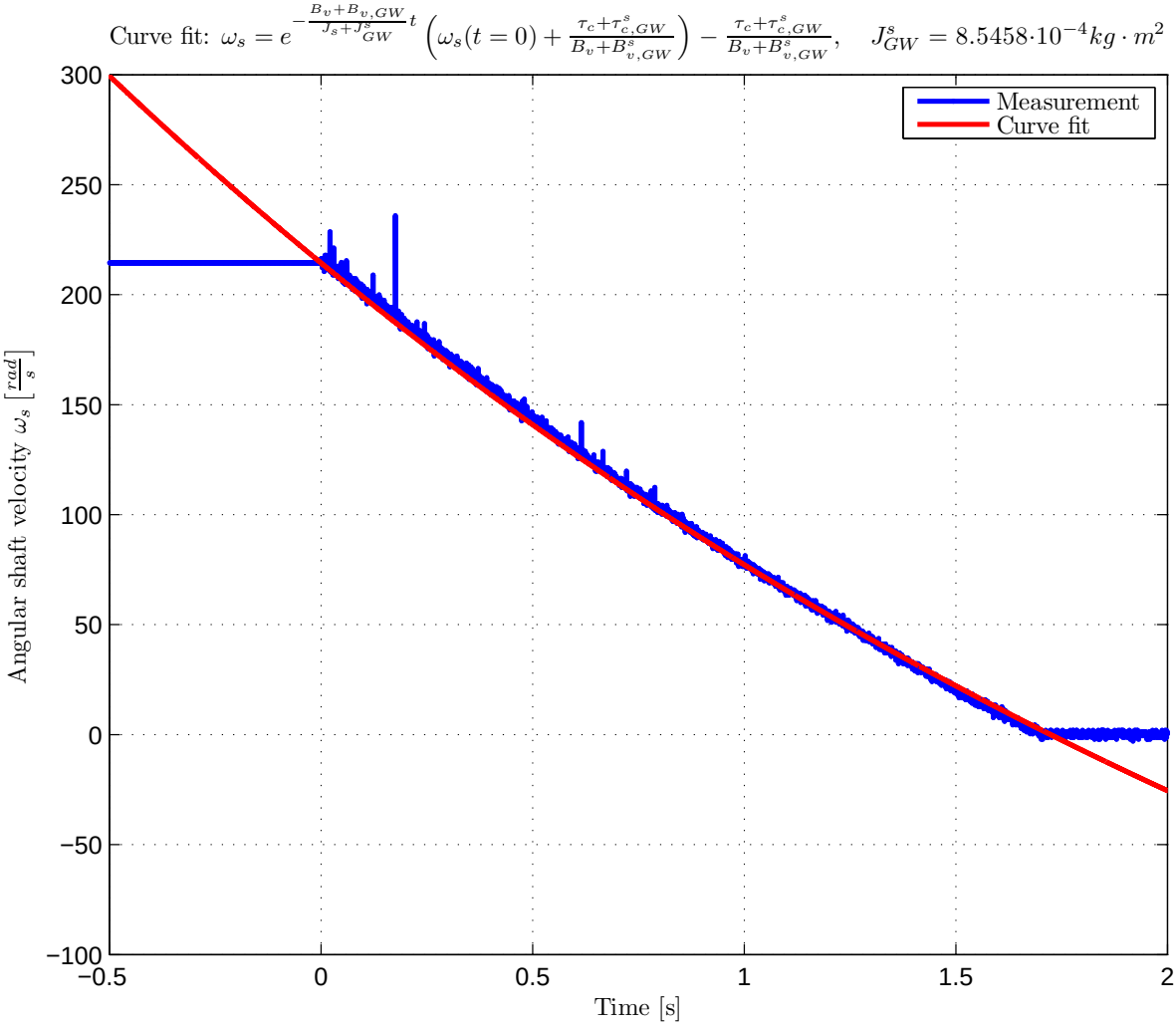

Figure B.9: Inverse step in order to determine the moment of inertia of the gear and wheel.

The angular shaft velocity and moment of inertia are calculated similar to Equation (B.13) and Equation (B.14). Therefore

$$\omega_s = e^{-\frac{B_v+B^s_{v,gw}}{J_s+J^s_{gw}}t}\left(\omega_s(t=0)+\frac{\tau_c+\tau^s_{c,gw}}{B_v+B^s_{v,gw}}\right)-\frac{\tau_c+\tau^s_{c,gw}}{B_v+B^s_{v,gw}} \tag{B.27}$$

$$J^s_{gw} = J_s + \frac{B_v+B^s_{v,gw}}{\log\left(\omega_s+\frac{\tau_c+\tau c,gw^s}{B_v+B^s_{v,gw}}\right)-\log\left(\omega_s(t=0)+\frac{\tau_c+\tau^s_{c,gw}}{B_v+B^s_{v,gw}}\right)}t \tag{B.28}$$

Mass

The equivalent mass of the gear and wheel can be calculated from the kinetic energy, i.e.

$$\frac{1}{2}J^s_{gw}\omega_s^2 = \frac{1}{2}M_{gw}v^2_{Truck} \qquad [\mathrm{J}] \tag{B.29}$$

$$v_{Truck} = \omega_w r_w = \frac{\omega_s}{G}r_w \qquad [\mathrm{m/s}] \tag{B.30}$$

$$\Downarrow$$

$$M_{gw} = J^s_{gw}\left(\frac{G}{r_w}\right)^2 \qquad [\mathrm{kg}] \tag{B.31}$$

where	M_{gw}	$[\mathrm{kg}]$	Mass of wheel and rotating part of gear-box
	v_{Truck}	$[\mathrm{m/s}]$	Truck velocity
	$r_w = 0.224$	$[\mathrm{m}]$	Wheel radius

Summary of Gear-Box Parameters

The parameters of the gear and wheel are shown in Table B.4.

Moment of inertia	J^s_{gw}	$8.55 \cdot 10^{-4}\,\mathrm{kgm^2}$
Mass of gear and wheel	M_{gw}	$3.83\,\mathrm{kg}$
Viscous friction coefficient	$B^s_{v,gw}$	$1.3 \cdot 10^{-3}\,\mathrm{Nms/rad}$
Coulomb friction	$\tau^s_{c,gw}$	$1.04\,\mathrm{Nm}$

Table B.4: Motor parameters.

B.4 CONCLUSION

In this appendix the drive train of the original GMR Truck has been modeled by laboratory experiments. The drive train consists of separately excited DC machines, gear-boxes, and the driving wheels. The models make it possible to calculate the power flow between the electric machine terminals and the driving wheels. The maximum efficiency of the electric machine has been calculated to $\eta_{max} = 77\,\%$.

C Fuel Cell Converter Equations

In this chapter the steady-state equations and transfer functions of the fuel cell converter will be derived for the buck, boost, and buck-boost-modes. Current controllers will also be designed and verified.

C.1 Circuit Diagram

The fuel cell converter is of type non-inverting buck-boost converter, and its circuit diagram can be seen in Figure C.1.

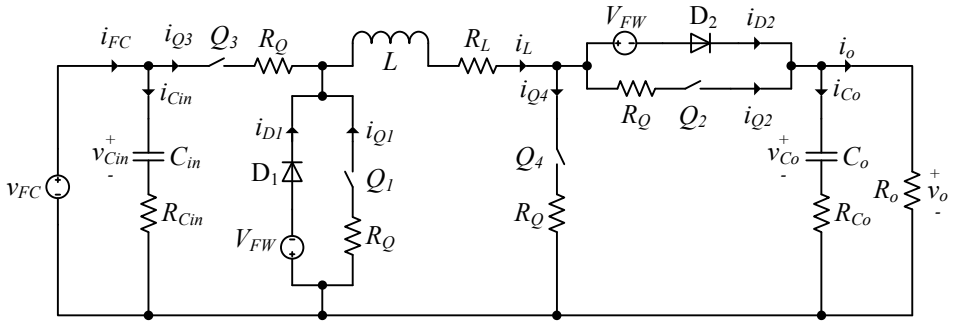

Figure C.1: Equivalent circuit diagram of the non-inverting buck-boost converter.

C.2 Modes of Operation

The inductor current and the gate signals of the switches Q_1-Q_4 can be seen in Figure C.2. The operation modes are shown for buck-mode, boost-mode, and buck-boost-mode, respectively.

C.3 Method

The converter will be derived in the classic way, i.e. [23, 53]

1. Write state equations for all the states of the switches of the converter
2. Average the state equations over the switching period
3. Perturbation of the states by an AC and DC part
4. Dividing the average perturbated state equations into an AC and DC part
5. Converting the AC parts into Laplace domain and derive transfer functions

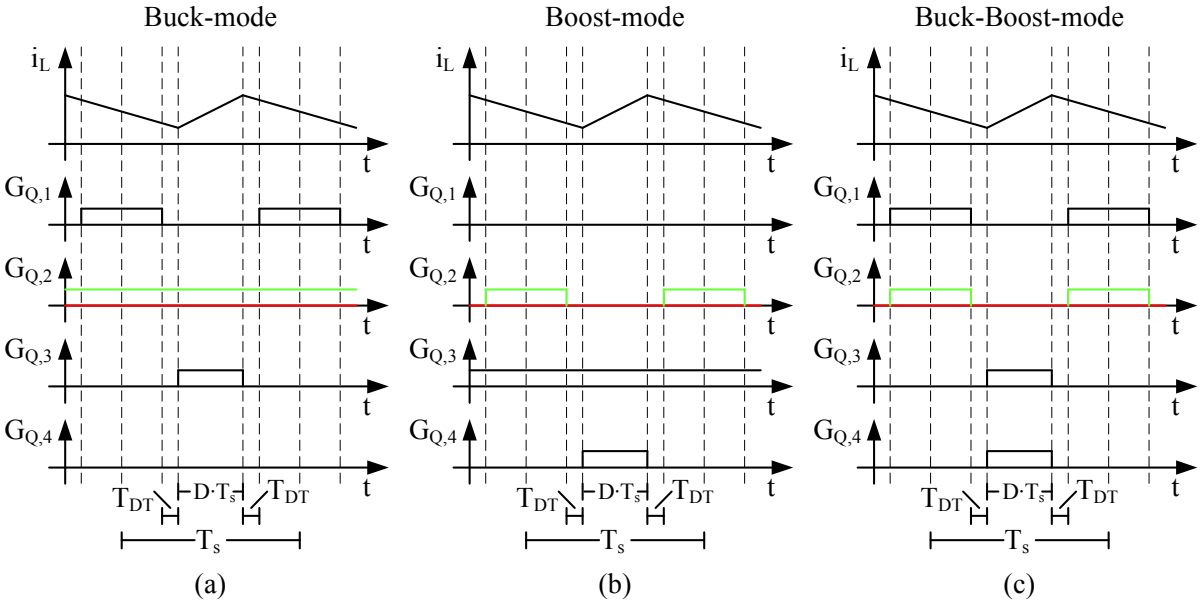

Figure C.2: Inductor current and gate signals due to the operation modes of the non-inverting buck-boost converter. (a) Buck-mode. Red line of G_{Q_2}: Switch-mode 1. Green line of G_{Q_2}: Switch-mode 2. (b) Boost-mode. Red line of G_{Q_2}: Switch-mode 3. Green line of G_{Q_2}: Switch-mode 4. (c) Buck-Boost-mode. Red line of G_{Q_2}: Switch-mode 5. Green line of G_{Q_2}: Switch-mode 6.

The equations and transfer functions are derived for the ideal cases, and for the cases with and without the synchronous rectifier Q_2. It is assumed that the converter is operated in continuous conduction mode (CCM). From the equivalent circuit diagram in Figure C.1 and the switch-pattern in Figure C.2 the method described above can now be followed.

State Equations in Interval dT_s

When using Kirchkow's current and voltage rules one obtains

$$L\frac{di_L}{dt} = \begin{cases} v_{FC} - v_o & \text{Ideal Buck-mode} \\ v_{FC} - v_o - V_{FW} - (R_Q + R_L)i_L & \text{Switch-mode 1} \\ v_{FC} - v_o - (2R_Q + R_L)i_L & \text{Switch-mode 2} \\ v_{FC} & \text{Ideal Boost-mode} \\ v_{FC} - (2R_Q + R_L)i_L & \text{Switch-mode 3-4} \\ v_{FC} & \text{Ideal Buck-Boost-mode} \\ v_{FC} - (2R_Q + R_L)i_L & \text{Switch-mode 5-6} \end{cases} \tag{C.1}$$

$$C_{in}\frac{dv_{C_{in}}}{dt} = i_{FC} - i_L \text{ All modes} \tag{C.2}$$

$$= \begin{cases} C_{in}\frac{dv_{FC}}{dt} & \text{Ideal modes} \\ \frac{v_{FC}-v_{C_{in}}}{R_{C_{in}}} & \text{Switch-mode 1-6} \end{cases} \tag{C.3}$$

$$C_o\frac{dv_{C_o}}{dt} = \begin{cases} i_L - i_o & \text{Buck-mode} \\ -i_o & \text{Boost-mode} \\ -i_o & \text{Buck-Boost-mode} \end{cases} \tag{C.4}$$

$$= \begin{cases} C_o\frac{dv_o}{dt} & \text{Ideal modes} \\ \frac{v_o-v_{C_o}}{R_o} & \text{Switch-modes 1-6} \end{cases} \tag{C.5}$$

State Equations in Interval $(1 - d - 2D_{DT})T_s$

When using Kirchkow's current and voltage rules one obtains

$$L\frac{di_L}{dt} = \begin{cases} -v_o & \text{Ideal Buck-mode} \\ -v_o - V_{FW} - (R_Q + R_L)\, i_L & \text{Switch-mode 1} \\ -v_o - (2R_Q + R_L)\, i_L & \text{Switch-mode 2} \\ v_{FC} - v_o & \text{Ideal Boost-mode} \\ v_{FC} - v_o - V_{FW} - (R_Q + R_L)i_L & \text{Switch-mode 3} \\ v_{FC} - v_o - (2R_Q + R_L)i_L & \text{Switch-mode 4} \\ -v_o & \text{Ideal Buck-Boost-mode} \\ -v_o - V_{FW} - (R_Q + R_L)\, i_L & \text{Switch-mode 5} \\ -v_o - (2R_Q + R_L)\, i_L & \text{Switch-mode 6} \end{cases} \tag{C.6}$$

$$C_{in}\frac{dv_{C_{in}}}{dt} = \begin{cases} i_{FC} & \text{Buck-mode} \\ i_{FC} - i_L & \text{Boost-mode} \\ i_{FC} & \text{Buck-Boost-mode} \end{cases} \tag{C.7}$$

$$= \begin{cases} C_{in}\frac{dv_{FC}}{dt} & \text{Ideal modes} \\ \frac{v_{FC}-v_{C_{in}}}{R_{C_{in}}} & \text{Switch-mode 1-6} \end{cases} \tag{C.8}$$

$$C_o\frac{dv_{C_o}}{dt} = i_L - i_o \text{ All modes} \tag{C.9}$$

$$= \begin{cases} C_o\frac{dv_o}{dt} & \text{Ideal modes} \\ \frac{v_o-v_{C_o}}{R_o} & \text{Switch-modes 1-6} \end{cases} \tag{C.10}$$

State Equations in Interval $D_{DT}T_s$

When using Kirchkow's current and voltage rules one obtains

$$L\frac{di_L}{dt} = \begin{cases} -v_o & \text{Ideal Buck-mode} \\ -2V_{FW} - R_L i_L - v_o & \text{Switch-mode 1} \\ -v_o - V_{FW} - (R_Q + R_L)i_L & \text{Switch-mode 2} \\ v_{FC} - v_o & \text{Ideal Boost-mode} \\ v_{FC} - v_o - V_{FW} - (R_Q + R_L)i_L & \text{Switch-mode 3-4} \\ -v_o & \text{Ideal Buck-Boost-mode} \\ -v_o - 2V_{FW} - R_L i_L & \text{Switch-mode 5-6} \end{cases} \tag{C.11}$$

$$C_{in}\frac{dv_{C_{in}}}{dt} = \begin{cases} i_{FC} & \text{Buck-mode} \\ i_{FC} - i_L & \text{Boost-mode} \\ i_{FC} & \text{Buck-Boost-mode} \end{cases} \tag{C.12}$$

$$= \begin{cases} C_{in}\frac{dv_{FC}}{dt} & \text{Ideal modes} \\ \frac{v_{FC}-v_{C_{in}}}{R_{C_{in}}} & \text{Switch-mode 1-6} \end{cases} \tag{C.13}$$

$$C_o\frac{dv_{C_o}}{dt} = i_L - i_o \text{ All modes} \tag{C.14}$$

$$= \begin{cases} C_o\frac{dv_o}{dt} & \text{Ideal modes} \\ \frac{v_o-v_{C_o}}{R_o} & \text{Switch-modes 1-6} \end{cases} \tag{C.15}$$

Averaging

When averaging in one switching period one obtains

$$
L\left\langle \frac{di_L}{dt} \right\rangle_{T_s} = \begin{cases}
\langle v_{FC} \rangle_{T_s} \langle d \rangle_{T_s} - \langle v_o \rangle_{T_s} & \text{Ideal Buck-mode} \\
\langle v_{FC} \rangle_{T_s} \langle d \rangle_{T_s} - \langle v_o \rangle_{T_s} - V_{FW}\left(1 + 2D_{DT}\right) & \\
- \left(R_Q\left(1 - 2D_{DT}\right) + R_L\right) \langle i_L \rangle_{T_s} & \text{Switch-mode 1} \\
\langle v_{FC} \rangle_{T_s} \langle d \rangle_{T_s} - \langle v_o \rangle_{T_s} - 2V_{FW} D_{DT} - \left(2R_Q\left(1 - D_{DT}\right) + R_L\right) \langle i_L \rangle_{T_s} & \text{Switch-mode 2} \\
\langle v_{FC} \rangle_{T_s} - \langle v_o \rangle_{T_s} \left(1 - \langle d \rangle_{T_s}\right) & \text{Ideal Boost-mode} \\
\langle v_{FC} \rangle_{T_s} - \langle v_o \rangle_{T_s} \left(1 - \langle d \rangle_{T_s}\right) - V_{FW}\left(1 - \langle d \rangle_{T_s}\right) & \\
- \left(R_Q\left(1 + \langle d \rangle_{T_s}\right) + R_L\right) \langle i_L \rangle_{T_s} & \text{Switch-mode 3} \\
\langle v_{FC} \rangle_{T_s} - \langle v_o \rangle_{T_s} \left(1 - \langle d \rangle_{T_s}\right) - 2V_{FW} D_{DT} & \\
- \left(2R_Q\left(1 - D_{DT}\right) + R_L\right) \langle i_L \rangle_{T_s} & \text{Switch-mode 4} \\
\langle v_{FC} \rangle_{T_s} \langle d \rangle_{T_s} - \langle v_o \rangle_{T_s} \left(1 - \langle d \rangle_{T_s}\right) & \text{Ideal Buck-Boost-mode} \\
\langle v_{FC} \rangle_{T_s} \langle d \rangle_{T_s} - \langle v_o \rangle_{T_s} \left(1 - \langle d \rangle_{T_s}\right) - V_{FW}\left(1 - \langle d \rangle_{T_s} + 2D_{DT}\right) & \\
- \left(R_Q\left(1 + \langle d \rangle_{T_s} - 2D_{DT}\right) + R_L\right) \langle i_L \rangle_{T_s} & \text{Switch-mode 5} \\
\langle v_{FC} \rangle_{T_s} \langle d \rangle_{T_s} - \langle v_o \rangle_{T_s} \left(1 - \langle d \rangle_{T_s}\right) - 4V_{FW} D_{DT} & \\
- \left(2R_Q\left(1 - 2D_{DT}\right) + R_L\right) \langle i_L \rangle_{T_s} & \text{Switch-mode 6}
\end{cases} \tag{C.16}
$$

$$C_{in}\left\langle\frac{dv_{C_{in}}}{dt}\right\rangle_{T_s} = \begin{cases} \langle i_{FC}\rangle_{T_s} - \langle i_L\rangle_{T_s}\langle d\rangle_{T_s} & \text{Buck-mode} \\ \langle i_{FC}\rangle_{T_s} - \langle i_L\rangle_{T_s} & \text{Boost-mode} \\ \langle i_{FC}\rangle_{T_s} - \langle i_L\rangle_{T_s}\langle d\rangle_{T_s} & \text{Buck-Boost-mode} \end{cases} \tag{C.17}$$

$$= \begin{cases} C_{in}\left\langle\frac{dv_{FC}}{dt}\right\rangle_{T_s} & \text{Ideal modes} \\ \frac{\langle v_{FC}\rangle_{T_s} - \langle v_{C_{in}}\rangle_{T_s}}{R_{C_{in}}} & \text{Switch-mode 1-6} \end{cases} \tag{C.18}$$

$$C_o\left\langle\frac{dv_{C_o}}{dt}\right\rangle_{T_s} = \begin{cases} \langle i_L\rangle_{T_s} - \langle i_o\rangle_{T_s} & \text{Buck-mode} \\ \langle i_L\rangle_{T_s}\left(1-\langle d\rangle_{T_s}\right) - \langle i_o\rangle_{T_s} & \text{Boost-mode} \\ \langle i_L\rangle_{T_s}\left(1-\langle d\rangle_{T_s}\right) - \langle i_o\rangle_{T_s} & \text{Buck-Boost-mode} \end{cases} \tag{C.19}$$

$$= \begin{cases} C_o\left\langle\frac{dv_o}{dt}\right\rangle_{T_s} & \text{Ideal modes} \\ \frac{\langle v_o\rangle_{T_s} - \langle v_{C_o}\rangle_{T_s}}{R_o} & \text{Switch-modes 1-6} \end{cases} \tag{C.20}$$

Perturbation

For a given operation point each state of the converter can be divided into a DC-part and AC-part, i.e. the state $\langle x\rangle_{T_s} = X + \tilde{x}$ is given by DC-part X and AC-part $\tilde{x}$. Therefore

$$\langle i_L\rangle_{T_s} = I_L + \tilde{i}_L \qquad \langle d\rangle_{T_s} = D_{Q_3} + \tilde{d}_{Q_3} \qquad \langle v_o\rangle_{T_s} = V_o + \tilde{v}_o \tag{C.21}$$

$$\langle v_{C_o}\rangle_{T_s} = V_{C_o} + \tilde{v}_{C_o} \qquad \langle v_{C_{in}}\rangle_{T_s} = V_{C_{in}} + \tilde{v}_{C_{in}} \qquad \langle v_{FC}\rangle_{T_s} = V_{FC} + \tilde{v}_{FC} \tag{C.22}$$

The perturbations are inserted in the average equations. If two average signals are multiplied, the non-linear part will be ignored, as it is assumed that it is negligible, i.e.

$$\langle x\rangle_{T_s}\langle y\rangle_{T_s} = (X+\tilde{x})(Y+\tilde{y}) = \underbrace{XY}_{\text{DC-part}} + \underbrace{Y\tilde{x} + X\tilde{y}}_{\text{AC-part}} + \underbrace{\tilde{x}\tilde{y}}_{\approx 0} \tag{C.23}$$

When the perturbations are inserted in the average equations, the result is divided into a DC-part and AC-part.

The DC-Parts are extracted from the average equations:

$$D = \begin{cases} \frac{V_o}{V_{FC}} & \text{Ideal Buck-mode} \\ \frac{V_o+V_{FW}(1+2D_{DT})+\sqrt{(V_o+V_{FW}(1+2D_{DT}))^2+4V_{FC}I_{FC}\left(R_Q(1-2D_{DT})+R_L\right)}}{2V_{FC}} & \text{Switch-mode 1} \\ \frac{V_o+2V_{FW}D_{DT}+\sqrt{(V_o+2V_{FW}D_{DT})^2+4V_{FC}I_{FC}\left(2R_Q(1-D_{DT})+R_L\right)}}{2V_{FC}} & \text{Switch-mode 2} \\ \frac{V_o-V_{FC}}{V_o} & \text{Ideal Boost-mode} \\ \frac{V_o+V_{FW}-V_{FC}+\left(R_Q+R_L\right)I_{FC}}{V_o+V_{FW}-R_QI_{FC}} & \text{Switch-mode 3} \\ \frac{V_o-V_{FC}+2V_{FW}D_{DT}+\left(2R_Q(1-D_{DT})+R_L\right)I_{FC}}{V_o} & \text{Switch-mode 4} \\ \frac{V_o}{V_{FC}+V_o} & \text{Ideal Buck-Boost-mode} \\ \frac{V_o+V_{FW}(1+2D_{DT})+I_{FC}R_Q}{2(V_{FC}+V_o+V_{FW})} + \frac{\sqrt{\left(V_o+V_{FW}(1+2D_{DT})+I_{FC}R_Q\right)^2+4(V_{FC}+V_o+V_{FW})I_{FC}\left(R_Q(1-2D_{DT})+R_L\right)}}{2(V_{FC}+V_o+V_{FW})} & \text{Switch-mode 5} \\ \frac{V_o+4V_{FW}D_{DT}+\sqrt{(V_o+4V_{FW}D_{DT})^2+4(V_{FC}+V_o)I_{FC}\left(2R_Q(1-2D_{DT})+R_L\right)}}{2(V_{FC}+V_o)} & \text{Switch-mode 6} \end{cases} \tag{C.24}$$

$$I_L = \begin{cases} \frac{I_{FC}}{D} & \text{Buck-mode} \\ I_{FC} & \text{Boost-mode} \\ \frac{I_{FC}}{D} & \text{Buck-Boost-mode} \end{cases} \tag{C.25}$$

$$I_o = \begin{cases} I_L & \text{Buck-mode} \\ I_L\,(1-D) & \text{Boost-mode} \\ I_L\,(1-D) & \text{Buck-Boost-mode} \end{cases} \tag{C.26}$$

$$V_{FC} = V_{C_{in}} \text{ All modes} \tag{C.27}$$

$$V_o = V_{C_o} \text{ All modes} \tag{C.28}$$

The AC-parts are extracted from the average equations, i.e.

$$L\frac{d\tilde{i}_L}{dt} = \begin{cases} D\tilde{v}_{FC} + V_{FC}\tilde{d} - \tilde{v}_o & \text{Ideal Buck-mode} \\ D\tilde{v}_{FC} + V_{FC}\tilde{d} - \tilde{v}_o - \left(R_Q\left(1-2D_{DT}\right)+R_L\right)\tilde{i}_L & \text{Switch-mode 1} \\ D\tilde{v}_{FC} + V_{FC}\tilde{d} - \tilde{v}_o - \left(2R_Q\left(1-D_{DT}\right)+R_L\right)\tilde{i}_L & \text{Switch-mode 2} \\ \tilde{v}_{FC} + V_o\tilde{d} - \left(1-D\right)\tilde{v}_o & \text{Ideal Boost-mode} \\ \tilde{v}_{FC} + V_o\tilde{d} - \left(1-D\right)\tilde{v}_o + V_{FW}\tilde{d} - \left(R_Q\left(1+D\right)+R_L\right)\tilde{i}_L - I_L R_Q\tilde{d} & \text{Switch-mode 3} \\ \tilde{v}_{FC} + V_o\tilde{d} - \left(1-D\right)\tilde{v}_o - \left(2R_Q\left(1-D_{DT}\right)+R_L\right)\tilde{i}_L & \text{Switch-mode 4} \\ D\tilde{v}_{FC} + \left(V_{FC}+V_o\right)\tilde{d} - \left(1-D\right)\tilde{v}_o & \text{Ideal Buck-Boost-mode} \\ D\tilde{v}_{FC} + \left(V_{FC}+V_o+V_{FW}-I_L R_Q\right)\tilde{d} - \left(1-D\right)\tilde{v}_o & \\ \quad - \left(R_Q\left(1+D-2D_{DT}\right)+R_L\right)\tilde{i}_L & \text{Switch-mode 5} \\ D\tilde{v}_{FC} + \left(V_{FC}+V_o\right)\tilde{d} - \left(1-D\right)\tilde{v}_o - \left(2R_Q\left(1-2D_{DT}\right)+R_L\right)\tilde{i}_L & \text{Switch-mode 6} \end{cases} \tag{C.29}$$

$$C_{in}\frac{d\tilde{v}_{C_{in}}}{dt} = \begin{cases} \tilde{i}_{FC} - \tilde{i}_L D - I_L\tilde{d} & \text{Buck-mode} \\ \tilde{i}_{FC} - \tilde{i}_L & \text{Boost-mode} \\ \tilde{i}_{FC} - \tilde{i}_L D - I_L\tilde{d} & \text{Buck-Boost-mode} \end{cases} \tag{C.30}$$

$$= \begin{cases} C_{in}\frac{d\tilde{v}_{FC}}{dt} & \text{Ideal modes} \\ \frac{\tilde{v}_{FC}-\tilde{v}_{C_{in}}}{R_{C_{in}}} & \text{Switch-mode 1-6} \end{cases} \tag{C.31}$$

$$C_o\frac{d\tilde{v}_{C_o}}{dt} = \begin{cases} \tilde{i}_L - \tilde{i}_o & \text{Buck-mode} \\ \left(1-D\right)\tilde{i}_L - I_L\tilde{d} - \tilde{i}_o & \text{Boost-mode} \\ \left(1-D\right)\tilde{i}_L - I_L\tilde{d} - \tilde{i}_o & \text{Buck-Boost-mode} \end{cases} \tag{C.32}$$

$$= \begin{cases} C_o\frac{d\tilde{v}_o}{dt} & \text{Ideal modes} \\ \frac{\tilde{v}_o-\tilde{v}_{C_o}}{R_o} & \text{Switch-modes 1-6} \end{cases} \tag{C.33}$$

The small-signal equations are converted into Laplace. Therefore

$$
LsI_L(s) = \begin{cases}
DV_{FC}(s) + V_{FC}D(s) - V_o(s) & \text{Ideal Buck-mode} \\
DV_{FC}(s) + V_{FC}D(s) - V_o(s) - \left(R_Q\left(1-2D_{DT}\right)+R_L\right)I_L(s) & \text{Switch-mode 1} \\
DV_{FC}(s) + V_{FC}D(s) - V_o(s) - \left(2R_Q\left(1-D_{DT}\right)+R_L\right)I_L(s) & \text{Switch-mode 2} \\
V_{FC}(s) + V_oD(s) - \left(1-D\right)V_o(s) & \text{Ideal Boost-mode} \\
V_{FC}(s) + V_oD(s) - \left(1-D\right)V_o(s) + V_{FW}D(s) & \\
\quad - \left(R_Q\left(1+D\right)+R_L\right)I_L(s) - I_LR_QD(s) & \text{Switch-mode 3} \\
V_{FC}(s) + V_oD(s) - \left(1-D\right)V_o(s) - \left(2R_Q\left(1-D_{DT}\right)+R_L\right)I_L(s) & \text{Switch-mode 4} \\
DV_{FC}(s) + \left(V_{FC}+V_o\right)D(s) - \left(1-D\right)V_o(s) & \text{Ideal Buck-Boost-mode} \\
DV_{FC}(s) + \left(V_{FC}+V_o+V_{FW}-I_LR_Q\right)D(s) - \left(1-D\right)V_o(s) & \\
\quad - \left(R_Q\left(1+D-2D_{DT}\right)+R_L\right)I_L(s) & \text{Switch-mode 5} \\
DV_{FC}(s) + \left(V_{FC}+V_o\right)D(s) - \left(1-D\right)V_o(s) & \\
\quad - \left(2R_Q\left(1-2D_{DT}\right)+R_L\right)I_L(s) & \text{Switch-mode 6}
\end{cases} \tag{C.34}
$$

$$
C_{in}sV_{C_{in}}(s) = \begin{cases}
I_{FC}(s) - I_L(s)D - I_LD(s) & \text{Buck-mode} \\
I_{FC}(s) - I_L(s) & \text{Boost-mode} \\
I_{FC}(s) - I_L(s)D - I_LD(s) & \text{Buck-Boost-mode}
\end{cases} \tag{C.35}
$$

$$
= \begin{cases}
C_{in}sV_{FC}(s) & \text{Ideal modes} \\
\frac{V_{FC}(s)-V_{C_{in}}(s)}{R_{C_{in}}} & \text{Switch-mode 1-6}
\end{cases} \tag{C.36}
$$

$$
C_osV_{C_o}(s) = \begin{cases}
I_L(s) - \frac{V_o(s)}{R_o} & \text{Buck-mode} \\
\left(1-D\right)I_L(s) - I_LD(s) - \frac{V_o(s)}{R_o} & \text{Boost-mode} \\
\left(1-D\right)I_L(s) - I_LD(s) - \frac{V_o(s)}{R_o} & \text{Buck-Boost-mode}
\end{cases} \tag{C.37}
$$

$$
= \begin{cases}
C_osV_o(s) & \text{Ideal modes} \\
\frac{V_o(s)-V_{C_o}(s)}{R_o} & \text{Switch-modes 1-6}
\end{cases} \tag{C.38}
$$

Transfer functions

The duty cycle-to-inductor current transfer function is derived by neglecting the contribution from the input source, i.e. $V_{FC}(s) = 0$. Thereby, the transfer functions in Table C.1 is obtained.

C.4 CURRENT CONTROLLER

In order to cancel out the poles of the duty cycle to inductor current transfer function $\frac{I_L(s)}{D_{Q_3}(s)}$ the poles of this transfer function will be the zeros of the controller. In order to improve the low-frequency gain and to sufficiently damp the high-frequency gain of the controller a double integrator has been included in the denominator of the controller. The digital controller is obtained by discretizing the continuous controller by Tustin's method.

The block diagram of the current controller can be seen in Figure C.3.

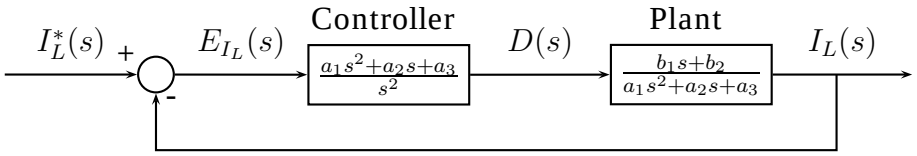

Figure C.3: Block diagram inductor current controller.

The sampling frequency has been set to the same as the switching frequency, i.e. $f_s = 25\,\mathrm{kHz}$. The closed loop bandwidth should therefore be at least 30 times slower in order to insure that the performance of the digital controller will match that of a continuous controller [28]. It is desired that the current drawn from the fuel cell should be nice and smoothly. Therefore the current controller of the fuel cell converter does not need to be very fast. It has been decided to design the current controllers with a bandwidth of $f_{i,BW} = \frac{f_s}{600} \approx 41.5\,\mathrm{Hz}$. This provides a satisfactory performance of the controller in all the points of operation [76].

The magnitude and phase of the duty cycle-to-inductor current transfer function is shown in Figure C.4 (a) and (c), respectively. It can be seen that at the pole there is a difference between the ideal transfer function and the detailed transfer function of approximately $10\,\mathrm{dB}$. The magnitude and phase of the closed loop inductor current transfer function can be seen in Figure C.4 (b) and (d), respectively. It can be seen that only in the detailed transfer function the dominating pole is sufficiently damped.

The bode plots of the duty cycle-to-inductor current transfer function and closed loop inductor current in boost-mode are shown in Figure C.5.

The bode plots of the duty cycle-to-inductor current transfer function and closed loop inductor current in buck-boost-mode are shown in Figure C.6.

Verification of Current Controllers

Discrete current controllers for the three modes of operation have been implemented in a DSP and in Saber®. A simulated and measured step response of the inductor current in three different modes can be seen in Figure C.7(a)-(f). It is seen that simulations and measurements fit very well. However, generally the inductor ripple current

Ideal Buck-mode:
$\frac{I_L(s)}{D(s)} = \frac{V_{FC}R_oC_os+V_{FC}}{LR_oC_os^2+Ls+R_o}$
Switch-mode 1:
$\frac{I_L(s)}{D(s)} = \frac{V_{FC}(R_{C_o}+R_o)C_os+V_{FC}}{L(R_{C_o}+R_o)C_os^2+\left(L+\left(R_Q(1-2D_{DT})+R_L\right)(R_{C_o}+R_o)+R_{C_o}R_o\right)C_o)s+R_Q(1-2D_{DT})+R_L+R_o}$
Switch-mode 2:
$\frac{I_L(s)}{D(s)} = \frac{V_{FC}(R_{C_o}+R_o)C_os+V_{FC}}{L(R_{C_o}+R_o)C_os^2+\left(L+\left(2R_Q(1-D_{DT})+R_L\right)(R_{C_o}+R_o)+R_{C_o}R_o\right)C_o)s+2R_Q(1-D_{DT})+R_L+R_o}$
Ideal Boost-mode:
$\frac{I_L(s)}{D(s)} = \frac{V_oR_oC_os+2V_o}{LR_oC_os^2+L+\left(1-D_{Q_4}\right)^2R_o}$
Switch-mode 3:
$\frac{I_L(s)}{D(s)} = \frac{\left((V_o+V_{FW}-I_LR_Q\right)(R_{C_o}+R_o)+V_oR_{C_o})C_os+2V_o+V_{FW}-I_LR_Q}{L(R_{C_o}+R_o)C_os^2+\left(L+\left(R_Q\left(1+D_{Q_4}\right)+R_L\right)(R_{C_o}+R_o)+\left(1-D_{Q_4}\right)^2R_oR_{C_o}\right)C_o\right)s+R_Q(1+D)+R_L+\left(1-D_{Q_4}\right)^2R_o}$
Switch-mode 4:
$\frac{I_L(s)}{D(s)} = \frac{V_o(2R_{C_o}+R_o)C_os+2V_o}{L(R_{C_o}+R_o)C_os^2+\left(L+\left(\left(2R_Q(1-D_{DT})+R_L\right)(R_{C_o}+R_o)+\left(1-D_{Q_4}\right)^2R_oR_{C_o}\right)C_o\right)s+2R_Q(1-D_{DT})+R_L+\left(1-D_{Q_4}\right)^2R_o}$
Ideal Buck-Boost-mode:
$\frac{I_L(s)}{D(s)} = \frac{(V_{FC}+V_o)R_oC_os+V_{FC}+2V_o}{LR_oC_os^2+Ls+(1-D)^2R_o}$
Switch-mode 5:
$\frac{I_L(s)}{D(s)} = \frac{\left((V_{FC}+V_o+V_{FW}-I_LR_Q\right)(R_{C_o}+R_o)+V_oR_{C_o})C_os+V_{FC}+2V_o+V_{FW}-I_LR_Q}{L(R_{C_o}+R_o)C_os^2+\left(L+\left(\left(R_Q\left(1+D_{Q_{34}}-2D_{DT}\right)+R_L\right)(R_{C_o}+R_o)+\left(1-D_{Q_{34}}\right)^2R_{C_o}R_o\right)C_o\right)s+R_Q(1+D-2D_{DT})+R_L+\left(1-D_{Q_{34}}\right)^2R_o}$
Switch-mode 6:
$\frac{I_L(s)}{D(s)} = \frac{((V_{FC}+V_o)(R_{C_o}+R_o)+V_oR_{C_o})C_os+V_{FC}+2V_o}{L(R_{C_o}+R_o)C_os^2+\left(L+\left(\left(2R_Q(1-2D_{DT})+R_L\right)(R_{C_o}+R_o)+\left(1-D_{Q_{34}}\right)^2R_{C_o}R_o\right)C_o\right)s+2R_Q(1-2D_{DT})+R_L+\left(1-D_{Q_{34}}\right)^2R_o}$

Table C.1: Duty cycle-to-inductor current transfer functions.

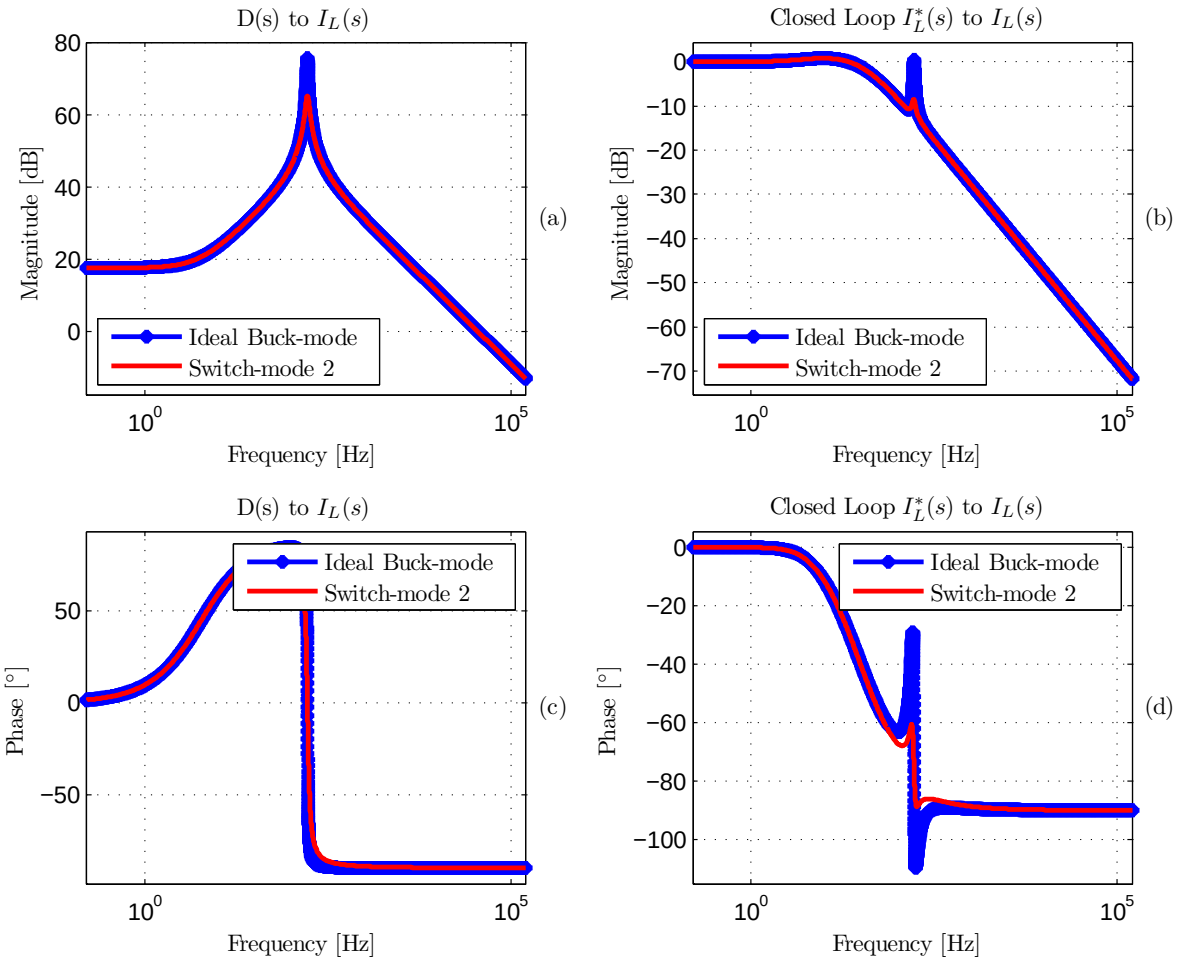

Figure C.4: Ideal and detailed bode plots of the converter in buck-mode. (a) Magnitude of control-to-output transfer function. (b) Magnitude of closed-loop transfer function. (c) Phase of control-to-output transfer function. (d) Phase of closed-loop transfer function.

seems to be higher in the simulation, than in the measurements. This could either be because the actual inductance was higher than specified, or because of the relatively low sampling frequency of the oscilloscope. The switching frequency of the converter is in Table 6.3 specified to be $f_s = 25\,\text{kHz}$. The oscilloscope can only save 10,000 samples spread over the $100\,\text{ms}$ shown in Figure C.7. This means that the sampling frequency of the oscilloscope is four times higher than the switching frequency. It is therefore not sure, that the oscilloscope catches the peaks and buttons of the inductor current.

C.5 CONCLUSION

In this appendix detailed transfer functions and steady-state equations of the non-inverting buck-boost-converter have been derived for the buck-mode, boost-mode, and buck-boost-mode. Current controllers for the three modes have been designed, and verified by simulation and laboratory experiments.

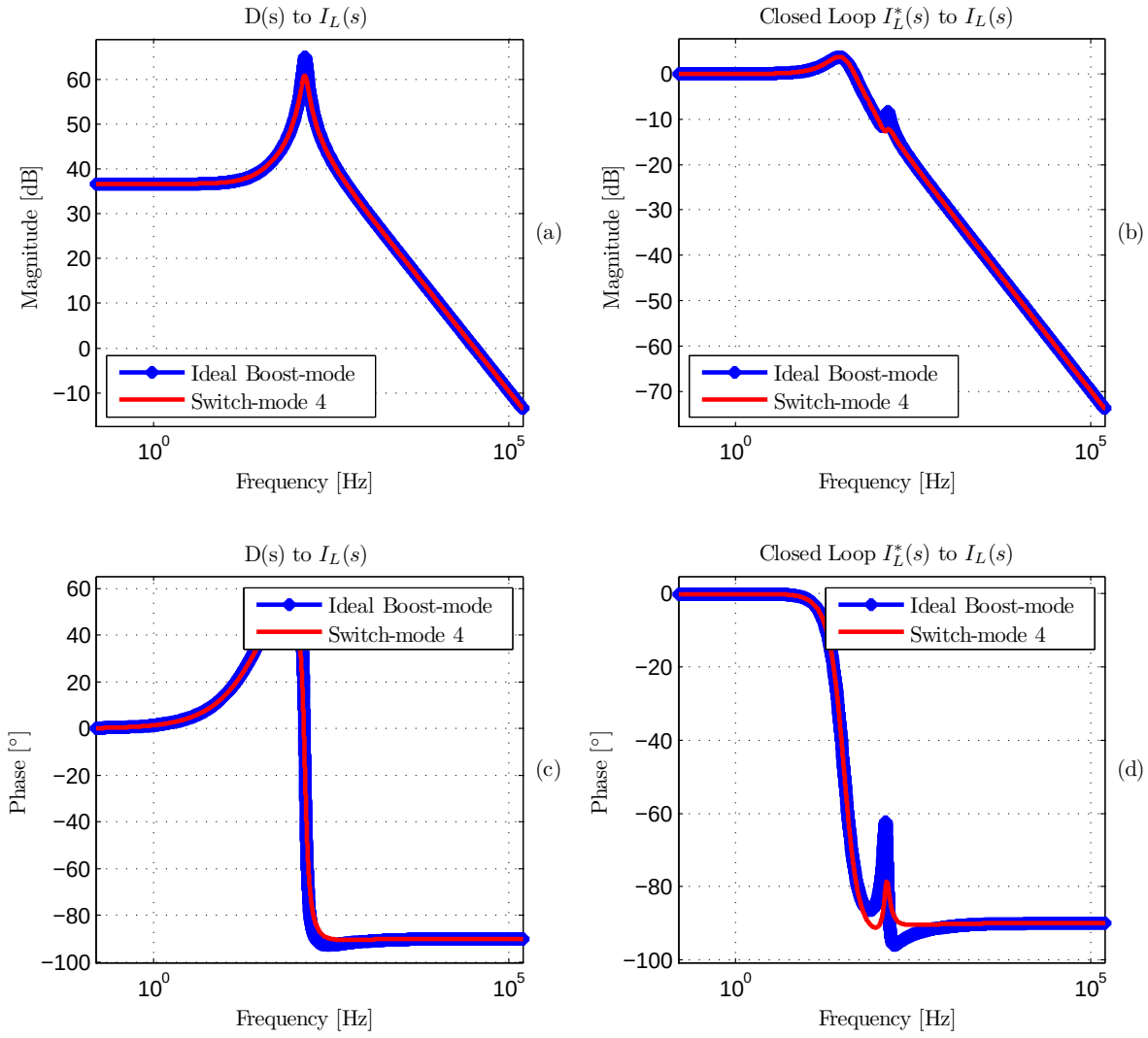

Figure C.5: Ideal and detailed bode plots of the converter in boost-mode. (a) Magnitude of control-to-output transfer function. (b) Magnitude of closed-loop transfer function. (c) Phase of control-to-output transfer function. (d) Phase of closed-loop transfer function.

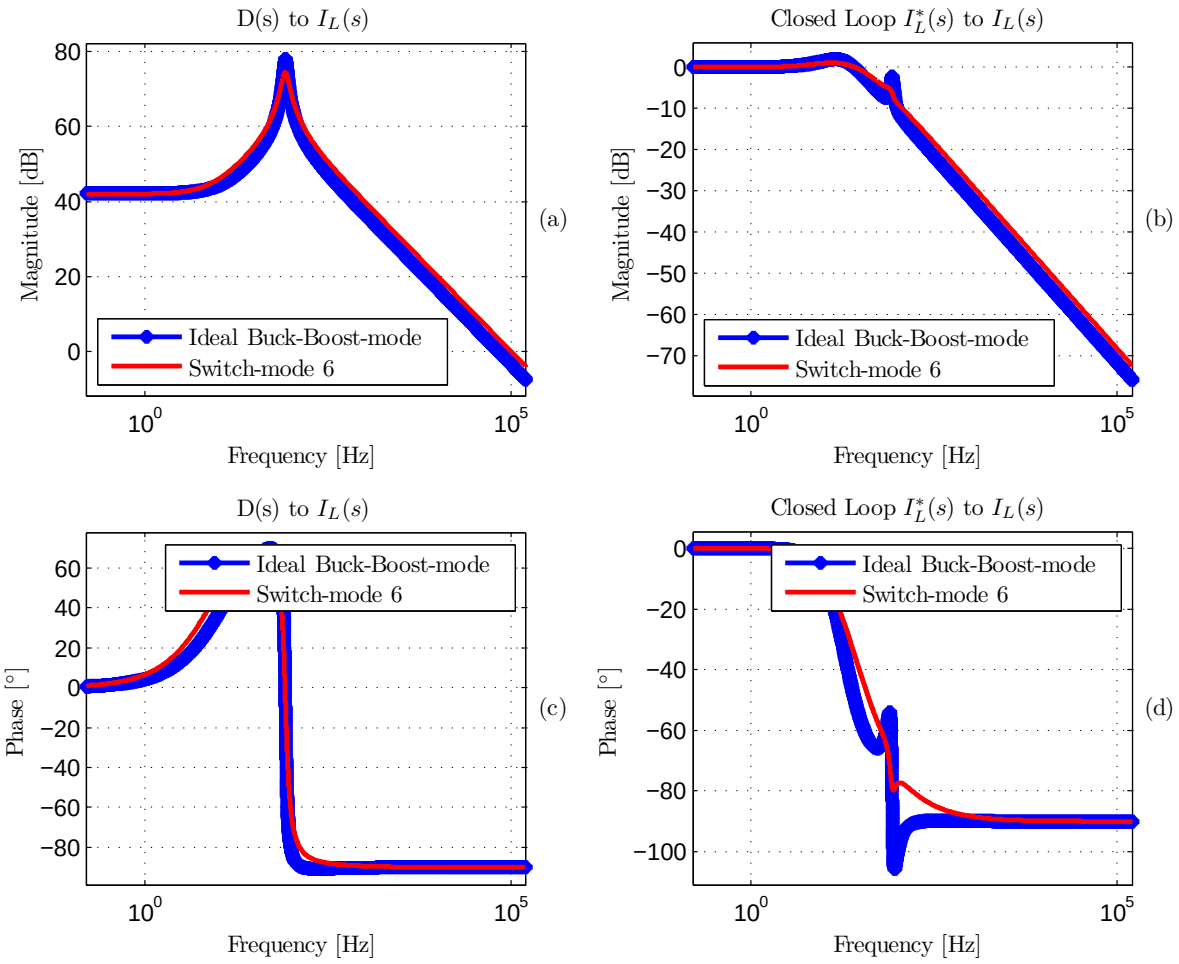

Figure C.6: Ideal and detailed bode plots of the converter in buck-boost-mode. (a) Magnitude of control-to-output transfer function. (b) Magnitude of closed-loop transfer function. (c) Phase of control-to-output transfer function. (d) Phase of closed-loop transfer function.

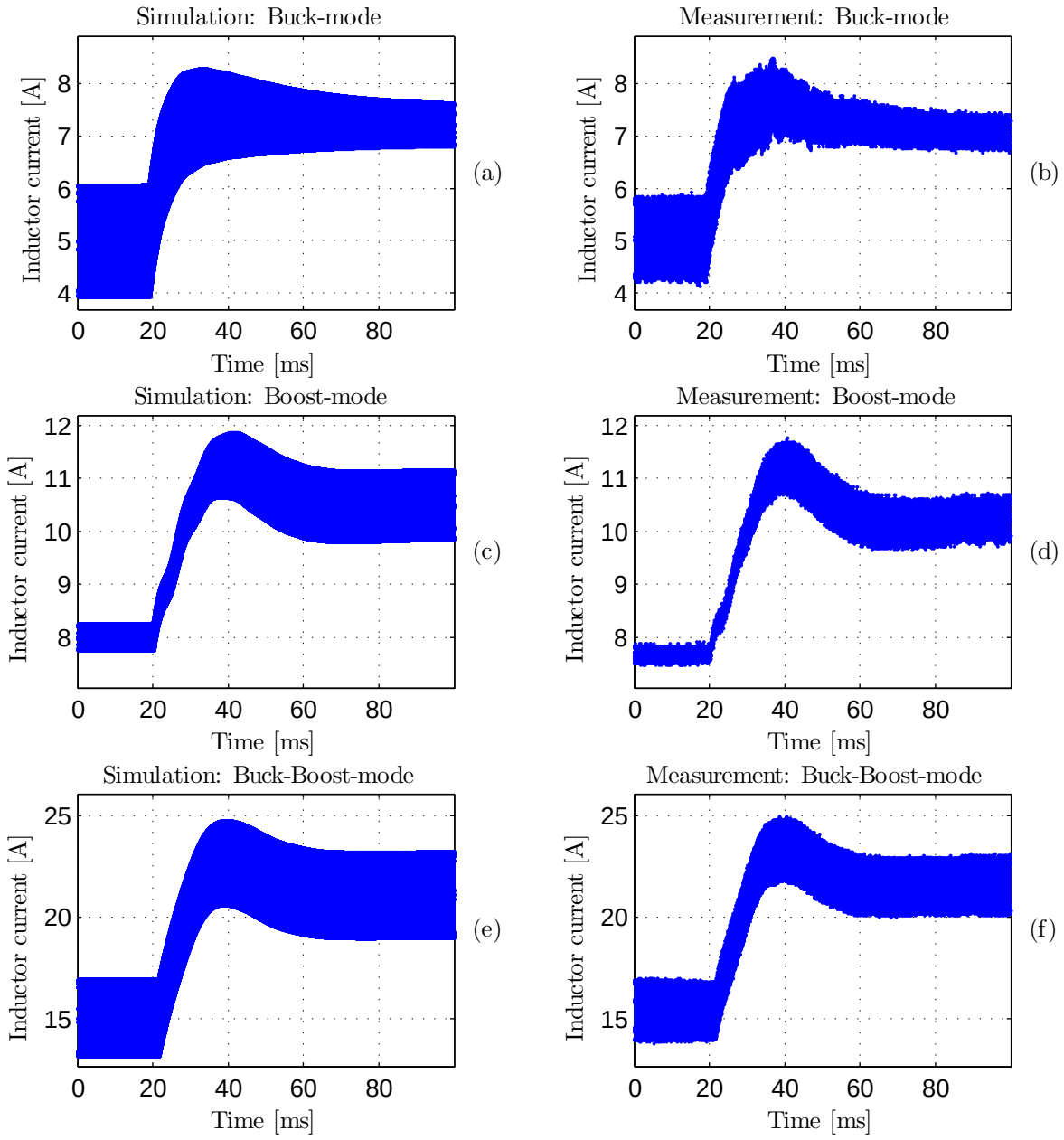

Figure C.7: Simulation and measurements of inductor current due to a step. (a) Buck-mode: simulation. (b) Buck-mode: measurement. (c) Boost-mode: simulation. (d) Boost-mode: measurement. (e) Buck-boost-mode: Simulation. (f) Buck-boost-mode: measurement.

D Equations of Bi-Directional DC/DC Converter

Steady-state equations of a bi-directional non-inverting buck-boost converter are here derived. The equations are used for calculating the power flow through the converter.

D.1 Circuit Diagram

The circuit diagram of the bi-directional converter can be seen in Figure D.1. The converter will here be analyzed in the four quadrants. For each switch Q_n a diode D_n is connected in parallel. The switches are capable of conducting the current in both directions, i.e. they will sometimes function as synchronous rectifiers. The diodes are therefore only conducting in a short interval in order to avoid a shoot through of two switches. All switches have on-resistance R_Q. The diodes are assumed to be ideal due to their short conducting time. It is assumed that the converter operated in continuous conduction mode.

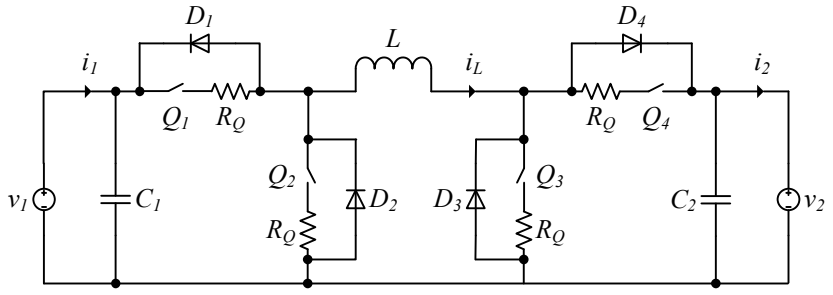

Figure D.1: Circuit diagram of bi-directional buck-boost converter.

D.2 Quadrant 1

In this quadrant the converter is operated under the following constraints

- $v_1 \geq v_2$
- $i_L \geq 0$
- Switch Q_1 and Q_4 are conducting in interval DT_s
- Switch Q_2 and Q_4 are conducting in interval $(1-D)T_s$
- Switch Q_3 are non-conducting in interval T_s

State Equations

$$\underbrace{\begin{array}{rcl} L\frac{di_L}{dt} = & v_1 - v_2 - 2R_Q i_L \\ C_1\frac{dv_1}{dt} = & i_1 - i_L \\ C_2\frac{dv_2}{dt} = & i_L - i_2 \end{array}}_{\text{Interval } DT_s} \quad \underbrace{\begin{array}{rcl} L\frac{di_L}{dt} = & -v_2 - 2R_Q i_L \\ C_1\frac{dv_1}{dt} = & i_1 \\ C_2\frac{dv_2}{dt} = & i_L - i_2 \end{array}}_{\text{Interval } (1-D)T_s} \tag{D.1}$$

State-Equation Averaging

$$\begin{aligned} L\frac{di_L}{dt} &= (v_1 - v_2 - 2R_Q i_L)d - (v_2 + 2R_Q i_L)(1-d) \\ &= v_1 d - v_2 - 2R_Q i_L \end{aligned} \tag{D.2}$$

$$\begin{aligned} C_1\frac{dv_1}{dt} &= (i_1 - i_L)d + i_1(1-d) \\ &= i_1 - i_L d \end{aligned} \tag{D.3}$$

$$\begin{aligned} C_2\frac{dv_2}{dt} &= (i_L - i_2)d + (i_L - i_2)(1-d) \\ &= i_L - i_2 \end{aligned} \tag{D.4}$$

Steady-State Equations

$$V_2 = V_1 D - 2R_Q I_L \tag{D.5}$$

$$I_1 = I_L D \tag{D.6}$$

$$I_2 = I_L \tag{D.7}$$

$$D = \begin{cases} \frac{V_2 + \sqrt{V_2^2 + 8R_Q I_1}}{2V_1} & \text{Calculated from } I_1 \\ \frac{V_2 + 2R_Q I_2}{V_1} & \text{Calculated from } I_2 \end{cases} \tag{D.8}$$

D.3 QUADRANT 2

In this quadrant the converter is operated under the following constraints

- $v_1 \geq v_2$
- $i_L < 0$
- Switch Q_2 and Q_4 are conducting in interval DT_s
- Switch Q_1 and Q_4 are conducting in interval $(1-D)T_s$
- Switch Q_3 are non-conducting in interval T_s

State Equations

$$\underbrace{\begin{array}{rcl} L\frac{di_L}{dt} = & -v_2 - 2R_Q i_L \\ C_1\frac{dv_1}{dt} = & i_1 \\ C_2\frac{dv_2}{dt} = & i_L - i_2 \end{array}}_{\text{Interval } DT_s} \quad \underbrace{\begin{array}{rcl} L\frac{di_L}{dt} = & v_1 - v_2 - 2R_Q i_L \\ C_1\frac{dv_1}{dt} = & i_1 - i_L \\ C_2\frac{dv_2}{dt} = & i_L - i_2 \end{array}}_{\text{Interval } (1-D)T_s} \tag{D.9}$$

State-Equation Averaging

$$\begin{aligned} L\frac{di_L}{dt} &= (-v_2 - 2R_Q i_L)d + (v_1 - v_2 - 2R_Q i_L)(1-d) \\ &= v_1(1-d) - v_2 - 2R_Q i_L \end{aligned} \tag{D.10}$$

$$\begin{aligned} C_1\frac{dv_1}{dt} &= i_1 d + (i_1 - i_L)(1-d) \\ &= i_1 - i_L(1-d) \end{aligned} \tag{D.11}$$

$$\begin{aligned} C_2\frac{dv_2}{dt} &= (i_L - i_2)d + (i_L - i_2)(1-d) \\ &= i_L - i_2 \end{aligned} \tag{D.12}$$

Steady-State Equations

$$V_1 = \frac{V_2 + 2R_Q I_L}{1-D} \tag{D.13}$$

$$I_1 = I_L(1-D) \tag{D.14}$$

$$I_2 = I_L \tag{D.15}$$

$$D = \begin{cases} \frac{2V_1 - V_2 - \sqrt{V_2^2 + 8R_Q V_1 I_1}}{2V_1} & \text{Calculated from } I_1 \\ \frac{V_1 - V_2 - 2R_Q I_2}{V_1} & \text{Calculated from } I_2 \end{cases} \tag{D.16}$$

D.4 QUADRANT 3

In this quadrant the converter is operated under the following constraints

- $v_1 < v_2$
- $i_L \geq 0$
- Switch Q_1 and Q_3 are conducting in interval DT_s
- Switch Q_1 and Q_4 are conducting in interval $(1-D)T_s$
- Switch Q_2 are non-conducting in interval T_s

State Equations

$$\underbrace{\begin{array}{rcl} L\frac{di_L}{dt} &=& v_1 - 2R_Q i_L \\ C_1\frac{dv_1}{dt} &=& i_1 - i_L \\ C_2\frac{dv_2}{dt} &=& -i_2 \end{array}}_{\text{Interval } DT_s} \qquad \underbrace{\begin{array}{rcl} L\frac{di_L}{dt} &=& v_1 - v_2 - 2R_Q i_L \\ C_1\frac{dv_1}{dt} &=& i_1 - i_L \\ C_2\frac{dv_2}{dt} &=& i_L - i_2 \end{array}}_{\text{Interval } (1-D)T_s} \tag{D.17}$$

State-Equation Averaging

$$\begin{aligned} L\frac{di_L}{dt} &= (v_1 - 2R_Q i_L)d + (v_1 - v_2 - 2R_Q i_L)(1-d) \\ &= v_1 - v_2(1-d) - 2R_Q i_L \end{aligned} \tag{D.18}$$

$$\begin{aligned} C_1\frac{dv_1}{dt} &= (i_1 - i_L)d + (i_1 - i_L)(1-d) \\ &= i_1 - i_L \end{aligned} \tag{D.19}$$

$$\begin{aligned} C_2\frac{dv_2}{dt} &= -i_2 d + (i_L - i_2)(1-d) \\ &= i_L(1-d) - i_2 \end{aligned} \tag{D.20}$$

Steady-State Equations

$$V_2 = \frac{V_1 - 2R_Q I_L}{1-D} \tag{D.21}$$

$$I_1 = I_L \tag{D.22}$$

$$I_2 = I_L(1-D) \tag{D.23}$$

$$D = \begin{cases} \frac{V_2 - V_1 + 2R_Q I_1}{V_2} & \text{Calculated from } I_1 \\ \frac{2V_2 - V_1 - \sqrt{V_1^2 - 8R_Q V_2 I_2}}{2V_2} & \text{Calculated from } I_2 \end{cases} \tag{D.24}$$

D.5 QUADRANT 4

In this quadrant the converter is operated under the following constraints

- $v_1 < v_2$
- $i_L < 0$
- Switch Q_1 and Q_4 are conducting in interval DT_s
- Switch Q_1 and Q_3 are conducting in interval $(1-D)T_s$
- Switch Q_2 are non-conducting in interval T_s

State Equations

$$\underbrace{\begin{array}{rcl} L\frac{di_L}{dt} &=& v_1 - v_2 - 2R_Q i_L \\ C_1\frac{dv_1}{dt} &=& i_1 - i_L \\ C_2\frac{dv_2}{dt} &=& i_L - i_2 \end{array}}_{\text{Interval } DT_s} \qquad \underbrace{\begin{array}{rcl} L\frac{di_L}{dt} &=& v_1 - 2R_Q i_L \\ C_1\frac{dv_1}{dt} &=& i_1 - i_L \\ C_2\frac{dv_2}{dt} &=& -i_2 \end{array}}_{\text{Interval } (1-D)T_s} \tag{D.25}$$

State-Equation Averaging

$$\begin{aligned} L\frac{di_L}{dt} &= (v_1 - v_2 - 2R_Q i_L)d + (v_1 - 2R_Q i_L)(1-d) \\ &= v_1 - v_2 d - 2R_Q i_L \end{aligned} \tag{D.26}$$

$$\begin{aligned} C_1\frac{dv_1}{dt} &= (i_1 - i_L)d + (i_1 - i_L)(1-d) \\ &= i_1 - i_L \end{aligned} \tag{D.27}$$

$$\begin{aligned} C_2\frac{dv_2}{dt} &= (i_L - i_2)d - i_2(1-d) \\ &= i_L d - i_2 \end{aligned} \tag{D.28}$$

Steady-State Equations

$$V_1 = V_2 D + 2R_Q I_L \tag{D.29}$$

$$I_1 = I_L \tag{D.30}$$

$$I_2 = I_L D \tag{D.31}$$

$$D = \begin{cases} \frac{V_1 - 2R_Q I_1}{V_2} & \text{Calculated from } I_1 \\ \frac{V_1 + \sqrt{V_1^2 - 8R_Q V_2 I_2}}{2V_2} & \text{Calculated from } I_2 \end{cases} \tag{D.32}$$

D.6 SUMMARY

For all four quadrants the power of source 2 P_2 can be expressed as the power of source 1 P_1 and the loss of the switches P_Q:

$$\underbrace{V_2 I_2}_{P_2} = \underbrace{V_1 I_1}_{P_1} - \underbrace{2R_Q I_2^2}_{P_Q} \qquad [\mathrm{W}] \tag{D.33}$$

This means that the current of source 1 and 2 are

$$I_2 = \frac{-V_2 + \sqrt{V_2^2 + 8R_Q P_1}}{4R_Q} \qquad [\mathrm{A}] \tag{D.34}$$

$$I_1 = \frac{P_2 + 2R_Q I_2^2}{V_1} \qquad [\mathrm{A}] \tag{D.35}$$

D.7 CONCLUSION

Steady-state equations of a bi-directional non-inverting buck-boost converter are derived for all four quadrants in order to be able to calculate the power flow through it. Only the resistive switch loss is considered for simplicity.